Observed Circulation and Inferred Sediment Transport in Hudson Submarine Canyon

by

Frances Luellen Stephenson Hotchkiss

A.B., Oberlin College
(1976)

S.M., Massachusetts Institute of Technology
(1980)

SUBMITTED IN PARTIAL FULFILLMENT
OF THE REQUIREMENTS FOR THE
DEGREE OF

DOCTOR OF PHILOSOPHY

at the

MASSACHUSETTS INSTITUTE OF TECHNOLOGY

and the

WOODS HOLE OCEANOGRAPHIC INSTITUTION

May 1982

Signature of Author_____
Joint Program in Oceanography
Massachusetts Institute of Technology
Woods Hole Oceanographic Institution
May 24, 1982

Certified by_____
Erik Mollo-Christensen
Thesis Supervisor

Accepted by_____
Lindgren / Joseph Pedlosky
Chairman, Joint Committee for Physical Oceanography

Observed Circulation and Inferred Sediment Transport
in
Hudson Submarine Canyon

by

Frances Luellen Stephenson Hotchkiss

Submitted to the MIT-WHOI Joint Program in
Physical Oceanography on May 24, 1982
in partial fulfillment of the requirements
for the degree of Doctor of Philosophy

ABSTRACT

Velocity and temperature time series from Hudson Submarine Canyon and hydrographic surveys of seven canyons of the Middle Atlantic Bight indicate that the effects of storms, tides, and incoming internal waves are intensified in submarine canyons. Storms with strong eastward and westward wind stress were found to cause strong upwelling and downwelling through the upper layers of Hudson Canyon. Storm-forced upwelling also caused strong down-canyon flows at the canyon floor.

Internal waves were found to be concentrated in the canyon head and near the floor, in agreement with theoretical predictions. Slope water apparently circulates slowly through the outer part of the canyon and is mixed in near-floor layers which could be caused by breaking internal waves.

Internal tides are generated at the floor in the central part of the canyon. Oscillations at tidal frequencies dominate the near-floor velocity field below the thermocline, and are accompanied by high-frequency spikes that may be nonlinear interface waves propagating on the top of the bottom mixed layer. A numerical model was used to calculate mixing in the canyon's bottom boundary layer caused by an unstable density gradient during flood tide.

Energetic internal wave activity is apparently responsible for sediment sorting in the canyon head; the internal waves become more energetic as the sediment grain size increases. Below the thermocline, the tidal oscillations vary in amplitude with the phases of the moon; the observed deposition of mud can easily occur during weeks of low velocity.

Thesis supervisor: Dr. Erik Mollo-Christensen
Professor of Physical Oceanography, MIT

Acknowledgements

This project has required more than five years to complete, and I have had much help and encouragement from teachers, friends and family. I especially thank my advisor, Erik Mollo-Christenson, for his practical advice, scientific knowledge, and personal enthusiasm. To Bill Grant for his help with the material on fluid mechanics and boundary layers, and to Bob Beardsley for perspective on my data, I am grateful. I thank Carl Wunsch for starting this project and for allowing me to finish it.

I am grateful to Captain E. Mysona and the crew of the R/V Oceanus for making the work at sea possible. R. Millard played an essential role in the acquisition and reduction of the CTD data. R. Reid set and recovered the moorings.

Charmaine King's work with the MIT computer has made it possible for me to be in touch with my data. I am very appreciative of the moral and practical support of Gail Czarnecki and the Ocean Engineering Department of Florida Atlantic University. Most of all, I thank my husband Dan Hotchkiss, who has typed, programmed, spelled, and helped in every way possible, and my father Charles Stephenson, without whose constant confidence that I could become a scientist, this work would be neither completed nor begun.

This work has been supported by a National Science Foundation graduate fellowship and by the Office of Naval Research under Contracts N00014-75-C-0291 and N00014-80-C-0273.

Table of Contents

Chapter I

Introduction

Submarine canyons are deep valleys in the continental margin that have steep walls, rocky outcrops, tributaries, and, usually, winding courses and v-shaped profiles (Shepard and Dill, 1966, p. 5). Hudson Canyon is one of at least 26 submarine canyons that notch the continental slope off the east coast of the United States in a series that extends from offshore of Chesapeake Bay to the east end of Georges Bank. Recently, Shepard and his co-workers measured near-floor currents in many submarine canyons and concluded that strong oscillatory currents and occasional very strong turbidity currents are responsible for enough sediment transport and erosion to maintain and modify the canyons (Shepard et al., 1979). Mooers et al. (1979) and Ruzecki (1979) surveyed the water masses around two East Coast canyons and concluded that submarine canyons are important sites for the exchange of water between the continental shelf and the deep sea. I will present a more extensive study of the circulation in Hudson Submarine Canyon, investigate the physical processes responsible for the strong currents in this East Coast canyon, and

evaluate their ability to move sediment and water between the shelf and the deep sea.

A. Currents and sediment transport

Previous research on submarine canyons indicates that they contain complex circulations that vary significantly in both space and time. Some universality was documented by Shepard et al. (1979), who demonstrated that currents near the floors of many submarine canyons are similar in character and of significant strength. In the 25 canyons of their sample, strong oscillatory currents prevailed near the floor, and distinctive internal wave trains could be observed to travel along the axes, usually going up-canyon. Occasionally slow turbidity currents were also observed. Turbidity currents are widely thought to be gravity currents caused by suspended sediment in the near-bottom water. The weight of the sediment is said to sustain down-slope currents fast enough to cause sufficient turbulence to keep the sediment in suspension. From visual observations, Shepard et al. estimated that sediment transport will occur when the velocity 3 m above the floor is above 25 to 35 cm/sec. They observed such speeds commonly, more frequently in the down-canyon than in the up-canyon direction.

Inman et al. (1976) explain strong canyon currents as the result of interactions among strong winds, surface waves, set-up at the coast, and canyon bathymetry. This theory, and

Shepard's observed patterns, are largely based on the canyons of the California coast, which have near-shore heads in shallow water. For example, Scripps Canyon is within 300 m of shore and the water around its head is only 20 m deep. East Coast submarine canyons, shown in figure 1-1, are at the outside edge of a much wider continental shelf. Their heads lie at least 80 km from shore, and in water 80 to 200 m deep. Near-shore and sea-surface processes are not likely to affect these canyons as strongly or as frequently as they affect those on the West Coast.

The East Coast canyons are frequently divided into "active" and "inactive" groups. The canyons near Georges Bank contain gravel and sometimes have clear rock floors, so they are said to be actively transporting coarse sediment and perhaps cutting deeper into the continental shelf. The canyons to the southwest, including Block, Hudson, Baltimore, and Wilmington Canyons, contain fine sediments such as silt and clay and are called "inactive" because strong currents should keep this material swept clear. Keller and Shepard (1978) point out that a difference in current activity is not the only explanation for the difference in sediment size since the source sediments entering the "active" canyons are coarser than those entering the "inactive" canyons.

The pattern of variation of relative grain size is similar in all the East Coast canyons, both "active" and "inactive," which suggests that the pattern of their circu-

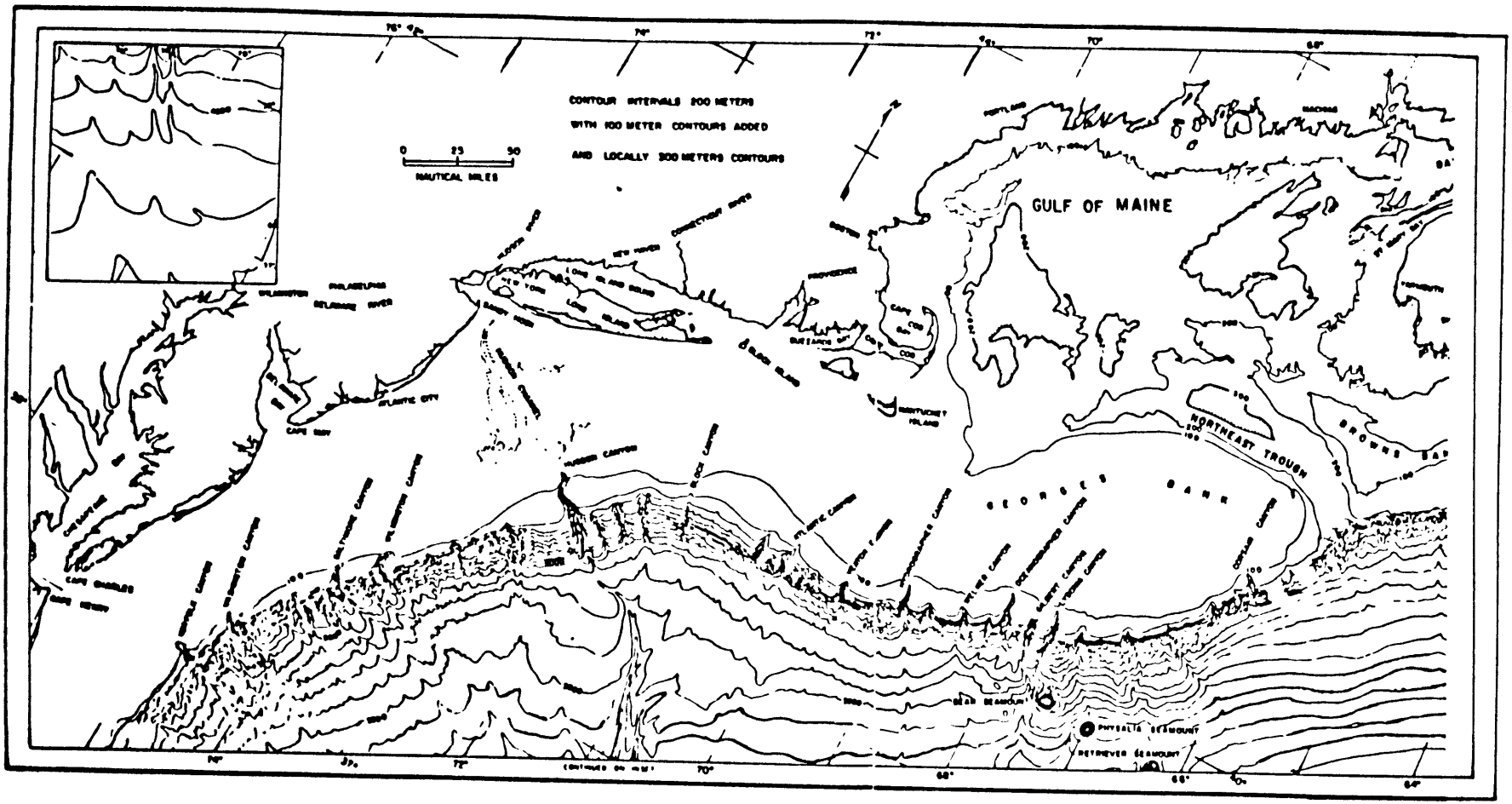

Figure 1-1. The canyons off the northeastern United States. From Shepard, et al. (1979). Bathymetry from Uchupi (1965).

lation is also similar. In each canyon, the coarsest grains are found in the canyon head, and from there a zone of gradually decreasing grain size extends down the floor of the canyon. This indicates that currents in the head and along the floor are occasionally strong enough to carry the coarse grains in and frequently strong enough to carry any finer grains out, and that the currents weaken with increasing depth. In the deep parts of many East Coast canyons, where their axes are roughly 2000 m deep, the floor sediment records the effects of occasional currents strong enough to transport sand. Here the sand forms ripple marks and scoured depressions around boulders, and is sometimes covered by a thin blanket of mud that has accumulated while the current was weak. (See papers by Stanley, 1967 and 1974; Stanley and Kelling, 1968; Dillon and Zimmerman, 1970; Ross, 1968; and Cacchione et al., 1978.) Sediment cores from deep parts of Veatch, Washington, and Norfolk Canyons indicate that sporadic events have carried sand down these canyons in the recent past. (Forde, 1981).

Keller and Shepard (1978) report that near-floor currents in five East Coast canyons (Hydrographer, Hudson, Wilmington, Washington and Norfolk) oscillate between up- and down-canyon with a roughly semidiurnal period. Speeds are frequently higher in the canyon heads than farther out in the canyons. In all cases, speeds are higher 3 m above the floor than 30 m above the floor. Mean velocities are more often

down-canyon than up. Keller and Shepard assessed the sediment-transporting ability of these currents by extrapolating to their 3-meter instrument height the velocity threshold for initiation of sediment motion developed by Miller et al. (1977). This involved assuming a logarithmic velocity profile and known bottom roughness. Using this criterion and estimates of sediment grain size they found that the current velocities at 3 m in the canyons were often sufficient to initiate motion of the underlying sediments. They concluded that bedload transport occurs frequently in the heads of many East Coast canyons.

Hudson Canyon shares the common pattern of relative sediment size variation at its shallow and deep ends, but has in addition an accumulation of fluffy mud in its mid-section. The energetic head zone of Hudson Canyon extends to a depth of 400 m, and the muddy section extends from there to about 1000 m. Deeper than 1000 m, the floor sediments in Hudson Canyon resemble those in the deep parts of other East Coast canyons. These zones are shown on figure 1-2.

Coarse sand covers the floor of upper Hudson Canyon only to 275 m depth. Keller used the submersible ALVIN to observe the sediment in the canyon head. He (Keller and Shepard, 1978) reported that grains were hopping about on the floor erratically, as in the turbulence under a "breaker zone" but on a smaller scale. Water samples collected several meters above the floor at 200 m and at 300 m included grains of fine

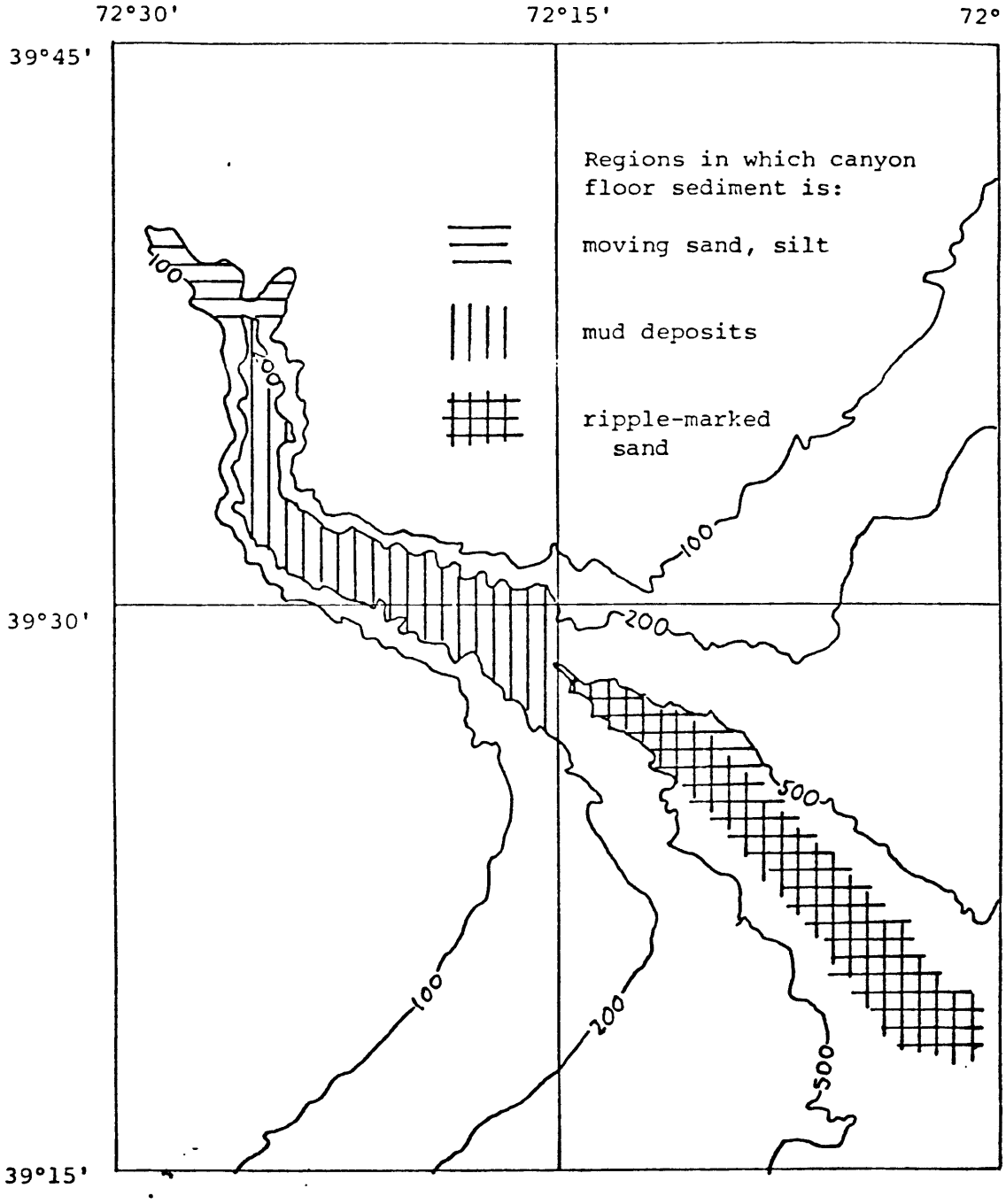

Figure 1-2. Bathymetry of Hudson Submarine Canyon (depths in fathoms) showing sediment zones. (Chart adapted from NOAA 0807 N-52.)

sand and silt. Grains of this size settle to the bottom quickly after being suspended. These grain sizes were not found in water samples collected over the canyon walls or over the surrounding shelf, so the grains found in the canyon must have been suspended locally by strong bottom shear stress immediately before the samples were taken. In the head of Hudson Canyon, three days after a hurricane passed through New York Bight, ALVIN encountered turbid water at a site where the water had been clear the day before the hurricane and where it was again clear two days later (Keller and Shepard, 1978).

At a depth of about 400 m, the floor of the canyon changes from fine sands and silts to thick deposits of mud, silty clay and clayey silt. Although this unconsolidated mud seemed very susceptible to erosion, Keller et al. (1973) found it was not affected by velocities up to 27 cm/sec. In the canyon head, concentrations of fine suspended material are five times the normal shelf concentration level. The concentration of fine suspended material decreases with depth over the mud deposits in the canyon and is negligible down-canyon of them (Biscaye and Olsen, 1976). Drake et al. (1978) note a difference between the near-floor tidal currents that Shepard measured at a depth of 1254 m and those in the canyon head. In the canyon head, the current direction shifts quite abruptly between up- and down-canyon, while the speed remains high. At greater depths, the speed is very

low during long intervals while the direction changes. Drake et al. suggest that the lull in water speed allows the mud to settle out. Once the mud is deposited, a very strong current is apparently needed to resuspend it.

Fine sand again makes up the floor in the deeper part of Hudson Canyon. A thin surface layer of mud is frequently reported, but scour marks around boulders and ripple marks in the sand indicate that occasional strong currents sweep through. The currents measured in the deep part of the canyon are usually less than 10 cm/sec (Cacchione et al., 1978).

Near-floor currents in the muddy mid-section of Hudson Canyon were observed for seven weeks by Amos et al. (1977). The observed currents were dominated by up- and down-canyon oscillations of tidal period, of higher amplitude than tidal currents measured on the adjacent continental slope. The cross-canyon velocity component was of higher frequency and lower amplitude than the along-canyon component. Velocity spectra from these observations show little or no inertial energy, which is consistent with the general suppression of inertial waves near seamounts and slopes. The peak velocities measured by various investigators in Hudson Canyon range from 35 cm/sec in the canyon head to 2 cm/sec at 2000 m.

B. Hydrography

In the Middle Atlantic Bight, a distinct water mass

(called shelf water) lies over the continental shelf and is separated from the water masses of the continental slope (collectively called slope water) by the shelf-slope front. The slope water can be divided into five water masses (following Gordon et al., 1976). The properties of the deep layers are largely determined by the general circulation of the Western North Atlantic: North Atlantic deep water at depths greater than 2000 m, a mixture of Labrador Sea water and Mediterranean Sea overflow at depths between 1000 and 2000 m, Irminger Atlantic water at 300 to 1000 m, and a mixture of North Atlantic central water and Scotian Slope water from 300 m up to a salinity maximum at about 100 m. The surface water over the slope is North Atlantic central water with a strong shelf water component. The processes which introduce shelf water into the slope water are not completely understood; submarine canyons are thought to play an important role.

The shelf water undergoes a strong seasonal cycle. In the winter it is only weakly stratified and ranges in temperature from 10° at the shelf break to 4° at the coast. Vernal warming and fresh runoff create a strong pycnocline which lasts through the summer months. The cold, fresh bottom water isolated under the pycnocline along the outer shelf is called the cold pool. In October and November, overturning and mixing eradicate the shelf pycnocline and cold pool and return the shelf water to its winter mixed state. The

schematic hydrographic sections of figure 1-3 illustrate typical conditions at the edge of the continental shelf in September.

Gordon et al. (1976) surveyed a hydrographic section through Hudson Canyon in October, 1974, along with sections across the nearby shelf and slope. Hurricane Becky and two tropical storms had passed east of the Middle Atlantic Bight in August and September, 1974. In October, Gordon et al. found a 50-meter thick mixed surface layer on the shelf, with a shallow tongue of slope water intruding above Hudson Canyon and on the shelf just southwest of it. Unusually salty water at temperatures of 8° to 9° was only found inside the canyon, suggesting enhanced mixing between slope water masses there. An important product of this survey is a description of the oxygen contents of the shelf and slope water masses. Gordon et al. measured high oxygen concentrations, above 5 ml/l, near the surface and in the deep slope water. The lowest oxygen concentrations were about 3.5 ml/l and were found in the cold pool and just below the pycnocline in the slope water.

Ruzecki (1979) compared the volumes and positions of the water masses near Norfolk Canyon with those in a canyon-less region that crosses the shelf break and slope south of Norfolk Canyon. He surveyed these regions in November 1974, September 1975, January 1976, and June 1977, covering all four seasons. Ruzecki found that although different proces-

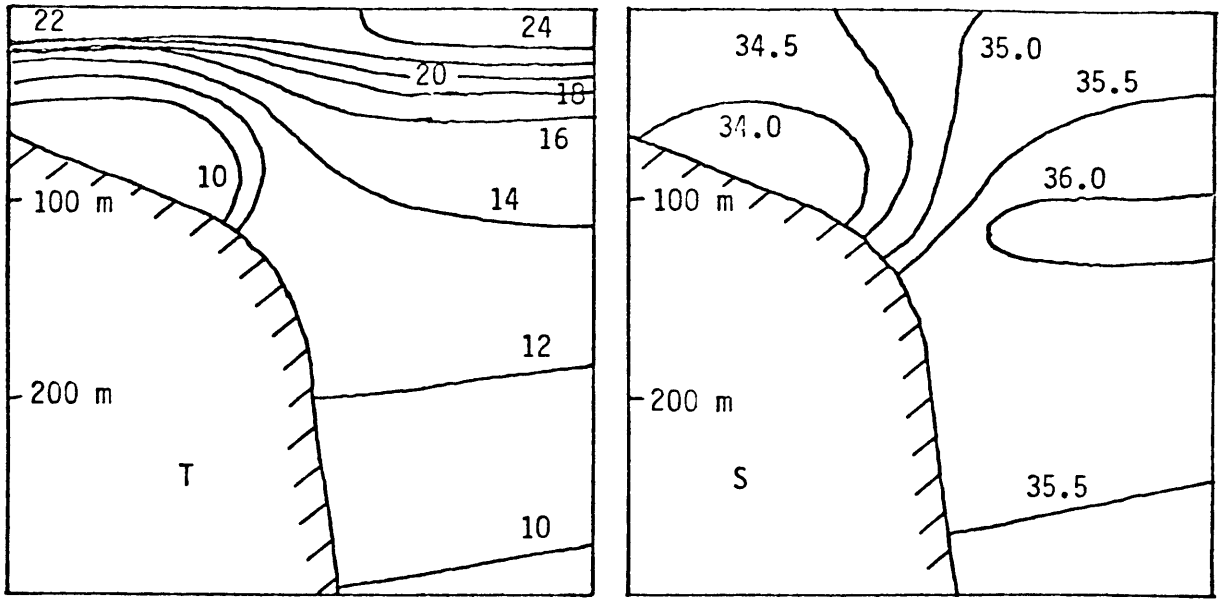

Figure 1-3. Schematic sections showing typical distributions of temperature, salinity, density, and water masses at edge of Middle Atlantic Shelf in late summer.

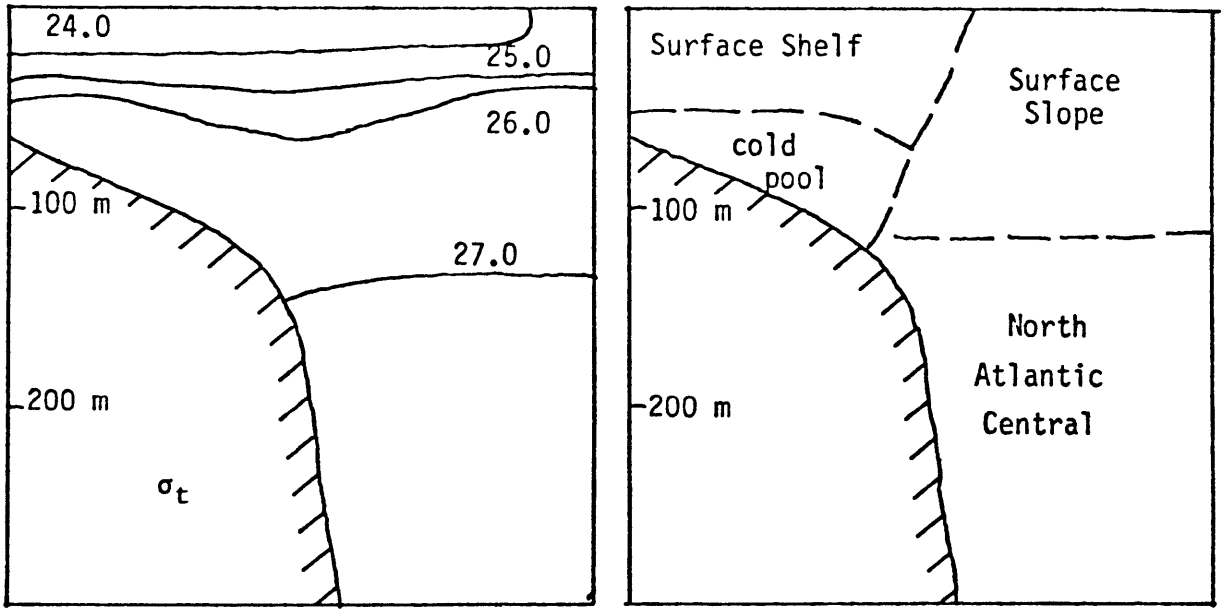

ses were important in different seasons, Norfolk Canyon was continually the site of enhanced exchange across the shelf-slope front. In general, the canyon water was predominantly slope water, with stratification similar to that above the continental slope outside the canyon. The shelf-slope front was unusually steep and was displaced shoreward over the canyon. Mixtures of slope waters and shelf waters were found in greater volumes in the sections along Norfolk Canyon than in other across-slope sections, indicating that the slope water is continually mixing with the overlying shelf water in the canyon.

During Ruzecki's summer (September) survey, stratification was strong and many thin filaments and tongues of water masses interleaved along the canyon. Interleaving and calving were less common in the rest of the survey area. Less interleaving was observed in spring and autumn, and none at all in winter. The winter survey found a distinct tongue of Western North Atlantic water protruding up the canyon and spilling onto the shelf at the canyon head, perhaps forced by an eddy further offshore. Upwelling had apparently also occurred prior to the November survey when the dominant mode of slope water in the canyon was colder than the dominant mode found at the same depths above the slope.

Mooers et al. (1979) carried out two quasi-synoptic surveys of the shelf break region around Baltimore and Wilmington Canyons, including a high-resolution survey of

Wilmington Canyon, in July, 1977. At the time, two anti-cyclonic eddies were near the survey area and tended to pull water off the shelf in the south part of the region. Off-shelf flow was particularly strong near the bottom along the southwest side of Wilmington Canyon. This suggests that the effects of eddies on shelf circulation are enhanced in the vicinity of submarine canyons. Mooers et al. found that the cold pool, a distinctive mass of cold bottom water found near the edge of the shelf, was bounded by a much more convoluted surface in the vicinity of the canyons than elsewhere in the survey area. The cold pool appeared to be in the early stages of calving; the ends of two intrusions of the cold pool into the slope water appeared to be pinching off to form discrete parcels of cold pool water embedded in slope water. Mooers et al. concluded that, except over submarine canyons, deformations of the shelf-slope front can be coherently mapped from hydrographic stations spaced 10 km apart across the shelf, 20 km apart along the shelf, and repeated at 10-day intervals. At Wilmington Canyon, they found that daily sampling with a resolution of several kilometers is required for proper description of the calving process.

Welch (1981) noted that intrusions of slope water across the shelf-slope front are sometimes observed in the seasonal thermocline when the front has only a weak density signal but the thermocline is thinner over the shelf than over the

slope. He proposed the following explanation for these intrusions: Mixing processes on the shelf produce a very thin thermocline compared to that in the slope water. Under hydrostatic conditions, the difference in thermocline thickness produces an offshore pressure gradient in the region where the thermocline thickness changes. Assuming that the pressure gradient forces a steady, rotational, horizontal flow with vertical frictional forces (Ekman dynamics), the result is a net transport of water northward along the front. The across-front flows balance each other, but consist of a thin layer flowing onshore at the center of the thermocline between more diffuse offshore flows. These produce interleaving across the shelf-slope front, and tend to reduce the contrast in thermocline thickness.

C. Overview

I am reporting here on a single hydrographic survey that covered a larger area less intensively than those summarized above, and on an array of moored instruments that covered only the part of Hudson Canyon that is inshore of the shelf break, but covered more of the water column and was in place for a longer period that previous arrays. These data were used to examine which physical processes have important effects on sediment transport and exchange across the shelf-slope front through the Hudson Canyon.

Our hydrographic survey included surveys of the regions

of Baltimore, Hydrographer, and Hudson Canyons and additional sections through Wilmington, Block, Veatch, and Oceanographer Canyons. Our survey was in late September and early October, beginning at Baltimore Canyon and going north and east to Oceanographer Canyon as the mixing season progressed. We found several intrusions around Baltimore and Wilmington Canyons, the remnants of two intrusions near Hudson Canyon, and no sign of intrusions near Veatch, Hydrographer, or Oceanographer Canyon. This progression fits the pattern found by Ruzecki, with increasing latitude adding to the temporal effect of advancing season. As shown in figure 1-4, eddies were present during our hydrographic survey, near Veatch and Hydrographer Canyons and Baltimore and Wilmington Canyons.

Reservoirs of cold water were found in both Wilmington and Hudson Canyons; the cold pool in Hudson Canyon disappeared during a storm. The effects of this storm in the Hudson Canyon region indicate that the storms which cause mixing of the shelf water in autumn may have significant effects on the circulation in East Coast canyons. Evidence of enhanced vertical mixing was found in many of the canyons we surveyed.

Our moored array in Hudson Canyon was designed primarily to observe the internal waves there. Concentrations of internal wave energy were found near the canyon floor and in the canyon head. The shape of the velocity oscillation

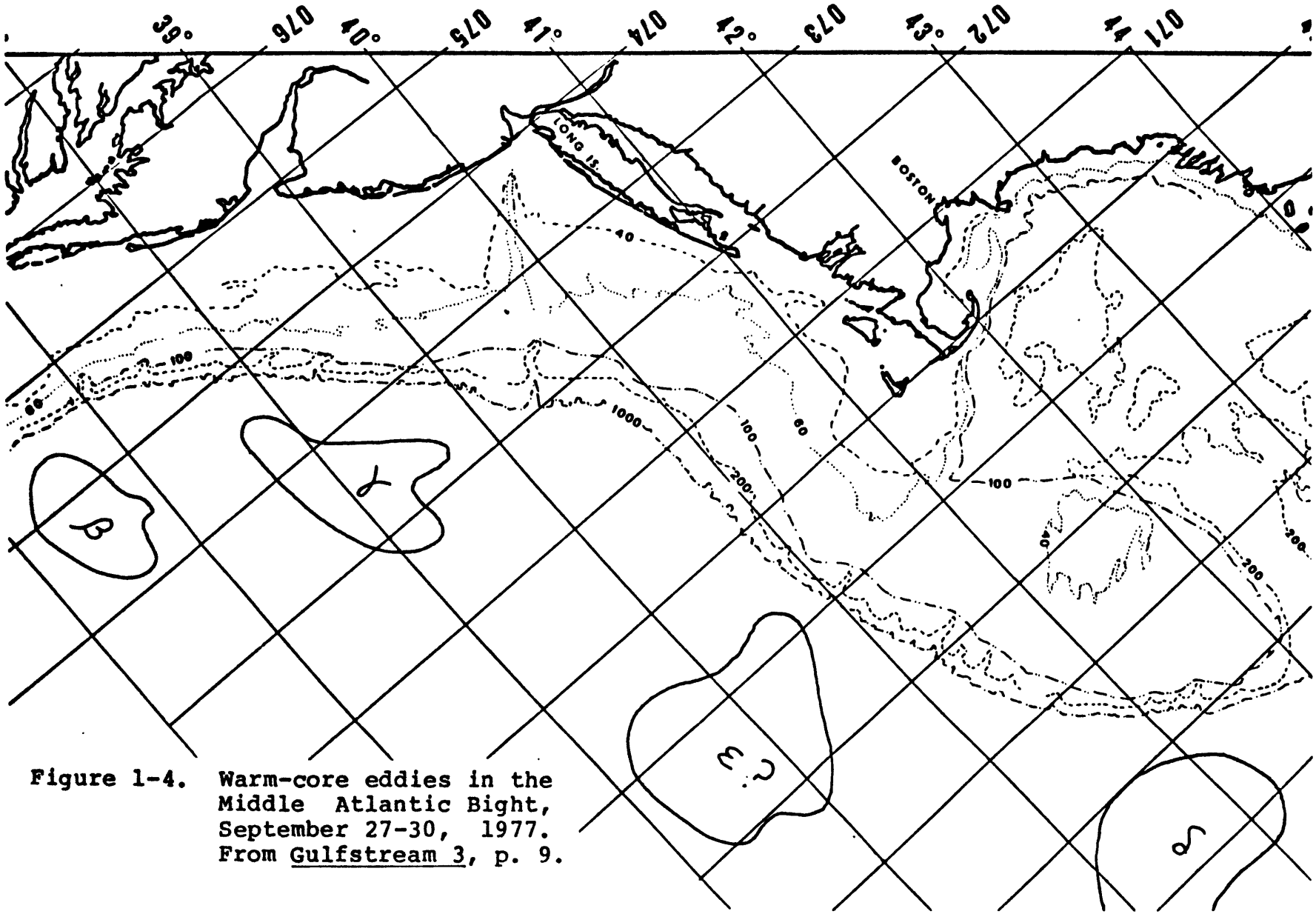

Figure 1-4. Warm-core eddies in the Middle Atlantic Bight, September 27-30, 1977. From Gulfstream 3, p. 9.

varied along the canyon consistent with the pattern noted by Drake et al. (1978): smooth oscillation in the canyon head changing to isolated sharp spikes in the deeper part of the canyon. The internal waves in Hudson Canyon were anisotropic, with velocities aligned with the canyon axis and near-floor phase lags that indicate propagation up-slope from the open ocean. The semidiurnal frequency band contained half the internal wave energy; internal tides are apparently being generated along the floor in the central part of the canyon.

The lower-frequency currents in Hudson Canyon were dominated by the effects of storms and of winter cooling and mixing of the overlying shelf water. Storms with strong westerly winds caused strong upwelling currents in the upper layers of the canyon and strong down-canyon flows along the canyon floor. Storms with strong easterly winds caused downwelling of shelf water into the canyon head and down-canyon currents above the thermocline in the canyon. The mixed water found in the canyon head in early autumn became stratified as winter cooling progressed.

Near the floor in the outer canyon, strong pulses at semidiurnal and diurnal frequencies dominated the measured currents. The strength of these pulses increased at spring tides. On most days, the down-canyon pulses were stronger than the up-canyon pulses. I suggest that the water near the canyon floor overturns and mixes during the up-canyon (flood)

tide, creating a bottom mixed layer. Irregularities in the layer thickness form trains of nonlinear interface waves that propagate down the canyon during the ebb tide and increase the near-floor velocity. I found the bottom shear stress under these pulses frequently strong enough to initiate the motion of non-cohesive grains the size of mud. The currents we measured at the edge of the canyon head were strong enough to move the sediment only about once a week. Current measurements in the shallowest part of the canyon head and a better understanding of cohesive sediments are needed to fully understand the sediment transport in Hudson Canyon.

Chapter II

Hydrography

We measured temperature, conductivity, pressure, and dissolved oxygen concentration in seven Middle Atlantic Bight canyons (Baltimore, Wilmington, Hudson, Block, Veatch, Hydrographer, and Oceanographer) and in adjacent shelf and slope regions, September 22 through October 3, 1977. Carl Wunsch designed the survey as chief scientist of Oceanus Cruise 34. Robert Millard provided a Neil Brown CTD and supervised data collection and calibration. See Appendix A for a complete data report.

A. Hydrography of Hudson Canyon

Our survey included two sections through Hudson Canyon. The stations of the first section were included in a regional survey conducted on September 24-27, following a week of westward (downwelling-favorable) winds (at JFK Airport) which reached a maximum of 8 m/sec on September 25 (yearday 268, see figure 2-1). In this early survey of Hudson Canyon (shown in figure 2-2) we found the canyon head full of light, relatively fresh water with the cold pool extending over the canyon head. On September 28, high seas caused by a hurri-

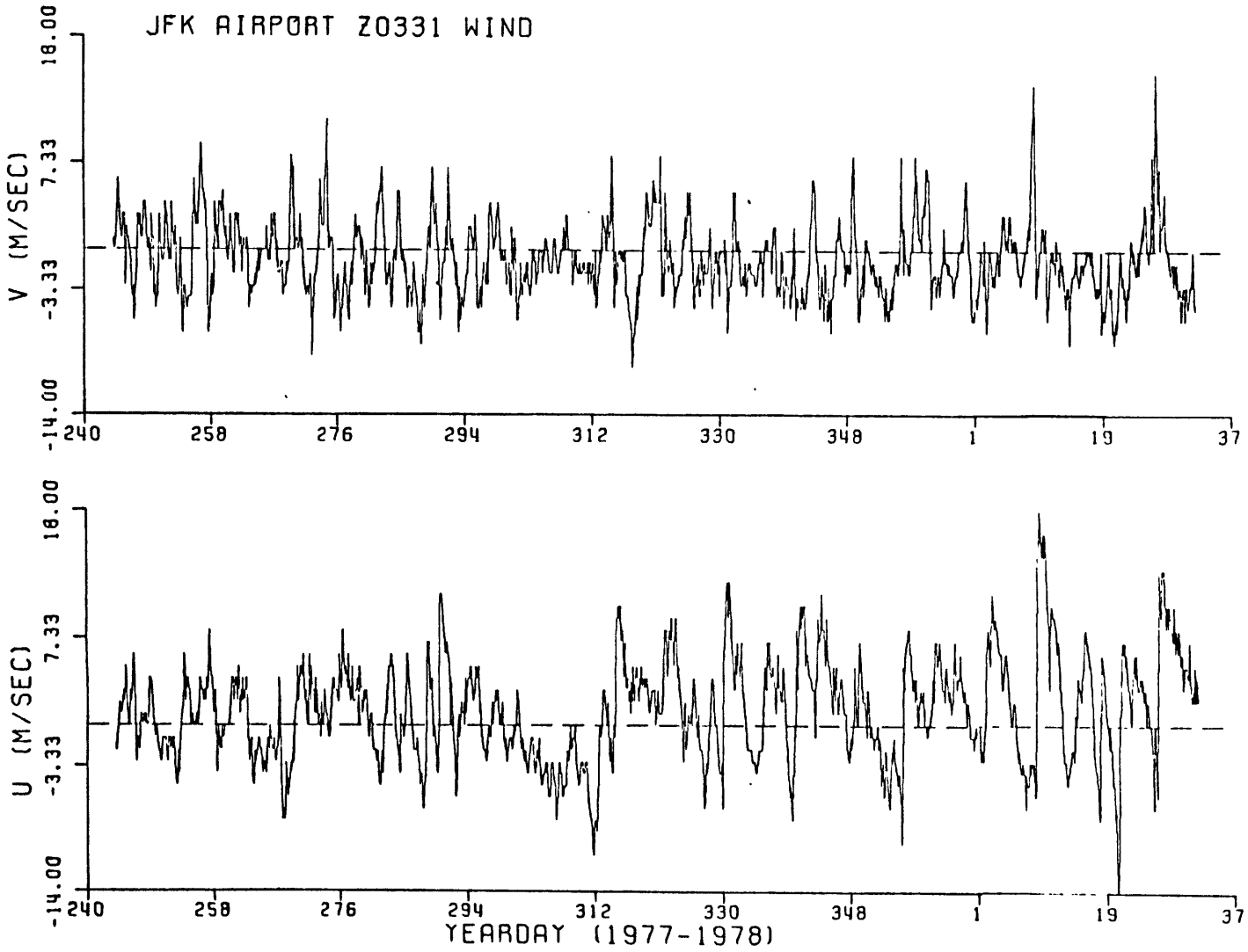

Figure 2-1. Eastward (U) and northward (V) wind speed at JFK Airport, New York City, September 1977 through January 1978.

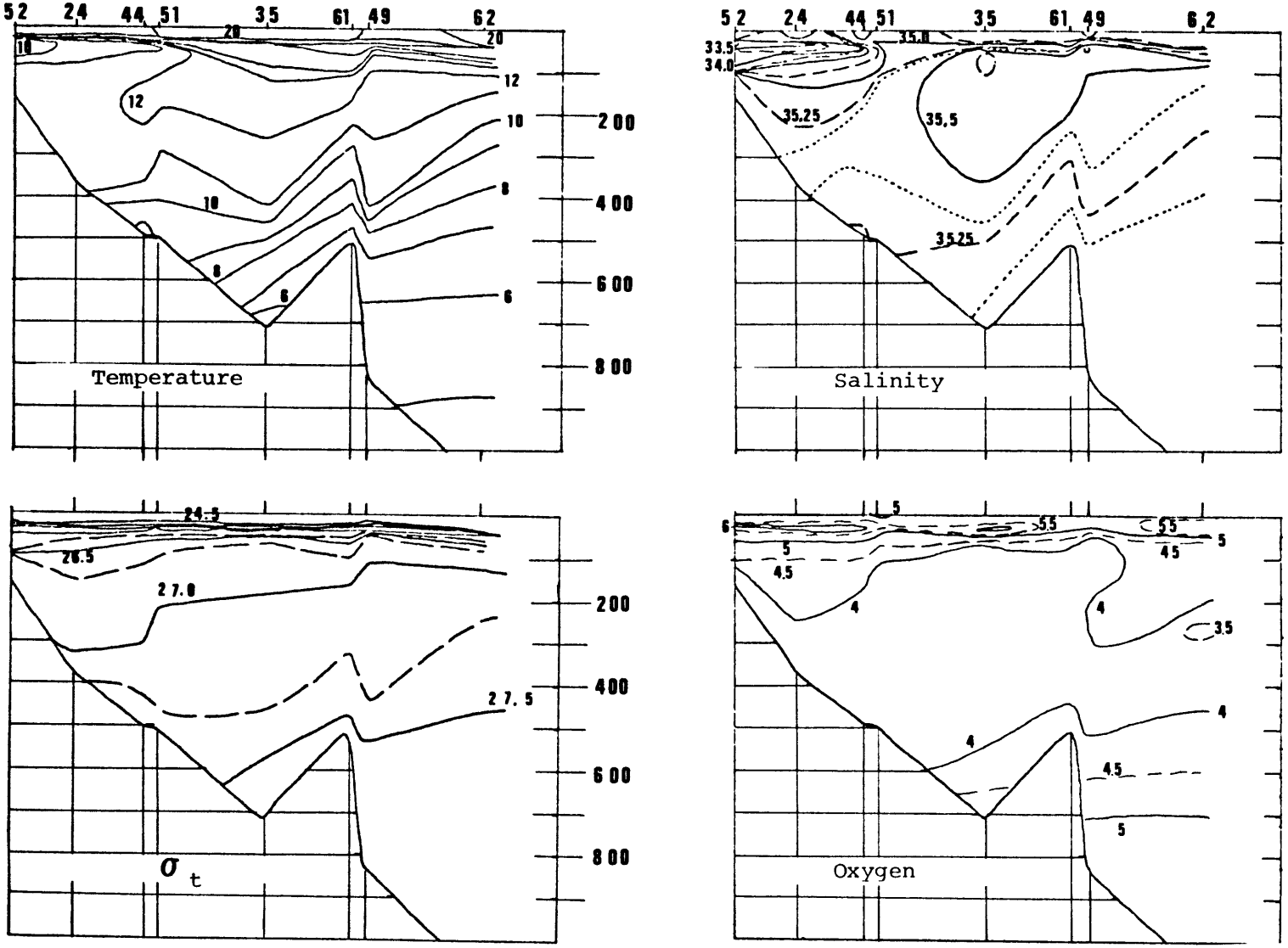

Figure 2-2. Sections of (a) temperature, (b) salinity, (c) density, and (d) dissolved oxygen concentration, from the early survey of Hudson Canyon, September 24-27.

cane passing east of Bermuda forced us to interrupt the survey. When we resumed on September 29 we again surveyed Hudson Canyon.

The second Hudson Canyon section was completed in 15 hours on September 29 and 30. As shown in figure 2-3, the canyon hydrography changed considerably in the two days between the early and late sections. Slope water flowed up into the canyon head and forced the fresh water back onto the shelf (compare the σ_t = 27.0 isopycnals of figures 2-2 and 2-3). In the second section, slope water fills the canyon and the cold pool no longer extends over the canyon head. The water in the canyon head is fairly well mixed, with temperatures close to 12° and salinities near 35.25‰. A layer of cold salty water appears to be upwelling along the canyon floor.

Figure 2-4 compares two sections along the southwest flank of Hudson Canyon: one drawn from our September 1977 data, the other from data collected in October 1974 by Gordon et al. (1976). Our survey was earlier in the mixing season. Our surface mixed layer was 20 m deep; theirs was 50 m. Our surface temperatures are generally about 3° warmer than theirs. In this region, a surface temperature of 3° per month is usual from September to January (Schroeder, 1966).

The composite temperature-salinity diagram for our data differs from that of Gordon et al. (1976) in a manner consistent with being earlier in the mixing season. As shown

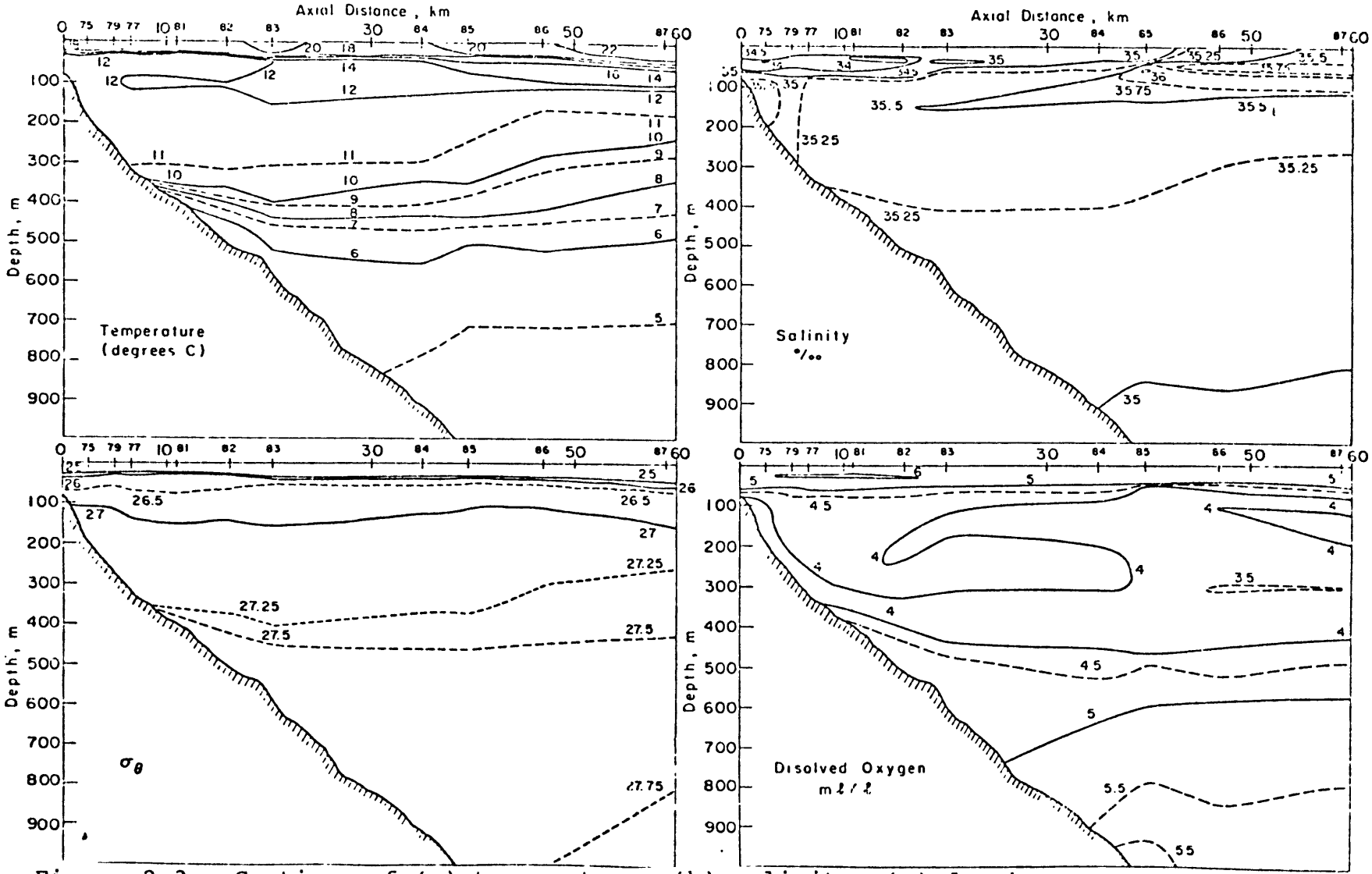

Figure 2-3. Sections of (a) temperature, (b) salinity, (c) density, and (d) dissolved oxygen concentration, from the late survey of Hudson Canyon, September 29-30.

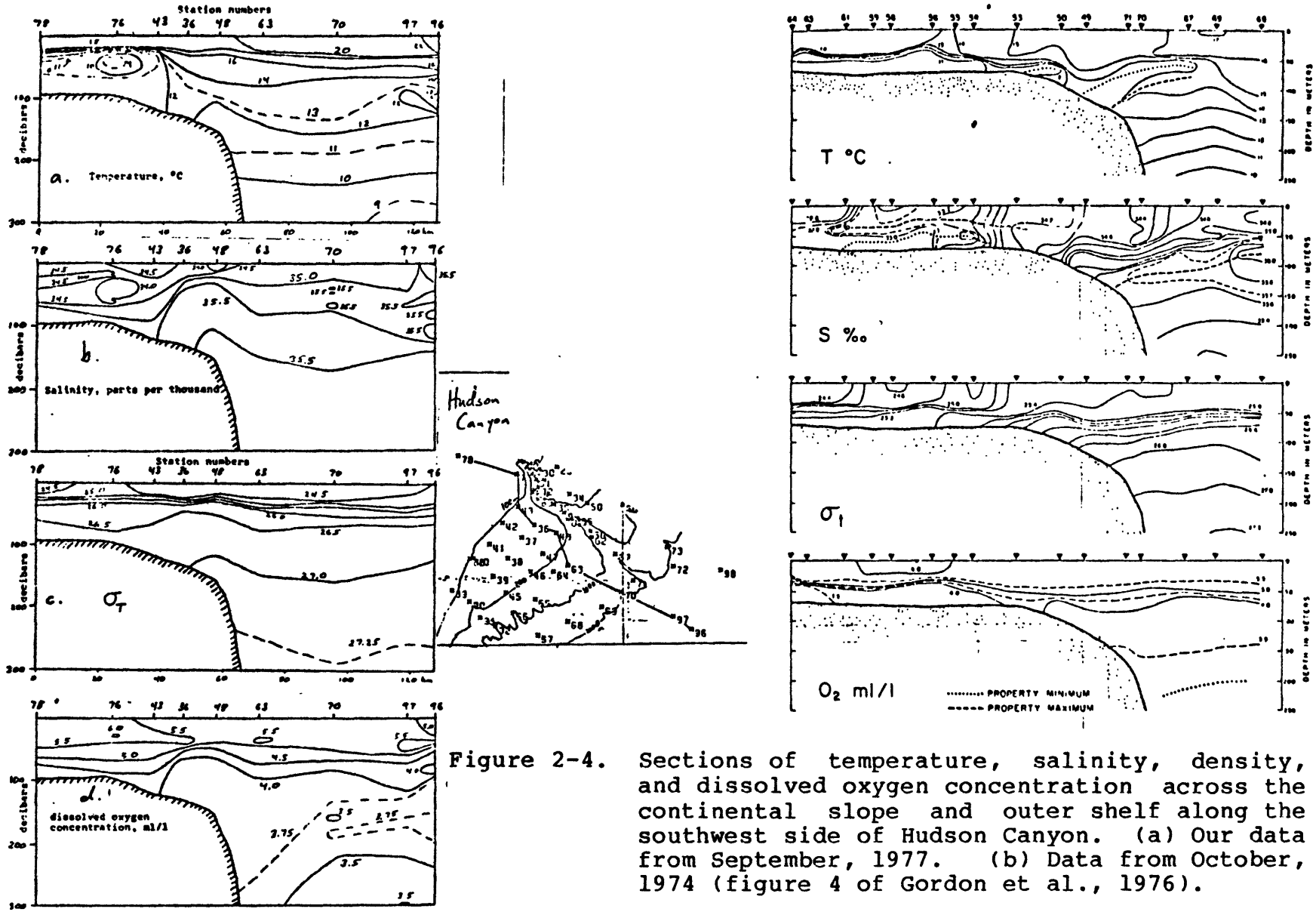

Figure 2-4. Sections of temperature, salinity, density, and dissolved oxygen concentration across the continental slope and outer shelf along the southwest side of Hudson Canyon. (a) Our data from September, 1977. (b) Data from October, 1974 (figure 4 of Gordon et al., 1976).

in figure 2-5, the two diagrams are similar in shape but the extreme warm-salty and cold-fresh points on our diagram are more extreme than on theirs, and their survey has more low-salinity points. Their low-salinity points represent water from stations closer to shore than any of our stations. The other differences between the two diagrams are qualitatively similar to the differences usually found between such diagrams from summer and winter (for example, by Ruzecki, 1979).

The difference between our oxygen measurements and those published by Gordon et al. (1976) is more difficult to explain. Composite salinity-oxygen diagrams for the two data sets are compared in figure 2-6. In our data, a mid-depth maximum in oxygen concentration occurs in the shelf water just above the cold pool. The maximum is highest in the vicinity of Hudson Canyon and extends northeast of the canyon although the cold pool does not. The relatively high oxygen concentration in the cold pool itself contrasts with the oxygen minimum that Gordon et al. found in the cold pool. In our data, the lowest oxygen concentrations are at 100 db in the slope water, in agreement with the oxygen minimum that they found below the pycnocline in the slope water.

B. Mixing in canyons

The temperature-salinity curve for slope water in the Middle Atlantic Bight has a bend at about 8°, 35.1‰ (see

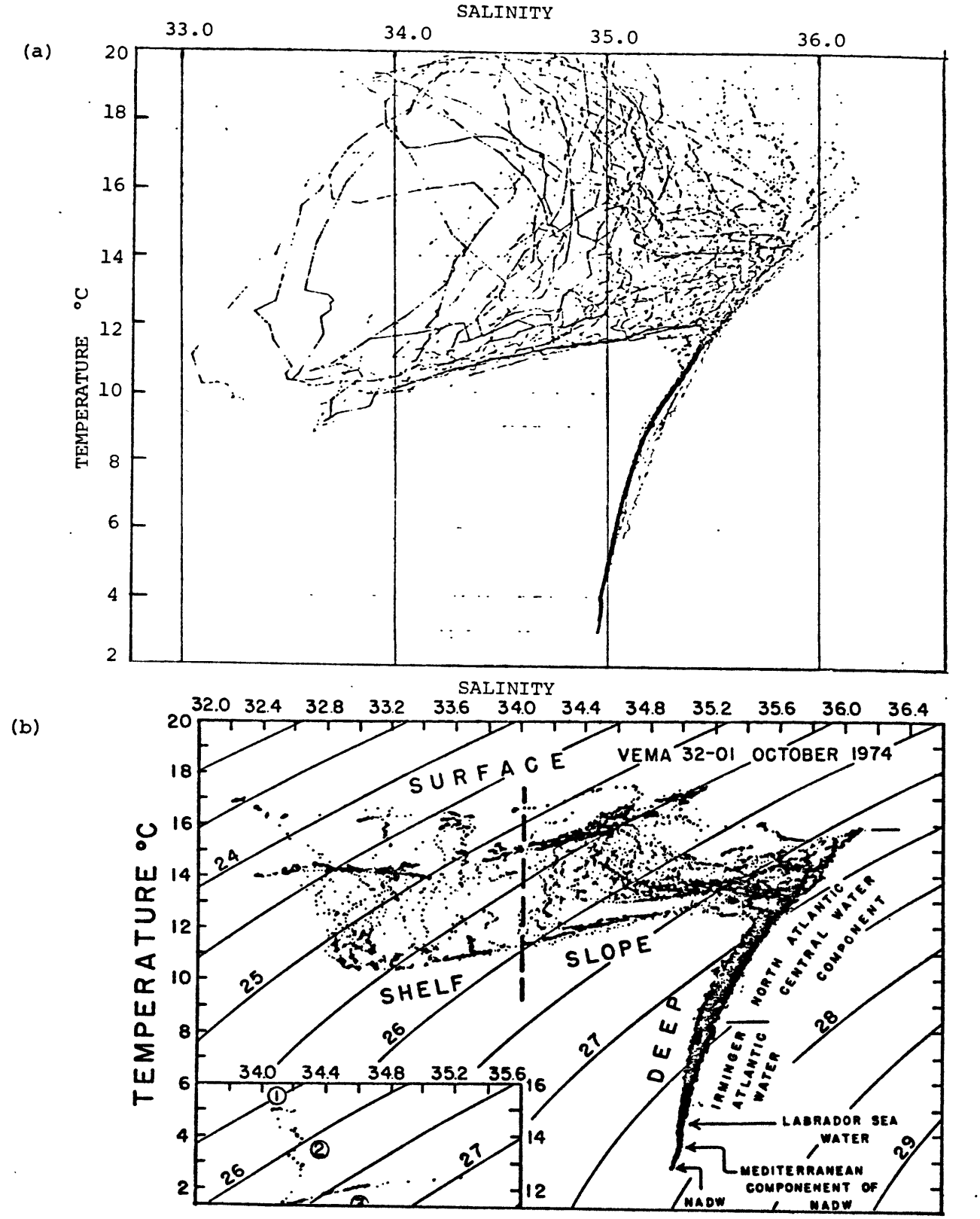

Figure 2-5. Temperature-salinity diagrams for the Hudson Canyon region. (a) Our data from September, 1977. (b) Data from October, 1974 (figure 2 of Gordon et al., 1976).

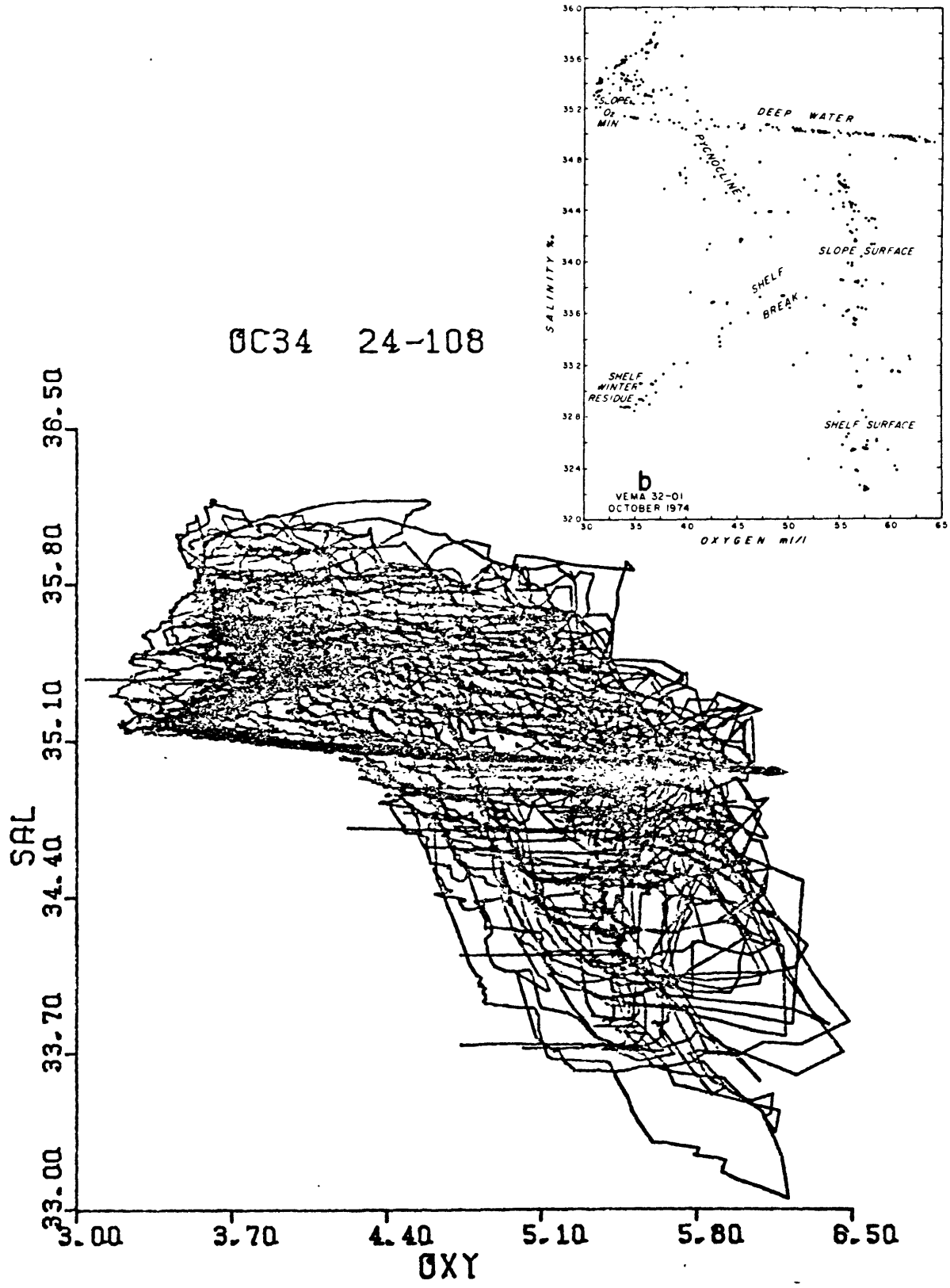

Figure 2-6. Salinity-oxygen diagrams for the Hudson Canyon region. (a) Our data from September, 1977. (b) Data from October, 1974 (figure 5b of Gordon et al., 1976).

figure 2-7). This bend was identified by Gordon et al. (1976) as the boundary between Irminger Atlantic water (colder and fresher) and North Atlantic central water. Gordon et al. observed unusually salty 8° to 9° water in Hudson Canyon and suggested that it resulted from enhanced mixing of two slope water masses.

The T-S curves of our canyon data also record unusually salty water that cuts the corner between Irminger Atlantic water and North Atlantic central water (see figure 2-7). In Hudson, Hydrographer, and Oceanographer Canyons, the bend in the T-S curve progressively straightens and approaches a straight line with higher salinity as the station locations approach the canyon head.

A measure of the degree of mixing between Irminger Atlantic water and North Atlantic central water is the salinity anomaly at σ_t = 27.3° C. As shown in figure 2-8, we found salinity anomalies greater than .14‰ only within submarine canyons. Nine of the twelve stations with salinity anomalies between .08‰ and .14‰ were in canyons. Only three of the 25 stations where salinity anomalies were negligible were inside canyons. The salinity seems to be generally at least .02‰ higher along the slope east of Block Canyon than in the regions of Hudson and Wilmington Canyon. In each region, isolated stations on the continental slope had high salinity anomalies. Most of these were near the mouths of submarine canyons.

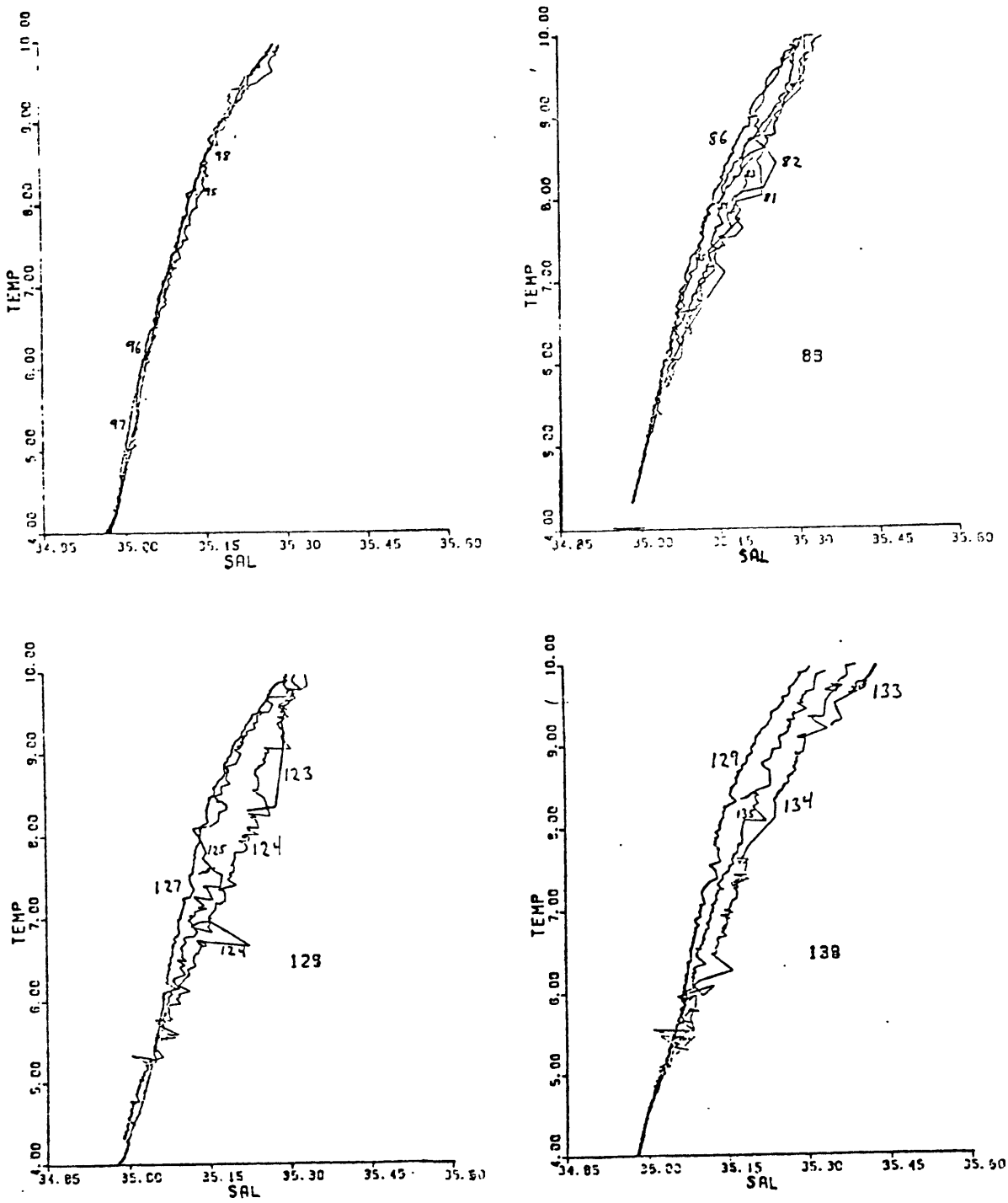

Figure 2-7. Temperature-salinity diagrams for temperatures between 4 and 10 degrees. The salinity scale is expanded to show the mixing of slope water masses that straightens the bend at about 9°, 35.15‰. (a) Data from above the continental rise outside Hudson Canyon. (b) Stations of the later section through Hudson Canyon. (c) Stations along Hydrographer Canyon. (d) Stations along Oceanographer Canyon.

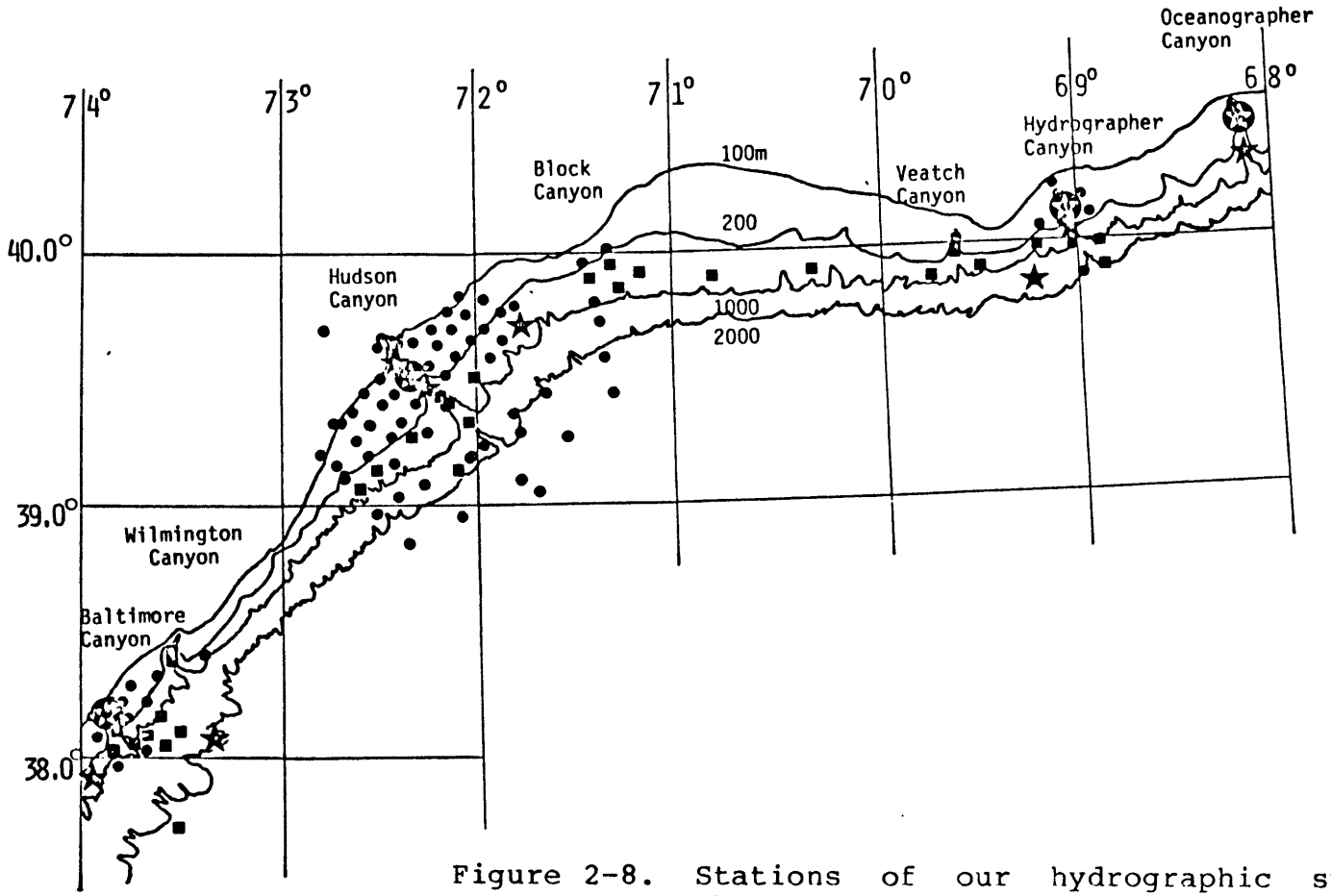

Figure 2-8. Stations of our hydrographic survey showing where we found high salinity anomalies at $\sigma_t = 27.3$, indicating mixtures of North Atlantic central water and Irminger Atlantic water.

- anomaly over .14‰
- anomaly .08 to .14‰
- anomaly .02 to .08‰
- other stations

Figure 2-9 is a graph of salinity anomaly against water depth for sections along submarine canyons. The canyon axes are roughly 1000 m deep when the canyons intersect the continental slope. For depths greater than 1000 m, water of $\sigma_t = 27.3$ is not confined between canyon walls but is free to flow along the continental slope. As shown in figure 2-9, the salinity anomaly in this water is roughly the same as that found outside the canyons along the slope. As the water depth decreases from 1000 m, the salinity anomaly tends to increase linearly. The exceptions are the Hudson Canyon sections. The mass of relatively fresh shelf water which we observed in the head of the canyon apparently mixed with the slope water, causing a decrease in salinity anomaly at the shallowest Hudson Canyon stations.

Examination of temperature-salinity correlations from Hydrographer and Wilmington canyons indicates that, at each point along the canyon, mixing is occurring in the deepest 200 to 400 m. In Oceanographer Canyon, the mixing is strongest at temperatures between 9° and 11.5°. These isotherms are in a pycnocline that meets the floor in the canyon head. The Oceanographer Canyon salinity anomalies are also higher than those in other canyons. Whether this is caused by stronger mixing or by slower advection through the canyon cannot be said.

In Hudson Canyon, the mixing occurs at the pycnocline between the slope water upwelling along the canyon floor and

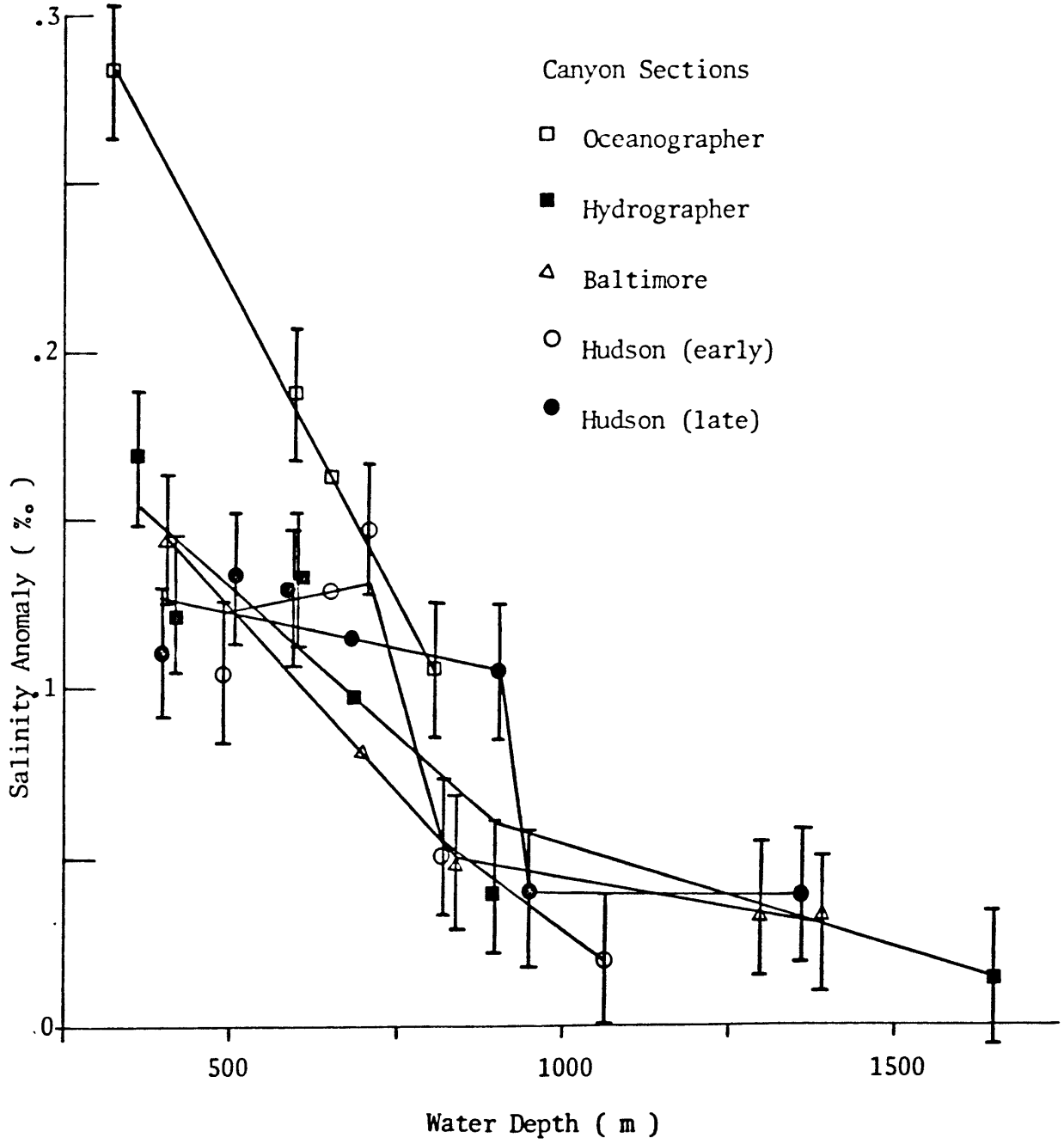

Figure 2-9. The variation in salinity anomaly at σ_t = 27.3 with water depths inside submarine canyons. Error bars represent maximum deviation of CTD salinities from water sample salinities used for calibration.

the 12° water which fills the canyon head. The mixing produces steps in the density profiles, apparently layers of mixed water that intrude into the slope water (see figure 2-10).

The energy used to mix the slope water was estimated from the potential energy of the later Hudson Canyon section. If the water was initially stratified like that at station 97, which is above the continental rise outside Hudson Canyon, then the energy used in mixing slope water in the canyon is $5(10^8)$ joules.

The observed mixing of Irminger Atlantic and North Atlantic central waters occurs mostly in canyon heads and near the floor, suggesting that shoaling and breaking internal waves may be responsible. Temperature-salinity correlations suggest that mixing in a given layer occurs in the part of the canyon where that layer is next to the floor. The variation in salinity anomaly along the canyons will result if the mixed water then flows out of the canyon and is progressively diluted as the canyon gets wider. There is apparently some circulation of slope water through submarine canyons, at least in response to downwelling events like the one we observed in Hudson Canyon.

C. Canyon effects on the shelf-slope front

The shelf-slope front divides the relatively cold, fresh shelf water from the warmer and saltier slope water at the

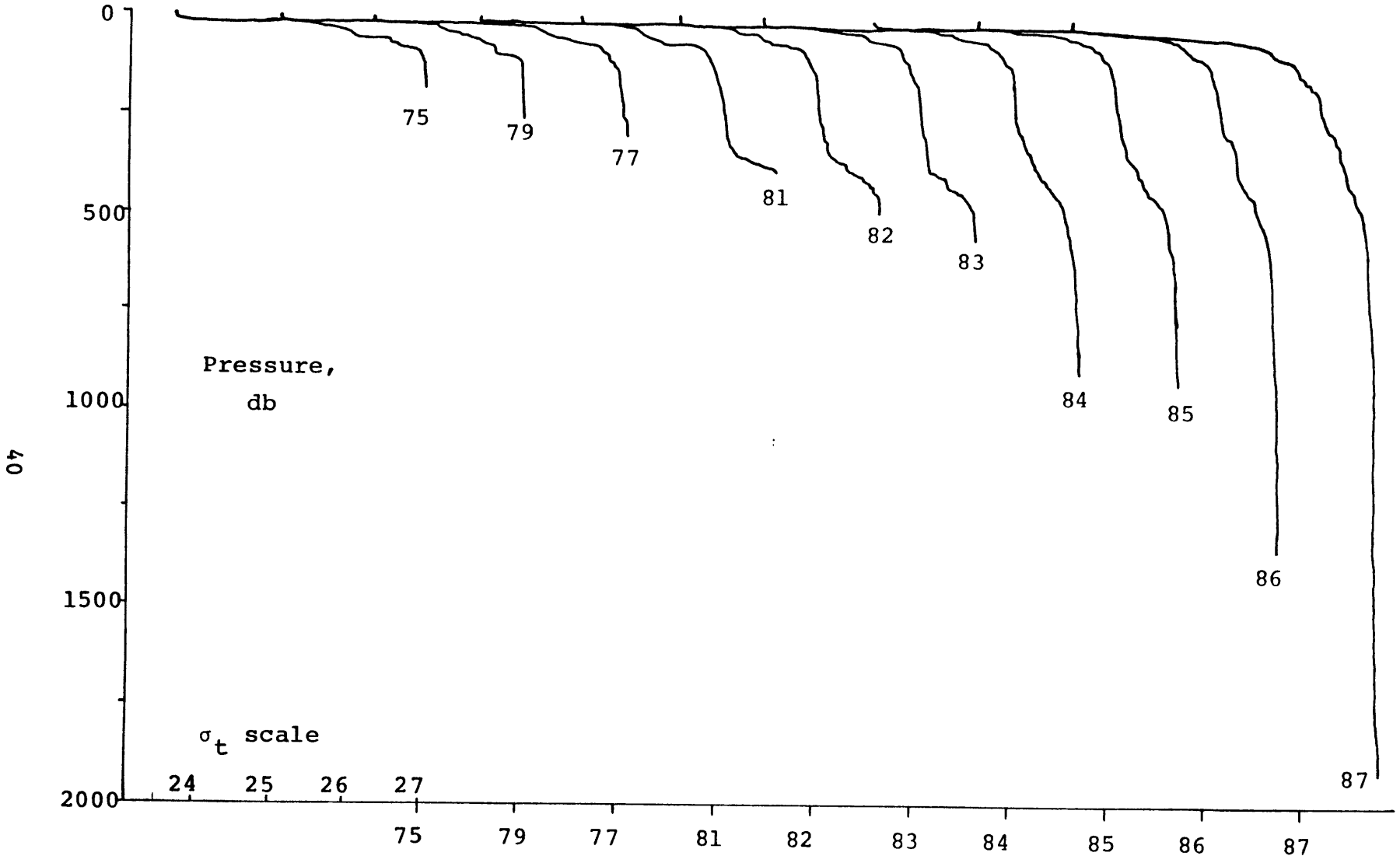

Figure 2-10. Density profiles of the second section through Hudson Canyon, showing layers of mixed water which intrude down-canyon along the thermocline. See figure 3-2 for station locations.

outer edge of the Middle Atlantic Bight. In its mean position, the front touches bottom near the break in floor slope at the top of the continental slope and leans out over the continental slope. The front often meanders in a wave-like pattern. In the summer, the cold pool lies just shoreward of the intersection of the shelf-slope front with the bottom. On the northern limb of the Middle Atlantic Bight (east of Hudson Canyon), the cold pool lies over the outer half of the continental shelf, with the front touching the bottom near the 100-meter isobath. South of Hudson Canyon, the cold pool frequently extends out over the continental slope (see Houghton et al., 1982).

With only a few exceptions, the stations of our hydrographic survey were in water deeper than 100 m. We only found the cold pool near Hudson, Wilmington, and Baltimore Canyons, consistent with its usual location. We found abnormal thicknesses of cold pool water in the heads of Wilmington and Hudson Canyons (during the early section, see figure 2-11). Before the second Hudson Canyon section, the cold pool water had moved out of the canyon but very cold shelf water was on the southwest side of the canyon head. This is consistent with data from the late summer of 1979 (see Houghton et al., 1978, figure 5), in which the coldest pools of cold pool water are found near heads of submarine canyons. I suggest that the cold pool downwells into the heads of submarine canyons during some autumn storms. There

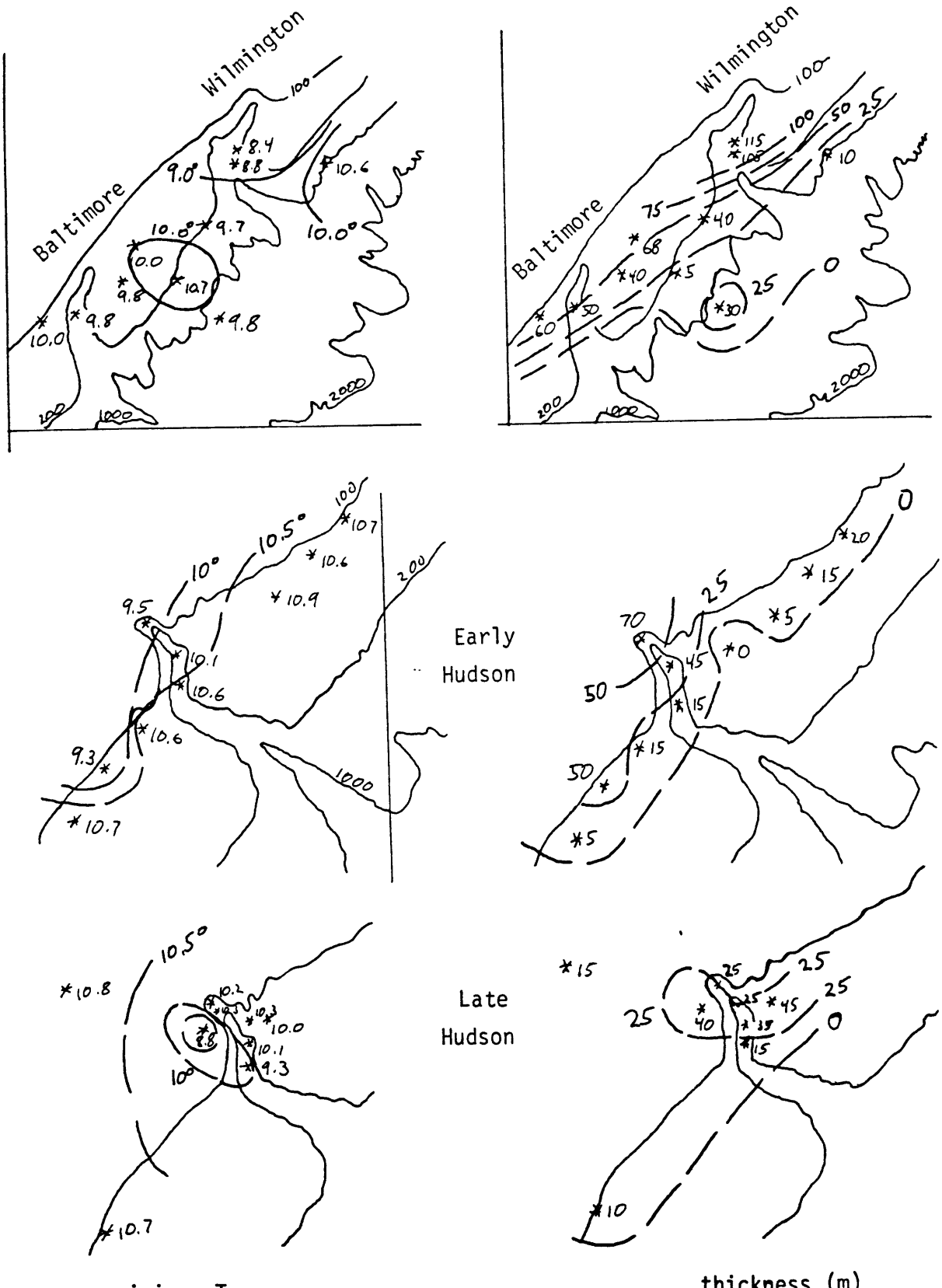

Figure 2-11. Minimum shelf water temperature and depth of the cold pool near Baltimore, Wilmington, and Hudson Canyons. Limits of cold pool were taken at 35‰ and 11°.

it is protected from mixing that dilutes the cold pool water left on the shelf. Then the shelf water is forced back out of the canyons, and the coldest shelf water is found near the heads of submarine canyons.

The shelf-slope front often meanders in a wave-like pattern. We found a meander that caused the front to lie along Baltimore Canyon. As shown in figure 2-12, the front was in a normal position northeast of the canyon. The front turned at the northeast edge of the canyon and went shoreward over the canyon. Southwest of Baltimore Canyon the front was steep and displaced onto the shelf from its normal position. As shown in figure 1-4, an eddy was near the continental slope in position to force the front shoreward at Baltimore Canyon.

Many observers have found intrusions interleaving across the shelf-slope front during summer and autumn, when the shelf water is stratified. Mooers et al. (1979) and Ruzecki (1979) concluded that these intrusions are more common near submarine canyons, particularly when Gulf Stream rings are nearby. Welch (1981) proposed a hypothesis that explains mid-depth intrusions as the results of gradients of hydrostatic pressure that arise when the thermocline is thinner above the shelf than it is above the slope. In the Welch hypothesis, the intrusions are continuous along the front and are associated with northward geostrophic jets.

We observed an apparently continuous mid-depth intrusion

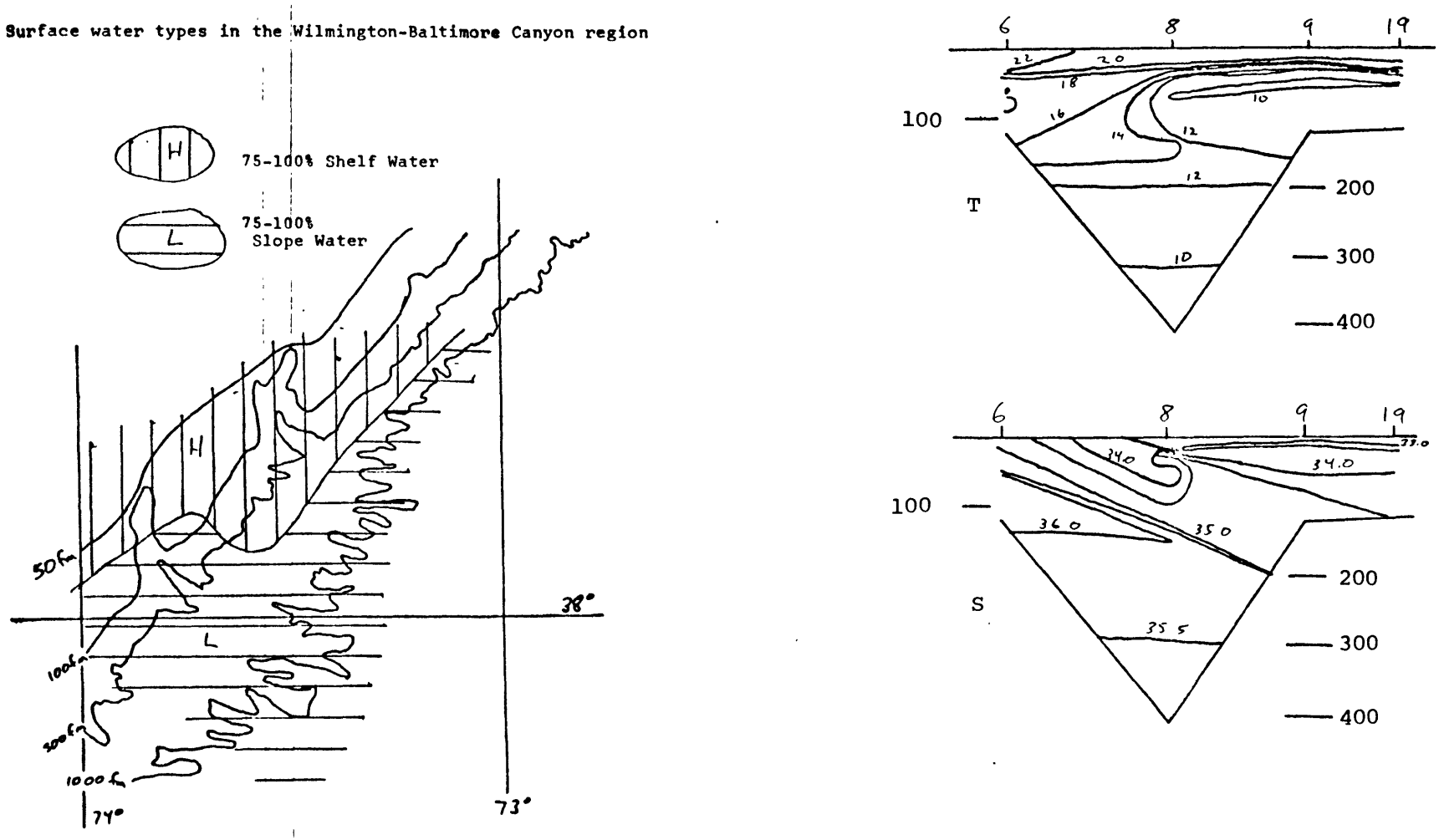

Figure 2-12. Data from the Baltimore-Wilmington Canyon region showing the meander of the shelf-slope front at Baltimore Canyon. (a) Surface water types; H is 75 to 100% shelf water, L is 75 to 100% slope water. (b) Temperature and salinity sections across the head of Baltimore Canyon.

near Baltimore Canyon that may fit the requirements of the Welch hypothesis. As shown in figure 2-13, a mid-depth salinity maximum in the head of Baltimore Canyon and at shallow stations to the southwest could have been either a long isolated "calf" or an intrusion still attached to the slope water. Below the level of the salinity maximum, a layer of fresh high-oxygen shelf water intruded into the slope water.

This mid-depth intrusion resembles those Welch describes, but its occurrence where the shelf-slope front was displaced onto the continental shelf suggests that it may have grown through baroclinic instability. Flagg and Beardsley (1978) examined the baroclinic stability of the shelf-slope front, and found that it was greatly increased by the high bottom slope which lies under the front's normal position. When the front is displaced onto the relatively flat continental shelf, it is more prone to baroclinic instability. The thickness of the intrusion southwest of Baltimore Canyon is consistent with its interpretation as a baroclinic instability.

According to Stern (1975, p. 73), a wave-like deflection on a front will be baroclinically unstable if its across-front length

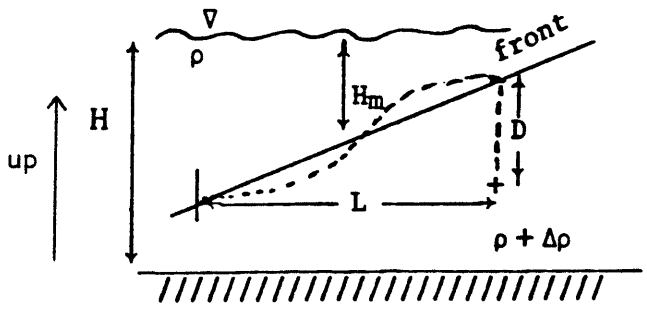

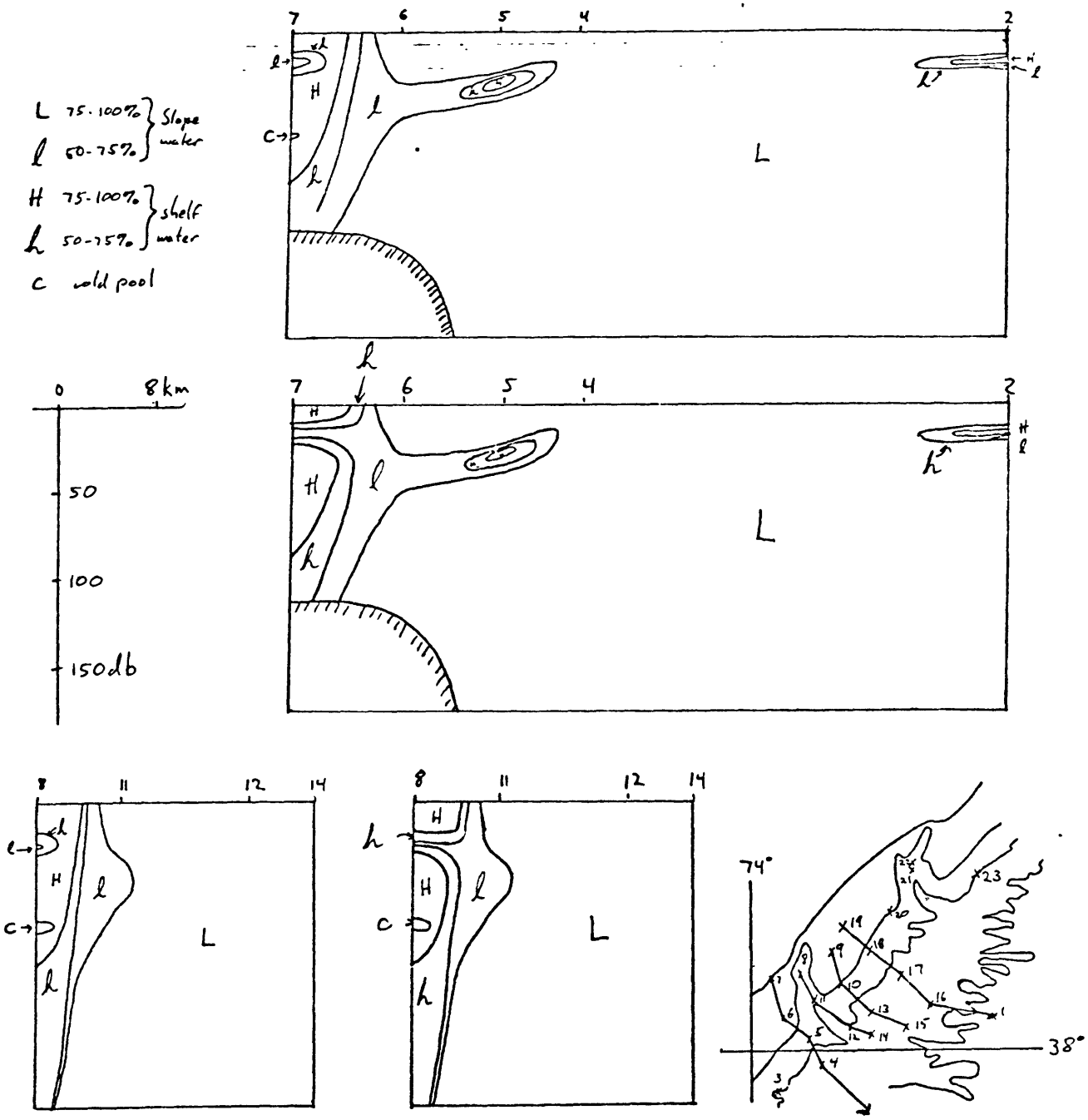

Figure 2-13. Sections crossing the shelf-slope front southwest of Baltimore Canyon showing the water masses of the upper 175 db. The high salinity layer in the shelf water can be contoured as an isolated lens (a) or as an intrusion (b). Note the intrusion of shelf water into the slope water below the high-salinity layer.

scale satisfies

$$L^2 \geq \frac{\pi^2}{2} g \frac{\Delta\rho}{\rho} \frac{\sqrt{Hm(H-Hm)}}{f^2}$$

For the intrusions southwest of Baltimore Canyon,

$$\frac{\Delta\rho}{\rho} \approx 5(10^{-4}) \text{ and } \sqrt{H_m(H-H_m)} \approx 44m.$$

So L > 11.2 km. The frontal slope is about 8 m/2.3 km so the vertical scale for baroclinic instability is D > 40 m. The combined thickness of the pair of intrusions we observed was 50 m, consistent with a baroclinic instability interpretation.

We found three apparently isolated calves of warm or cold shelf water in the Baltimore-Wilmington Canyon region and one in the Hudson Canyon region. These were all located south of canyon mouths. We found only one isolated calf of slope water in the shelf water (except possibly for the continuous salinity maximum discussed above). This difference was probably caused by stronger mixing on the shelf, which would also create the difference in thermocline thickness that is basic to Welch's hypothesis. Our finding calves of cold pool south of the canyon mouths is in agreement with the discovery (Mooers et al., 1979) of cold pool calving along the southwest side of Wilmington Canyon. These may be related to the downwelling of cold pool water into canyon heads which we observed in Wilmington and Hudson canyons.

Chapter III

The Hudson Canyon Moored Array

A moored array of instruments was deployed in Hudson Canyon during the CTD survey on September 24-26, 1977, and was recovered fifteen weeks later on January 12, 1978. The primary purpose of the array was to investigate changes in oceanic internal waves as they travel into the canyon and toward the canyon head. In addition, we found locally generated internal tides to be an important component of the canyon internal wave field, and observed the low-frequency events that storms cause in the canyon.

Hudson Canyon, although the largest of the East Coast canyons, is typical in shape (see figure 3-1). It lies at the edge of the continental slope, 200 km southeast of New York City. The canyon is at the bend of the shelf in the New York Bight, but locally the shelf break is straight and oriented 45° east of north. Figure 3-2 shows the bathymetry of the canyon. Taking the break in slope at the 165 m isobath as the edge of the continental shelf, the canyon head is 30 km shoreward of the edge, in 90 m of water. The walls of the canyon are 760 m high at the shelf edge.

In transverse profile the canyon is V-shaped, with a

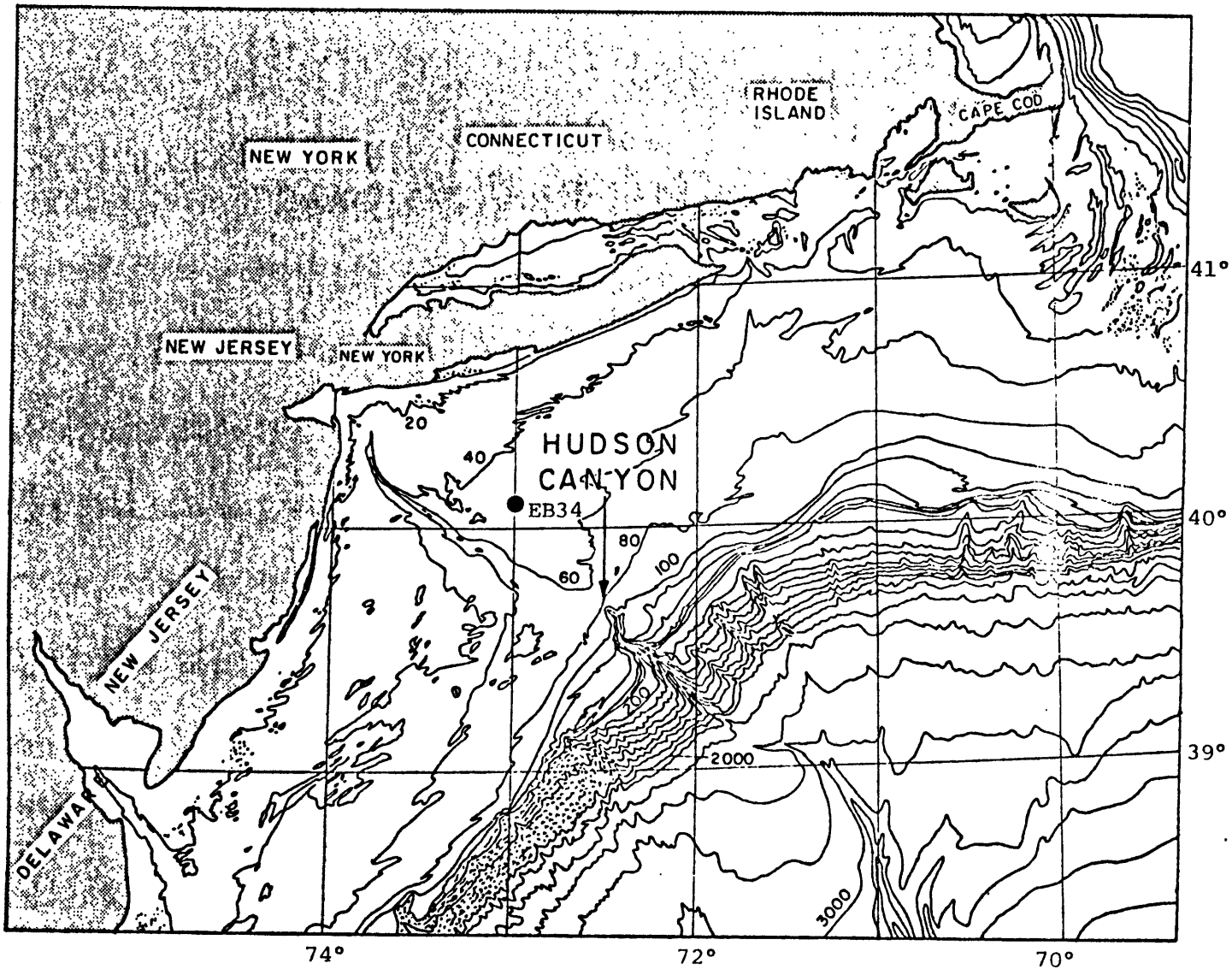

Figure 3-1. Bathymetry of the continental shelf from Delaware to Cape Cod, showing the location of Hudson Canyon. (Bathymetry from Uchupi, 1965.)

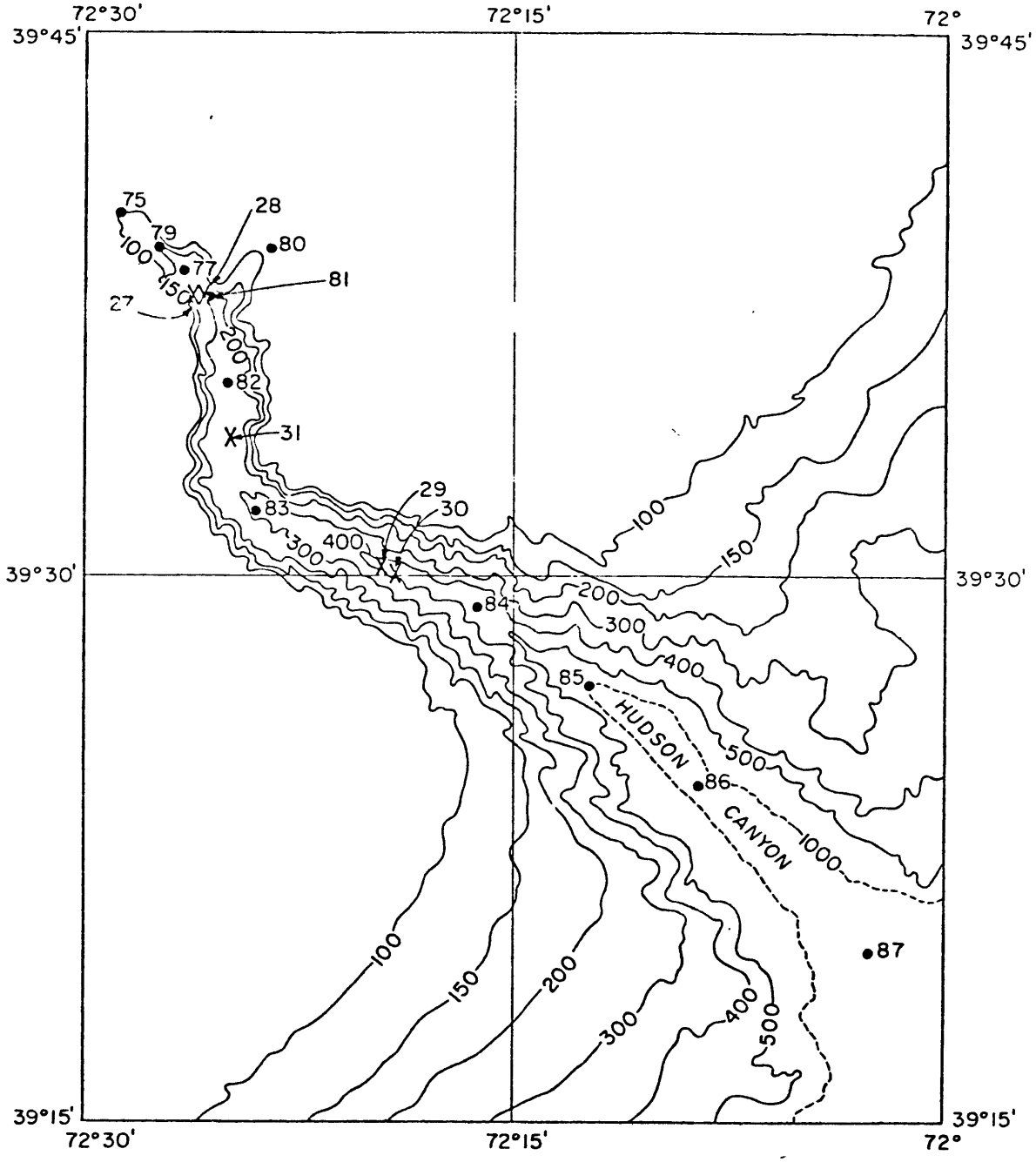

Figure 3-2. Bathymetry of Hudson Canyon (depths in fathoms) showing the locations of our moorings and the stations of the second CTD section. (Chart adapted from NOAA 0807 N52.)

narrow, sediment-covered floor. Its width increases from 3.5 km at the head to 13 km at the shelf-slope break. Figure 3-3 displays three transverse sections of the canyon. The walls are steep, with rocky outcrops and slopes of about 25%. Figure 3-4 is an axial section of the canyon from head to shelf break. The slope of the axis is about 20 m/km, with a general upward concavity and small steps.

The moored array consisted of fourteen instruments that recorded temperature and pressure, ten current meters, and a nephelometer, mounted on five moorings. Usable data were produced by all of the temperature-pressure recorders and by seven current meters. Figure 3-2 shows the locations of the moorings. A pair was in the canyon head 500 m apart, where the canyon axis is 350 m deep. Another pair of moorings was 800 m apart, deeper in the canyon, at 780 m depth. The fifth mooring was roughly midway between the two pairs along the canyon axis, at a depth of 500 m.

The locations of the individual moored instruments are indicated on the axial section of the canyon, figure 3-4. Most moorings held five instruments, current meters at the top and bottom and temperature-pressure recorders between. The shallowest mooring, number 27, had only two temperature-pressure recorders between. The deepest, number 30, held the nephelometer just above the bottom current meter. The bottom current meters were attached to the moorings 10 m above the anchors. Additional space shows below some of them on figure

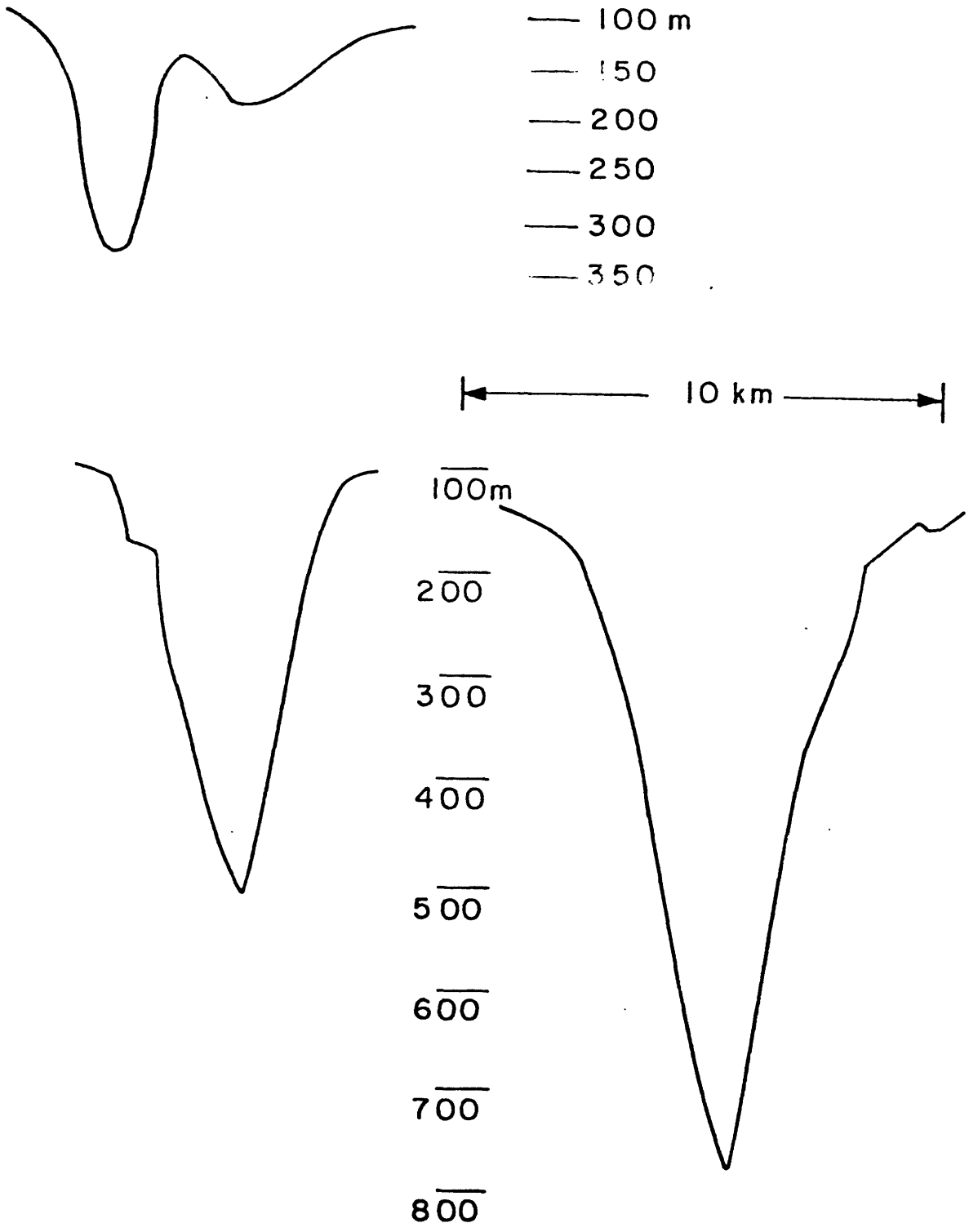

Figure 3-3. Sections of Hudson Canyon, normal to its axis, at the locations of (a) moorings 27 and 28, (b) mooring 31, and (c) moorings 29 and 30. (Bathymetry from NOAA 0807 N52).

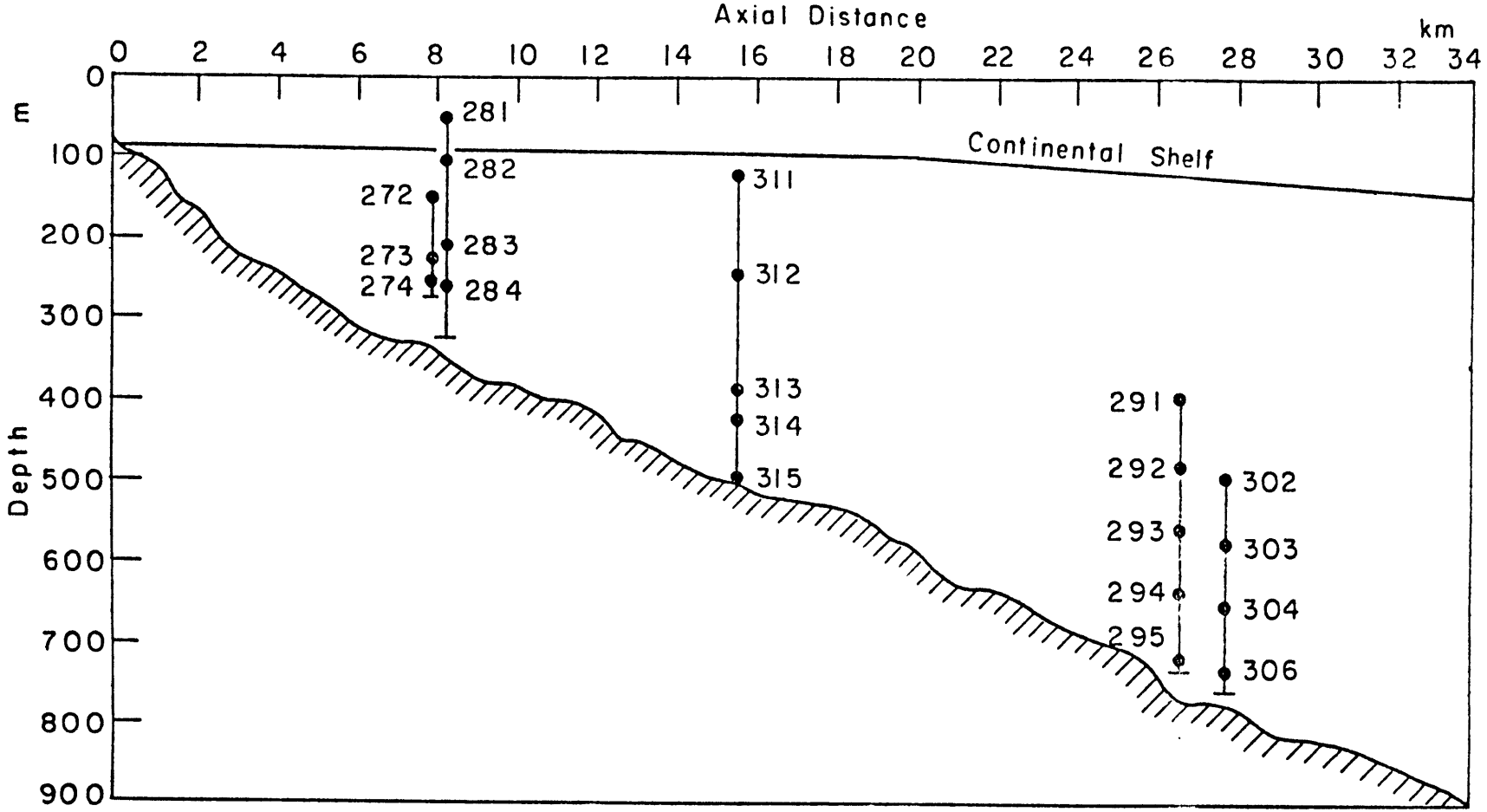

Figure 3-4. Axial section of Hudson Canyon showing the locations of the moored instruments. Most moorings landed toward the south side of the canyon so their bases are above the canyon axis. (Bathymetry from NOAA 0807 N-52.)

3-4 because the moorings landed toward the side of the canyon, where the floor is shallower than at the axis.

The current meters were Aanderaa models RCM4 and RCM5. They recorded pressure, temperature, and current speed and direction at twenty-minute intervals. The current data were transformed to eastward (u) and northward (v) velocity components before analysis. Aanderaa pressure data were used only to calculate the depths of the instruments. The temperature-pressure recorders acquired data at intervals of 16 minutes. All the temperature-pressure recorders worked properly, although the temperature ranges of instruments 284, 292, and 313 were exceeded at times. No data were obtained from the nephelometer or from current meters 271, 285, and 301.

The semidiurnal tide dominates the pressure records from all the temperature-pressure recorders. There are several sharp drops in pressure, indicating increases in the instruments' depths apparently in response to strong currents. The largest of these events occurred during the storm just before the moorings were recovered. At the head of the canyon (moorings 27 and 28) the temperature has strong oscillations at periods of several days. Deep-canyon temperature records (moorings 29 and 30) have large oscillations at a period of about two weeks. Temperature records from mooring 31 show both the two-week and the several-day periodicities.

The semidiurnal tide dominates the velocity field inside

the canyon. At the shallowest current meter, 281, strong low-frequency flows were also observed. Current velocities reach higher maxima at the shallow moorings than at the deep ones. In general, the plots of u and v (i.e., east and north components) against time oscillate smoothly about zero for the shallow moorings, whereas for the deep moorings the velocity records have sharp spikes, alternately positive and negative (compare figures 3-5 and 3-6). Several times during the experiment, events occurred that produced simultaneous temperature and velocity extremes in many of the records. One of these occurred on January 9-11, 1978, during a severe storm just before we recovered the moorings.

The January storm currents are distinctive in both duration and extent, and show up clearly in the pressure records of figures 3-5 and 3-6. The event is marked by sustained temperature and velocity signals that were recorded by every instrument operating. The pressure peak associated with them is the largest on each pressure record. Whereas the earlier events generally caused brief extreme values through amplification of roughly semidiurnal oscillations, in this event the oscillations were subdued. The storm that caused these currents was longer in duration and had stronger winds than any other of the experimental period. When we analyzed the data for internal waves, we excluded these surges by cutting off the last three days of data.

Figure 3-5. Northward and eastward velocity records and pressure and temperature records from the head of Hudson Canyon.

Figure 3-6. Northward and eastward velocity records and temperature and pressure records from the central mooring of the Hudson Canyon array.

Figure 3-5

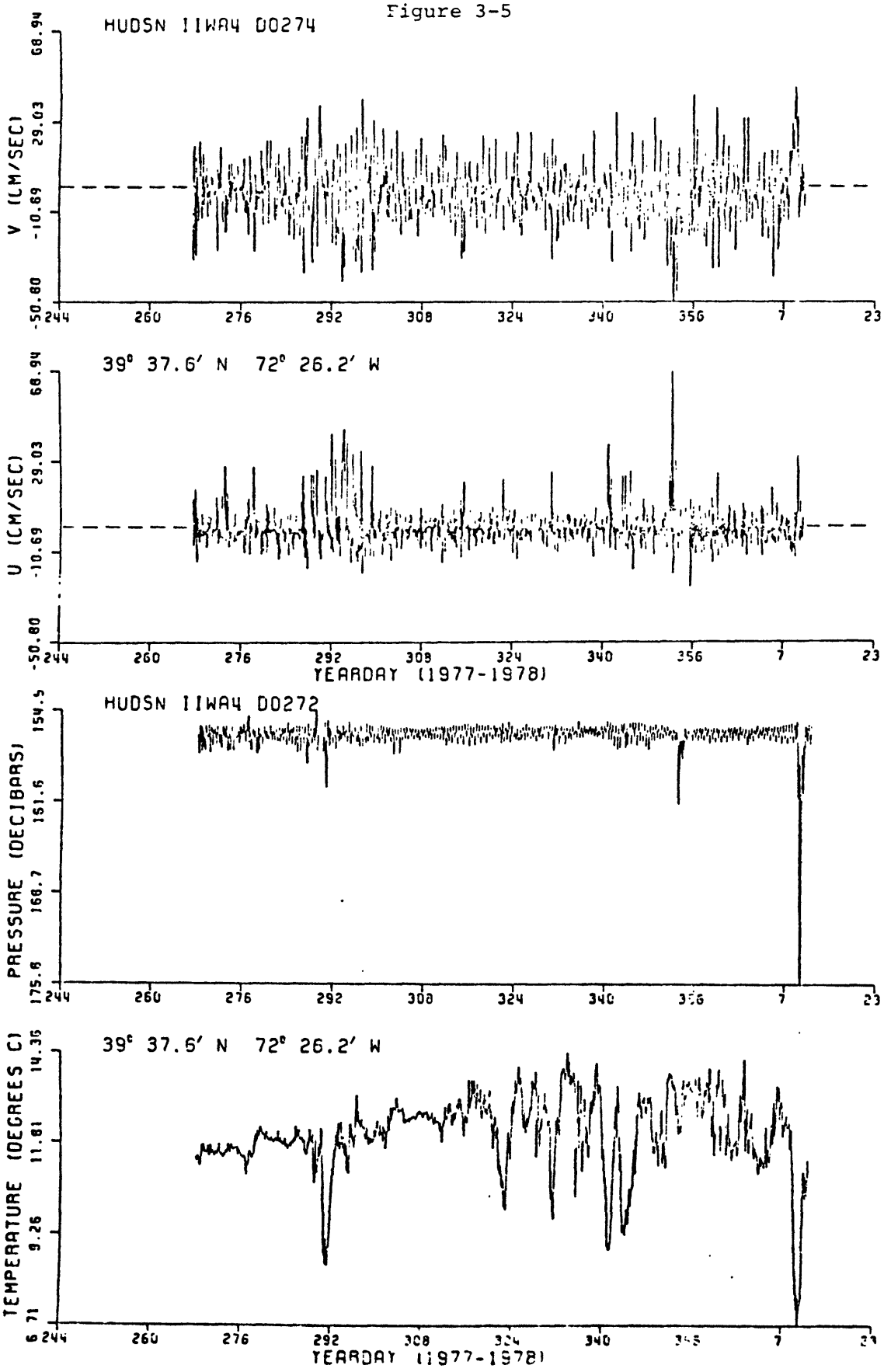
HUDSN IIWA4 D0274
V (CM/SEC)
68.94
29.03
-10.89
-50.80
244
260
276
292
308
324
340
356
7
23
39° 37.6' N 72° 26.2' W
U (CM/SEC)
68.94
29.03
-10.89
-50.80
244
260
276
292
308
324
340
356
7
23
YEARDAY (1977-1978)
HUDSN IIWA4 D0272
PRESSURE (DECIBARS)
154.5
151.6
168.7
175.8
244
260
276
292
308
324
340
356
7
23
39° 37.6' N 72° 26.2' W
TEMPERATURE (DEGREES C)
14.36
11.81
9.26
6.71
244
260
276
292
308
324
340
356
7
23
YEARDAY (1977-1978)

Figure 3-6

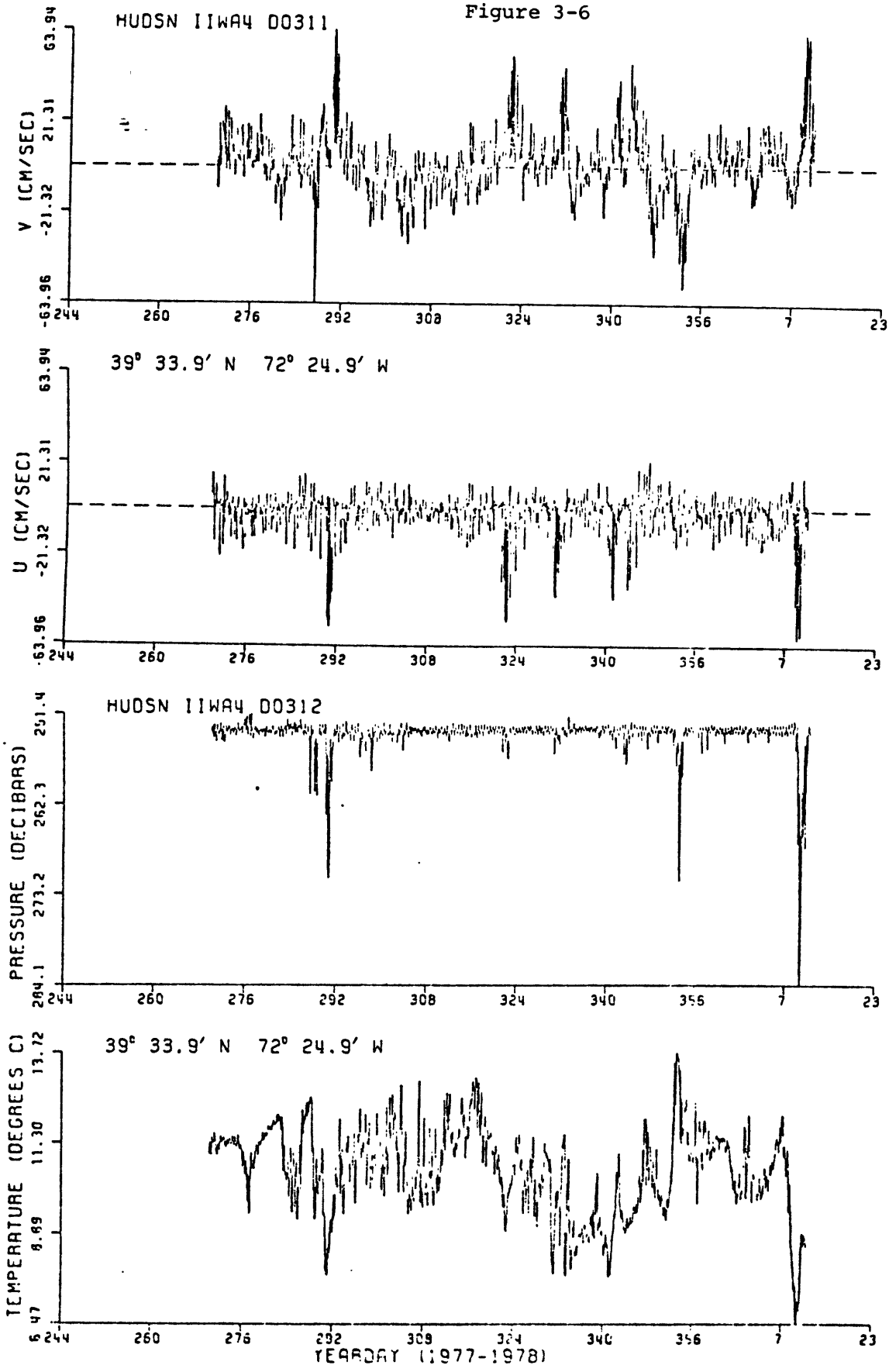
HUDSN IIWA4 D0311
V (CM/SEC)
63.94
21.31
-21.32
-63.96
244
260
276
292
308
324
340
356
7
23
39° 33.9' N 72° 24.9' W
U (CM/SEC)
HUDSN IIWA4 D0312
PRESSURE (DECIBARS)
251.4
262.3
273.2
284.1
39° 33.9' N 72° 24.9' W
TEMPERATURE (DEGREES C)
13.72
11.30
8.89
6.47
YEARDAY (1977-1978)

A. Low frequency currents

The low-frequency currents in Hudson Canyon are mostly caused by storms, and are stronger and more frequent in the upper layers of the canyon. Low-frequency temperature signals are caused by storms and, in the canyon head, by seasonal cooling. In the outer part of the canyon, the temperature field is largely determined by the water over the continental slope outside the canyon. Low-frequency temperature signals are brought into Hudson Canyon by a slow circulation of slope water through the outer canyon. These processes can be seen in spectra and low-pass filtered time series from our Hudson Canyon array, and in the structure of high-energy events that occurred during our experiment.

1. Kinetic energy and temperature spectra. Low-frequency currents on the Middle Atlantic shelf are predominantly forced by the wind stress under cyclonic storms, particularly during the winter when these storms are the strongest and occur about 5 times a month (Beardsley and Boicourt, 1981). Low-frequency currents over the continental slope can have other causes, such as topographic Rossby waves, Gulf Stream meanders, and warm-core Gulf Stream rings. Ou and Beardsley (1980) note that kinetic energy and temperature spectra from the continental margin reflect these differences in low-frequency forcing. Spectra from above the continental slope have roughly a σ^{-2} dependence on frequency σ for periods of one to fourteen days. Above the shelf,

atmospheric forcing dominates this frequency band and produces less steep spectra. Spectra from above the continental rise are steeper than those from the continental slope, with slopes up to -3 on the log-log plots.

Figure 3-7 shows horizontal kinetic energy spectra for the current meters of the Hudson Canyon array. For the instruments above and near the top of the canyon walls (281, 311), the low-frequency spectral slope is between -1 and -2, with the steeper slope for the higher frequencies. These are similar to the spectra that Ou and Beardsley (1980, see their figure 15) found above the continental shelf and to power density spectra of wind stress records from the New York Bight (Beardsley and Boicourt, 1981). This is evidence that the currents measured by instruments 281 and 311 are essentially shelf currents, which are dominantly forced by wind stress at low frequencies.

Deeper in the canyon, at instruments 291 and 274, the spectra are nearly level for periods of 2 to 14 days. Spectra from the near-floor instruments outside the canyon head, 315, 295, and 306, have positive slopes of about 0.5. It is apparent that the low-frequency currents of the continental slope have little effect in Hudson Canyon. Atmospheric forcing is effective in the upper layers and head of the canyon, judging from the slight negative slope of spectra 291 and 274, but not near the floor in the deep parts of the canyon. A thermocline/front usually lies between

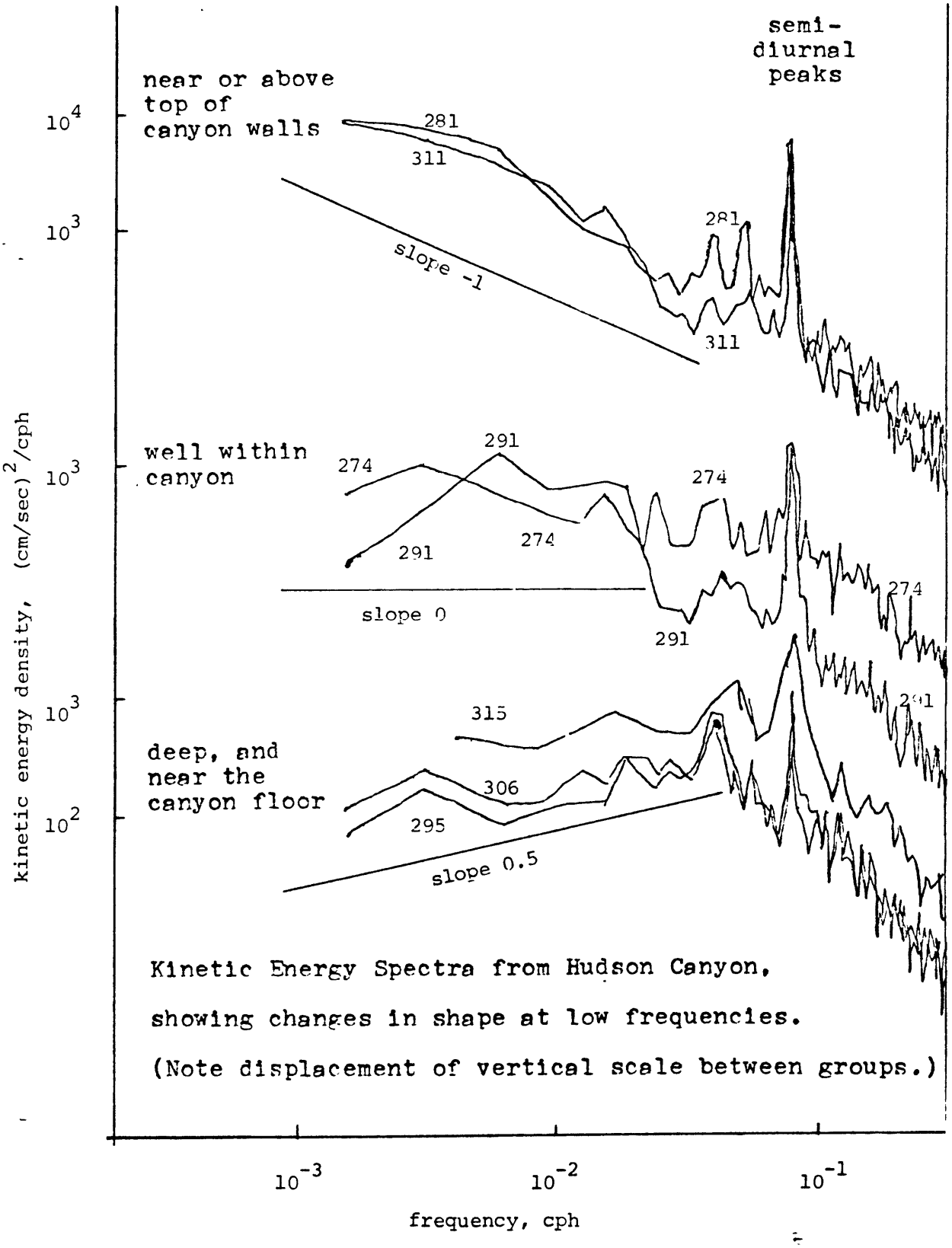

Kinetic Energy Spectra from Hudson Canyon, showing changes in shape at low frequencies. (Note displacement of vertical scale between groups.)

Figure 3-7.

these two regions and seems to be responsible for the isolation of the deeper part of the canyon.

The temperature spectra from the deep, outer parts of the canyon (see figure 3-8) contain low-frequency energy absent from the kinetic energy spectra measured by the same instruments. These slow temperature variations seem to result from a slow flow of slope water through the outer canyon. Where our moorings 29 and 30 landed, toward the southwest wall of the canyon, we measured a mean down-canyon flow of about 2 cm/sec. If there is a compensating up-canyon flow on the other side of the canyon, then slope water could flow up into the canyon along one wall, across the floor, and back out to the slope along the other wall, following the 800-meter isobath, in six weeks. This slow mean flow would bring in the low-frequency temperature signal of the slope water without causing a low-frequency velocity signal.

2. Low-pass filtered time series. The data were low-pass filtered using a Gaussian filter with a 24-hour half-width. The resulting time series consisted of points at 24-hour intervals corresponding to days of universal time. Figure 3-9 shows low-passed time series for the canyon current meters and for wind recorded at John F. Kennedy airport, New York City. There is a consistent flow down the canyon at the near-floor instruments 274, 315, 295, and 306. Up-shelf (northeastward) flow at instrument 281, above the canyon walls, seems to correspond to up-canyon flow at the

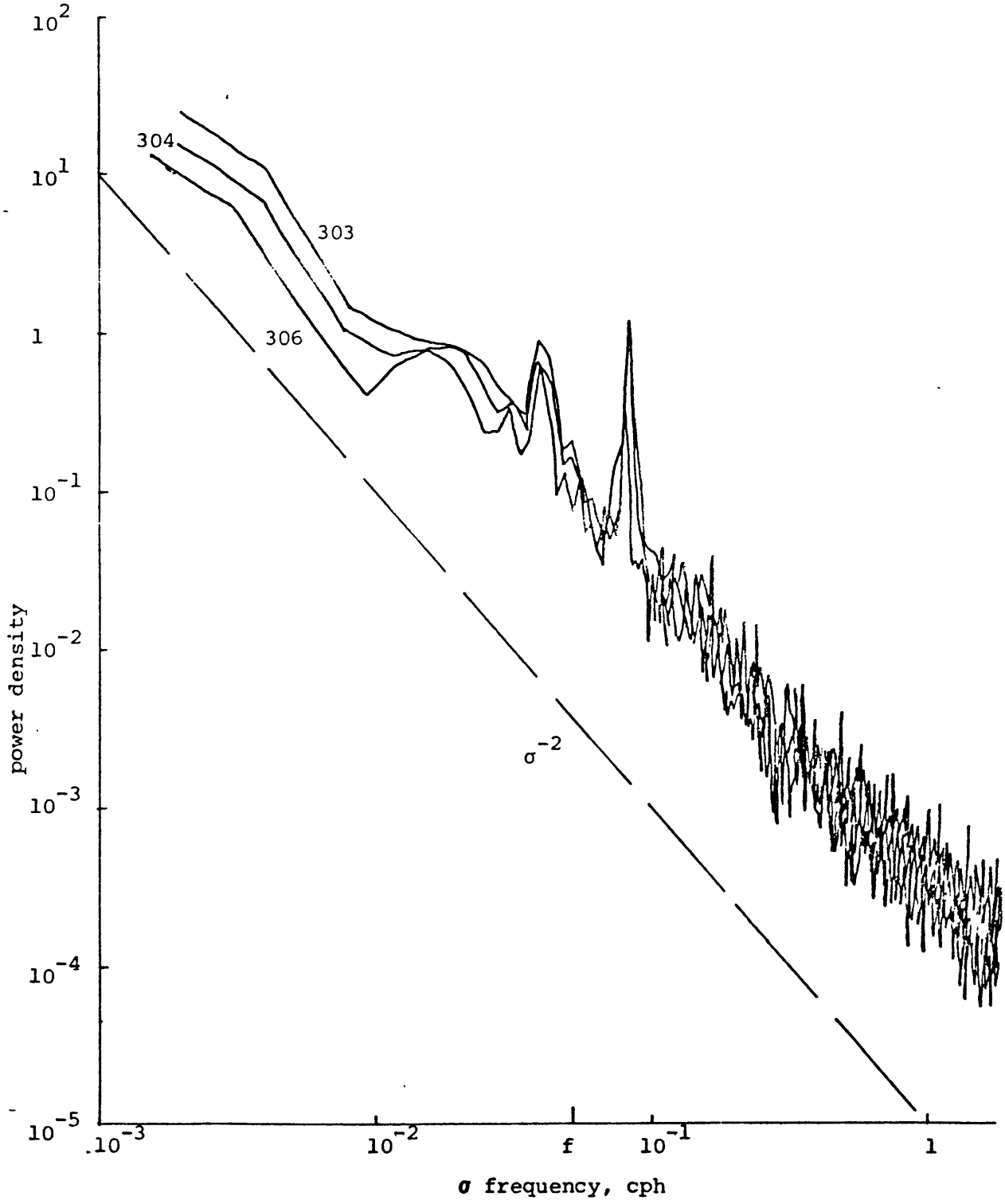

Figure 3-8. Temperature power density spectra from the three lower instruments of mooring 30. Note approximate σ^{-2} dependence on frequency σ at low frequencies contrasting with the deep, near-floor kinetic energy spectra of figure 3-7.

Figure 3-9. Vector plots of low-pass filtered velocity data. Horizontal scale is marked at weekly intervals.

(a) Wind at JFK Airport, New York City. Velocity scale is marked at intervals of 12 m/sec. Vertical direction is up-shelf, 25 east of north.

(b) Currents at our instrument 281, above the canyon walls. Velocity scale is marked at intervals of 12 cm/sec. Vertical direction is up-shelf, 25 east of north.

(c) - (h) Current records within the canyon. Velocity scale marked at intervals of 12 cm/sec. Vertical direction is up-canyon. See figure 3-4 for instrument locations.

(c) 274	(f) 291
(d) 311	(g) 295
(e) 315	(h) 306

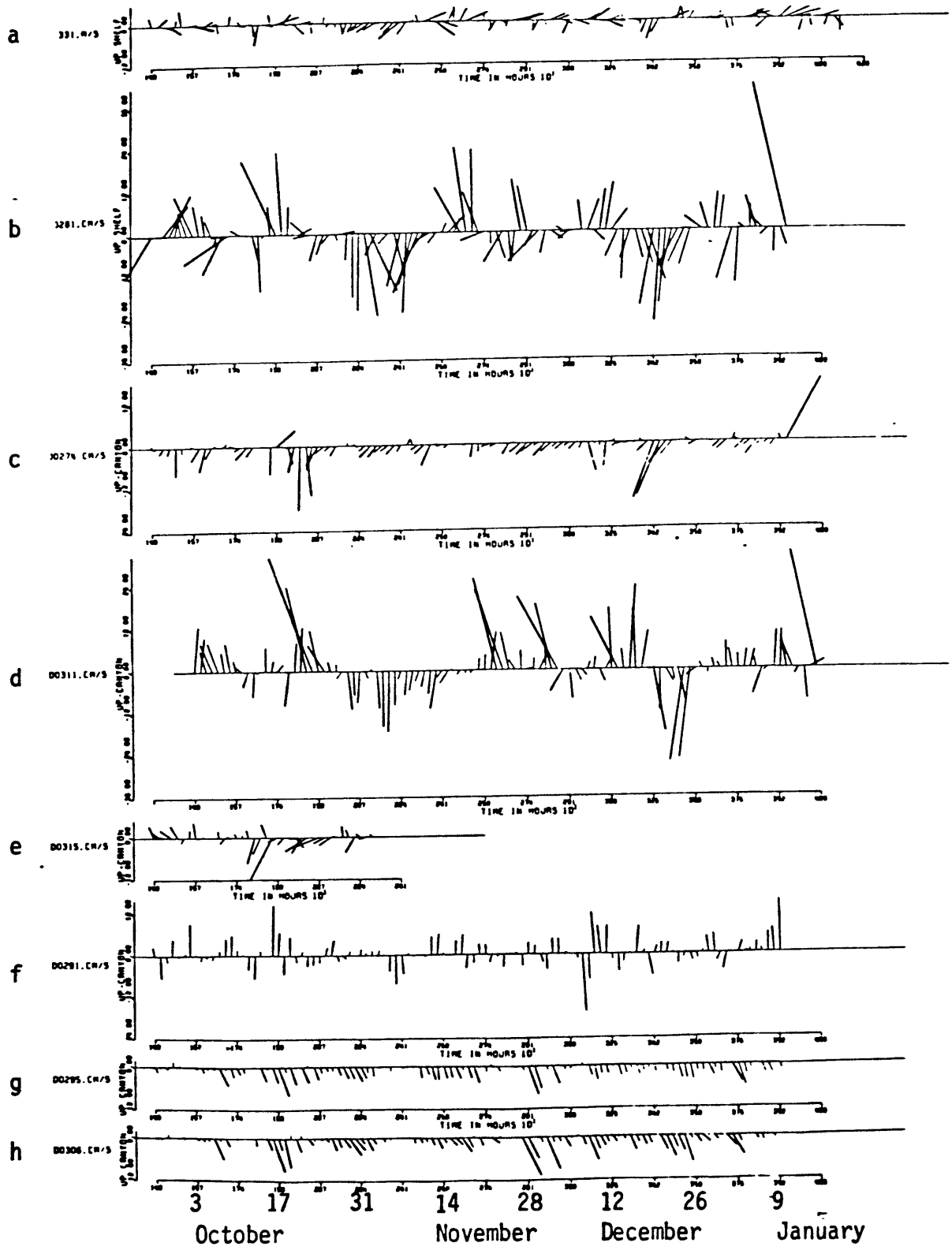
a
b
c
d
e
f
g
h
3
17
31
14
28
12
26
9
October
November
December
January

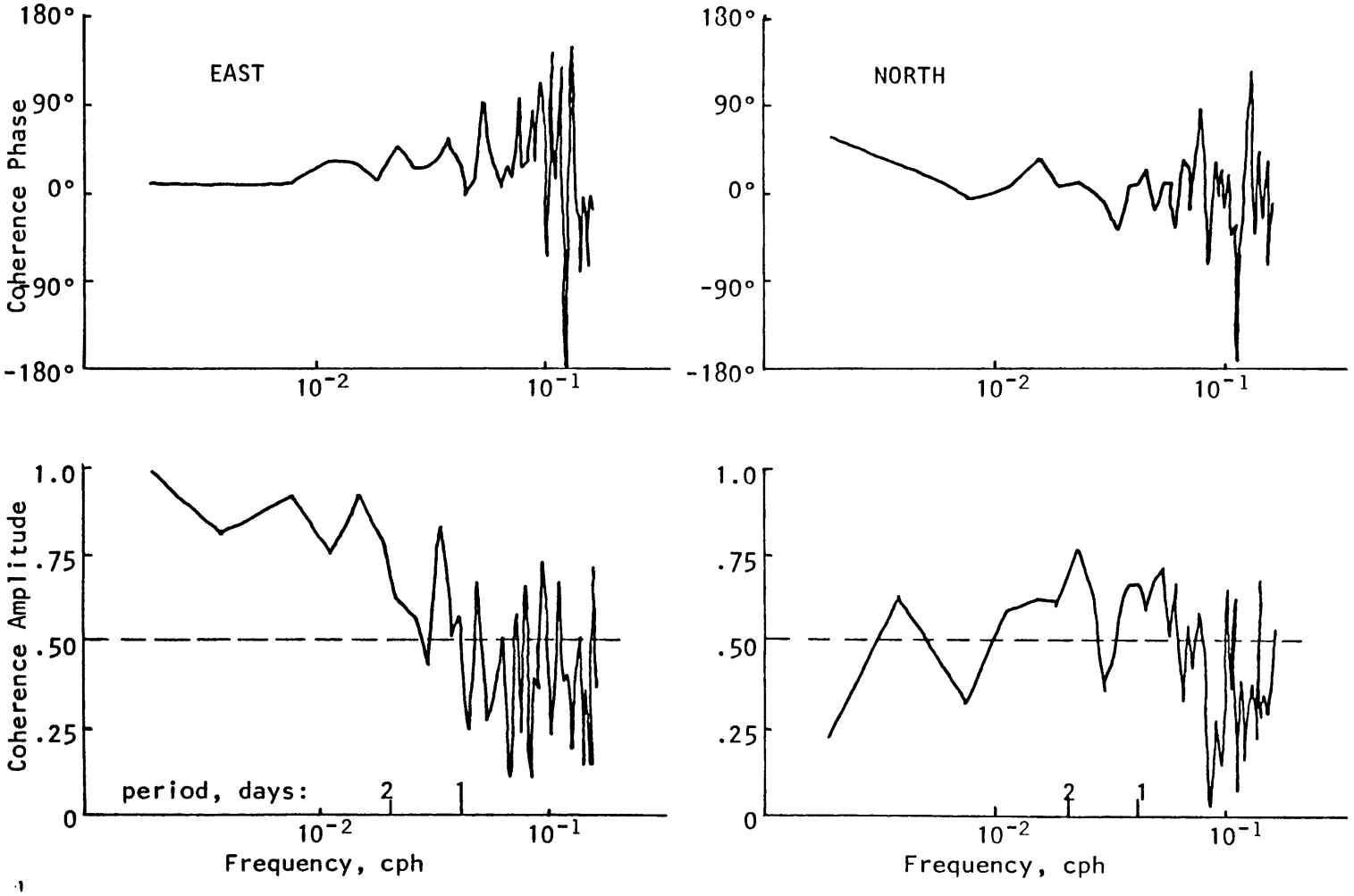

Figure 3-10. Coherence between north and east wind components at JFK airport and EB34. Note higher coherence between east components.

upper current meters, particularly 311. This would be expected if 281 measures the shelf water's geostrophic response to an across-shelf pressure gradient, which forces along-canyon flow in Hudson Canyon where across-canyon pressure gradients can balance Coriolis force.

To test the proposition that 281 is essentially measuring the flow on the continental shelf, I examined its coherence with overlapping records from the MESA long-term mooring at 40.1° N, 73.0° W, on the shelf 65 km northwest of the canyon head. Temperature and velocity records were significantly coherent at the 90% confidence level for the semidiurnal and lowest frequency bands. These bands dominate both records.

Several events that caused coinciding low-frequency flows are apparent in figure 3-9. About October 17, up-canyon (up-shelf) currents at instruments 291, 311, (and 281) preceded down-canyon currents at the other current meters, all of which are near the canyon floor. Southwestward (down-shelf) winds accompanied strong down-canyon and down-shelf currents in mid-December. At the end of the experiment, January 9, strong eastward winds coincided with strong up-shelf flow at instrument 281 and up-canyon currents at 274, 311, and 291.

The east-west wind component ("up-shelf" on figure 3-9 is 25° east of north) has a stronger low-frequency signal than the north-south component, and seems to determine the

sign of the low-frequency currents. Wind stress data from NOAA environmental buoy EB34 are available for much of the experimental period. This buoy is at 73.0° W, 40.1° N, 65 km northwest of the canyon head. As shown in figure 3-10, the eastward components of wind stress from EB34 and JFK were quite coherent from October, 1977 through January, 1978, but the northward components were barely coherent at the 90% confidence level. Thus the east wind component at JFK is more representative of wind stress over the outer shelf than the north component is, and it is not surprising that the coherence between JFK wind and Hudson Canyon currents is associated with the east wind component.

There is also a physical reason why the true east component of wind stress in the New York Bight should be associated with the strongest currents in Hudson Canyon. The canyon currents are apparently part of the upwelling which balances wind-forced flows out of the bight. In the Middle Atlantic Bight, coastal sea level changes are caused mainly by winds parallel to the local coastline (see Wang, 1979). Along New Jersey, this direction is roughly 25° east of north; along Long Island, the along-shore direction is 10° north of east. Because the coast forms a corner, east and west winds along the Long Island shore should be more efficient at causing upwelling than the winds along the New Jersey shore. Eastward winds cause offshore transport in the geostrophic layer as well as the Ekman layer, and westward

winds cause shoreward transport in both layers. For north and south winds, the Ekman and geostrophic transports into the bight are of opposite signs, so that less upwelling or downwelling is required to balance them.

The temperature data from Hudson Canyon were also low-pass filtered. For each day of the experiment, the low-passed temperature values for the 21 instruments of the array were plotted as functions of location on along-canyon sections. The pattern of isotherms in these sections changed as the canyon stratification responded to autumnal cooling.

During the first two weeks of the experiment, the canyon stratification was as we found it during the hydrographic survey: the water in the canyon head was mixed, with a front separating it from slope-like stratification in the outer canyon (see figure 3-11a). A strong thermocline was 400 to 500 m deep in the central canyon. Coincident with the upwelling of October 17, the canyon head became stratified and the deep thermocline disappeared. The water in the canyon head was again mixed during the week of October 27 to November 3.

From November 5 to December 12, a strong shallow thermocline separated the canyon head from unusually warm water just above the canyon (figure 3-11b). This probably resulted from overturning that warmed the deep shelf water before the whole water column started cooling for the winter. After December 21, there was moderate stratification

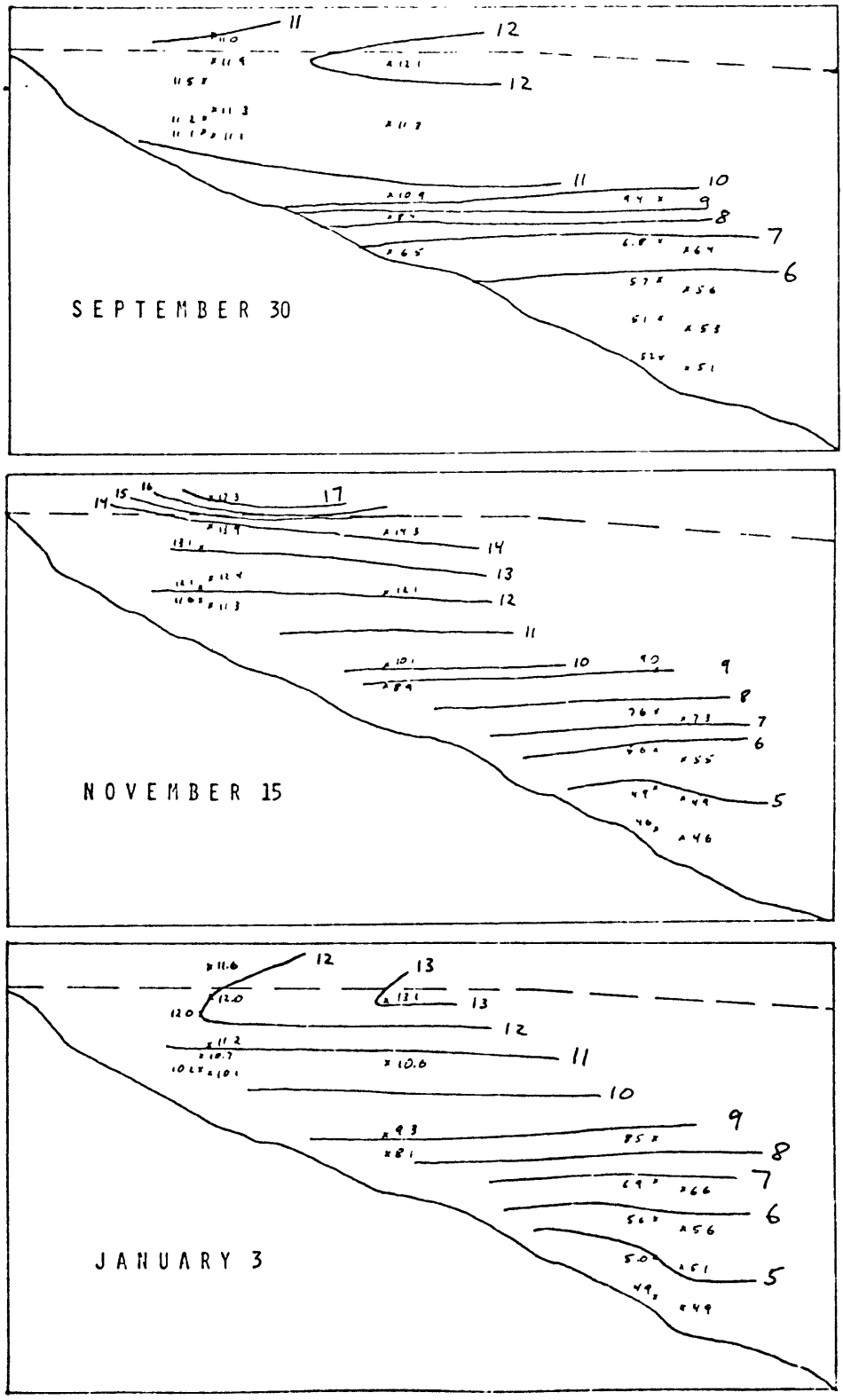

Figure 3-11. Typical sections of low-pass filtered temperature. (a) Mixed canyon head in October. (b) shallow thermocline in November and early December. (c) Moderate stratification in late December.

throughout the canyon with only a weak front separating the head and the outer part of the canyon (figure 3-11c). This is perhaps the normal wintertime situation.

The low-pass filtered temperature sections indicate that the slope water to a large extent fixes the number of isotherms in the canyon, so that neither very strong nor very weak stratification can occur in the whole canyon at once. Instead, strong stratification in the head is balanced by the lack of a deep thermocline; when the canyon head is well-mixed, the isotherms are bunched together in a strong deep thermocline.

3. Storm-forced events. While the array was in place, a series of low-frequency events occurred that caused coincident strong currents and extreme temperatures at many of the moored instruments. The timing of these events associates them with strong upwelling- or downwelling-favorable winds in some cases, and with spring tides in others (discussed in section B). The experiment was only 15 weeks long, too short to permit a proper statistical analysis of these events, so they have been considered individually to understand the relationships between outside forcing and canyon currents. Climatological wind and tide data can then be used to infer the long-term importance of these kinds of events.

The canyon currents associated with upwelling are exemplified by the event that occurred during the last three

days of the experiment. The currents and the wind that forced them were the strongest and most prolonged of the experiment, but the other upwelling events tended to follow the same pattern.

The final event can be characterized by a 30-hour lag between causes and effects as shown in figure 3-12. Winds rose at JFK airport about noon on January 8, blowing initially from the southeast but shifting to the west as they reached their maximum, 18 m/sec, 30 hours later. At the time of the maximum wind, strong up-canyon flows in the upper part of the canyon started at the outer moorings, and at all the other moorings within 5 hours. All current meters except 295 and 306 recorded this up-canyon flow. Speeds built up gradually over a period of 30 hours and reached a maximum of 112 cm/sec at instrument 281. Peak speeds were lower at the deeper instruments; at 291 the maximum was only 32 cm/sec. The up-canyon peaks occurred at zero hours (±4 hours), January 11, and coincided with a decrease in the speed of the wind to about 8 m/sec and the beginning of a down-canyon flow at instruments 295 and 306. This down-canyon current built over a period of 16 hours to a maximum of 60 cm/sec, then died out in 4 hours. Immediately after the down-canyon flow, a shorter and weaker up-canyon flow was recorded, which gradually declined into another down-canyon flow a day after the first. Instruments 291 and 274 also reported a down-canyon flow, beginning at noon on the 11th. This was a

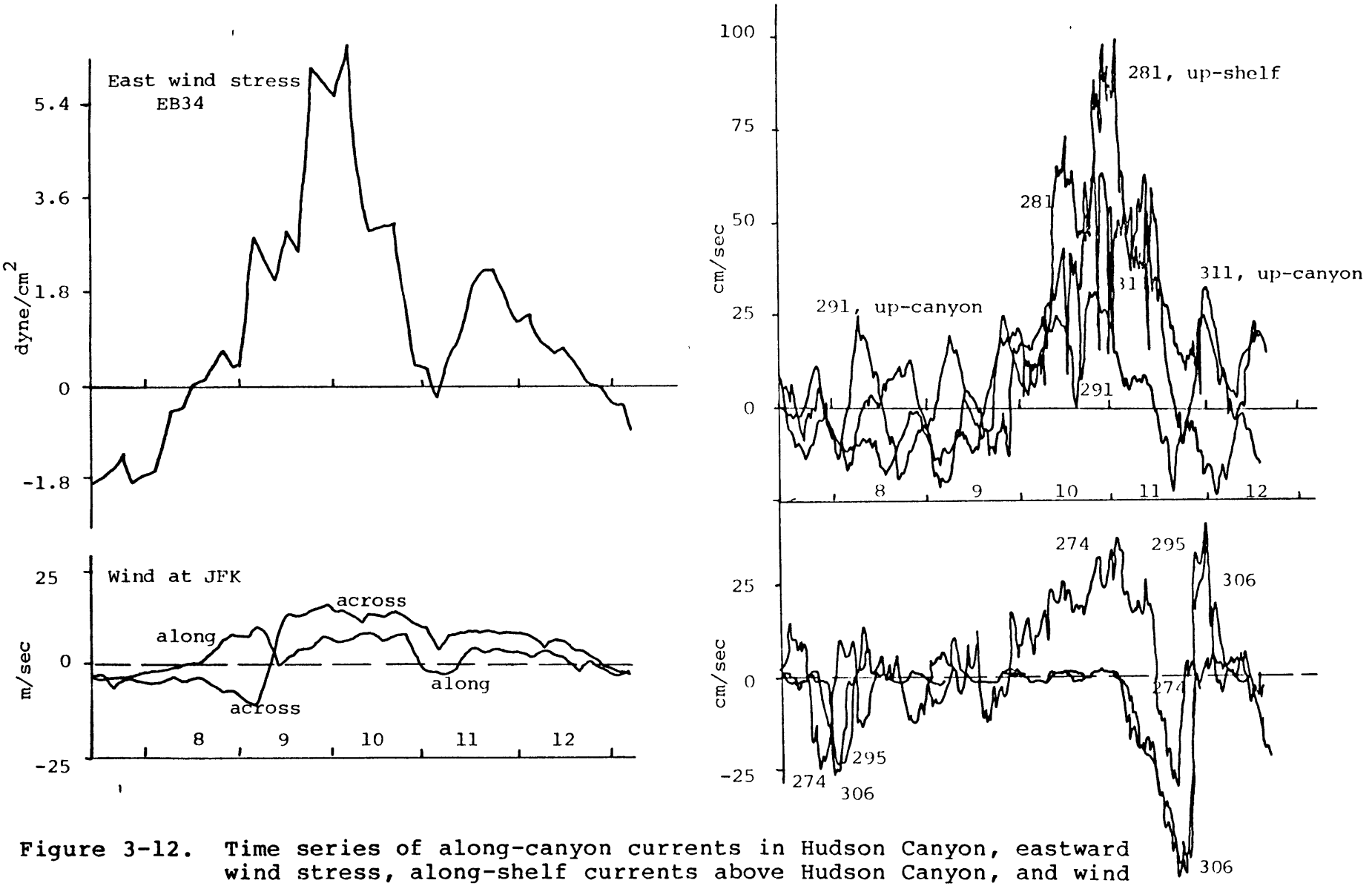

Figure 3-12. Time series of along-canyon currents in Hudson Canyon, eastward wind stress, along-shelf currents above Hudson Canyon, and wind at JFK airport, during the January storm currents.

milder current that reached only 22 and 33 cm/sec, respectively. The wind finally dropped below 5 m/sec and became variable in direction at noon, January 12.

The maximum eastward wind stress at EB34 during this event was 6.6 dyne/cm^2 (using a constant drag coefficient, C = 0.002). The other events that followed eastward wind stresses in excess of 3.6 dyne/cm^2 followed the same pattern: strong up-shelf (at 281) and up-canyon (at 311) flows that lasted about as long as the wind stress, and up-canyon currents in the canyon that decrease in magnitude and duration with depth, followed by down-canyon currrents that increase in strength with depth. At the current meters below the thermocline, 295, 306, and 315, the stronger wind events force unusually long down-canyon currents that interrupt the normal pattern of diurnal and semidiurnal oscillations.

This sequence of events can be understood as the result of upwelling that draws slope water onto the shelf above the thermocline in the canyon. If more dense water upwells than can spill out of the canyon head onto the shelf, the excess dense water depresses the thermocline in the head of the canyon and forces cold water down the canyon in the observed near-floor currents. This process can be seen in the sections of low-pass filtered temperature data from during an upwelling event on December 8-12 (figure 3-13). At the height of the currents, an unusual volume of 8° to 10° water was in the canyon head, with the 10° isotherm displaced

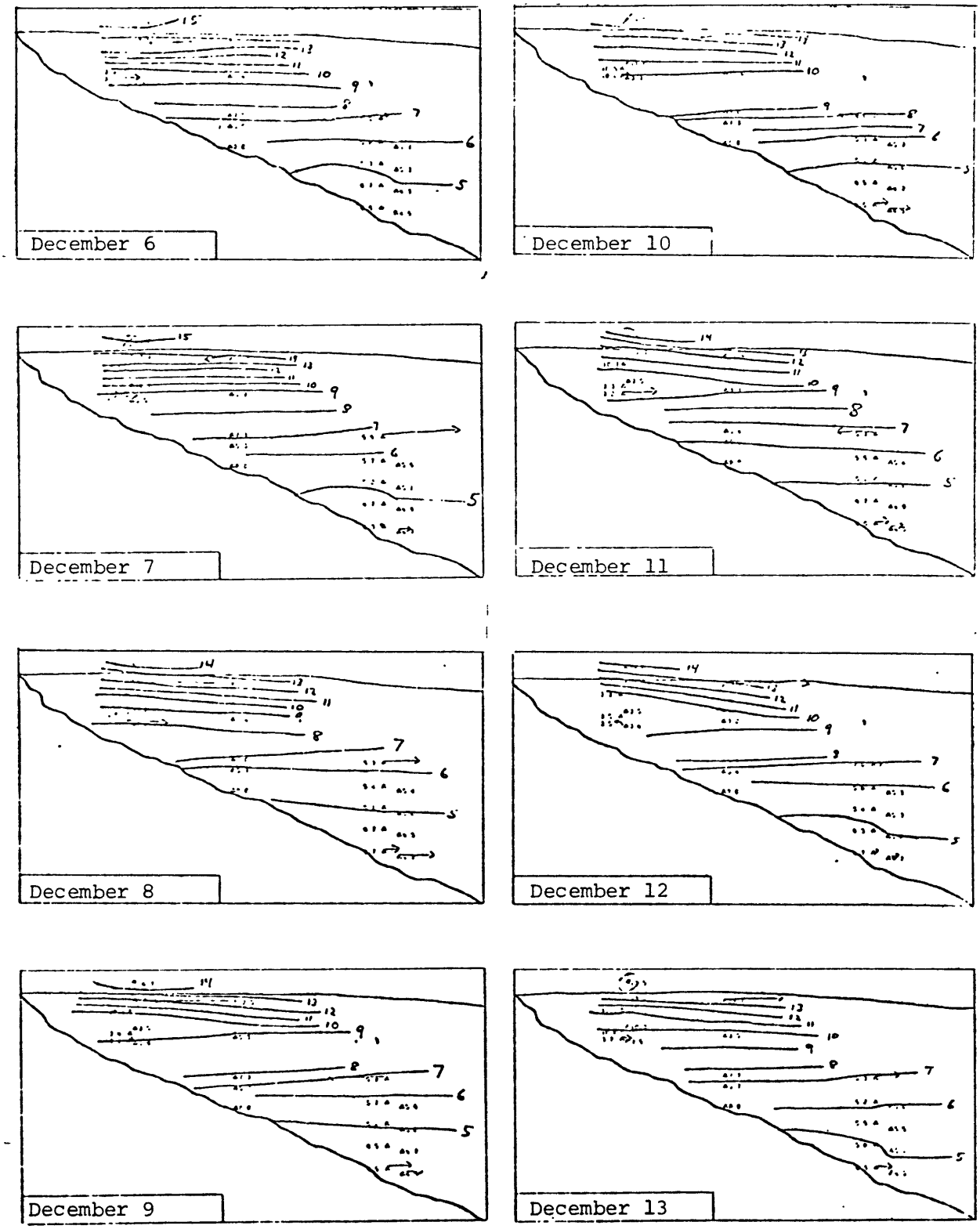

Figure 3-13. Canyon sections of low-pass filtered temperature data during the upwelling of December 8-12. Note the excess of 8° to 10° water in the canyon head on December 9-12.

upward and the 8° isotherm displaced downward.

Strong westward wind stress on December 19-21 caused the downwelling sequence shown in figure 3-14. The maximum wind stress was 6.4 dyne/cm^2. A down-shelf flow at 281 and a down-canyon flow at 311 lagged the wind stress by about 12 hours. The down-canyon current ended abruptly on December 22, whereas the down-shelf flow at 281 decreased gradually and was lost in tidal oscillations two days later. This contrasts with the upwelling pattern in which the currents at 281 and 311 have the same duration.

The effects of the down-welling on stratification in the canyon can be seen in the sections of low-passed temperature in figure 3-15. Cold shelf water filled the head of the canyon, setting up a horizontal temperature gradient between moorings 31 and 28. Strong down-canyon flows were recorded by instrument 274 as the warm water was forced out of the canyon head. The down-welling events had no apparent effects on currents measured below the thermocline at instruments 295 and 306.

The pattern of canyon response to storms in the New York Bight is sketched in figure 3-16. When strong eastward or westward wind stress sets up an across-shelf pressure gradient in the New York Bight, the water above Hudson Canyon flows along the shelf in geostrophic balance. Within the canyon, the water above the thermocline flows down the pressure gradient, which is along the canyon, and an across-

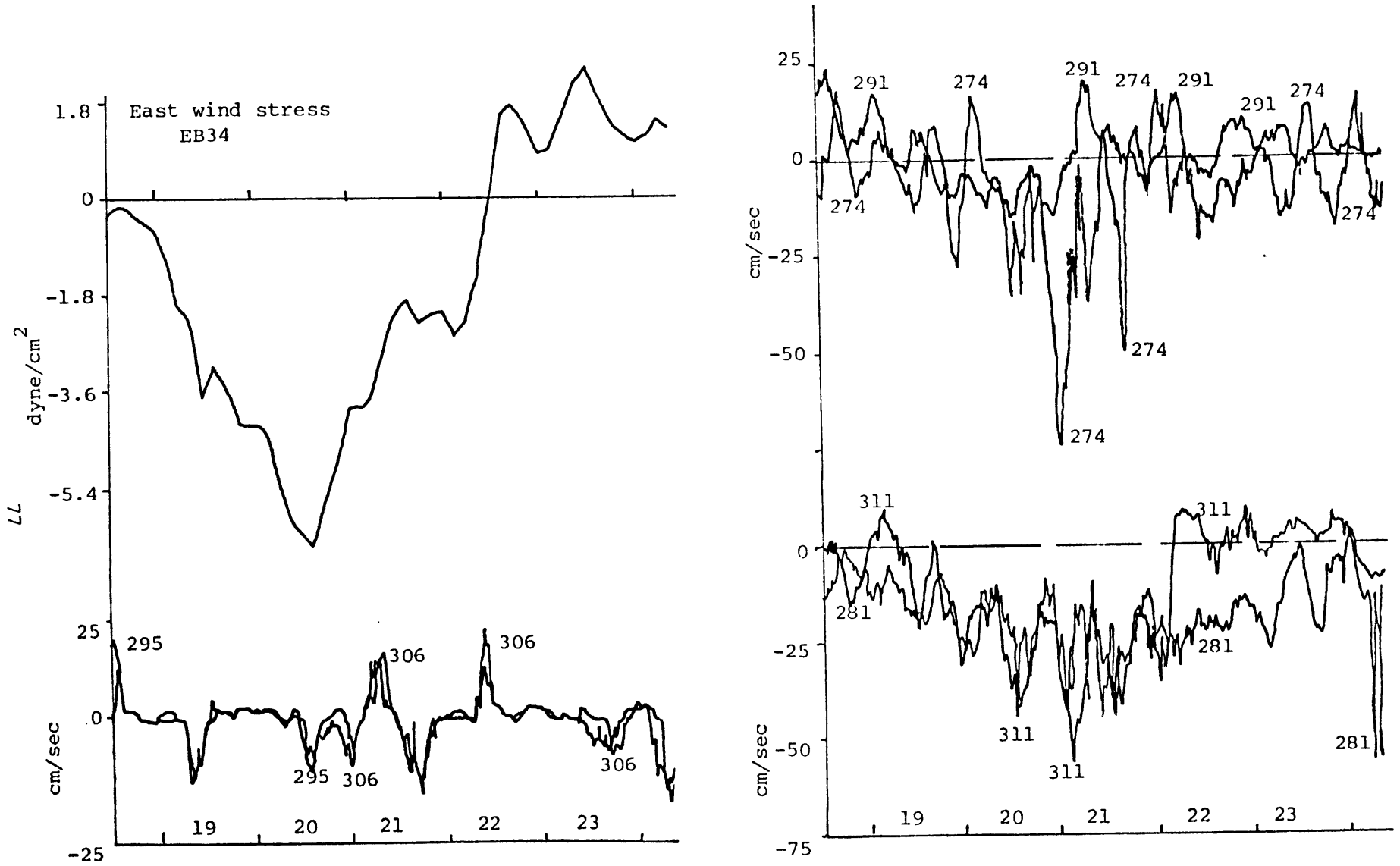

Figure 3-14. Time series of eastward wind stress, along-shelf currents above Hudson Canyon, and currents along Hudson Canyon during the downwelling of December 19-21.

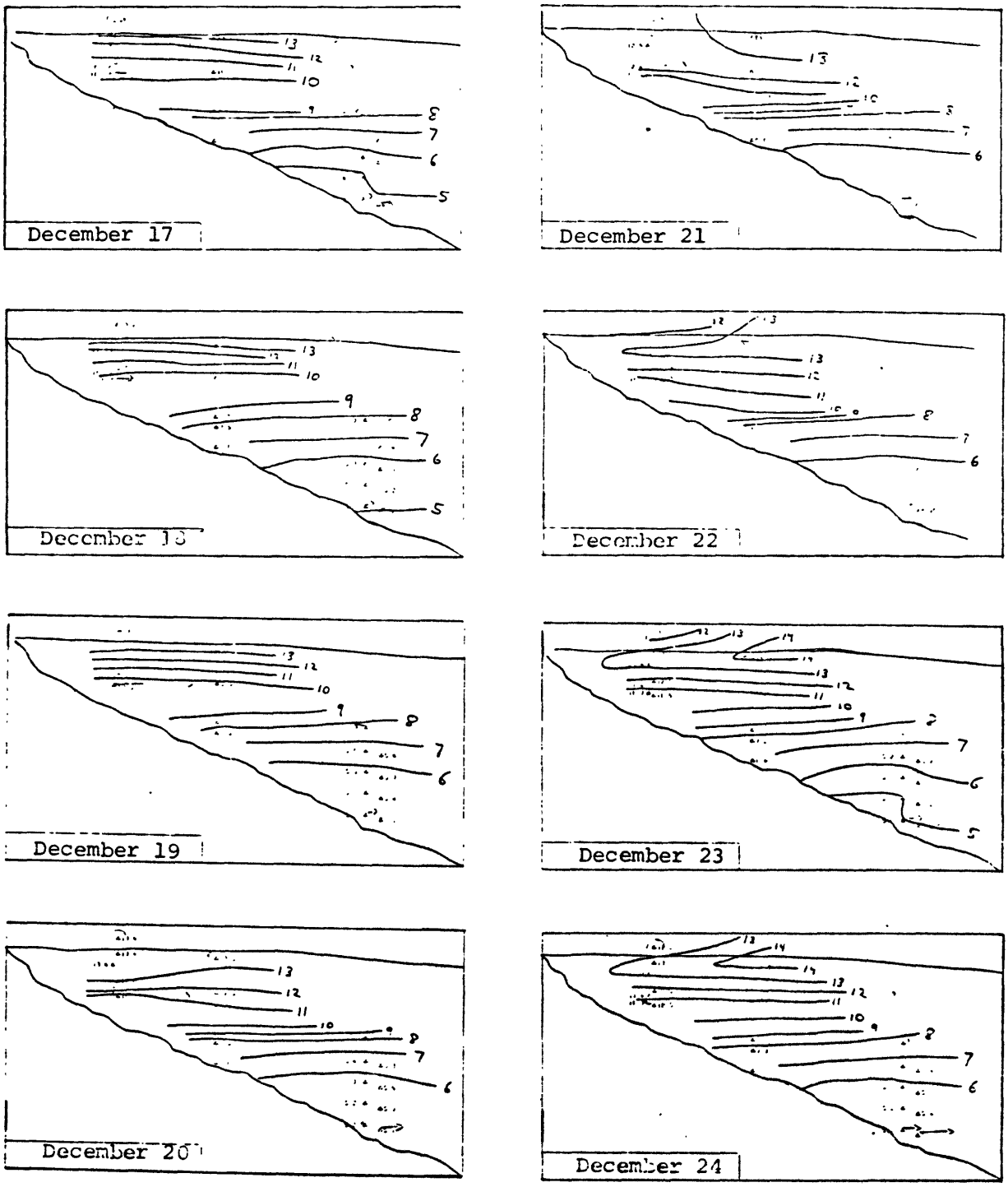

Figure 3-15. Canyon sections of low-pass filtered temperature data during the downwelling event of December 29-21. Note the front between moorings 28 and 31 on December 21-24.

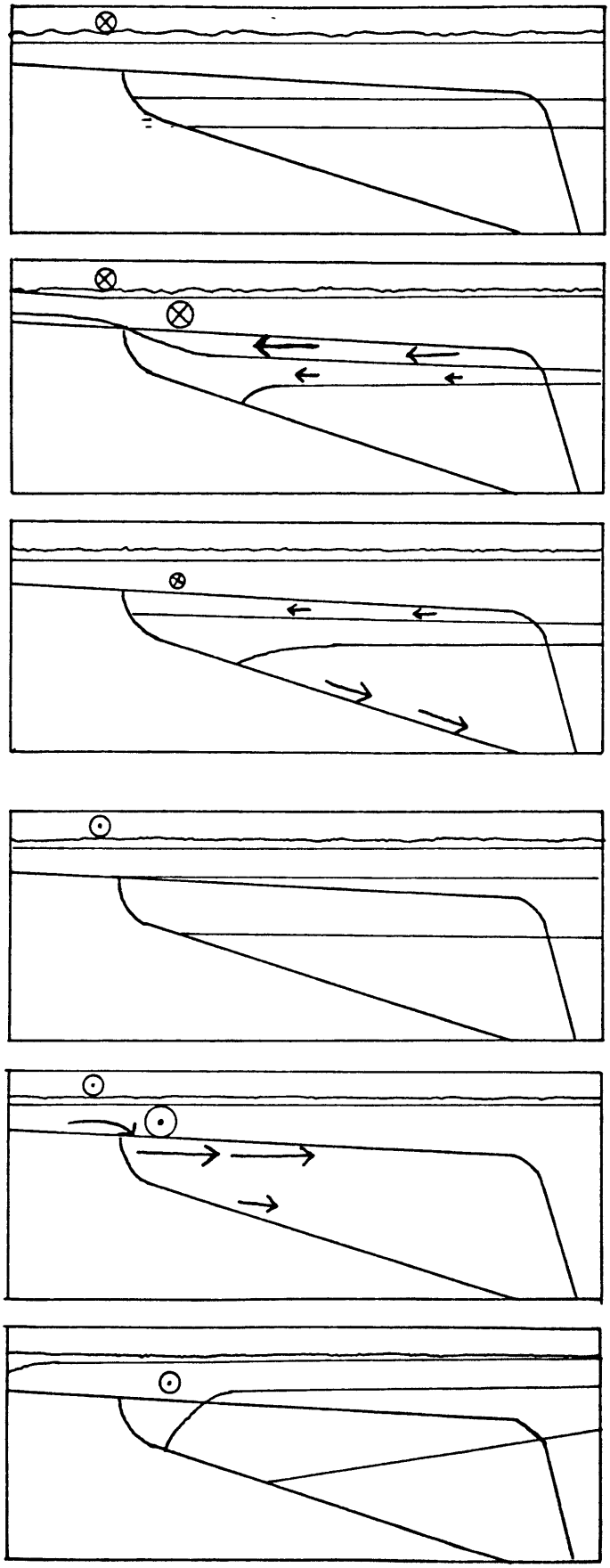

Figure 3-16.

Upwelling

1. Eastward wind, level isotherms

2. Upwelling in upper canyon displaces isotherms

3. Wind ends, currents down-canyon near floor

Downwelling

1. Westward wind, level isotherms

2. Downwelling into canyon and through upper canyon layers

3. Shelf water left in canyon head

canyon pressure gradient develops to balance the Coriolis force. These upwelling and downwelling currents are equivalent in strength to the along-shelf geostrophic flows at the top of the canyon, but their strength decreases with depth. The upwelling and downwelling currents extend to the floor in the canyon head. When westward winds are forcing downwelling, deep shelf water flows into the head of the canyon to replace the water which the pressure gradient forces down the canyon. The thermocline moves slightly down the canyon without strong currents near the floor. When eastward winds force the water above the thermocline to flow toward the canyon head, some of this water is too dense to spill out onto the shelf; it stays in the canyon head, held there by the along-canyon pressure gradient. When the winds and the pressure gradient weaken, this heavy water is released and causes strong down-canyon currents beneath the thermocline.

B. Tidal frequencies

Two processes dominate the velocity field of the Middle Atlantic Shelf: low-frequency flows forced by weather systems, and the semidiurnal (M_2) tide. Tidal velocities on the shelf are greater than in the open ocean and increase toward shore. Butman et al. (1979) measured near-floor currents on the outer shelf near the heads of Hudson and Wilmington Canyons and found tidal velocities with amplitudes between 5 and 10 cm/sec crossing the shelf. The low-frequency velocity component was primarily along the shelf, 5 to 20 cm/sec in strength, and coherent with wind stress.

The surface tide is a wave hundreds of kilometers long and not likely to be modified by a relatively small submarine canyon. The pressure field caused by its surface elevation will tend to force 5 to 10 cm/sec velocities along Hudson Canyon as it does on the adjacent continental shelf. The boundary conditions at the canyon walls can be satisfied through generation of internal waves at tidal frequency. Prinsenberg et al. (1974) and Baines (1973, 1974) have examined the interaction between the surface tide and sea-floor topography. They found two types of topography that result in strong generation of internal waves: floors that slope so that their critical frequencies are close to the tidal frequency, and regions of high topographic relief, such as continental slopes.

According to the Prinsenberg et al. theory, internal

tides would propagate away from the break in floor slope at the top of the continental slope, travelling normal to its trend. The internal tides going into deeper water would constitute a beam that slopes downward at the proper angle for internal waves of tidal period. Regal and Wunsch (1973) found a beam of internal tides above the Middle Atlantic continental rise and traced its probable path back to the continental slope. The break in slope at the top of the walls of a submarine canyon is also expected to generate internal tides. If this happens, the beam propagating into deeper water will reflect off the opposite wall and continue down into the canyon. Internal tides may also be generated along the floor of a submarine canyon if its critical frequency is near the tidal frequency. If the critical frequency is slightly below tidal frequency (the case along much of Hudson Canyon), the generated internal tides would propagate up into the canyon in a narrow, near-floor beam.

The turbulence generated when tidal currents cross the tops of the canyon walls can also be expected to generate packets of higher-frequency internal waves at regular intervals during the tidal cycle. This process has been observed by Farmer and Smith (1980) in a British Columbian fjord: strong tidal velocity across a sill causes lee waves that propagate away as packets of internal waves as the tidal velocity decreases and the internal Froude number passes through unity. A similar process may generate packets of

internal waves at the tops of the canyon walls in synchrony with the tide. If the carrier frequency of the packets is near but slightly less than the critical frequency of the canyon walls (0.2 to 0.4 cph for Hudson Canyon), the packet may propagate directly to the floor of the canyon. These packets would tend to be focussed at some points on the canyon floor, such as the insides of curves and bands equidistant from both walls, and may cause pockets of unusually energetic near-floor currents. Such currents may cause the band of coarse sediment observed along the floor of Hudson Canyon.

Figure 3-17 is a graph of the along-canyon near-floor velocity time series from instrument 315. Semidiurnal and diurnal oscillations dominate this record. When the moon is full, the oscillations are semidiurnal with amplitudes greater than 25 cm/sec, reaching 50 cm/sec. At other times, a diurnal modulation is evident. The lowest amplitude tidal oscillations occur at new moon.

The graphs in figure 3-18 illustrate the percentage of the total observed horizontal kinetic energy in each of five frequency bands. The semidiurnal peak contains about half of the energy in the whole internal wave frequency band, which contains about half of the total horizontal kinetic energy. The mean is an important fraction of the energy only at instruments 281 and 311, above and near the top of the canyon walls. High-frequency internal waves are relatively more

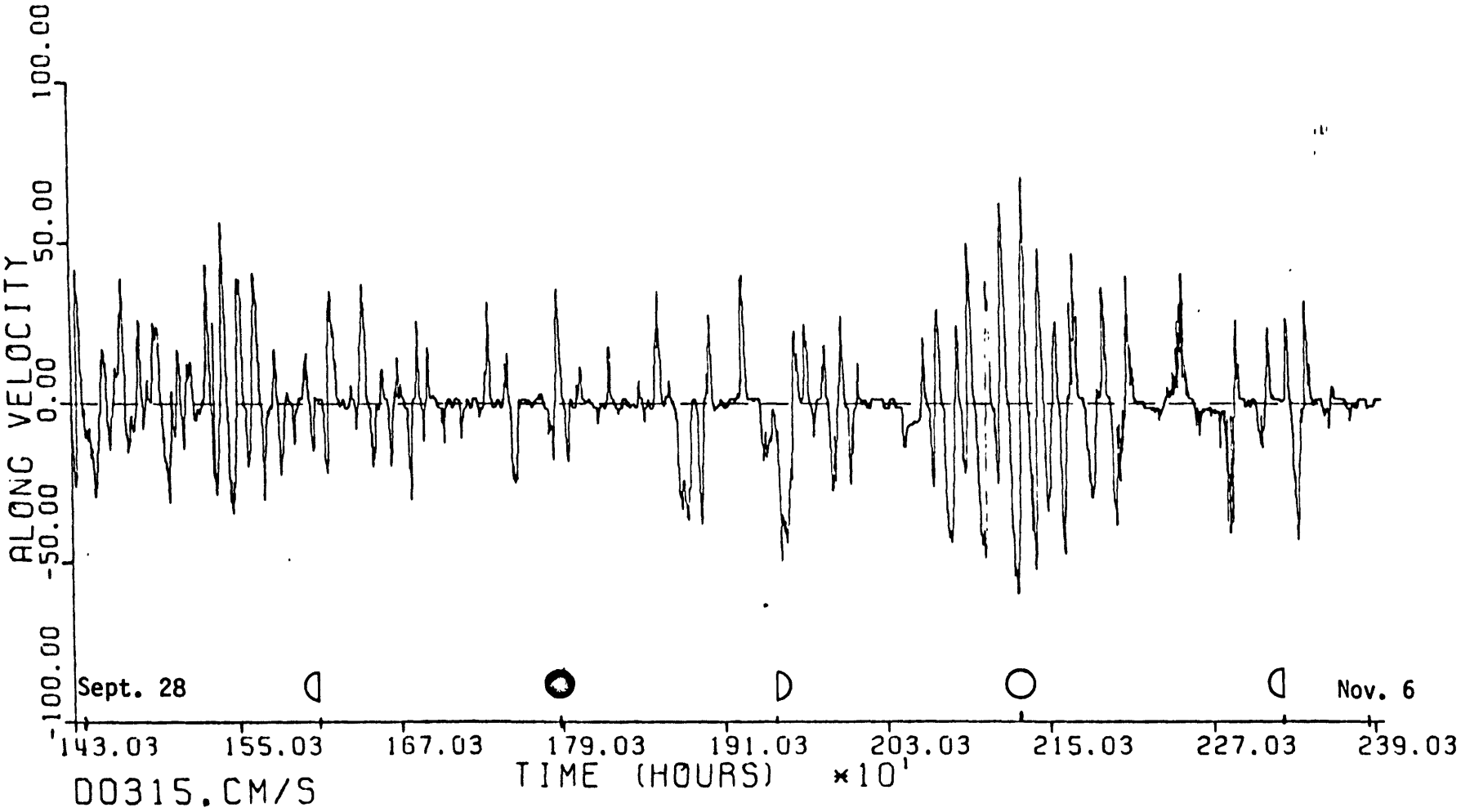

Figure 3-17. The along-canyon velocity record from current meter 315 (see figure 3-4 for location). Time axis is marked at intervals of 5 days, and phases of moon are indicated by standard symbols. Note strong semidiurnal oscillations at full moon and weaker diurnal oscillations at new moon.

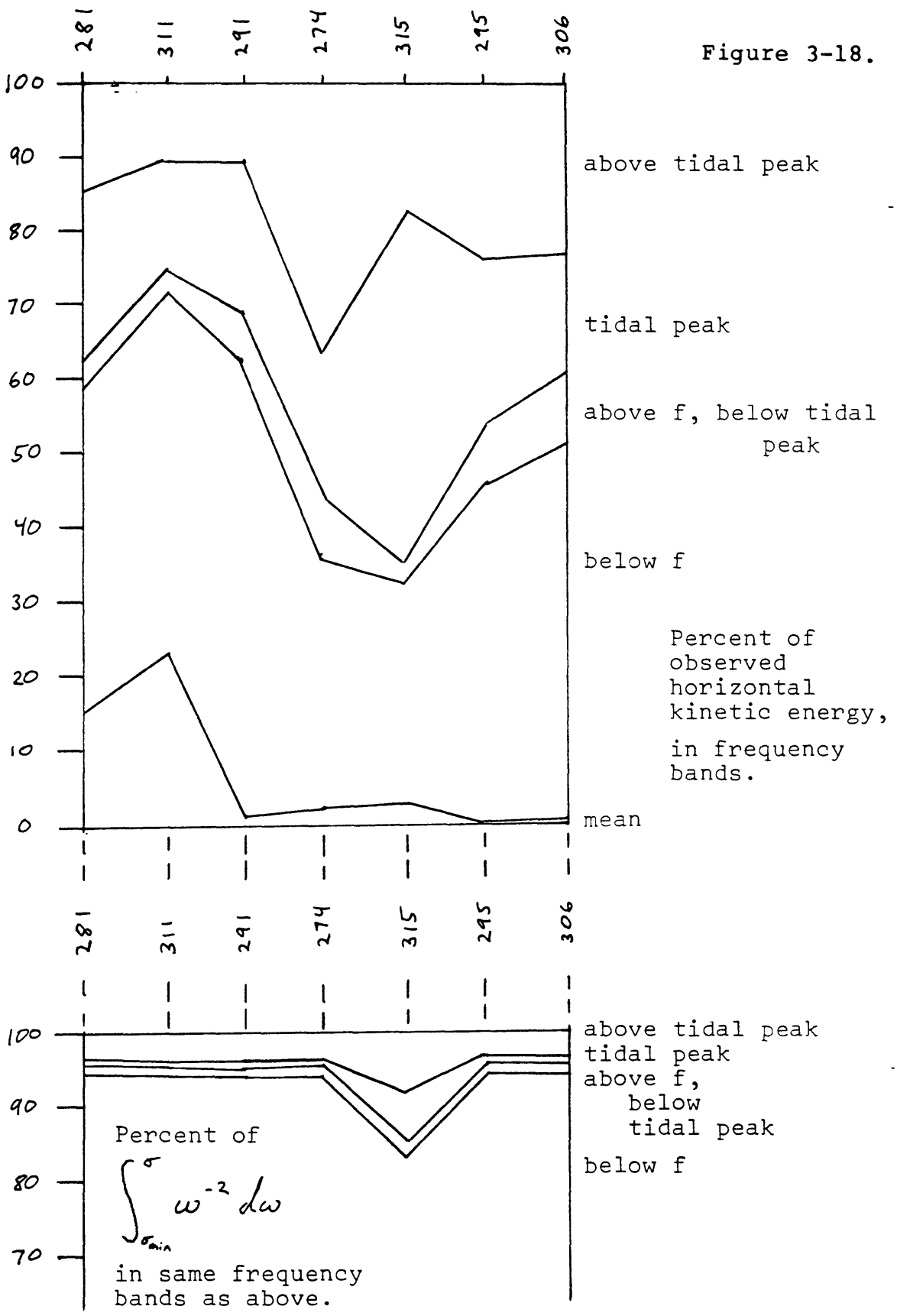
281
311
291
274
315
295
306
100
90
80
70
60
50
40
30
20
10
0
above tidal peak
tidal peak
above f, below tidal peak
below f
mean
Percent of observed horizontal kinetic energy, in frequency bands.
281
311
291
274
315
295
306
100
90
80
70
above tidal peak
tidal peak
above f, below tidal peak
below f
Percent of
$\int_{\sigma_{min}}^{\sigma} \omega^{-2} d\omega$
in same frequency bands as above.

Figure 3-18.

energetic at the near-floor instruments.

On horizontal kinetic energy spectra, the semidiurnal peaks are generally only one frequency band wide (with 60 degrees of freedom), which is 0.003 cph for most instruments and 0.008 cph for 315. For instrument 274 (near the floor in the canyon head), the peak is spread over two bandwidths (0.006 cph), probably as a result of non-linear processes. On raw Fourier transforms of the data, the semidiurnal peaks are generally three bandwidths wide, or 0.001 cph, with the most energy at 0.0806 cph. This is the frequency of the M_2 tidal component.

The size of the semidiurnal peaks on the temperature spectra implies that internal tides are present. There are also peaks at the diurnal frequency, below the Coriolis frequency and thus too low for free internal waves. This implies that internal tides are locally generated. The relative observed strengths of the baroclinic and barotropic components cannot be reliably estimated without hydrographic data more representative of the entire experimental period. However, theoretical considerations indicate that neither component is likely to be dominant: an essentially barotropic tide could not meet the conditions at the canyon boundaries, and the baroclinic tide would not be generated in the absence of the barotropic one. The coherence lengths and phase lags at tidal frequencies imply length scales appropriate for internal tides and an energy flux pattern consistent with

Wunsch's (1969) model of shoaling internal waves, and thus imply a strong baroclinic component.

At the semidiurnal frequency, horizontal coherence lengths are about 8 km (measured along the canyon). Vertical coherence lengths range from 75 m in the canyon head to 350 m at mooring 29. The significantly non-zero horizontal phase lags indicate propagation of internal tides into the head of the canyon at instruments 27 and 28, and out of its mouth at instruments 29 and 30. The significant vertical phase lags show the upper instrument leading, implying downward phase propagation and upward energy flux. These trends indicate that a significant amount of internal tide generation is occurring along the floor in the central part of the canyon.

The observed tidal-period oscillations changed in amplitude with the surface tide. Particularly strong near-floor oscillations were recorded at the times of the full moons in September (25-27) and December (25-31). At new moon, the velocity at instruments 295 and 306 is typically a series of up- and down-canyon surges separated by intervals of speed too low to turn the Aanderaa rotors. Throughout the month, the down-canyon speeds at 295 and 306 are higher than the up-canyon speeds, resulting in a down-canyon mean.

C. The internal wave field

1. Theory. The "normal" internal wave field, as found in the open ocean, approximately matches the frequency and wave number spectra proposed by Garrett and Munk (1972, 1975). Normally, the internal wave energy level varies in proportion to the buoyancy frequency, N, where

$$N^2 = - \frac{g}{\rho_o} \frac{\partial \rho}{\partial z}$$

Internal wave energy propagation appears to be horizontally isotropic and vertically symmetric throught most of the open ocean. Variations from the Garrett-Munk model have been found mostly near pronounced topographic relief, such as seamounts and submarine canyons (Wunsch, 1976, Wunsch and Webb, 1979).

Internal wave energy can be concentrated in the heads of submarine canyons because internal waves travel through the ocean at prescribed angles to the horizontal and maintain these angles when they reflect off solid boundaries. Internal waves range in frequency from the Coriolis frequency, f, to the buoyancy frequency N. The direction of an internal wave's group velocity is determined by its frequency relative to f and N. If α is the angle between the group velocity and a horizontal plane, and σ is the internal wave frequency, then

$$\tan^2\alpha = \frac{\sigma^2 - f^2}{N^2 - \sigma^2}$$

Figure 3-19.

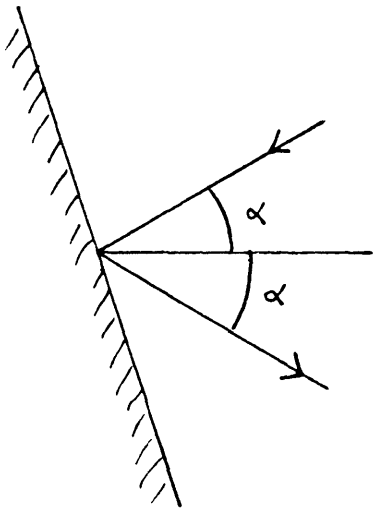

a. internal wave reflecting off a steeply sloping wall.

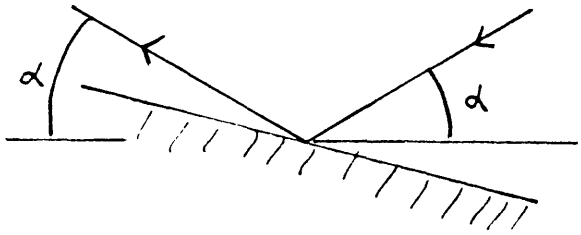

b. internal wave reflecting off a slightly sloping floor.

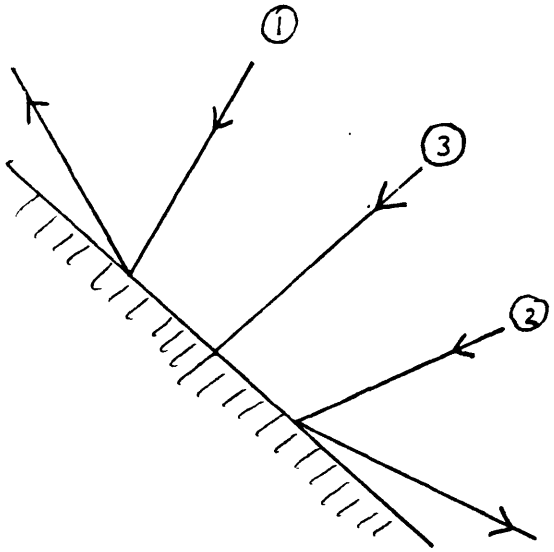

c. internal waves of frequencies above (1), below (2), and at (3) the critical frequency of a wall.

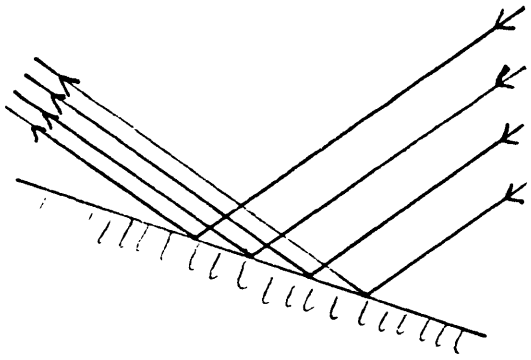

d. concentration of reflected internal wave rays near a sloping floor.

Thus internal waves with frequencies near N have nearly vertical group velocities; those with frequencies near f have nearly horizontal group velocities.

Since the angle of propagation α is fixed by stratification, the Coriolis force, and internal wave frequency, internal waves must conserve their angles of propagation with respect to the horizontal when they reflect off the sloping sea floor or off a sloping canyon wall. Because of this restriction on the angle of propagation, an internal wave travelling up a submarine canyon from the ocean will be reflected back toward the ocean if the slope of the canyon floor is steeper than the internal wave's trajectory (see figure 3-19a). If the floor is less steep (figure 3-19b), the internal wave can continue to travel up the slope to the canyon head. Internal waves entering the canyon from above can continue to travel down into the canyon only if they reflect off the canyon walls at points where the wall slope is steeper than their trajectories.

Consider a simplified continental margin of slope γ, so that the floor is at $z = -\gamma x$. The internal waves that encounter this slope shift from forward reflection to backward reflection at the critical frequency σ_c:

$$\sigma_c^2 = \frac{f^2 + \gamma^2 N^2}{\gamma^2 + 1}$$

(See figure 3-19c). The effects of a simple continental slope on internal waves entering from the ocean have been

examined using linear internal wave theory (see Wunsch, 1969, McKee, 1973, and Eriksen, 1981). As internal waves approach shallow water, they are refracted to travel normal to the isobaths. Those of frequency higher than the critical frequency will reflect forward off the floor and continue to travel up the slope, where their energy is concentrated into a smaller volume. High energy levels and short length scales are predicted at the top of the slope and make the linear development invalid there. In contrast, waves of frequency less than the critical frequency will reflect backward off the slope and not reach its top. In an inviscid theory, internal waves of critical frequency attain infinite velocities along the floor. Some near-floor intensification is expected at all frequencies, as shown in figure 3-19d.

Laboratory experiments (Cacchione and Wunsch, 1974) support the theoretical models qualitatively. When internal waves were near the critical frequency, a good deal of mixing with strong motion along the floor was observed. When the internal waves were well above the critical frequency, intensification was observed at the top of the slope, with shortening of wavelengths. The internal waves at the top of the slope broke catastrophically when sufficiently high energy intensities were reached.

Using three records from Hydrographer Canyon, Wunsch and Webb (1979) showed that the energy of the internal wave field grew by a factor of five from the mouth of the canyon to a

position well inside. This result suggests that theoretical and laboratory results may apply to submarine canyons.

Submarine canyon geometry is much more complex than the simple slopes used in the theories and laboratory experiments. Real canyons have sloping side walls and continental shelves around their heads. The "canyons" studied in the laboratory had vertical walls, flat sloping floors, and were not rotating. The internal waves studied simply advanced along the slope. Internal waves enter real canyons from above as well as through their mouths, and the sloping canyon walls will reflect the ones below their critical frequencies deeper into the canyon. Since the walls converge with depth, the internal wave energy is concentrated into smaller volumes and reaches greater intensities as it goes toward the canyon floor (see Gordon and Marshall, 1976). This process augments the focussing of internal wave energy caused by the sloping floor.

The critical frequencies of the walls of Hudson Canyon range from about 0.2 to 0.4 cph; that of the floor, using the slope along its axis, is about 0.056 cph. This value is barely above the local inertial frequency, 0.053 cph. Thus internal waves in the range of frequencies between 0.056 cph and about 0.3 cph should focus into the canyon both from above and from the mouth.

2. Internal wave results. The observed internal wave field was examined using the methods of spectral analysis.

Coherence, power density, and kinetic and potential energy spectra were computed using methods presented by Bendat and Piersol (1971) and Hotchkiss (1980).

a. Coherences. The mooring pairs, 27-28 and 29-30, are sufficiently close that temperature coherence magnitudes for instruments of the same depth are above 0.9 for frequencies as high as 0.1 to 0.2 cph. The semidiurnal peak at 0.08 cph is consistently present, even for horizontal coherences between moorings 28 and 31. Thus the horizontal coherence length for internal waves in Hudson Canyon is greater than the 0.8 km distance between moorings 29 and 30 but, except for semidiurnal and diurnal frequencies, less than the 6.6 km separation of moorings 28 and 31.

Vertical coherences, between temperature records from different instruments of the same mooring, also have significant peaks at 0.08 and 0.04 cph. Except for these peaks, the coherence magnitude was roughly constant for low frequencies then fell rapidly, at a frequency ω_t between .04 and .1 cph, to a level not significantly above zero. Both low-frequency coherence level and ω_t, the maximum frequency of high coherence, decrease as the separation of the instruments increases. Figure 3-20 shows graphs of these trends. Low-frequency coherence drops off fastest in the canyon head and slowest at the deepest moorings. A similar variation in the dependence of ω_t on separation can be discerned in Fig 3-20b; the further the mooring is from the canyon head, the

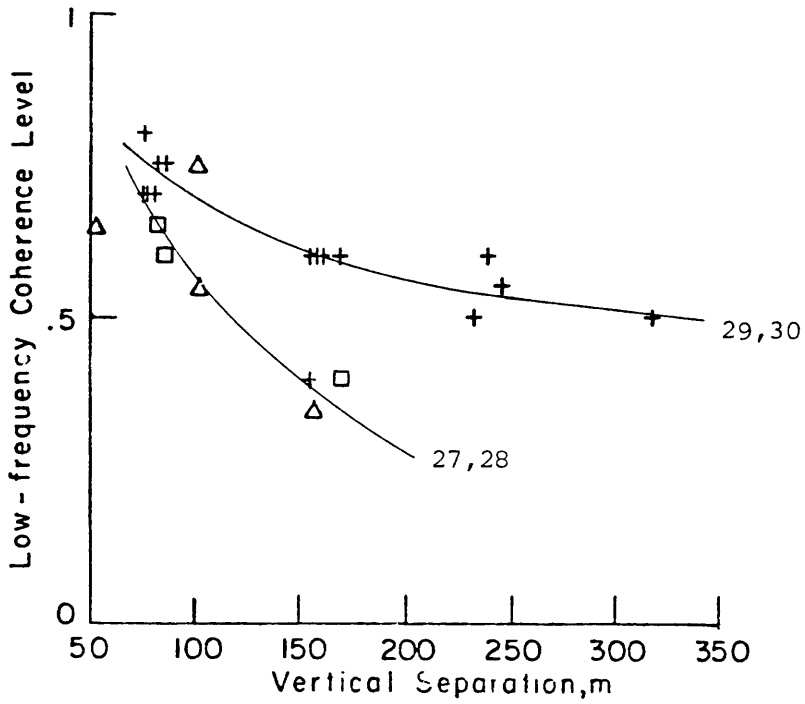

symbol	+	□	△
moorings	29,30	31	27, 28

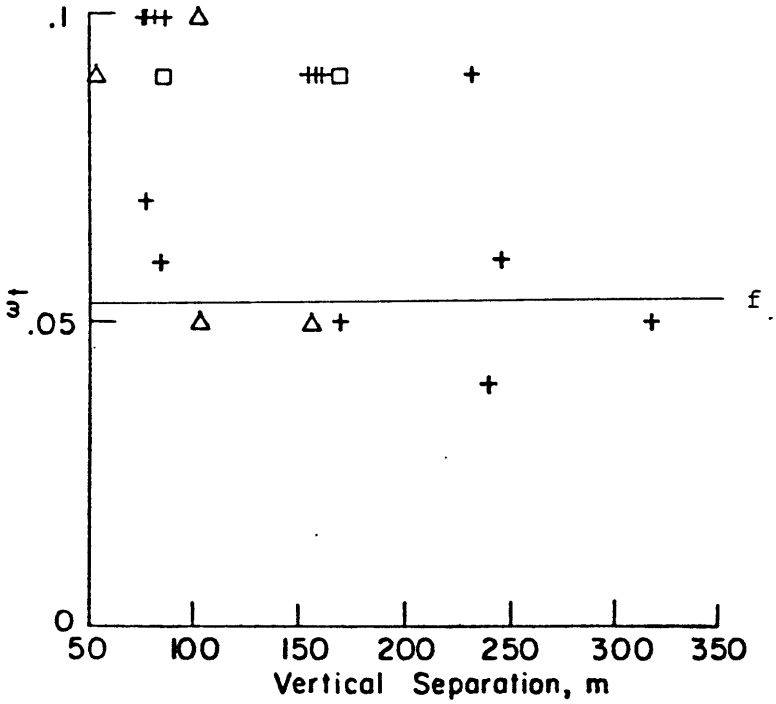

Figure 3-20. The low-frequency coherence level (a) and ω_t, the maximum frequency of high coherence (b) of vertically separated instruments, shown as functions of separation and location in canyon. Level of no significance is approximately .3.

greater is the maximum separation for which ω_t is greater than the inertial frequency. Figure 3-21 shows coherence spectra in which the decreasing coherence with increasing vertical separation can be seen.

The number of vertical modes present in the internal wave field can be inferred from coherence lengths. The vertical coherence length is proportional to twice the reciprocal of the bandwidth of vertical wavenumbers (Garrett and Munk, 1972). The ith mode has i/2 cycles over the depth of water, h, for a wavenumber $k_i = i\pi/h$. If a total of I modes is present, the bandwidth of vertical wavenumbers is:

$$\Delta k = k_I - k_1 = \frac{I\pi}{h} - \frac{\pi}{h} = \frac{(I-1)\pi}{h}$$

The vertical coherence length, Z, is then proportional to 2h/(I-1). Assuming that the modal structure of the canyon internal wave field is determined by the local water depth only, this method can be applied to the canyon data.

Using Figure 3-20, the vertical coherence length can be estimated as the maximum vertical separation for which any part of the internal wave band is highly coherent, i.e. the separation where ω_t becomes less than f. From the formula above, the number of vertical modes, I, can be estimated for each part of the canyon. Taking Z as 100, 150, and 250 m for the head, central and outer moorings, respectively, the vertical coherence length is seen to decrease in proportion to depth, consistent with 7 or 8 vertical modes throughout

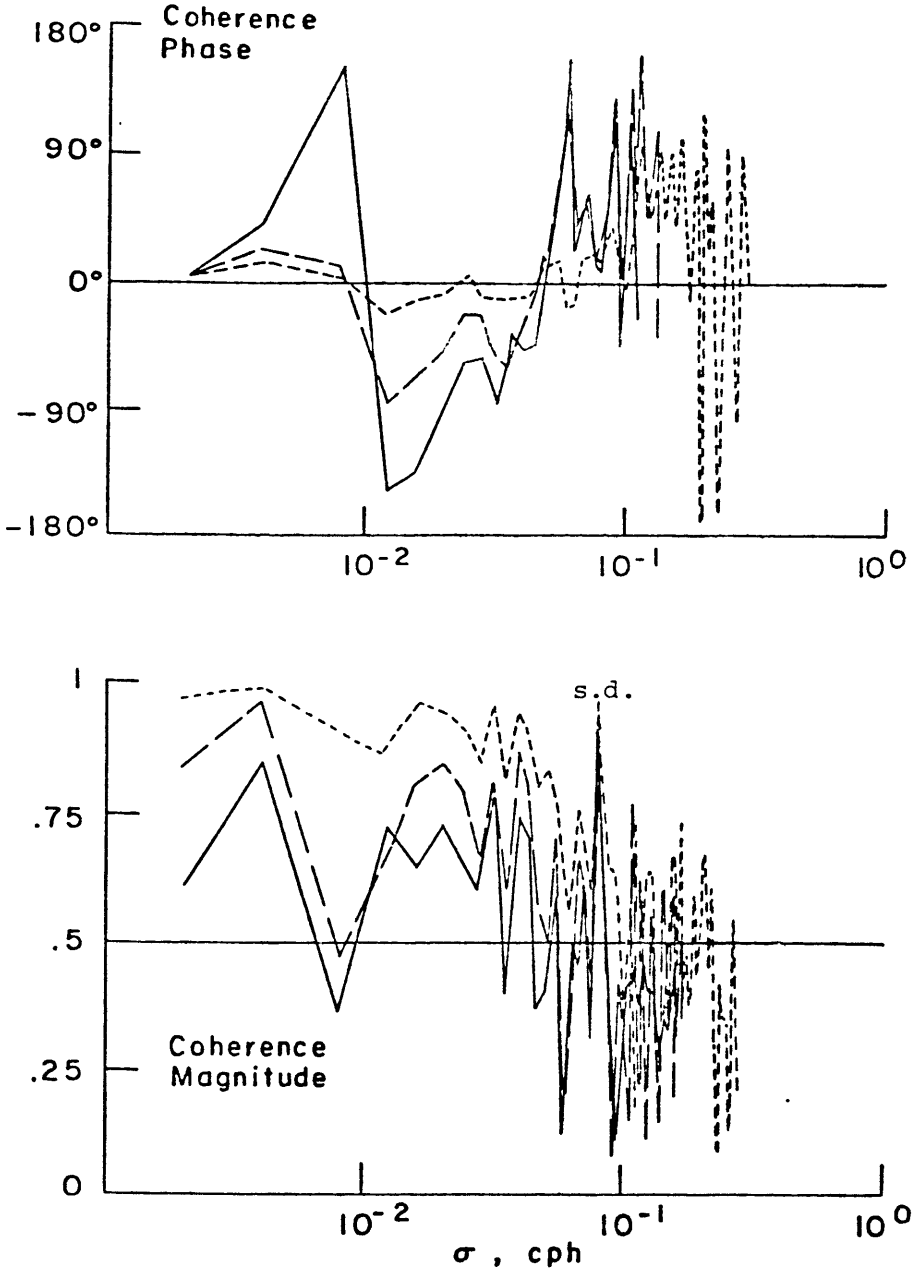

Symbol	Vertical Separation	Instrument Pair
———	247 m	302 – 306
— — —	170 m	303 – 306
-------	87 m	304 – 306

Figure 3-21. Coherence for mooring 30 showing changes with increasing vertical separation. Level of no significance is about .3.

the canyon, and thus also consistent with the deep ocean internal wave spectrum (Garrett and Munk, 1975).

Direction of energy propagation can be determined from the phase lag between coherent instruments. The phase lag indicates the direction of phase velocity; energy propagates in the same sense horizontally but in the opposite sense vertically, for internal waves.

Only moorings 29 and 30 are likely to be interpretable in simple terms; the moorings at the head of the canyon are in a region where the linear theories should break down, and the coherence results from these moorings fit no simple pattern. Where there is coherence between moorings 29 and 30 the results are fairly simple. The coherence between horizontally separated instruments was above the level of no significance for frequencies as great as 0.2 cph (5-hour periods), with phases generally consistent with up-canyon propagation except at tidal frequency. (The distance between moorings 29 and 30 is 0.8 km.) At both moorings, the near-bottom vertically adjacent instruments consistently had phase lags that indicate downward phase propagation (positive phases on figure 3-21), corresponding to upward energy flux. Phase lags between the upper vertically adjacent instruments were not consistently either significantly positive or significantly negative because of large confidence intervals resulting from low coherence magnitudes.

b. Power density. Power density spectra of pressure

and temperature from the canyon array consistently have strong semidiurnal and diurnal peaks (see figure 3-8). Only those from instruments near or above the top of the canyon walls have significant inertial peaks.

Velocity power density spectra all have a roughly σ^{-2} dependence in the internal wave band and significant semidiurnal peaks. Some also have diurnal peaks, and some have small but significant inertial peaks. The only large inertial peaks are in spectra for 281, the instrument above the canyon walls. As is expected, the along-canyon velocity is more energetic than the across-canyon velocity. This anisotropy is stronger for longer-period waves, and in the canyon head. Power density levels increase toward the canyon head for both along- and across-canyon components.

In shape, power spectra of the internal wave field well within Hudson Canyon resemble those of data from the upper continental slope which also have a general σ^{-2} dependence and lack a significant inertial peak. The outstanding differences between the canyon and slope spectra are the large semidiurnal and diurnal peaks on the canyon spectra. Two instruments of the canyon array produced spectra that resembled those of shelf data. These were current meters 281 and 311, which had inertial peaks and velocity coherences that indicated inertial waves. Inertial waves are common on the shelf (Mayer et al., 1979, Zenk and Briscoe, 1974).

c. Kinetic energy. All of the normalized horizontal

kinetic energy (hke) spectra have σ^{-2} dependence in the internal wave frequency band. Spectra of hke from the tops of moorings differ from those from bottoms of moorings by having more pronounced semidiurnal (0.08 cph) and inertial (0.05 cph) peaks and less pronounced diurnal (0.04 cph) peaks. As is shown in figure 3-22, normalized horizontal kinetic energy is generally higher at the bottoms of moorings than at the tops, and in the canyon head than at the outer moorings.

A crude value for the total horizontal kinetic energy in the internal wave band was obtained by assuming that the spectra are of the form $\Phi(\sigma) = a\sigma^{-b}$ and integrating

$$\int_{.05\ \text{cph}}^{.5\ \text{cph}} \Phi\, d\sigma = \frac{1}{b}\,[\Phi(.05) - \Phi(.5)]$$

where -b is the slope of the hke spectrum on the log-log plot. Note that 0.05 and 0.5 cph were consistently used as the limits of integration and that the integral omits the inertial and semidiurnal peaks. This simple power law for energy density thus estimates the energy in the part of the internal wave field which propagated in from the open ocean, while excluding the energy of locally-generated internal tides.

The total internal-wave horizontal kinetic energy resident in the canyon was estimated crudely by assigning to each current meter a portion of the canyon volume. The

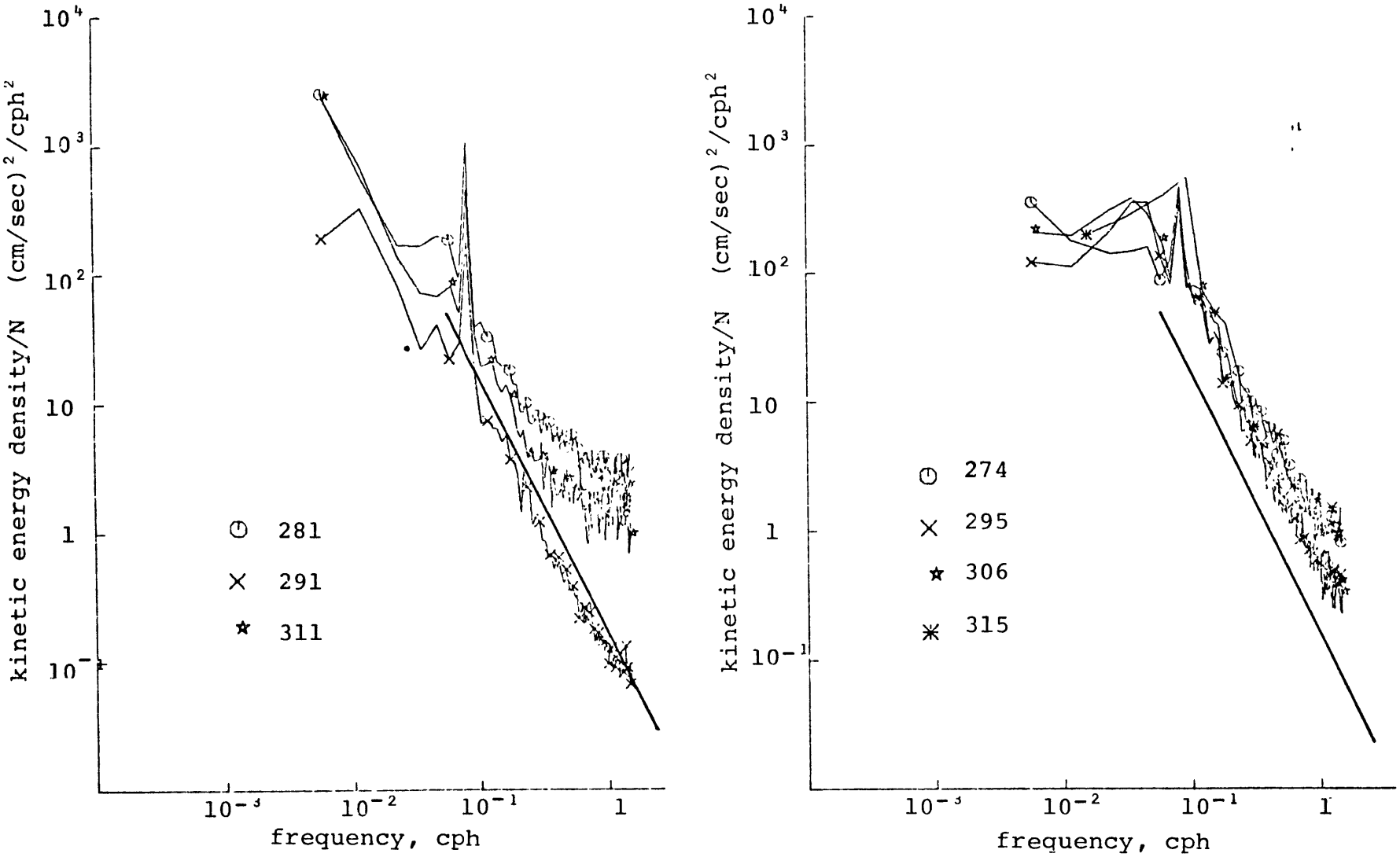

Figure 3-22. Normalized horizontal kinetic energy spectra showing increase in energy level toward the canyon head.

canyon headward of mooring 30 and below 146 m depth was divided into regions whose volumes were calculated. The hke of each region was the product of the integrated hke density of its current meter, the density of water, and the volume of the region (see figure 3-23). The regional horizontal kinetic energies were summed to get a canyon total of about 3.5 (10^{11}) joules.

d. Potential energy spectra. Spectra of the ratio of potential energy to buoyancy frequency generally have a σ^{-2} or $\sigma^{-1.5}$ dependence at high frequencies. The semidiurnal peak is generally large, the inertial peak small, and the diurnal peak of intermediate size. Normalized potential energy density increases a hundredfold toward the canyon head, and tenfold toward the bottom at moorings 29 and 30 (figure 3-24). The ratio of the normalized potential energy at the semidiurnal peak to that at the diurnal peak is two or three at the outer, upper instruments, but only one third to a half at the canyon head.

Potential energy was integrated over frequency and summed over canyon volume the same way horizontal kinetic energy was. The total was 1.0 (10^{12}) joules, about three times the resident hke. These potential energy spectra were calculated using mean temperature gradients and buoyancy frequencies calculated from CTD stations 77-84, measured at the beginning of the 15-week experiment. Since the canyon stratification is known to have changed during autumnal

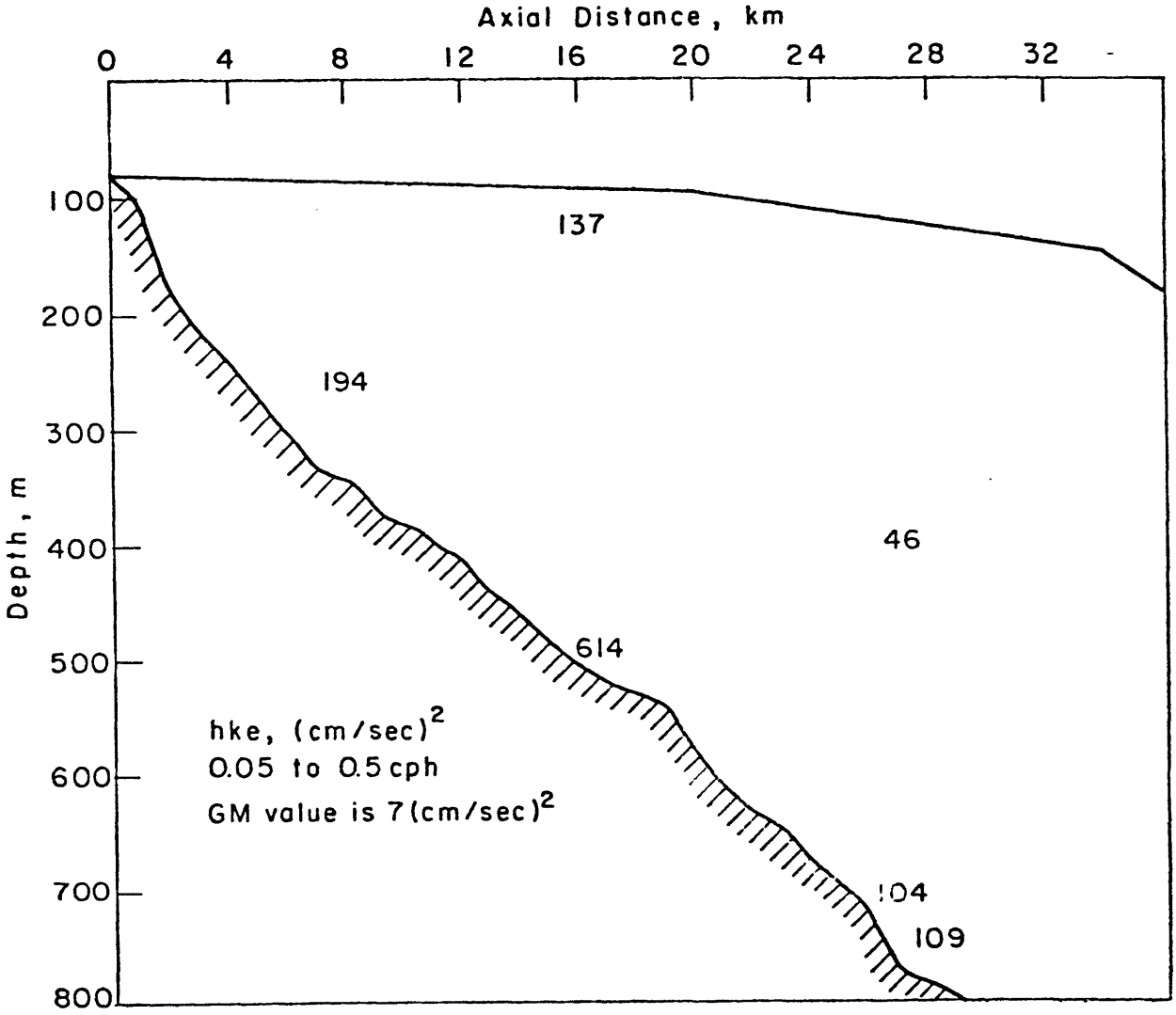

Figure 3-23. Horizontal kinetic energy density integrated over the internal wave band, shown as a function of position in the canyon.

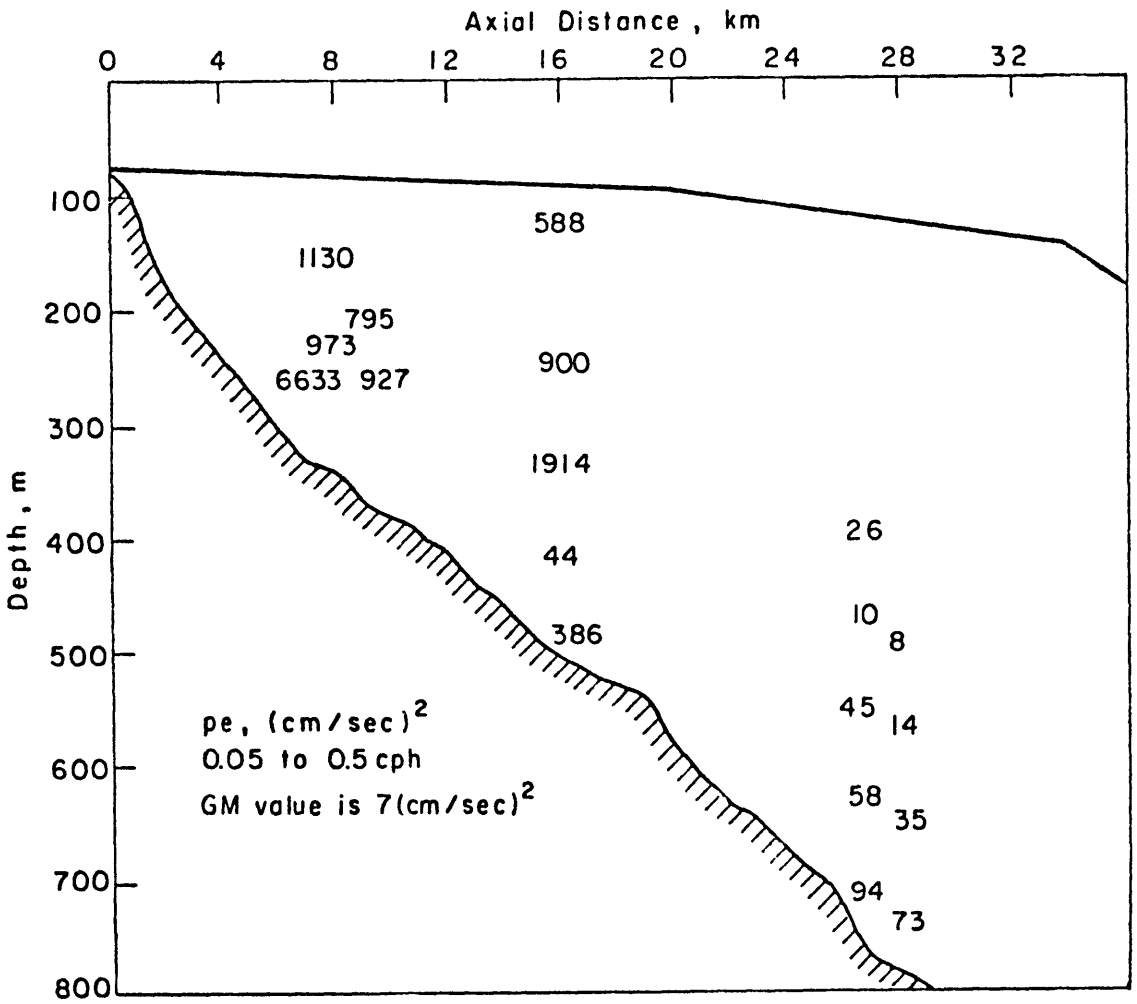

Figure 3-24. Potential energy density integrated over the internal wave band, shown as a function of position in the canyon.

cooling, the absolute potential energy values are highly approximate.

3. Discussion of internal wave field. Our study of Hudson Canyon reveals an internal wave field different from that of the deep ocean. The effects of the canyon on internal waves can be illuminated by comparison with the models of Garrett and Munk (1975, hereafter called GM), Prinsenberg, et al. (1974), and Wunsch (1969), and with internal wave observations from the continental shelf and slope.

Canyon internal waves are anisotropic both in their velocity components and in the sense of energy propagation. Velocity anisotropy is evident from the inequality of the velocity power density spectra; the along-canyon component is more energetic than the across-canyon one. Anisotropic internal waves like these with the strong component along the bathymetric contours have been measured near seamounts and submarine scarps (Wunsch and Webb, 1979), and are easily understood as the effects of nearby impermeable walls. Canyon velocities are more anisotropic where the canyon is narrower and for low frequencies that have the largest horizontal scales; these trends make sense if the walls cause the anisotropy.

On the continental shelf, anisotropic internal wave velocities are also found, but with the strong component normal to the isobaths (Gordon, 1978). In this case, the

cause of the velocity anisotropy is anisotropy of internal wave propagation. A large proportion of the internal waves on the shelf are propagating shoreward, normal to the trend of the shelf break. They were either generated there, as are internal tides, or were refracted as they entered shallow water from the ocean so that they crossed the shelf break normal to its trend (Wunsch, 1975).

Uni-directional energy propagation is indicated by the phase lags between coherent instruments that were at the same depth but horizontally separated (moorings 29 and 30). There we found a tendency toward up-canyon energy propagation. Thus internal waves in the canyon, like those on the shelf, predominantly propagate in from the sea. Internal tides are an exception. They propagate both up- and down-canyon from the central part of the canyon where they are apparently generated.

The upward energy propagation near the floor is predicted for up-canyon internal wave propagation by Wunsch's (1969) model of internal waves propagating up a slope. Coherence phases calculated using Wunsch's velocity solution evaluated at two different vertical levels are large only if one of the levels is near the floor, decrease rapidly as the lower level leaves the floor, and indicate upward energy propagation. For a first-mode wave of ten-hour period in 810 m of water, the phase lag between 800 m and 720 m is 56°, the lag between 720 m and 640 m is 17° , and that between 640 m

and 560 m is only 9°. This pattern agrees with those found (with a similar floor slope, f, and N) in the vertical coherences from canyon moorings 29 and 30 (see figure 3-21). (The distances between our instruments were too great to resolve the vertical coherences at higher frequencies.) The effect can be thought of as the necessary upward energy flux as the waves propagate along a rising floor. The energy that was deeper than the local floor depth must move upward to go toward the canyon head.

Dimensional normalized density spectra of horizontal kinetic energy and potential energy based on the GM model (Garrett and Munk, 1975) are appropriate for comparing the energy level of the internal wave field in the canyon to that in the open ocean. Frequency integrals of the GM spectra between values of f and N appropriate for Hudson Canyon are 6.8 $(cm/sec)^2$ for potential energy and 7.2 $(cm/sec)^2$ for horizontal kinetic energy.

As shown in figures 3-23 and 3-24, the energy in the internal wave band is higher everywhere in the canyon than is predicted by the GM model, (consistent with the Hydrographer Canyon results of Wunsch and Webb, 1979). Kinetic energy increases by large factors toward the canyon head and toward the floor at the outer moorings. Figure 3-22 compares normalized energy spectra for the different locations, demonstrating that the energy differences are not explained by variations in buoyancy frequency. Theoretically, the

expected effect of decreasing depth on internal waves is that energy should increase in inverse proportion to water depth. Energy increase inversely proportional to depth has been measured on slopes by Zenk and Briscoe (1974) and Gordon (1978). A three-dimensional version of this process apparently occurs in the canyon. As internal waves progress shoreward, they carry their energy into smaller widths as well as smaller depths, and the increase in local energy exceeds the decrease in depth. The canyon cross section decreases by about a factor of 6 between moorings 30 and 27; the observed energy intensification is somewhat greater than this. The difference could result from internal waves entering from above and being trapped by the canyon's sloping walls, as suggested by Gordon & Marshall (1976). Near-bottom energy intensification is also predicted by Wunsch's (1969) solutions for the effects of a sloping bottom.

The effects of the canyon's sloping walls may also result in the slight difference between the shape of energy spectra from the canyon and that of the GM model, at high internal wave frequencies. Although the integrals of the energy density spectra are greater than that of the GM model in all cases, the energy density at 0.2 cph is less than that of the model at the upper instruments of the outer moorings. This depletion of energy at high frequencies, while internal waves in general are amplified, may be related to the critical frequency of the canyon walls. For most frequen-

cies, the intensification of internal waves by the sloping floor is augmented by the converging walls. High frequency internal waves incident from above may encounter a wall of critical frequency less than their frequencies and be reflected up out of the canyon rather than down into it. The irregularity of the canyon walls makes this high-frequency cut-off gradual so the change in spectral shape is a subtle one. Since the average slope of the canyon walls produces a critical frequency of about 0.3 cph, the level of the energy density spectra near 0.2 cph is not a good indicator of the energy present in the canyon internal wave field.

The transport of energy into the canyon by internal waves is a useful quantity for comparison to the total internal wave energy in the canyon. Internal wave residence time for the canyon is approximately the ratio of total resident energy to the energy transport; its relationship to energy dissipation rates is a clue to the dynamics of the canyon internal wave field.

A rough estimate of energy transport was made using the velocity and pressure fields of the GM model (see Hotchkiss, 1980, for details of the calculation). The canyon was assumed to be bounded by a horizontal upper surface and a vertical cross-section at the edge of the continental shelf. Energy flux across each surface was represented as the average of the product of pressure deviation and normal velocity: <p'w'> for the upper surface and <p'u'> for the

seaward one. Garrett and Munk (1972, 1975) give expressions for u', w', and p' as functions of frequency, wavenumber, and stratification. These expressions were used to evaluate the fluxes with the stratification observed near the canyon boundaries.

The horizontal flux of energy was integrated over an area corresponding to the depth and width of the mouth of the canyon at the continental slope. The vertical flux of energy was summed over the upper surface of the canyon, taking only 1/2 the energy density of the GM spectrum to eliminate upward travelling energy. The Garrett-Munk spectrum, evaluated with parameters from our single CTD survey, is unlikely to fully describe the internal wave field outside the canyon at the shelf break, so this estimate of energy transport is only a rough approximation.

The total transport estimate is 2.5 (10^6) watts, with 60% entering through the upper boundary. Together with the resident energy total estimated from the array data, this yields a residence time roughly equal to a week. To completely describe the internal wave field of Hudson Canyon, processes need to be found which are capable of dissipating or otherwise transporting 2.5 (10^6) watts from the canyon. One dissipating process is the breaking of the internal waves as their energy levels increase and their wavelengths decrease toward the canyon head. This may cause mixing and produce the mixed slope water discussed in Chapter II. The

energy flux of internal waves that are not actually trapped in the canyon but instead escape after several reflections could also be important. Floor and wall friction cause dissipation whenever waves reflect or break against these boundaries, and will be considered in detail in chapter V.

Eriksen's (1978) microscale observations of oceanic internal waves indicate that internal waves break at a critical Richardson number that is close to 0.25. Thompson (1980) analysed these results and laboratory and numerical models to conclude that turbulence resulting from breaking internal waves converts one fourth of the dissipated kinetic energy into potential energy, with molecular viscosity disposing of the rest. Thus, if all the internal waves entering Hudson Canyon are dissipated by breaking, potential energy could be created at a rate of 6 (10^5) watts.

Cacchione and Wunsch (1974) observed internal waves shoaling on a slope in a laboratory tank. The waves broke on the floor near the top of the slope and generally resembled the surf and swash of surface waves breaking at a beach. Large amounts of mixing occurred only when the internal wave frequency was near the critical frequency of the slope, and produced tongues of mixed water that intruded into the interior of the tank. Applying these observations to the canyon case, perhaps half the internal wave energy is near enough to critical frequencies to cause mixing, so a poten-

tial energy production of 3 (10^5) watts is possible. The mixed water would be found in layers near the canyon floor, particularly toward the head of the canyon and down-canyon from regions where the semidiurnal frequency is critical. The other breaking waves, not near enough to critical frequency to cause mixing, are likely to be strongly dissipated by bottom friction and may carry sediment as Cacchione and Southard (1974) observed.

4. Summary of internal wave results. Canyon internal waves are anisotropic both in their velocity components and in the sense of energy propagation. Internal wave velocities are more anisotropic where the canyon is narrow and for low frequencies. The internal waves in the canyon predominantly propagate in from the sea.

The energy in the internal wave frequency band is higher than that of the Garrett-Munk (1975) model everywhere in Hudson Canyon. Internal wave energy increases in the canyon head by a larger factor than the decrease in cross-sectional area; this may result from additional internal waves entering from above and being trapped by the canyon's sloping walls.

The potential energy which can be produced by internal wave breaking is more than sufficient to explain the mixed slope water we observed in Hudson Canyon. Water mixed by internal wave breaking would be found spreading away from the sloping floor where the waves broke. This is consistent with our hydrographic results; we found the mixed slope water

concentrated near the canyon floors and apparently being diluted as it travelled down the canyons.

Chapter IV: Model of Near-Floor Currents

Currents of tidal frequency dominate the velocity records measured in the outer parts of most submarine canyons (Shepard et al., 1979). Our data from the outer moorings of the Hudson Canyon array are no exception: particularly near the floor, the current meters recorded a modulated series of up- and down-canyon flows, repeating at diurnal and semidiurnal frequencies (see figure 3-17). Near the floor at instruments 295 and 306, the down-canyon flows are generally stronger than the up-canyon flows, and are more likely to have high-frequency spikes contributing to their maxima (see figure 4-1). Shepard et al. (1979) report dominant tidal oscillations in the outer parts of four other East Coast canyons, at both 3 and 30 m above the floor. In their samples, the down-canyon flows were often stronger 3 m above the floor than they were at 30 m, although the up-canyon flows were about equal at both heights.

This observed asymmetry between up- and down-canyon near-floor flows may have important effects on the sediment transport through canyons. The high-frequency spikes are particularly interesting; by allowing the boundary layer less time to develop, high-frequency waves produce stronger bottom

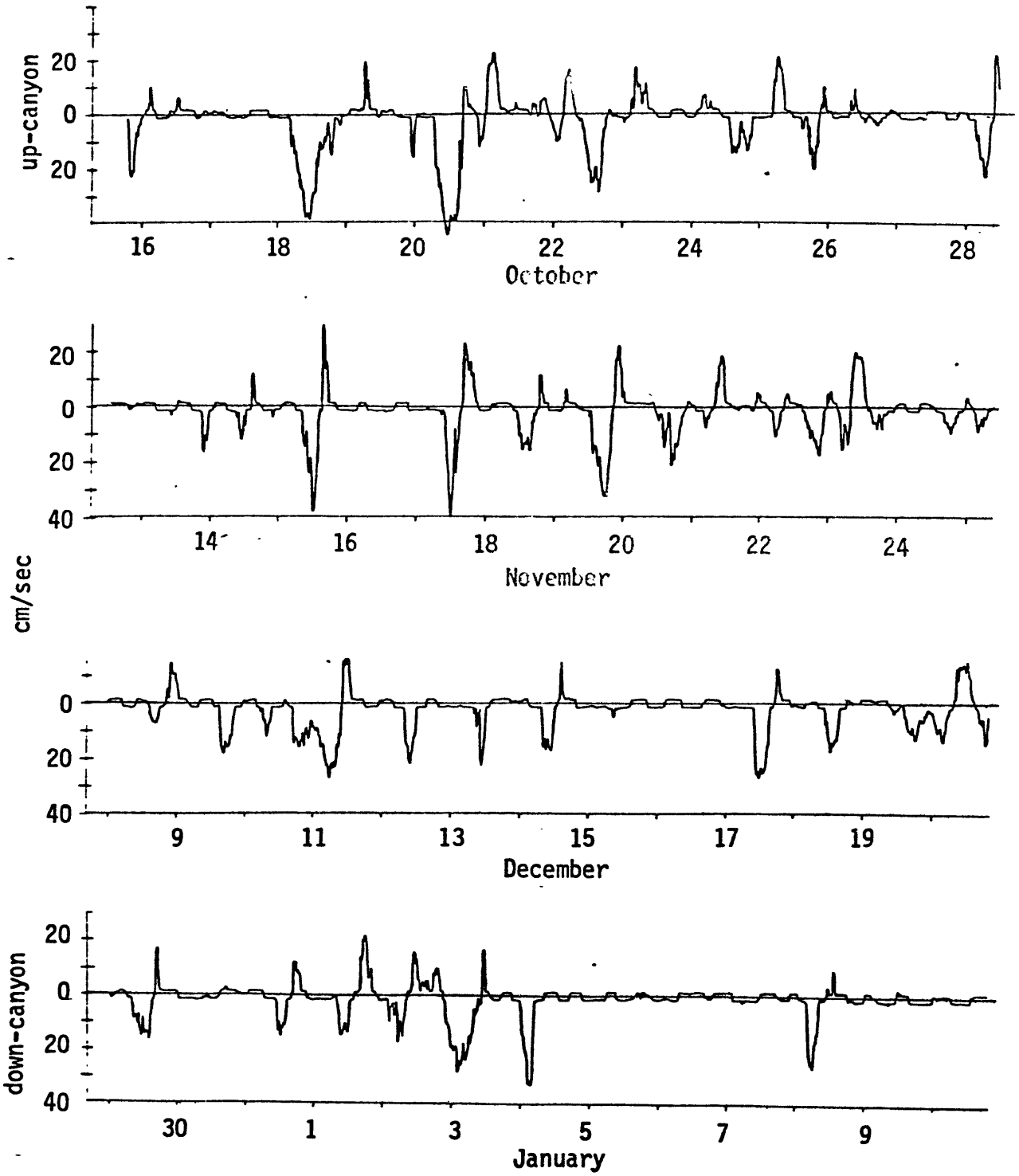

Figure 4-1. Excerpts from the along-canyon velocity record of current meter 306 (see figure 3-4 for location). Time axis is marked at 24-hour intervals. Note high-speed diurnal oscillations, low-speed semi-diurnal oscillations, and high-frequency spikes occurring mostly during high-speed oscillations.

stress than low-frequency waves of the same amplitude.

I propose the following physical explanation for the asymmetry of these near-floor oscillations: During the up-canyon flow (flood tide) a frictional boundary layer must develop to bring the velocity to zero at the floor. Since the canyon floor slopes and the water in the canyon is stratified, the slow-moving layers next to the floor will be overrun by faster-moving water that originated further down-slope. This down-slope water is denser, so overturning will result. A mixed bottom layer will grow because of this overturning during the flood tide. During the ebb tide, light water overruns heavy water so the mixed layer stops growing and may restratify slightly. Shear at the stable interface on top of the mixed layer will cause small wavelike disturbances to grow (Kelvin-Helmholtz instability). These interface waves can attain great size and cause the flow at the canyon floor and the bottom friction to be very different during the ebb tide than during flood tide.

I have developed a simple numerical model for the growth of the mixed bottom layer in Hudson Canyon in order to estimate its depth and density structure. The growth and propagation of the interface waves during the ebb tide can then be estimated by using analytical results from simpler geometries that include the relevant features and scales of the canyon mixed layer.

In the model of mixing under the flooding tide, bottom friction and tidal forcing determine the velocity field. Stratification and floor slope are assumed to be important in the density field; the magnitudes of their effects on velocity need to be considered. If x,u are parallel to the floor and along the canyon, the along-canyon momentum equation for water within the bottom mixed layer is

$$\frac{\partial u}{\partial t} + u\frac{\partial u}{\partial x} + v\frac{\partial u}{\partial y} + w\frac{\partial u}{\partial z} - fv = \frac{\rho - \Delta\rho}{\rho}\frac{\partial U}{\partial t} + \frac{\Delta\rho}{\rho} g \sin\alpha - \frac{\Delta\rho}{\rho} g \frac{\partial h}{\partial x} + \frac{1}{\rho}\frac{\partial \tau}{\partial z} \qquad (4.1)$$

The pressure gradient term has been expressed in terms representing the forcing of the tide far from the wall and the slope of the layer's interface:

$$\frac{\partial p}{\partial x} = \Delta\rho\, g \frac{\partial h}{\partial x} + \frac{\partial P}{\partial x}$$

where $\frac{\partial P}{\partial x}$ has been rewritten in 4.1 using

$$\frac{\partial U}{\partial t} = -\frac{1}{\rho - \Delta\rho}\frac{\partial P}{\partial x} + g \sin\alpha$$

The size of each term in the momentum (4.1) equation can be estimated from the length, time, density and velocity scales of the Hudson Canyon observations:

along-canyon length scale, L = 10 km (between bends)

canyon width scale, B = 1 km

semidiurnal frequency, w = 1.4 (10^{-4}) rad/sec

Coriolis frequency, f = 9 (10^{-5}) rad/sec

$$\text{density change, } \Delta\rho = \begin{cases} 10^{-6} \text{ at 295, 306} \\ 5\ (10^{-5}) \text{ at 315} \end{cases}$$

$$\text{floor slope, } \sin\alpha = .02$$

$$\text{tidal velocity amplitude, } U = \begin{cases} 10 \text{ cm/sec at 295, 306} \\ 30 \text{ cm/sec at 315} \end{cases}$$

Assuming $\frac{\partial u}{\partial t} \simeq 1$ and $\frac{1}{\rho}\frac{\partial \tau}{\partial z} \simeq 1$, the relative sizes of the other terms are:

$$u\frac{\partial u}{\partial x} + v\frac{\partial u}{\partial y} + w\frac{\partial u}{\partial z} \simeq \frac{U}{L\omega} = \begin{cases} .07 \text{ at 295, 306} \\ .21 \text{ at 315} \end{cases}$$

$$fv \simeq \frac{fB}{\omega L} = .06$$

$$\frac{\rho - \Delta\rho}{\rho}\frac{\partial U}{\partial t} \simeq 1 - \frac{\Delta\rho}{\rho} \cong 1$$

$$\left.\begin{matrix} \frac{\Delta\rho}{\rho} g \sin\alpha \\ \frac{\Delta\rho}{\rho} g \frac{\partial h}{\partial x} \end{matrix}\right\} \simeq \frac{1}{\omega U}\frac{\Delta\rho}{\rho} g \sin\alpha = \begin{cases} .014 \text{ at 295, 306} \\ .23 \text{ at 315} \end{cases}$$

Reducing the momentum equation (4.1) to

$$\frac{\partial u}{\partial t} = \frac{\partial U}{\partial t} + \frac{1}{\rho}\frac{\partial \tau}{\partial z} \qquad (4.2)$$

is thus a good approximation in the outer canyon (moorings 29 and 30), but only a rough approximation at mooring 31. I used this approximate form (4.2) of the momentum equation to write a simple numerical model that calculates the growth of a bottom mixed layer under the flood tide.

Such a simple model seems reasonable for the outer part of Hudson Canyon, in the vicinity of moorings 29 and 30 (see figure 3-2). The currents and stratification at instrument 315 (mooring 31, see figures 3-2 and 3-4) may be

interpretable by a model that retains the same basic physics, but also includes the nonlinear accelerations and the sloping floor and sloping interface terms in the momentum equation. In the head of the canyon, both theory and observations indicate a very complex velocity field in which internal waves are sufficiently energetic that both breaking and nonlinear effects can be important.

A. Boundary layer model

Consider a two-dimensional problem: the floor slopes at a small angle α, η is normal to the floor and positive upward, and ξ is parallel to the floor and positive down-slope.

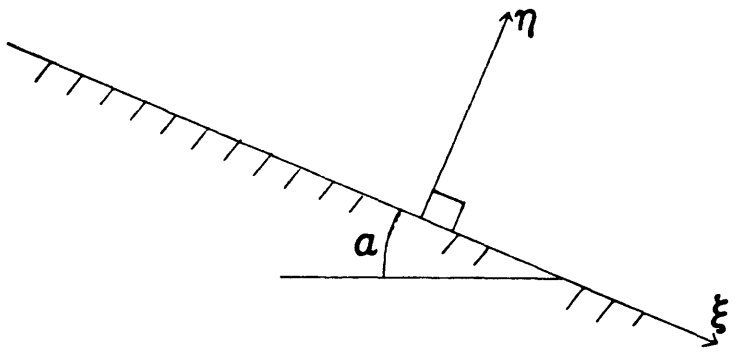

Initially, the stratification is horizontal with constant Brunt-Vaisala frequency N, except for a mixed layer of uniform depth h_0 lying along the floor. The density change at the top of the mixed layer is the constant ρ_1, and the initial density field is represented as

$$\rho(\xi,\eta,0) = \begin{cases} \rho_0\left[1 - \frac{N^2}{g}(\eta\cos\alpha - \xi\sin\alpha)\right] \text{ for } \eta \geq h_0 \\ \rho_1 + \rho\left[1 - \frac{N^2}{g}(h_0\cos\alpha - \xi\sin\alpha)\right] \text{for } \eta < h_0 \end{cases} \tag{4.3}$$

Within the mixed layer, density varies along the floor (with ξ) but not with height (with η).

Far from the floor, a sinusoidal velocity parallel to the floor is imposed:

$$u(\xi,\eta,t) = U = V \sin \omega t \text{ for large } \eta .$$

Near the floor the velocity component parallel to the floor satisfies (4.2)

$$\frac{\partial u}{\partial t} = -\frac{1}{\rho}\frac{\partial p}{\partial \xi} + \frac{1}{\rho}\frac{\partial \tau}{\partial \eta} \qquad (4.4)$$

with boundary conditions $\quad u = 0$ at $\eta = z_0 = .1$ cm

$u \to U$ as $\eta \to \infty$

Turbulent stress is expressed using an eddy viscosity, ε, that varies with η in three height ranges:

$$\varepsilon = \begin{cases} \varepsilon_0 & \text{in stratified region,} \quad \eta > h \\ \varepsilon(h) & \text{in most of mixed layer,} \quad H < \eta < h \\ \kappa |u_{*w}| \eta & \text{at bottom of mixed layer,} \quad \eta < H \end{cases}$$

where u_{*w} is the maximum friction velocity during the wave period, proportional to the square root of the maximum bottom stress τ_o:

$$\tau_{o,max} = \rho |u_{*w}| \, u_{*w}$$

The depths of the mixed layer and of the frictional sublayer (h and H) are determined by the stability of the density field.

The mixed layer is expected to grow by entraining the stratified water above it so that it maintains a critical

Richardson number at the interface (see Pollard et al., 1973). The stratification above the layer is sufficiently strong to prevent the water from being mixed by the shear, so the Richardson number there is greater than or equal to 1:

$$Ri = \frac{-\frac{g}{\rho}\frac{\partial \rho}{\partial \eta}}{\left(\frac{\partial u}{\partial \eta}\right)^2} \geq 1 \quad \text{at} \quad \eta \geq h \qquad (4.5)$$

The density above the mixed layer changes as water is advected up the slope from deeper original positions:

$$\rho(\xi,\eta,t_o) = \rho(\xi,\eta,0) - \frac{\partial \rho}{\partial \xi}\int_0^{t_o} u\, dt, \text{ for } \eta \geq h. \qquad (4.6)$$

In the mixed layer, the density is also changed by the entrainment of stratified water:

$$\rho(\xi,\eta,t_o) = \rho(\xi,0,0) - \frac{\partial \rho}{\partial \xi}\frac{1}{h}\int_0^h\int_0^{t_o} u\, dt\, d\eta - \int_0^{t_o}\frac{1}{h}\frac{\partial h}{\partial t}\left[\rho(\xi,0,t) - \rho(\xi,h,t)\right] dt \qquad (4.7)$$

When the near-floor velocity is up the slope, friction slows the water nearest the floor so that it is overtaken by water that originated further downslope and thus is denser. The stratification is unstable, and overturning occurs. This resembles an unstable atmospheric boundary layer; this analogy can be used to estimate the effective viscosities in the mixed layer.

According to Turner (1973), when turbulent heat transport maintains a condition of zero density gradient in the atmospheric boundary layer, the Richardson number is approximately the ratio of depth to the Monin-Obukov length L. This can be applied to the canyon boundary layer in which Richardson number is unity at the top of the mixed layer so that L is approximately equal to the mixed layer depth. Still following Turner, eddy viscosity is a function of the Monin-Obukov length:

$$\varepsilon = \frac{\kappa u_* \eta}{\phi_M} \tag{4.8}$$

$$\phi_M \cong 1 + 5\frac{\eta}{L} \tag{4.9}$$

Applying this to the canyon case, substitution of (4.9) into (4.8) gives an effective viscosity at the top of the mixed layer of $\kappa u_* h/6$. This sets the top of the sublayer (where effective viscosity is assumed to vary linearly with height: $\varepsilon = \kappa \eta u_* \varepsilon$.) as one-sixth the total depth of the mixed layer.

Ignoring the possible slow time dependence of mixed layer depth and the effective viscosity of the upper mixed layer, standard boundary layer solutions of (4.4) can be used by requiring the velocity to be continuous at the interfaces at $\eta = h$ and $\eta = h/6$. For $\eta < h/6$, using the results of Kajiura (1968), we obtain

$$u = U\{1 - \frac{1}{C_2}(A_2 \,\mathrm{ker}\, 2\sqrt{\eta/\ell} + B_2 \,\mathrm{kei}\, 2\sqrt{\eta/\ell})\}$$

$$A_2 = \mathrm{ker}\, 2\sqrt{z_o/\ell}\,, \quad C_2 = A_2^2 + B_2^2 \tag{4.10}$$

$$B_2 = \mathrm{kei}\, 2\sqrt{z_o/\ell}\,, \quad \ell = \frac{\kappa|u_{*\omega}|}{\omega}$$

Ker and kei are Kelvin functions. In the range $h/6 < \eta < h$ the effective viscosity is constant so the velocity profile is that of an oscillatory viscous flow (see Lamb, 1945, pp. 619-23):

$$u = U + e^{-\sqrt{\frac{\omega}{2\varepsilon}}\,\eta}\left[\sin \omega t\left(A_3 \cos \sqrt{\frac{\omega}{2\varepsilon}}\,\eta + B_3 \sin \sqrt{\frac{\omega}{2\varepsilon}}\,\eta\right) + \cos \omega t\left(B_3 \cos \sqrt{\frac{\omega}{2\varepsilon}}\,\eta - A_3 \sin \sqrt{\frac{\omega}{2\varepsilon}}\,\eta\right)\right] \tag{4.11}$$

Continuous velocity at $\eta = h/6$ requires that

$$A_3 = \frac{-V \exp\left(-\sqrt{\frac{\omega}{2\varepsilon}}\,h\frac{1}{6}\right)\left(A_2 \ker 2\sqrt{\frac{h}{6\ell}} + B_2 \operatorname{kei} 2\sqrt{\frac{h}{6\ell}}\right)}{C_2\left(\cos\sqrt{\frac{\omega}{2\varepsilon}}\,\frac{h}{6} + \sin\sqrt{\frac{\omega}{2\varepsilon}}\,\frac{h}{6}\tan\sqrt{\frac{\omega}{2\varepsilon}}\,\frac{h}{6}\right)}$$

$$B_3 = A_3 \tan\sqrt{\frac{\omega}{2\varepsilon}}\,\frac{h}{6}$$

as found by substitution of (4.11) into (4.10). For $\eta > h$,

$$u = U + e^{-\sqrt{\frac{\omega}{2\varepsilon_o}}\,\eta}\left[\sin \omega t\left(A_4 \cos \sqrt{\frac{\omega}{2\varepsilon_o}}\,\eta + B_4 \sin \sqrt{\frac{\omega}{2\varepsilon_o}}\,\eta\right) + \cos \omega t\left(B_4 \cos \sqrt{\frac{\omega}{2\varepsilon_o}}\,\eta - A_4 \sin \sqrt{\frac{\omega}{2\varepsilon_o}}\,\eta\right)\right] \tag{4.12}$$

And the constants are found from matching velocities at $\eta = h$,

$$A_4 = e^{\theta}(A_3 \cos\theta - B_3 \sin\theta)$$

$$B_4 = e^{\theta}(A_3 \sin\theta + B_3 \cos\theta)$$

$$\theta = \sqrt{\frac{\omega}{2\varepsilon_o}}\,h - \sqrt{\frac{\omega}{2\varepsilon}}\,h$$

The relationship between wave amplitude and maximum bottom stress was studied semi-empirically by Jonsson (1966). For fully developed turbulent boundary layers over rough beds, Jonsson found that the wave friction factor f_w is very close to that given by

$$\frac{1}{4\sqrt{f_w}} + \log_{10}\frac{1}{4\sqrt{f_w}} = \log_{10}\left(\frac{V}{\omega k_s}\right) - 0.12 \qquad (4.13)$$

where k_s is the equivalent sand roughness of the bed and the maximum bottom stress is

$$\tau_{om} = \tfrac{1}{2}\,\rho\, f_w\, V^2$$

The evolution of this system (equations 4.5-7 and 4.10-13) was studied numerically for semidiurnal tides of amplitudes ranging from 10 to 20 cm/sec using the program described in Appendix B and parameters listed in table 4-I. Figure 4-2 shows representative velocity profiles and the evolution of mixed layer depth.

The Froude number, defined as the ratio of the average velocity in the mixed layer to the linear-theory speed of interface waves:

$$F_r = \frac{\frac{1}{h}\int_0^h u\, d\eta}{\sqrt{\frac{\rho(o) - \rho(h)}{\rho(h)}\, gh}}$$

If $|F_r| < 1$, then small perturbations of the interface can propagate upstream away from their origins. Figure 4-3 shows

Table 4-I

Parameters of numerical model runs

Run	-V cm/sec	initial h m	final h m	ρ_1 (10^6) g/cm^3	u_{*m} cm/sec
1	15	8.0	17.9	1.27	.69
2	20	17.6	25.3	2.81	.89
3	15	10.3	17.6	1.64	.69
4	10	10.0	10.3	1.59	.48

Time step = .16 radians.

Brunt-Vaisala frequency N = 1.74 (10^{-3}) rad/sec.

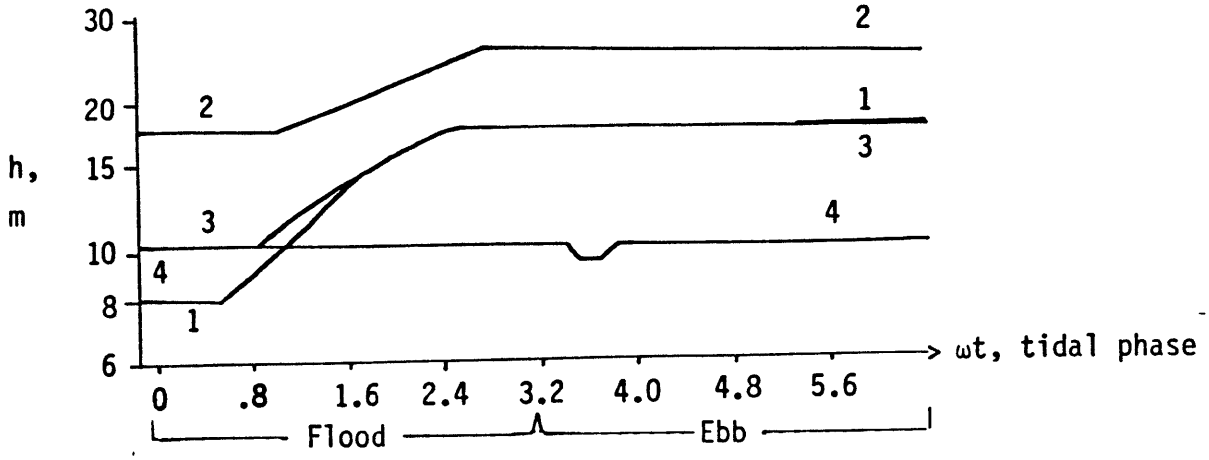

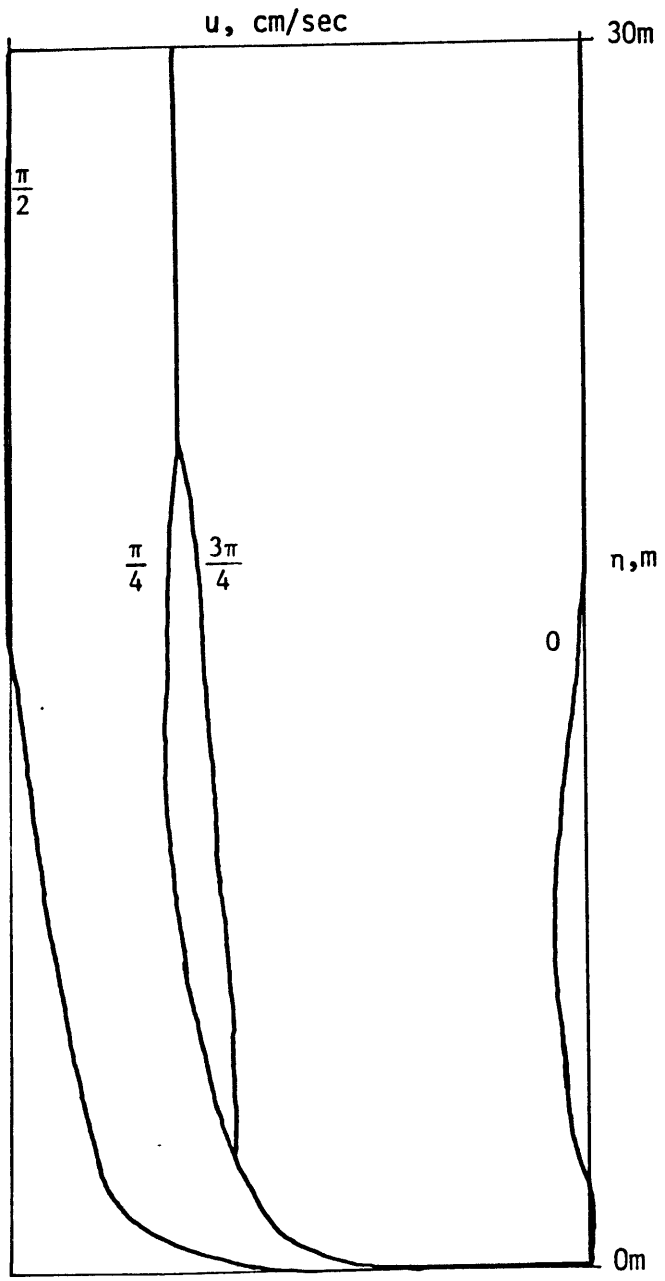

Figure 4-2. (a) Growth of mixed bottom layer during numerical runs 1 through 4 (see table 4-I). The curve for run 4 shows re-stratification occurring briefly during the ebb. The restratifiation that occurred during run 2 is not perceptible on this scale.

(b) Representative velocity profiles from run 3.

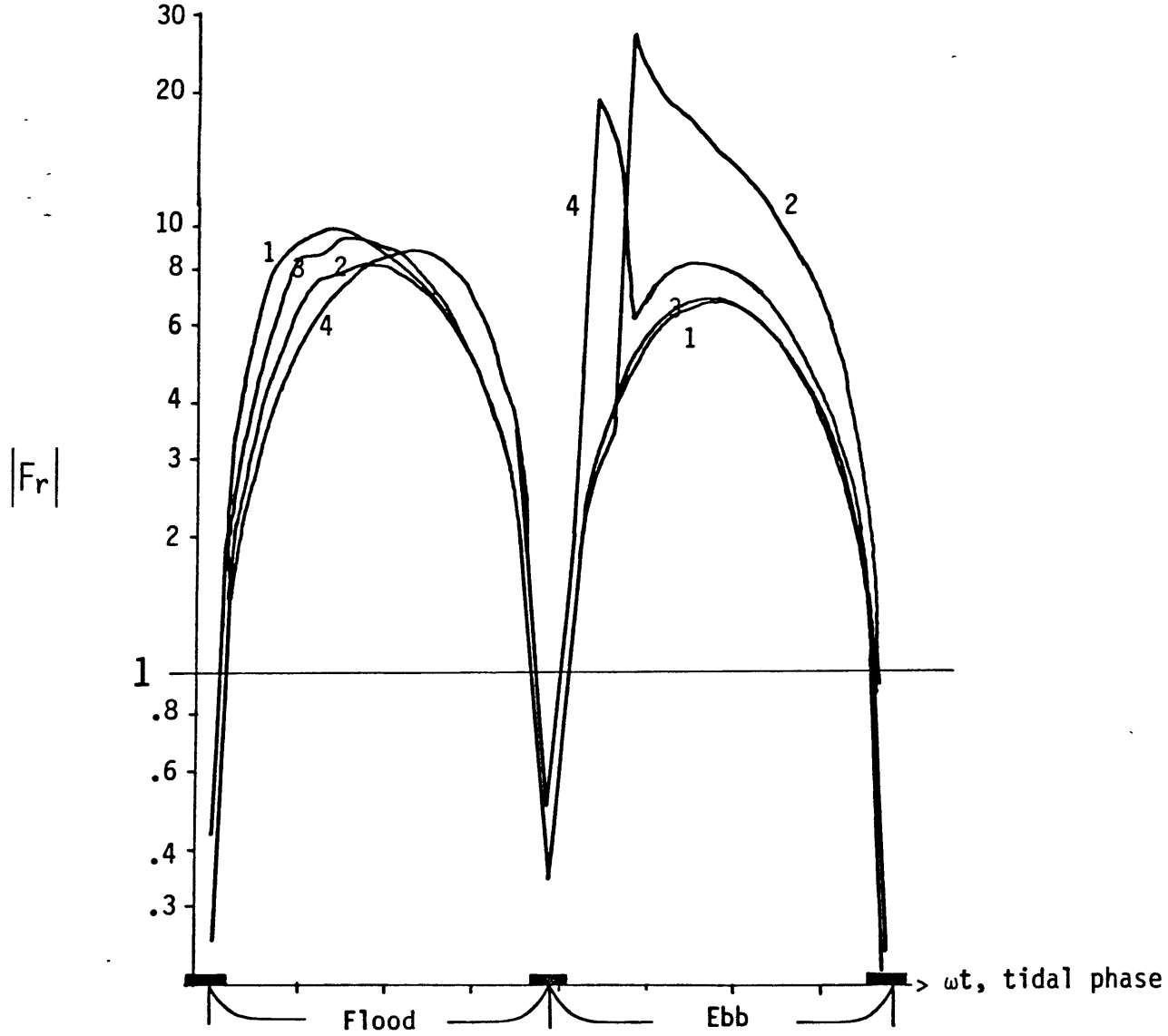

Figure 4-3. Froude number magnitude for numerical model runs 1 through 4 as functions of tidal phase . The bars on the time axis (▬) indicate the parts of the tidal cycle when Fr < 1 so that waves on the bottom mixed layer interface can propagate against the tidal flow.

how the Froude number varies with time for the model runs. Except for brief intervals at slack water, the Froude number is consistently greater than one, indicating that small waves cannot travel upstream. Mixing also kept the Froude number less than 10 except when the mixed layer became restratified during ebb and the computer was fooled: it calculated Fr for the lower, weaker interface instead of the old mixed layer top.

B. Interface waves

The model of section A used a very simple physical situation to calculate the depth and density of a bottom layer mixed by the flooding tide. The resulting mixed layers had depths of about 15 m and density changes at their tops as great as 10^{-5} gm/cm^3. The phase speed of linear waves propagating on the mixed layer interface is thus about 4 cm/sec. The high-frequency velocity spikes we measured near the floor of Hudson Canyon were frequently greater than 4 cm/sec in amplitude, so interface waves producing these spikes would be strongly nonlinear.

To simplify the model in section A, non-tidal forcing was ignored and velocity, stratification, and floor slope were assumed to be uniform. In actual canyons, incident internal waves and the irregularities of the floor and walls will produce local deflections of the mixed layer interface. Some of the Fourier components of these disturbances will

meet the criteria for Kelvin-Helmholtz instability and thus will grow by extracting energy from the velocity gradient.

The maximum wavelength for Kelvin-Helmholtz instability was estimated at each time step of the numerical boundary layer model by using simplified density and velocity profiles and linear stability theory. For a thin lower layer in uniform motion and a thick upper layer moving uniformly with velocity U relative to the lower layer, linear stability theory (see Turner, 1973, pp. 94-96) yields

$$U^2 > \frac{g}{k}\frac{\rho_2 - \rho_1}{\rho_1\rho_2}\,\frac{\rho_1 + \rho_2 \coth kh}{\coth kh}$$

as the condition for growth of small wave-like disturbances of wave number k.

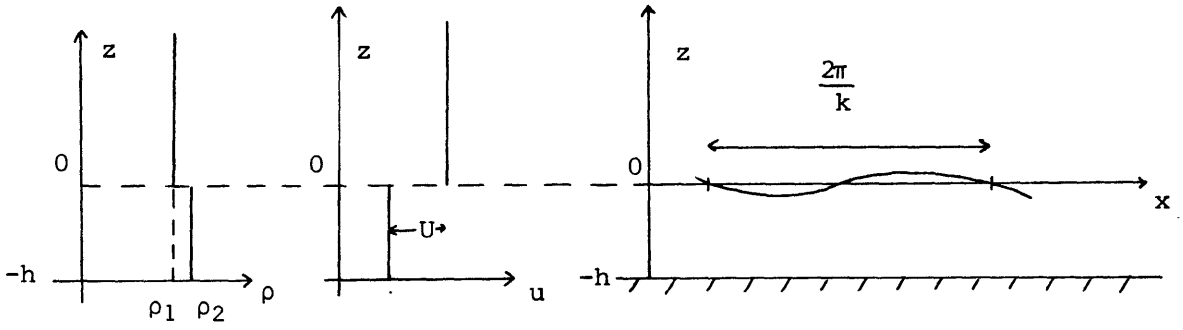

This slab model was matched to the calculated velocity and density profiles, using the following substitutions:

$$U = V \sin \omega t - \frac{1}{h}\int_0^h u \, d\eta$$

$$\rho_2 = \rho(\eta = 0)$$

$$\rho_1 = \rho(\eta = h)$$

For each time step, the minimum wave number k_o for Kelvin-

Helmholtz instability was calculated as the solution to

$$\rho_2\rho_1 U^2 k_o \coth k_o h - g(\rho_2 - \rho_1)(\rho_1 + \rho_2 \coth k_o h) = 0$$

Corresponding maximum wavelengths $2/k_o$ are listed in table 4-II.

For the main interface (ignoring weaker interfaces that result from restratification during ebb), the maximum unstable wavelengths occur during the maximum up-canyon flow. Generally, the mixed layer is growing by entrainment during this part of the cycle, so that these very long waves are lost in the entrainment process. For the remaining waves, the maximum wavelengths expected to grow through Kelvin-Helmholtz instability are mostly between 15 and 60 m, which are moderate to long interface waves for layers 10 to 25 m deep. Moderately long interface waves are thus likely to develop as the ebbing tide strengthens.

When these waves have progressed far enough that nonlinear effects become important, they should have the general characteristics of nonlinear dispersive waves, like the cnoidal and solitary waves described by the Korteweg-de Vries equation. Large, moderately long interface waves on a mixed bottom layer are best described by the mathematical theory developed by Benjamin (1967) for nonlinear dispersive waves on the interface between a thin bottom layer and an infinitely thick top layer. The governing equation, like the Korteweg-de Vries equation, has periodic and solitary wave solutions. Choosing a horizontal coordinate x that moves with

Table 4-II
Maximum Wavelengths for Kelvin-Helmholtz Instability
from Numerical Boundary Layer Model

Run-> ωt	1	2	3	4
0	*	5.4	6.3	*
0.16	1.6	0.7	0.6	0.2
0.32	0.8	0.3	1.0	0.2
0.48	25.0	4.0	18.4	2.4
0.64	*	32.0	50.9	6.2
0.8	*	50.7	60.8	33.1
0.96	*	58.1	*	47.0
1.12	*	*	*	54.2
1.28	& *	*	*	58.4
1.44	& *	*	& *	60.9
1.6	& *	& *	& *	62.6
1.76	& *	& *	& *	76.3
1.92	& *	& *	& *	88.2
2.08	& *	& *	& *	&
2.24	& *	& *	& *	&
2.4	& *	& *	& *	&
2.56	& *	& *	&	&
2.72	&	& *	&	&
2.88	&	&	&	&
3.04	&	&	&	&
3.2	&	&	&	&
3.36	&	0.1	0.1	0
3.52	0.2	0.4	0.6	%
3.68	1.9	2.6	4.0	& %
3.84	5.9	%	17.6	& *
4.0	21.7	% &	38.6	51.2
4.16	37.2	% &	47.8	56.2
4.32	44.9	% &	52.4	58.8
4.48	49.1	% &	55.0	60.2
4.64	51.3	% &	56.3	60.8
4.8	52.4	% &	&	&
4.96	52.6	% &	&	&
5.12	& *	% &	&	&
5.28	& *	% &	&	&
5.44	&	% &	&	&
5.6	&	% &	&	&
5.76	&	% &	&	&
5.92	&	% &	&	&
6.08	&	% &	&	&
6.24	2.5	% &	2.7	&

Wavelengths are in meters.
Special symbols: * Entrainment in progress
% Computer fooled by restratification of mixed layer
& Critical wavelength becoming stable as ΔU decreases

the wave, the interface displacement in the solitary wave solution is

$$\zeta(x,h) = \frac{a\lambda^2}{x^2 + \lambda^2} \tag{4.15}$$

where λ is a horizontal length scale given by

$$\lambda = \frac{4\rho_2}{3\rho_1}\frac{h^2}{a}$$

and a is the amplitude of the interface displacement. If η is the initial vertical coordinate of the stream line, the vertical displacement of the streamline in the wave is

$$\zeta(x,\eta) = \begin{cases} \eta \dfrac{a}{h} \dfrac{\lambda^2}{x^2 + \lambda^2} & \text{for } \eta \leq h \\ a \dfrac{(\lambda + \eta - h)^2}{x^2 + (\lambda + \eta - h)^2} & \text{for } \eta \geq h \end{cases} \tag{4.16}$$

With (4.15) and (4.16), u_w, the component of horizontal velocity caused by the wave, can be calculated from the continuity equation:

$$\frac{\partial u_w}{\partial \xi} + \frac{\partial w}{\partial \eta} = 0 \tag{4.17}$$

where ξ is the horizontal coordinate fixed relative to the bottom. If the initial, undisturbed water speed relative to the bottom is U and the wave speed is c, then

$$\xi = x + (U + c)t$$

and

$$w = \frac{\partial \zeta}{\partial t} = -(U + c)\frac{\partial \zeta}{\partial x}$$

so that (4.17) becomes

$$\frac{\partial u_w}{\partial \xi} = \frac{\partial U}{\partial \eta}\frac{\partial \zeta}{\partial x} + (U + c)\frac{\partial^2 \zeta}{\partial x \partial \eta} \tag{4.18}$$

Integrating (4.18), and noting that $u_w = 0$ far from the wave, the result is

$$u_w = \frac{\partial U}{\partial \eta}\zeta + (U + c)\frac{\partial \zeta}{\partial \eta} \tag{4.19}$$

Or, substituting (4.16) into (4.19) and assuming $\frac{\partial U}{\partial \eta} = 0$ in the upper layer,

$$u_w = \begin{cases} (U + c + \eta \frac{\partial U}{\partial \eta})\frac{a}{h}\frac{\lambda^2}{x^2 + \lambda^2} & \text{for } \eta < h \\ (U + c)\frac{2a x^2 (\lambda + \eta - h)}{[x^2 + (\lambda + \eta - h)^2]^2} & \text{for } \eta > h \end{cases} \tag{4.20}$$

Benjamin's solution for wave speed is

$$c^2 = \frac{\rho_2 - \rho_1}{\rho_2} gh\left(1 + \frac{3a}{4h}\right) \tag{4.21}$$

The shapes of the wave-forced velocity component in the mixed layer and just above the interface are shown in figure 4-4.

In nonlinear surface wave theory, for water of depth h, nonlinear and dispersive effects balance to produce solitary waves when $a\lambda^2 = \mathcal{O}(h^3)$. Benjamin (1967) found that a deep upper layer changes this relationship to $a\lambda = \mathcal{O}(h^2)$. When the disturbances of a mixed layer's interface grow and steepen enough to satisfy this condition, they develop into solitary waves. A very large disturbance will create a set

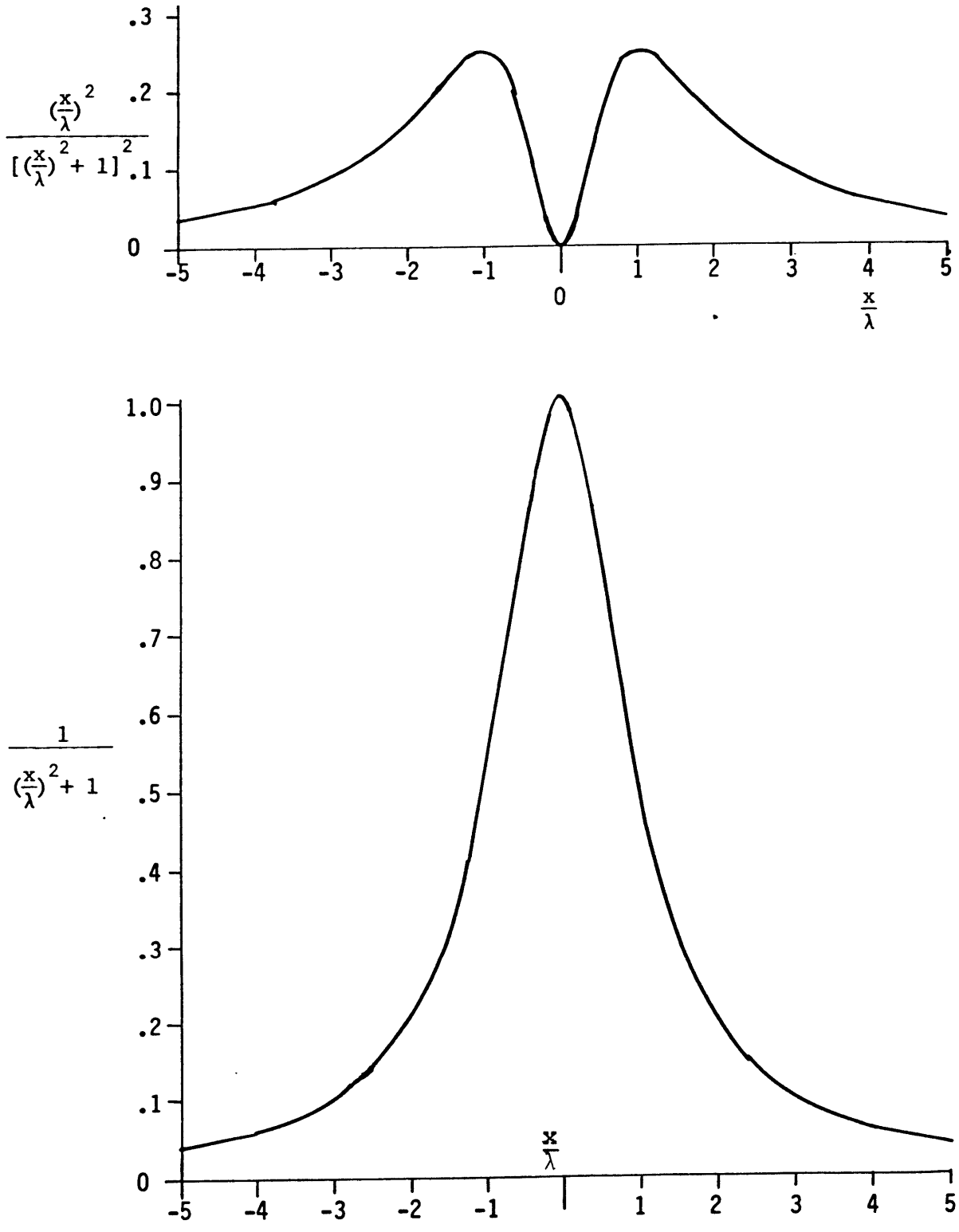

Figure 4-4. The non-dimensional shapes of the velocity signals of interface waves (see equation 4.20). x is the horizontal coordinate traveling with the wave, is the wave's horizontal length scale. Solutions are for depths (a) just above interface of the bottom mixed layer, and (b) within the bottom mixed layer.

of solitary waves; a very small disturbance will create a very small solitary wave. Large solitary waves propagate faster than small ones and will overtake and pass them until the waves progressing down the canyon are ordered in size, with the largest first. As the waves lose energy to bottom stress they can shrink and merge and leave the set with fewer waves than it started with.

Disturbances are likely to grow into finite amplitude waves by the Kelvin-Helmholtz instability when the interface is weak and the shear strong. During the flood tide, the stratification can become so weak that entrainment occurs because of instability, as described in (4.5), perhaps through the breaking of rapidly growing interface waves. Long-lived interface waves will develop most commonly at the maximum ebbing tide when the shear is high and the stratification is weak but growing more stable. In one of the numerical model runs (no. 4), the mixed layer was initially so deep that it did not grow by entrainment during the flooding tide. In the analogous canyon situation, a deep mixed layer may be left over from strong tidal currents so that interface waves can develop during the flooding tide without being destroyed by entrainment.

C. Comparison with observed currents

Two current meters of our Hudson Canyon array, 295 and 306, were 10 m above the floor in the outer part of the

canyon where the mixed layer model of section A is most likely valid (see figure 3-4). Except during storm events, these instruments measured oscillatory currents dominated by diurnal and semidiurnal frequencies. The strong oscillations, 10 to 25 cm/sec in amplitude, are often extended by higher-frequency spikes which may result from interface waves like those described in section B. During many weeks, the diurnal or semidiurnal oscillation is only 1.5 cm/sec in amplitude (and probably often slower; 1.5 cm/sec is the lowest speed that could be obtained from the Aanderaa rotor data). Many of the very low amplitude oscillations are augmented by higher-frequency spikes, producing the characteristic spikey nature of the velocity data.

The velocity signal produced by the interface waves of section B is, according to (4.20),

$$u_w = \begin{cases} (u_T + c + \eta \frac{\partial u_T}{\partial \eta}) \frac{a}{h} \frac{\lambda^2}{x^2 + \lambda^2} & \text{for } \eta < h \\ (u_T + c) \frac{2a x^2 (\lambda + \eta - h)}{[x^2 + (\lambda + \eta - h)^2]^2} & \text{for } \eta > h \end{cases}$$

where u_T is now used to represent the velocity of the tidal oscillations. In the mixed layer below the interface, the maximum wave velocity is of first order in $\frac{a}{h}$. Noting that $a\lambda = \mathcal{O}(h^2)$, the maximum wave velocity just above the interface is of second order in $\frac{a}{h}$. Since $\frac{a}{h} < 1$, current meters are most likely to record strong signals from interface waves

when they are within the mixed layer. This is likely to be the usual case for instruments 295 and 306, since the numerically calculated mixed layers for tidal amplitudes of 10 to 20 cm/sec were all more than 10 m deep.

Predicted maximum mixed layer velocity for interface waves during the ebbing tide were calculated using the results of section B and parameters from numerical run 3. For each value of tidal phase ωt, the linear wave speed c_o was calculated in the numerical model. For a given $\frac{a}{h}$, (4.21) was used to calculate the actual wave speed:

$$c = c_o \sqrt{1 + \frac{3}{4}\frac{a}{h}} \tag{4.22}$$

The tidal velocity was calculated from (4.11):

$$u_T = V \sin \omega t + e^{-\sqrt{\frac{\omega}{2\varepsilon}}\,\eta} \left(\sin \omega t \left(A_3 \cos \sqrt{\frac{\omega}{2\varepsilon}}\,\eta + B_3 \sin \sqrt{\frac{\omega}{2\varepsilon}}\,\eta \right) + \cos \omega t \left(B_3 \cos \sqrt{\frac{\omega}{2\varepsilon}}\,\eta - A_3 \sin \sqrt{\frac{\omega}{2\varepsilon}}\,\eta \right) \right) \tag{4.23}$$

where $\eta = 10^3$ cm is the distance from the bottom to the near-floor current meters, $\frac{h}{6} < \eta < h$, and run 3, for $\omega t > \frac{3\pi}{4}$, gives

$V = -15$ cm/sec

$\varepsilon = 80.9$ cm^2/sec

$A_3 = 2.46$ cm/sec

$B_3 = .689$ cm/sec

$h = 17.6$ m

The maximum interface wave velocity was calculated using (4.20):

$$u_{w,max} = (u_T + c + \eta \frac{\partial u_T}{\partial \eta}) \frac{a}{h} \qquad (4.24)$$

where

$$\eta \frac{\partial u_T}{\partial \eta} = \eta \sqrt{\frac{\omega}{2\varepsilon}}\ e^{-\sqrt{\frac{\omega}{2\varepsilon}}\eta} \left[\sin \omega t \left((B_3 - A_3)\cos \sqrt{\frac{\omega}{2\varepsilon}}\eta - (A_3 + B_3)\sin \sqrt{\frac{\omega}{2\varepsilon}}\eta \right) + \cos \omega t \left((A_3 - B_3)\sin \sqrt{\frac{\omega}{2\varepsilon}}\eta - (A_3 + B_3)\cos \sqrt{\frac{\omega}{2\varepsilon}}\eta \right) \right]$$

The time rate of change of wave velocity can be represented by $\frac{1}{u_w} \frac{\partial u_w}{\partial t}$, by analogy to the radian frequency of sinusoidal waves. The maximum value of this is $\frac{u_{w,max}}{\lambda}$. The width of the interface wave's signal on a time record is thus about

$$\frac{\pi \lambda}{u_{w,max}} \qquad (4.25)$$

This spike width was calculated using Benjamin's (1967) definition of λ (see equation 4.15).

Figure 4-5a shows the total velocity $u_T + u_{w,max}$ which the combination of interface waves and tidal oscillations can produce, as a function of tidal phase ωt and interface wave size $\frac{a}{h}$. Figure 4-5b is a graph of spike width, in hours, also as a function of ωt and $\frac{a}{h}$. If $\frac{a}{h} < .2$, the wave "spike" is so broad that it may not be distinguished from the 6-hour tidal flow. Waves of amplitude $\frac{a}{h} > .6$ have such short spikes that they could not be properly recorded by our Aanderaa current meters with 20-minute sampling intervals. The

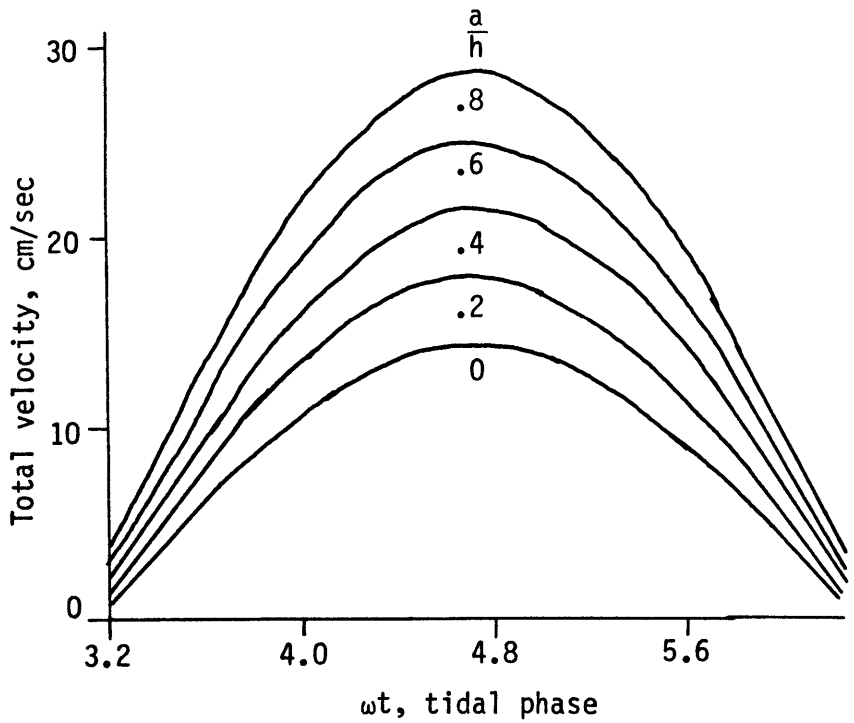

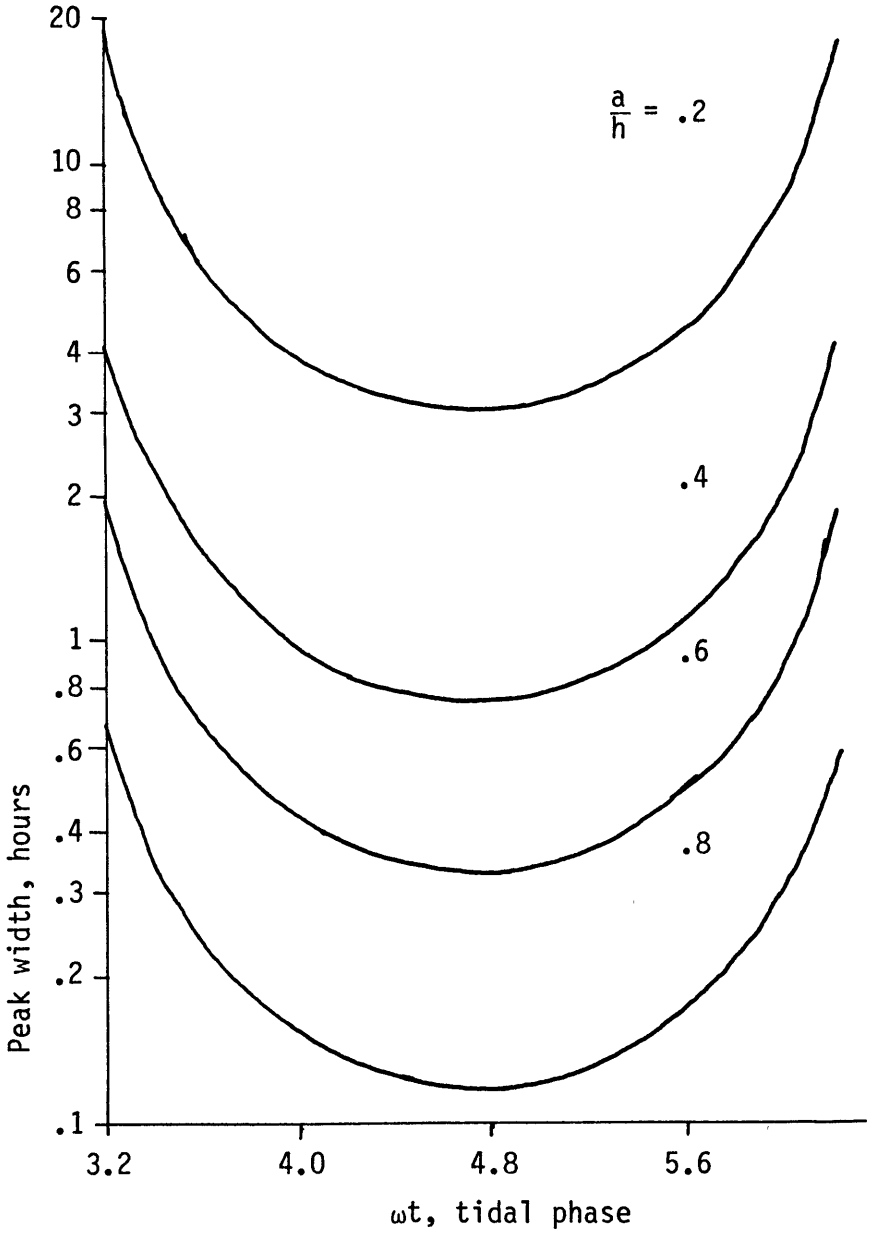

Figure 4-5. (a) The maximum velocity $u_T + u_{w,max}$ (see equations 4.23 and 4.24) produced by nonlinear interface waves during an ebbing tide of amplitude 15 cm/sec. The maximum velocity is a function of tidal phase ωt and wave amplitude $\frac{a}{h}$.
(b) The duration of velocity signals in the bottom mixed layer produced by nonlinear waves on the layer's interface (see equation 4.25). This duration is the width of spikes on time series plots, and is a function of tidal phase ωt and wave amplitude $\frac{a}{h}$.

interface waves that may be resolved in our Hudson Canyon data are thus predicted to increase the tidal velocity by 30 to 75% (from figure 4-5a).

Figure 4-6 is similar to 4-5, but the tide was assumed to have only a 2 cm/sec amplitude, while the mixed layer was still 17.6 m deep. The resolvable peak widths in this situation are for wave amplitudes between .4 and .8, which produce speeds of 3.5 to 5.5 cm/sec.

Figure 4-7 shows excerpts from the along-canyon velocity record from instrument 295, plotted at a scale which shows the high-frequency spikes. November 12-15, December 11-19, and January 2-9 were times when the spikes on strong diurnal or semidiurnal oscillations seem to be of appropriate height to be the signals of nonlinear interface waves. In several instances, the spikes are arranged in order of size as if the waves have had time to sort themselves out. The spikes on low-amplitude oscillations, November 8-12, are also of roughly the right magnitude to be non-linear interface waves. But during much of the record the spikes are of such large amplitudes that such interface waves would not be resolved on the record (note the velocity plot for October 9-24). These may be records of trains of large amplitude interface waves, which produce broad spikes because the sampling interval of the instrument (20 minutes) is roughly the same as the time scale of the signal.

The evidence is not complete, but suggests that non-

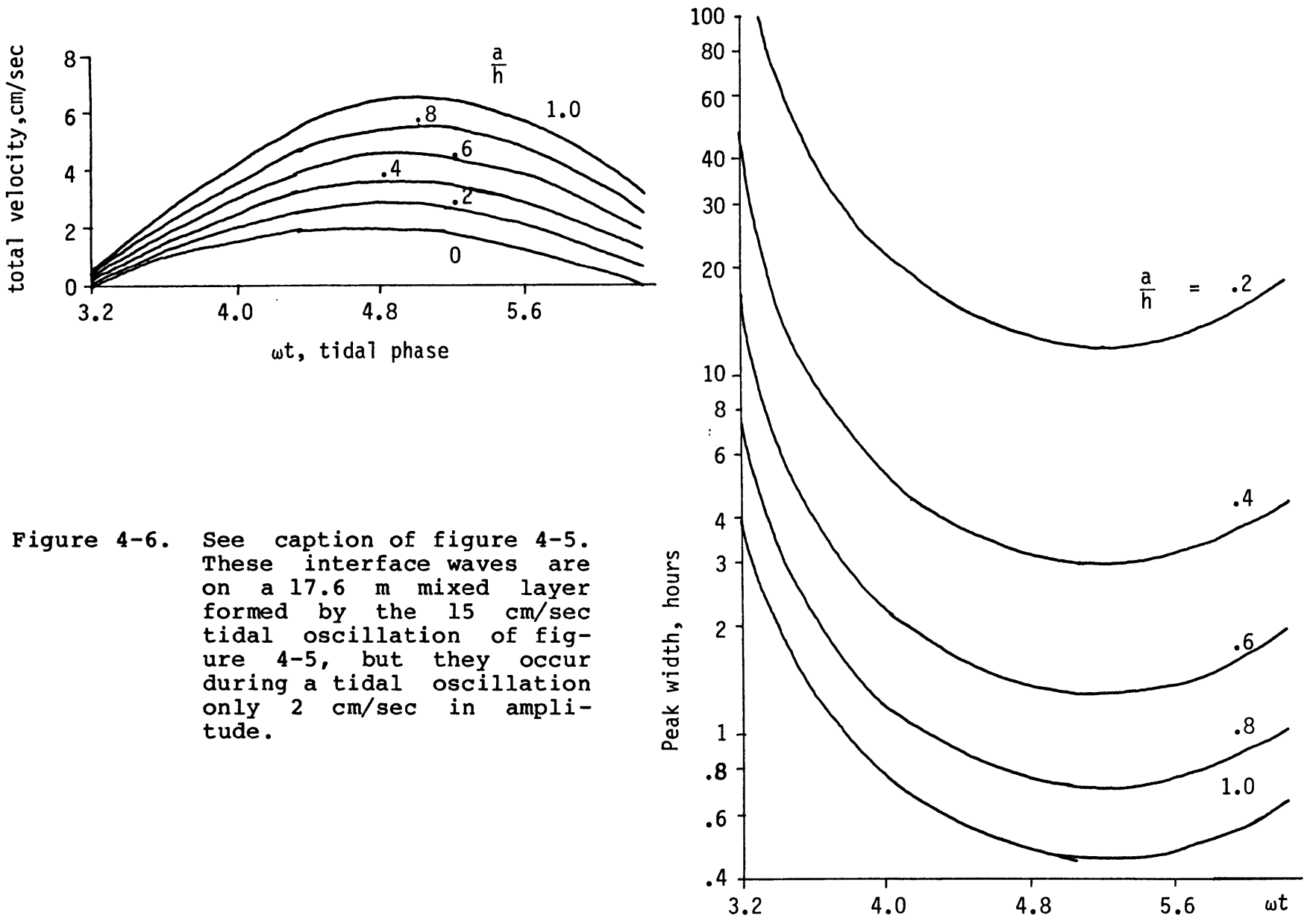

Figure 4-6. See caption of figure 4-5. These interface waves are on a 17.6 m mixed layer formed by the 15 cm/sec tidal oscillation of figure 4-5, but they occur during a tidal oscillation only 2 cm/sec in amplitude.

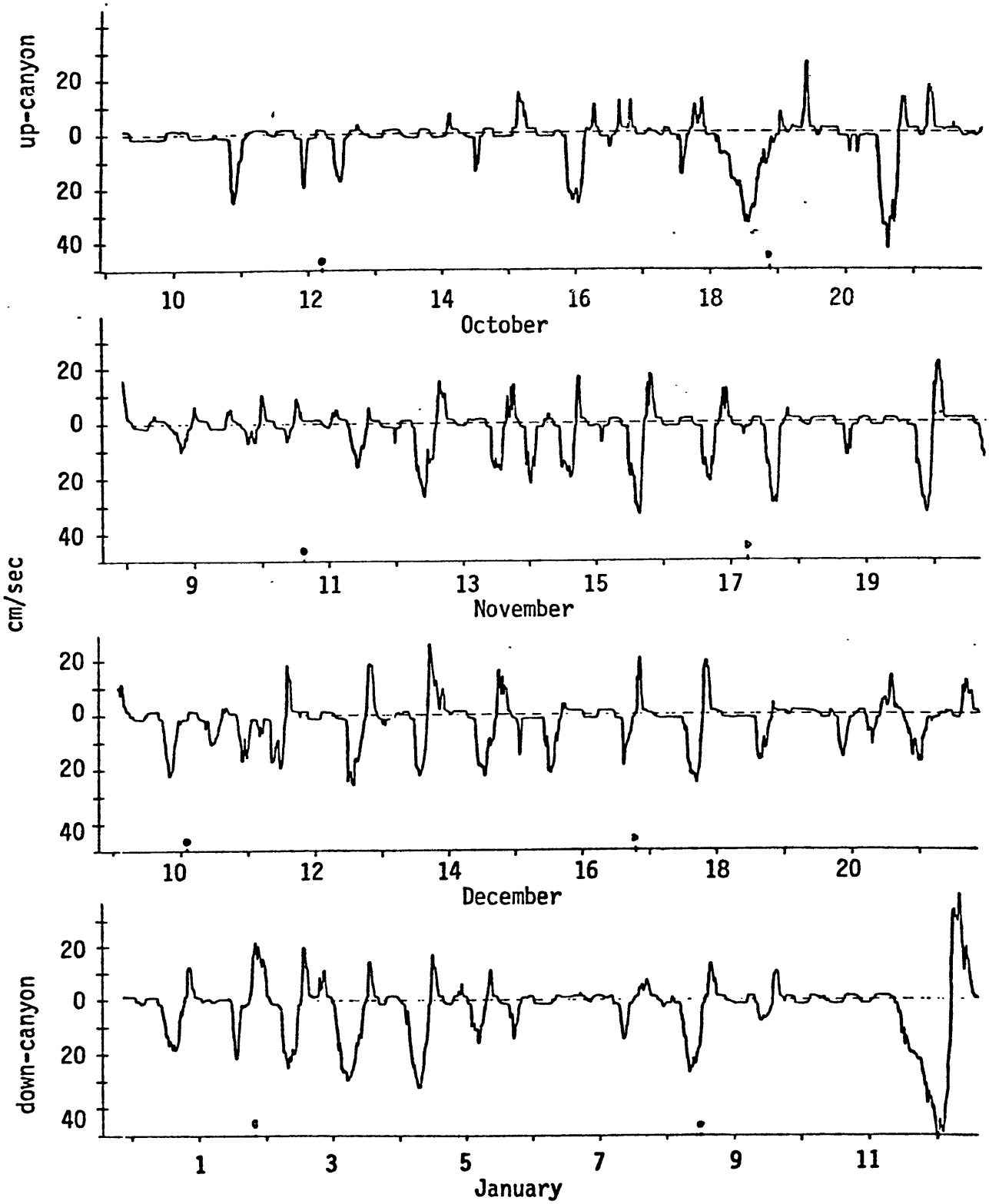

Figure 4-7. Excerpts from the along-canyon velocity record of current meter 295 (see figure 3-4 for location) showing high-frequency spikes on tidal oscillations. Spike width and height are consistent with a nonlinear interface wave interpretation.

linear interface waves are present and account for much of the high-frequency variability near the canyon floor. These waves seem to involve interface displacements as great as the mixed layer depth (roughly 15 m), velocity maxima of about 30 cm/sec and time scales as small as 6 minutes.

High-frequency waves produce bottom stresses significantly greater than those produced by steady currents of the same amplitude. Thus the velocity spikes under interface waves will suspend bottom sediment when the tidal oscillations, alone, would not. The low-frequency tidal flow can then transport the sediment a significant distance before it settles to the floor. The bottom stress that these currents produce and their ability to initiate sediment motion will be considered quantitatively in Chapter 5.

Chapter V

Boundary Stress and Sediment Transport

The heads of submarine canyons are natural sediment traps. The canyons of the California coast are major conduits through which the sand that rivers bring to the continental shelf is transported to the deep sea floor, building fans of sediment at the canyon mouths (see Shepard, 1973, p. 140). Fans of sediment have also built up beyond submarine canyons of the East Coast, including Wilmington, Hudson, and Hydrographer Canyons (Shepard and Dill, 1966; Kelling and Stanley, 1976).

Butman et al. (1979) have observed sediment being transported both as bedload and in suspension on the outer continental shelf near Hudson and Wilmington Canyons. Bedload transport, grains rolling and hopping along the floor, is caused there by strong waves and winter storms. There will be net transport into canyons even when the bedload on the shelf is just moving back and forth under waves, since the grains that fall into canyons will not be pulled back out. Fine sediments are frequently suspended in the bottom water over the continental shelf. Both gravity and diffusion tend to pull suspended material into the canyon as the bottom

water flows over the canyon. Storm-forced downwelling could also bring large amounts of fine material into the canyon. Grains will be suspended by the strong storm currents on the shelf, and may have time to settle to the floor in the relatively tranquil canyon.

Observations of the floor sediment in upper Hudson Canyon (summarized in Chapter 1) indicate continual sorting of the incoming sediment, punctuated by episodes of express transport through the canyon. The pebbles and sand seen actively moving in the canyon head are not observed throughout the canyon. Instead, the floor sediment gets gradually finer with depth, as if sorted by gradually weakening currents. A layer of mud has accumulated below the thermocline (roughly 400 m deep) in the canyon. In a core taken at 430 m, Drake et al. (1978) found layers of sand and silt that were probably formed by strong current episodes at intervals of roughly 1000 years. Cacchione et al. (1978) observed wall erosion, ripple marks, and patches of pebbles in Outer Hudson Canyon at depths between 3000 and 3600 m, and concluded that strong episodic currents, such as turbidity currents, were responsible for them.

I have used standard boundary layer models and criteria for the initiation of sediment motion to evaluate the sediment-transporting ability of the currents we observed in Hudson Canyon. The methods I have used were developed for regions much simpler than the canyon floor, but can be used

for rough estimates. Although our 15-week experiment was very short compared to erosional time scales, the processes we observed may cause the continual sorting and local sediment transport that produce the surficial sediment pattern observed in the upper part of Hudson Canyon. In addition, the storm of January 8-11, 1978, caused a strong current episode below the thermocline and may illuminate the mechanism of express sediment transport.

A. Criteria for initiation of sediment motion

Formulas for the initiation of sediment motion, and for the velocity and stress fields near a sediment bed, are predominantly empirical. They were determined using beds of artificially uniform grains, or, if the beds were of mixed sizes, the median grain diameter was usually used in the formulas. Thus estimates of sediment stability in Hudson Canyon depend on obtaining observed values of the median grain sizes of the beds involved.

Qualitative descriptions of the surface sediment types in and around Hudson Canyon are readily available. For example, from their exploration of the canyon in a submersible, Keller et al. (1973) report that the floor is covered with sand and well-rounded pebbles in the canyon head, progressing to silt and clayey silt at a depth of 400 m, and that the floor at depth of 400 to 1000 m is covered by a thick layer of silty clay, of low apparent cohesion but high resistance

Figure 5-1.

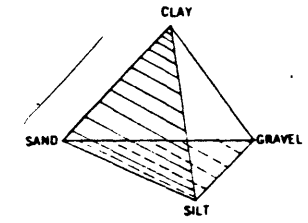

TETRAHEDRON OF SEDIMENT NAMES

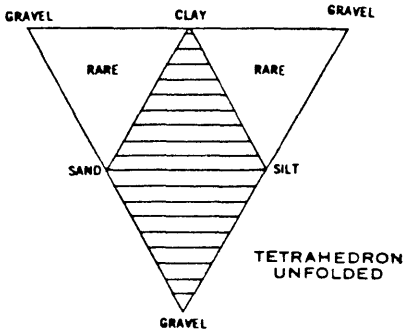

TETRAHEDRON UNFOLDED

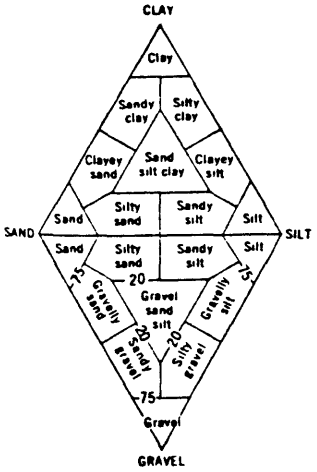

From Uchupi, 1963.

Sediment grain size scales

Millimeters	Microns	Phi (ϕ)	Wentworth Size Class	
4096		−12		
1024		−10	boulder	
256		− 8		
			cobble	
64		− 6		
16		− 4	pebble	Gravel
4		− 2		
3.36		− 1.75		
2.83		− 1.5	granule	
2.38		− 1.25		
2.00		− 1.0		
1.68		− 0.75		
1.41		− 0.5	very coarse sand	
1.19		− 0.25		
1.00		0.0		
0.84		0.25		
0.71		0.5	coarse sand	
0.59		0.75		
0.50	500	1.0		
0.42	420	1.25		
0.35	350	1.5	medium sand	Sand
0.30	300	1.75		
0.25	250	2.0		
0.210	210	2.25		
0.177	177	2.5	fine sand	
0.149	149	2.75		
0.125	125	3.0		
0.105	105	3.25		
0.088	88	3.5	very fine sand	
0.074	74	3.75		
0.0625	62.5	4.0		
0.053	53	4.25		
0.044	44	4.5	coarse silt	
0.037	37	4.75		
0.031	31	5.0		
0.0156	15.6	6.0	medium silt	
0.0078	7.8	7.0	fine silt very fine silt	Mud
0.0039	3.9	8.0		
0.0020	2.0	9.0		
0.00098	0.98	10.0		
0.00049	0.49	11.0	clay*	
0.00024	0.24	12.0		
0.00012	0.12	13.0		
0.00006	0.06	14.0		

*some use 9ϕ as clay boundary

Source: Folk 1974

From Freeland and Swift, 1978.

to erosion. Clayey silt means less than 20% sand and gravel, 50 to 75% silt, and less than 50% clay. Further, silt means grain diameters of 3.9 to 31 microns, etc. See figure 5-1.

Shepard and Cohee (1936) published a detailed survey of median grain diameters in the Hudson Canyon area shown in figure 5-2. As can be seen from figure 5-2c, their sediment descriptions agree with the recent qualitative observations.

For abiotic flat beds of uniform, non-cohesive grains, the critical shear stress for the initiation of sediment motion is known empirically. This may be expressed in the Shields diagram (see Graf, 1971), a plot of critical Shields parameter:

$$\psi_c = \frac{\tau_c}{(s - 1)\rho\, g\, d}$$

where

τ_c is the critical boundary shear stress for the initiation of motion,

$(s - 1)$ is the difference in specific gravity between the sediment and the water,

d is the sediment diameter, and

ρ is the density of water.

The abscissa of the Shields diagram is boundary Reynolds number:

$$Re_* = \frac{u_*}{\nu d}, \quad \text{where} \quad u_* = \sqrt{\frac{\tau}{\rho}}$$

where ν is viscosity, and τ boundary stress. A Shields dia-

Figure 5-2.

From Shepard and Cohee (1936).

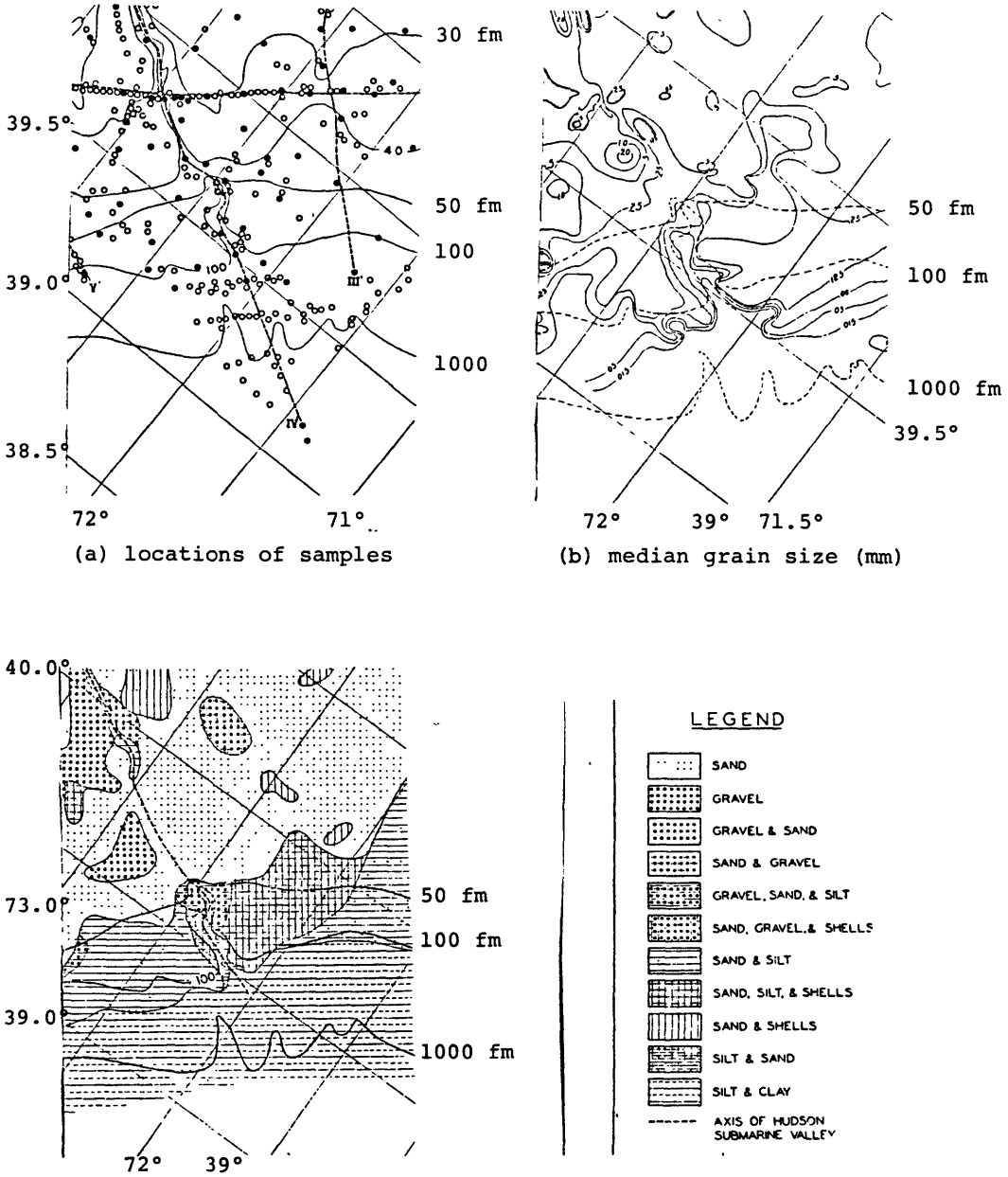

(a) locations of samples

(b) median grain size (mm)

(c) sediment types, see legend at right.

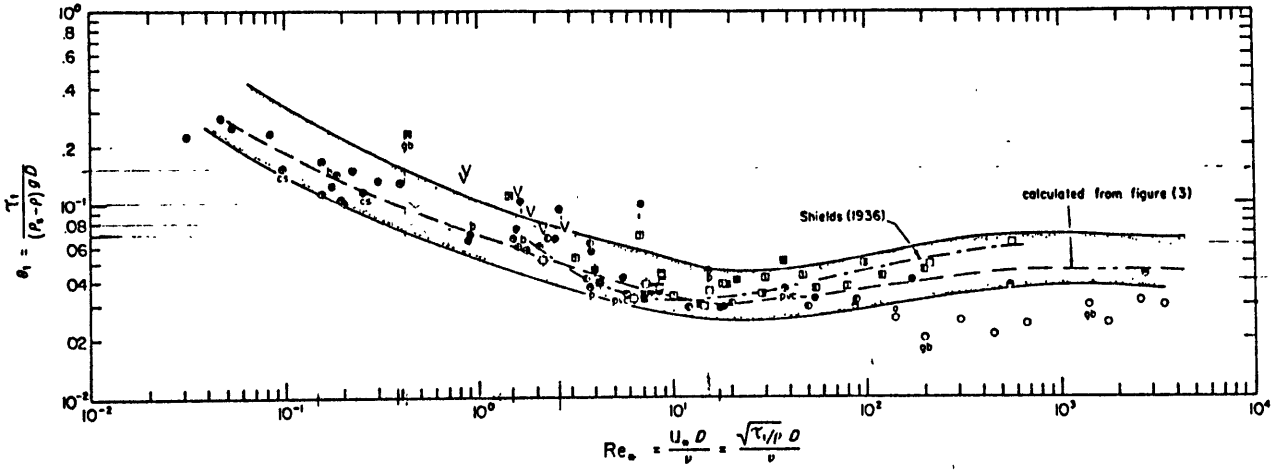

Fig. 2. The proposed modified Shields curve of θ_t versus Re_* based on additional carefully selected data. See Table 1 for identification of the symbols.

Figure 5-3. Shields diagram from Miller et al. (1977).

gram for small boundary Reynolds number has been obtained by Miller, et al. (1977). It is reproduced in figure 5-3; note that the line for critical Shields parameter is drawn through the middle of a cloud of experimentally determined points. I used this line to construct a "modified" Shields diagram (see Madsen and Grant, 1976), in which the abscissa does not depend on boundary shear stress but is simply a non-dimensional parameter describing the properties of the sediment and fluid, easily obtainable, for each point, from ψ_c and Re_*:

$$S_* = \frac{d}{4\nu}\sqrt{(s-1)\,g\,d} = \frac{Re_*}{4\sqrt{\psi_c}}$$

A portion of this modified Shields diagram is drawn in figure 5-4.

It is now a simple matter to calculate the critical friction velocity u_{*c} for each contour of median grain size given by Shepard and Cohee (1936). The sediment involved is mostly quartz and feldspar (Freeland and Swift, 1978) with specific gravity close to 2.65. From CTD data, the bottom temperature in the canyon is between 5° and 12°C. The viscosity of seawater at this temperature and pressure (from Stanley and Batten, 1969) is about 0.014 cm /sec. Thus the nondimensional sediment-fluid parameter is

$$S_* = 700\,(cm^{-3/2})\,d^{3/2}$$

ψ_c can be found on figure 5-4, and

$$u_{*c}^2 = 1620\,(cm/sec^2)\,\psi_c\,d\,.$$

Figure 5-5 is a map of these contours of equal u_{*c} for the

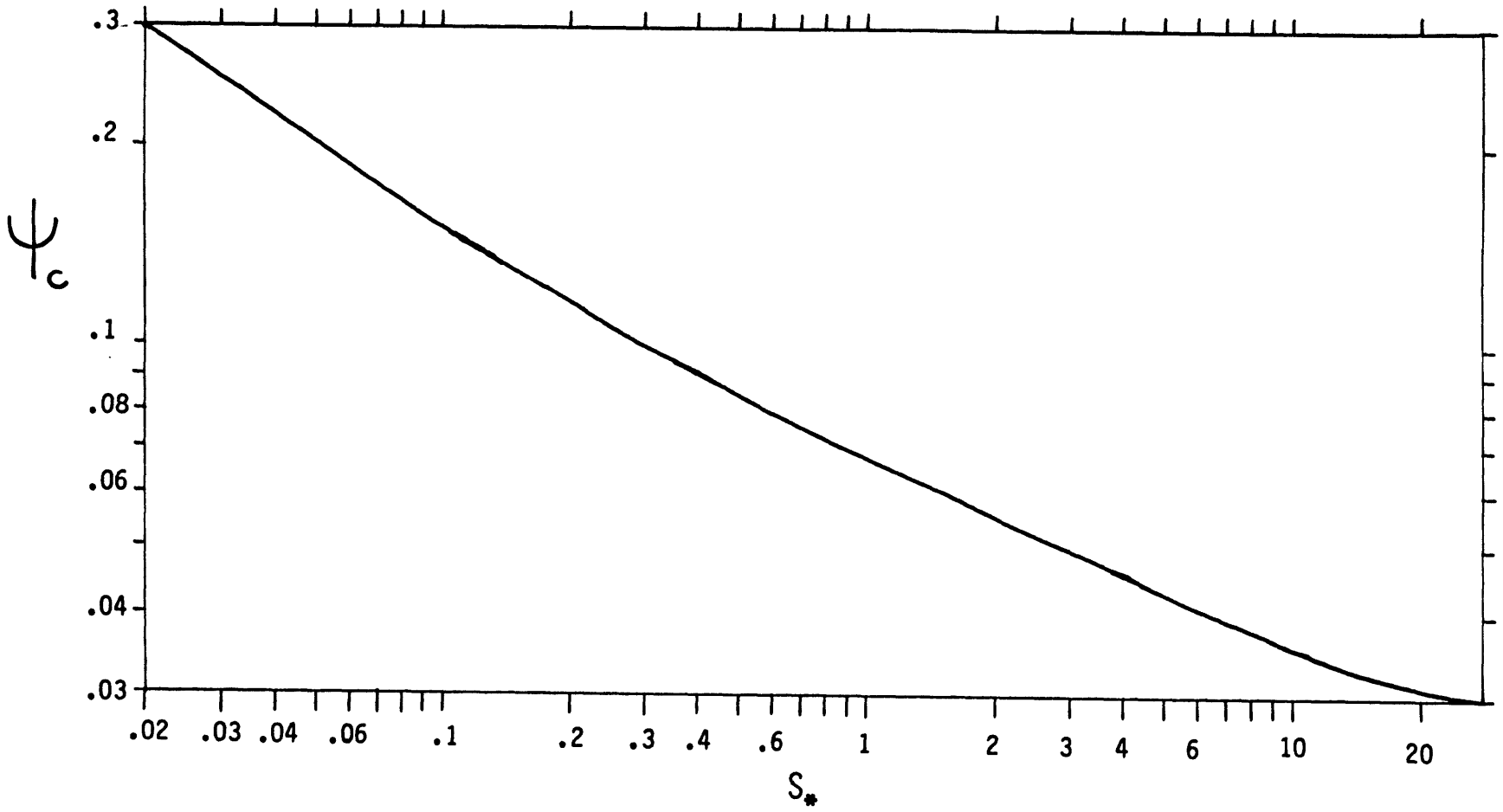

Figure 5-4. Modified Shields diagram constructed from figure 5-3.

$$\psi_c = \frac{\tau_c}{(s-1)\rho g d} \qquad S_* = \frac{d}{4\nu}\sqrt{(s-1)gd} = \frac{Re_*}{4\sqrt{\psi_c}}$$

Figure 5-5

Critical u_* for initiation of sediment motion

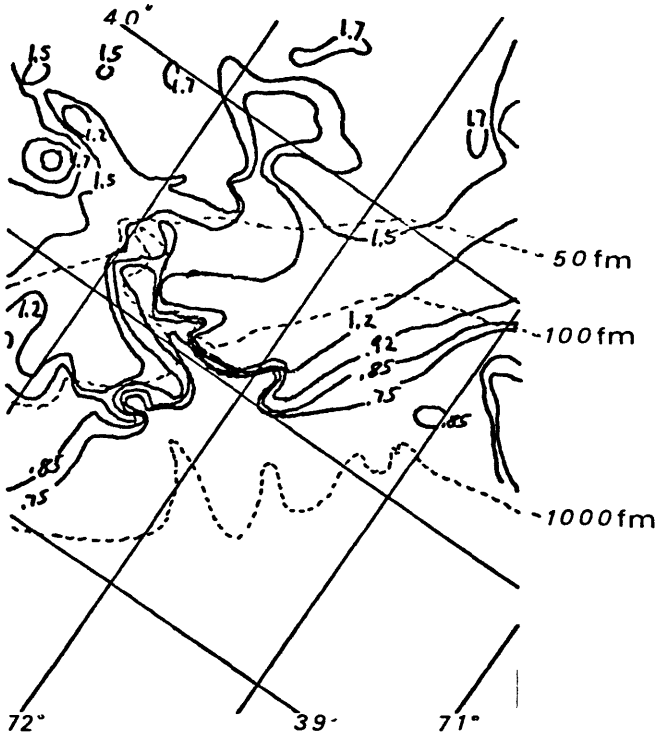

$$u_* = \sqrt{\frac{\tau_o}{\rho}}$$

in cm/sec

Median grain size map from Shepard and Cohee (1936).

u_* calculated using figure 2 of Miller, McCave, and Komar (1977).

canyon area.

The sediment transport potential of the observed currents can be evaluated by estimating the boundary shear stress they produce. At a given point in Hudson Canyon, sediment motion can be assumed not to occur unless stress velocity u_{*c} is greater than the value given on figure 5-5. Biologically-induced adhesion has been observed to prevent sediment motion when the stress velocity is up to 4 times the value given by the Shields curve (Grant et al., 1982).

It is the instantaneous bottom stress which puts sediment into motion, but the bottom stress itself depends on boundary layer development, and thus on the history and time rate of change of the velocity. For this reason, boundary layers, shear stress, and potential for sediment transport will be considered separately for low-frequency storm currents and higher-frequency oscillations. For each process, I will estimate the threshold amplitude for the initiation of sediment motion. The observed velocity fields will be compared with these thresholds to estimate the frequency of sediment transport.

B. Low-frequency flows

The variation of velocity with height in a simple turbulent boundary layer is expressed in the "law of the wall." Schlichting (1979, pp. 596-620) gives a formula for this empirical law that is good for walls of all roughnesses:

$$\frac{u(z)}{u_*} = 5.75 \log \frac{z}{k_s} + B \qquad (5.1)$$

where $k_s = d$ for a flat bed of sand grains

and B is a function of the roughness of the bed through the boundary Reynolds number $\frac{u_* k_s}{\nu}$.

For $\frac{u_* k_s}{\nu} < 5$ the flow is smooth turbulent, there is a viscous sublayer next to the bed and

$$B = 5.5 + 2.5 \ln \frac{u_* k_s}{\nu}$$

For a fully rough bed, $\frac{u_* k_s}{\nu} > 70$ and $B = 8.5$.

Observations of the floor of Hudson Canyon (Rowe et al., 1974) indicate that benthic animals such as crabs, sea urchins, and sea stars are actively burrowing and tracking the sediment. These activities create lumps and furrows that cause the floor roughness to be much greater than the grain size, so $k_s = 3$ cm may be appropriate. Roughness of this magnitude results in a boundary Reynolds number (taking $u_* = 1$ cm/sec) well within the fully rough range:

$$\frac{u_* k_s}{\nu} = 214.$$

The rough turbulent boundary layer was used to calculate threshold velocities at $z = 10$ m for the initiation of sediment motion. The result is $u_c(10\text{ m}) = 23\ u_{*c}$. Threshold velocities for the median size contours of figure 5-2 are given in table 5-I.

Table 5-I

Threshold Velocities for Initation of Sediment Motion by Steady Flow

d (cm)	u_* (cm/sec)	u_c (10m) (cm/sec)
.05	1.73	40
.025	1.47	34
.0125	1.18	27
.006	.92	21
.003	.85	20
.0015	.75	17

Without stratification, a slight slope of the floor has no major effects on the structure of the boundary layer. One minor effect is that z should be measured normal to the bed rather than vertically up from it. Thus the proper value to be used in the law of the wall is

$$z = 10 \text{ m} \cos S.$$

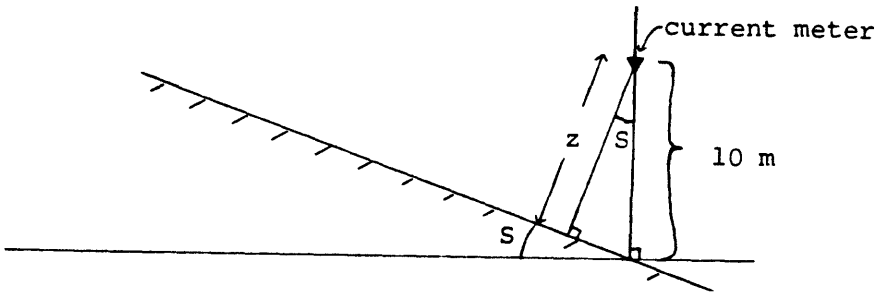

For Hudson Canyon, the local floor slope ranges from 0 to 6°, so the correction in z/d is at most 0.5% and that in u (10 m) is at most 0.2%.

Without modifying the boundary layer, a sloping bed makes it easier for a down-slope current to suspend a grain. The component of the grain's weight directed into the bed is cos S times that on a flat bed, and the weight of the grain has a destabilizing component based on the ratio of the slope to the natural angle of repose of the sediment. Graf (1971, pp. 113-116) gives the following formula for critical Shields parameter on a sloping bed:

$$\psi_{sc} = \psi_c \left| \cos S \left(1 - \frac{\tan S}{\tan \phi}\right) \right|$$

where ϕ is the angle of repose, approximately 35°. The

Shields parameter correction factor for a 6° slope is 0.85. This can be neglected, considering the uncertainty introduced by biological processes.

Stratified boundary layers over sloping beds. The boundary layer at the canyon floor is complicated by the interactions of many factors: stratification, rotation, oscillation of the velocity above the layer, non-uniformity, sloping floor, and confining sidewalls. There is some hope that the combination of stratification and sidewalls will allow the set-up of an across-canyon pressure gradient to keep pace with the Coriolis force and balance it. Further, it seems reasonable to assume that the velocity in the canyon is along the canyon, and that the velocity can be considered locally uniform. The remaining complications - stratification, floor slope, and time variability - can interact in several ways. Density currents result when the stratification is so strong that the bottom layer is pulled down the slope by gravity. Unless the layer is very dense, it will separate from the floor and intrude into the water column when it reaches denser water in the ambient stratification. In the canyon, suspended sediment could produce sufficiently dense bottom water to force a long-lived density current. Such a turbidity current could be limited to the immediate vicinity of the bed by its strong stratification, and might have passed our instruments without detection.

A more moderate interaction between stratification and

floor slope was explored in Chapter 4: when outside forces cause oscillatory currents along the canyon floor, overturning during up-canyon flows creates a bottom mixed layer as thick as the frictional boundary layer. Some restratification may occur during the down-canyon flows. The rate of restratification is proportional to the product of the vertical velocity gradient and the density gradient along the floor. Since the tendency of shear to keep the layer mixed is proportional to the square of the velocity gradient, restratification tends to occur only at the top of the mixed layer where shear is low. Thus the combination of stratification, time variability, and floor slope produce a mixed boundary layer near the canyon floor.

As demonstrated in Chapter 4, two effects of combined stratification and floor slope need to be considered in the thermocline where instrument 315 was placed. These are the along-canyon component of gravity acting on the excess density of the mixed layer, and the pressure gradient resulting from the slope of the surface of the mixed layer (which roughly parallels the floor). These will tend to increase the floor stress for an arbitrary current speed at 10 m.

The threshold velocities given in table 5-I are thus representative of the steady current speeds required to start sediment moving in most of Hudson Canyon. The strong stratification in the vicinity of instrument 315 (see figures 2-11, 3-4) may allow sediment motion at lower speeds. Before

applying these results to the Hudson Canyon data, it is necessary to consider the development of boundary layers under oscillatory currents and ascertain how low a current's frequency must be for the steady results to be applicable.

C. Simple oscillatory flows

A critical Shields parameter can be used to express the bottom stress necessary for initiation of sediment motion under waves if the bottom stress used is the maximum during the wave period (see Madsen and Grant, 1976):

$$\psi_c = \frac{\tau_{om}}{\rho g(s - 1)d} = \frac{u_{*m}^2}{g(s - 1)d}$$

The maximum bottom shear stress, τ_{om}, can be expressed as

$$\tau_{om} = \rho u_{*m}^2 = \frac{1}{2} \rho f_w u_b^2 \qquad (5.2)$$

for near-floor (but outside the boundary layer) wave velocity of amplitude u_b and a wave friction factor f_w. The critical Shields parameter ψ_c for oscillatory flow falls within the cloud of experimental points defining the curve of figure 5-4 so the critical wave friction velocity u_{*mc} is the same as the steady u_{*c} calculated in section A and contoured in figure 5-5.

The wave friction factor f_w is used to connect maximum wave velocity u_b with maximum shear stress τ_{om}. According to Jonsson (1966), the wave friction factor for fully rough turbulent flows is close to that given by

$$\frac{1}{4\sqrt{f_w}} + \log_{10}\frac{1}{4\sqrt{f_w}} = \log_{10}\frac{A_b}{k_s} - 0.12 \qquad (5.3)$$

where $A = \frac{u_b}{\omega}$ is the particle excursion length under the wave. Solutions of (5.2) and (5.3) were found for the range of values of u_{*m} found to be critical in Hudson Canyon. The resulting values of $u_b(\omega)$ are shown in figure 5-6.

The thickness of the wave boundary layer increases with increasing wave period. For the semidiurnal and diurnal oscillations typical of Hudson Canyon, the wave boundary layer may be thick enough that the velocity measured 10 m above the floor differs from u_b. To extrapolate from u_b to u(10 m), I used a velocity profile obtained by Kajiura (1968, see also Smith, 1977) who used a turbulent viscosity distribution analogous to that used to obtain the familiar logarithmic layer in steady flow:

$$\nu_{turb.} = \kappa|u_{*m}|\, z$$

The bottom boundary condition is zero velocity at $z = z_o = \frac{k_s}{30}$;

; for Hudson canyon I used z_o = .1 cm. The solution for velocity in the boundary layer is

$$u = u_b \sin\omega t\left(1 - \frac{\ker 2\sqrt{\zeta}\,\ker 2\sqrt{\zeta_o} + \mathrm{kei}\,2\sqrt{\zeta}\,\mathrm{kei}\,2\sqrt{\zeta_o}}{\ker^2 2\sqrt{\zeta_o} + \mathrm{kei}^2 2\sqrt{\zeta_o}}\right) \qquad (5.4)$$

where ker and kei are Kelvin functions, which are modified Bessel fuctions, and

$\zeta = \frac{z\omega}{\kappa u_{*m}}$ is the scaled vertical coordinate of the layer,

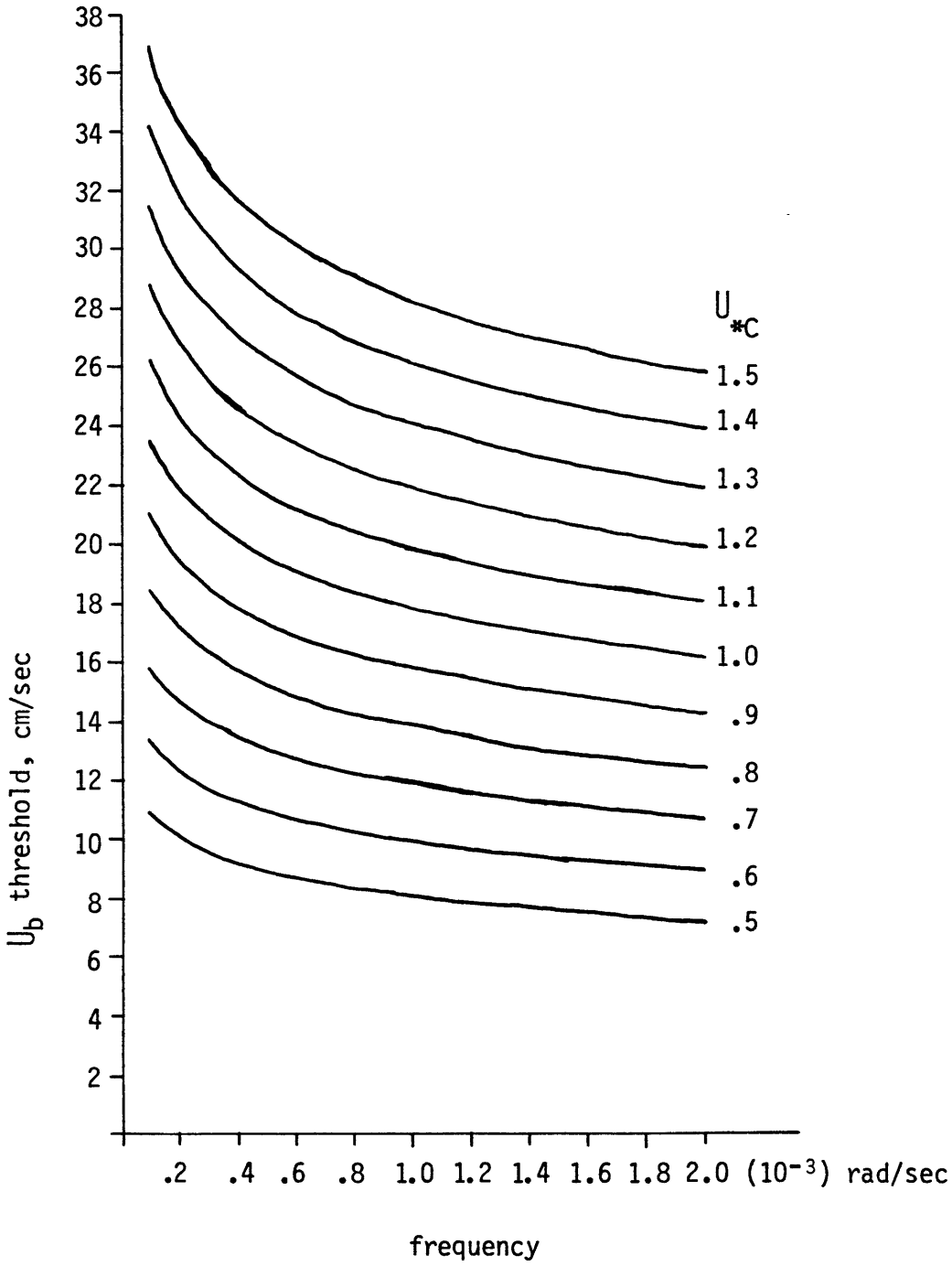

Figure 5-6.
Threshold wave velocity measured outside the boundary layer for initiation of sediment motion, as a function of frequency ω and critical friction velocity u_{*c}. See (5.2) and (5.3).

$$\zeta_o = \frac{z_o \omega}{\kappa u_{*m}} .$$

Solutions of (5.4) for the ratio $\frac{u_b(10m)}{u_{b,c}}$ are shown in figure 5-7 for the range of values of u found to be critical in Hudson Canyon. These were found numerically by using the polynomial expansions for ker and kei given by Abramowitz and Stegun (1964, p. 384). The difference between u(10 m) and u_b is less than 2% except for wave periods longer than 4.6 hours. The difference is greatest for large u_*. The threshold velocities of figure 5-6 were adjusted to produce figure 5-8, a graph of threshold velocity at 10 m. The critical steady velocity (from equation 5.1) is included as the low-frequency limit.

The small effect of the floor slope may be expected to cause an asymmetry in the sediment transport of sinusoidal waves, the down-canyon velocity being more effective than the up-canyon one in moving sediment. From section B, the critical Shields parameter for flow down a 6° slope (the highest along the canyon axis) is 85% of that for a horizontal bed. Using the same formula, the Shields parameter value for an up-slope flow would be 115% of the horizontal-bed parameter. Waves very near the minimum magnitude for initiation of sediment transport can be expected to move sediment only during the down-canyon halves of their cycles. Since the Shields parameter is proportional to u_*^2 and u(10 m) is roughly proportional to u_*, this zone of one-directional transport will be

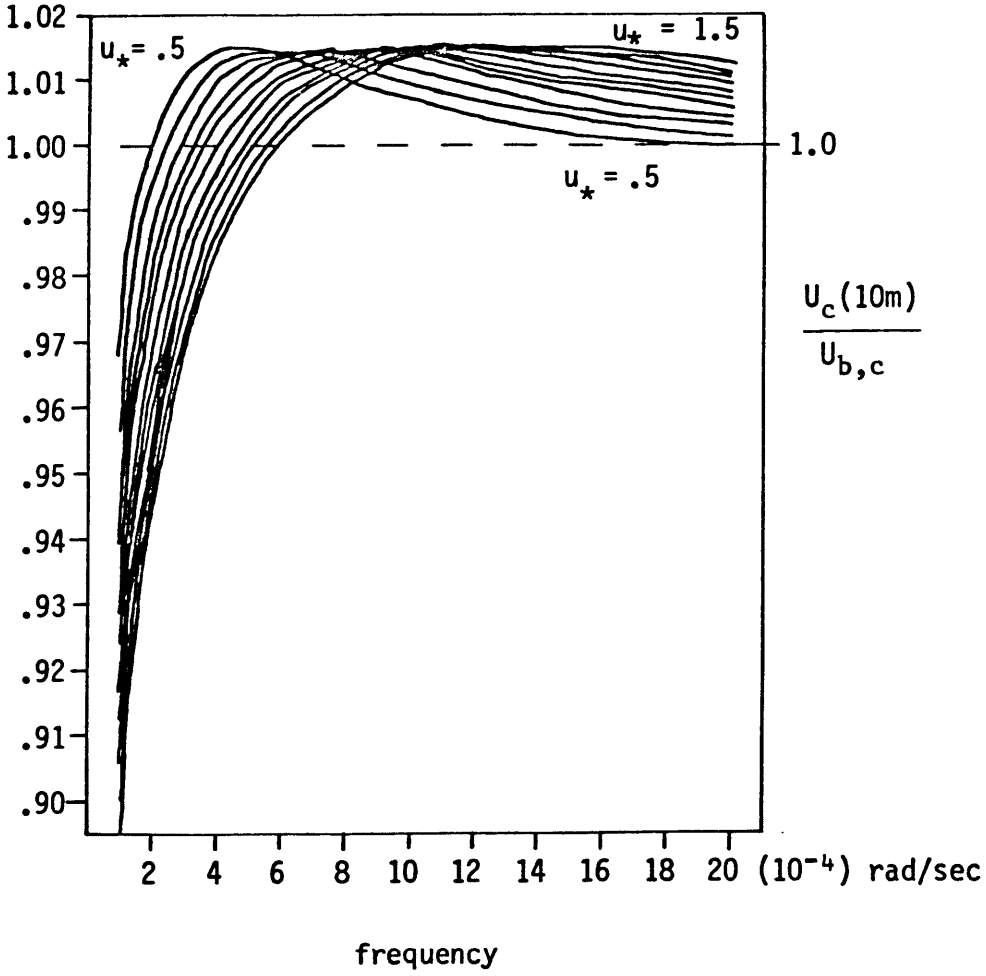

Figure 5-7. Ratio of maximum wave velocity measured at 10 m above the bottom to maximum wave velocity outside the boundary layer. See (5.4).

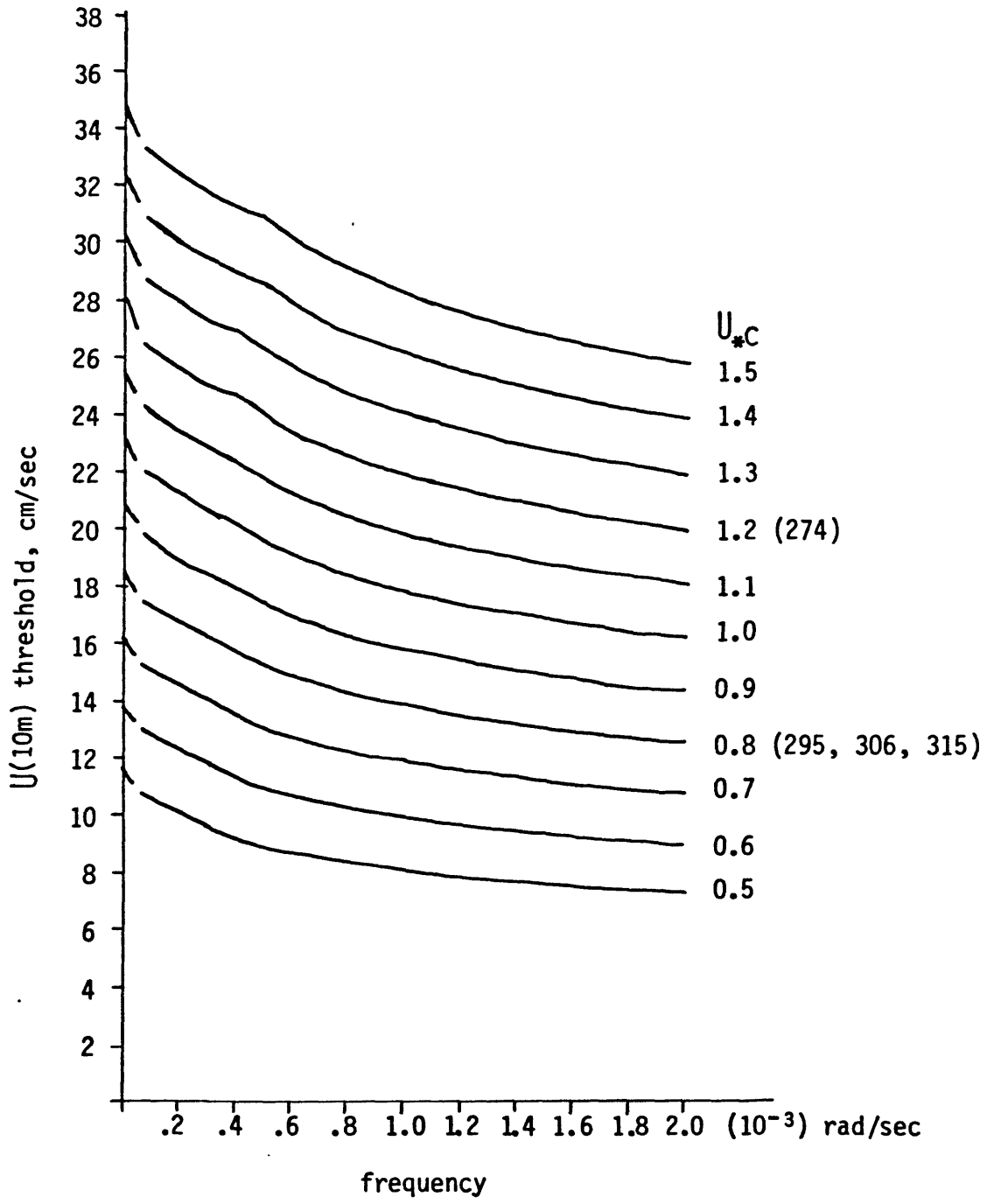

Figure 5-8. Threshold wave velocity measured 10 m above the bottom for the initiation of sediment motion.

$$\sqrt{.85} < u(10\,m)/u_c(10\,m) < \sqrt{1.15}$$

or

$$u(10\,m) = u_c(10\,m) \pm 8\%$$

Considering the impossibility of estimating u_{*c} with an accuracy of ±8%, this range is very small. However, if waves of near-critical magnitude are common, this effect must be taken seriously.

D. Sediment transport in Hudson Canyon

I have used the threshold velocities for initiation of sediment motion (calculated in sections B and C and summarized in figure 5-8) to estimate how often the currents we observed in Hudson Canyon were transporting sediment. The results can be checked against geological observations of deposition and erosion in the canyon: Keller et al. (1973) saw sand grains moving along the floor in the canyon head, but found a thick blanket of mud lying passively on the floor at depths of 400 to 1000 m. Measurements of suspended matter in the canyon (Biscaye and Olsen, 1976) indicate that mud is being deposited on this blanket.

Median grain diameters in the head of Hudson Canyon range from .0125 to .006 cm, for critical friction velocities of 1.2 to .92 cm/sec. Our near-floor current record from the canyon head is 274, which was positioned in the outer part of the head (axial depth 350 m) and toward the southwest wall from the canyon axis. Using figure 5-7 and a critical u_* of

1.0 cm/sec, the 10-meter threshold velocity at current meter 274 ranges from 16.5 cm/sec for internal waves of one-hour period to 21.5 cm/sec for semidiurnal oscillations. The currents measured by 274 exceed these threshold speeds only about once a week, down-canyon in direction.

The contradiction between observed ongoing sediment transport in the canyon head and calculated thresholds which usually exceed observed velocities could be resolved in several ways. Instrument 274 landed toward the side of the canyon; axial velocities may be stronger than those we measured. The measured velocity field indicates that high-frequency internal waves and semidiurnal oscillations are roughly equal in amplitude at 274; their nonlinear interaction near the bed should produce higher stresses than the simple analysis indicates (see Grant and Madsen, 1979, for a model of bottom stress in an analogous case: the combination of surface waves and a mean flow). Finally, linear internal wave theory predicts a 50% increase in internal wave energy density between the location of instrument 274 and the shallowest part of the canyon head. Possibly the observations of active sediment motion were in the shallower parts of the canyon. Weekly sediment transporting events as indicated by the 274 data may suffice to keep the sediment sorted in the outer part of the canyon head.

On the mud deposits, Shepard and Cohee (1936, see figure 5-2) report median grain diameters of .003 to .0015 cm, for

critical friction velocities of .75 to .85 cm/sec. Using figure 5-7 and a critical u_* of .8 cm/sec, the 10-meter threshold velocity ranges from 12.5 cm/sec for waves of 1-hour period to 17.5 cm/sec for diurnal oscillations. These speeds were exceeded daily by the oscillations at 315 except during week-long periods at new moon. At instruments 295 and 306, the threshold was exceeded by half the diurnal down--canyon flows during about half of each month, so that 8-hour sediment transporting events should occur about 8 times a month. The only up-canyon currents that exceeded the thresholds were high-frequency spikes, amounting to possibly 8 one-hour sediment-transporting events a month.

Again the observed currents and calculated velocity thresholds contradict geological observations: they predict sediment motion where large quantities of mud are apparently accumulating. This could result from using sediment transport criteria developed for beds of abiotic noncohesive grains, when the actual sediment is bioturbated mud: probably very cohesive. From the geological data, the currents caused by the January storm are the only reasonable prospect for causing sediment transport. If 50 cm/sec is the actual 10-meter steady threshold velocity for initiation of sediment motion, the required friction velocity is 2.2 cm/sec.

The qualitative changes we found in the currents in Hudson Canyon correspond to the sediment zones described by Keller et al. (1973). We found week-long periods of very low

current speeds where mud is apparently being deposited. In the head of the canyon, where the floor is covered with mobile sand, we found high-frequency internal waves to dominate the velocity field. Our analysis indicates that these internal waves increase in amplitude as the floor sediment increases in size toward the canyon head. This correspondence between the current and sediment patterns implies that the currents we observed are responsible for sorting the sediment into zones. Quantitative analysis of this process fails because we cannot estimate the shear stress required to resuspend mud from the central part of the canyon, and because we measured velocity in the canyon head at an unrepresentative location.

E. Internal wave dissipation

Hudson Canyon is an efficient internal wave trap, as discussed in Chapter 3. Internal waves that enter the canyon from the shelf or the deep sea tend to be concentrated near the canyon floor and funnelled into the canyon head. As the waves propagate up the slope, their steepness increases until they break, causing strong near-floor velocities similar to those caused by surface waves breaking at a beach.

In Chapter 3, I estimated that internal waves carry energy into Hudson Canyon at a rate of about 2.5 (10^6) watts, with a residence time of roughly a week. The importance of boundary shear stress in dissipating internal waves is sug-

gested by their concentration near the floor, their creation of large near-floor velocities when they break, and the multiple reflections necessary for internal waves to escape from the canyon. In this section, I will estimate the rate of internal wave dissipation by boundary shear stress.

For fully turbulent boundary layers under simple sinusoidal waves, the boundary shear stress is approximately (see Madsen, 1976):

$$\tau_o = \frac{1}{2} \rho f_w u_b^2 |\cos \omega t| \cos \omega t \qquad (5.5)$$

Ignoring the small phase lag between velocity and stress, the rate of energy dissipation by bottom stress is

$$P_D = \tau_o u = \tau_o u_b \cos \omega t \qquad (5.6)$$

Substituting (5.5) into (5.6) and averaging over time, the mean rate of energy dissipation is found to be

$$\overline{P_D} = \frac{2}{3\pi} \rho f_w u_b^3 \qquad (5.7)$$

As shown in section C, the rough turbulent wave friction factor f_w depends on wave frequency as well as wave amplitude. To estimate the frictional dissipation in Hudson Canyon I used frequencies and amplitudes representative of the near-floor current records to estimate the dissipation occurring in the canyon regions where the current meters were located. In the canyon head, f_w was based on a semidiurnal frequency, which is the strongest frequency in the record from current meter 274, but amplitude u_b was estimated by

assuming the shear stress is sufficient to initiate sediment motion. Below the thermocline, the amplitude and frequency of the dominant tidal oscillations were allowed to change with the phase of the moon. The assumed and calculated values are shown in table 5-II.

The resulting estimate of the rate of internal wave dissipation in Hudson Canyon is 1 (10^6) watts, two fifths of the estimated rate of internal wave influx into the canyon. Both estimates are crude, but they do indicate that boundary shear stress is dissipating a significant portion of the internal waves that are concentrated in Hudson Canyon.

TABLE 5-II
Estimation of internal wave dissipation by bottom stress

Current meter	Ub cm/sec	Frequency rad/sec	Rate of dis. watts/cm2	Fraction of time
295	20	7E-05	6.08705E-07	.25
295	10	7E-05	8.69087E-08	.5
295	1.5	1.4E-04	5.24782E-10	.25

Total dissipation rate (watts/cm2) = 1.95762E-07
Area of floor (km2) = 50.4
Total dissipation in this region (watts) = 98663.9

Current meter	Ub cm/sec	Frequency rad/sec	Rate of dis. watts/cm2	Fraction of time
315	40	1.4E-04	4.86939E-06	.25
315	25	7E-05	1.14093E-06	.5
315	5	7E-05	1.25128E-08	.25

Total dissipation rate (watts/cm2) = 1.79094E-06
Area of floor (km2) = 39.4
Total dissipation in this region (watts) = 705630

Current meter	Ub cm/sec	Frequency rad/sec	Rate of dis. watts/cm2	Fraction of time
274	22	1.4E-04	9.0815E-07	1

Total dissipation rate (watts/cm2) = 9.0815E-07
Area of floor (km2) = 24.1
Total dissipation in this region (watts) = 218864

Dissipation in the whole canyon (watts) = 1.02316E+06

Chapter VI

Conclusions and Suggestions for Further Work

The effects of storms, tides, and incoming internal waves are intensified by the confining, funnel-like bathymetry of Hudson Submarine Canyon. The strong currents which result are apparently in equilibrium with the canyon's morphology and sediment load. The canyon and the processes that occur within it also have noticeable effects on the waters of the shelf and slope and on the shelf-slope front.

Storms that produce strong eastward wind stress in the New York Bight cause upwelling in the upper layers of Hudson Canyon. These upwelling currents can be stronger than those outside the canyon because the upper layers in the canyon are not significantly affected by friction. Prolonged upwelling can displace the deeper layers in the canyon head and cause strong down-canyon currents along the canyon floor.

During storms that produce strong westward wind stress, shelf water downwells into the head of Hudson Canyon. Temporary residence in the canyon head apparently protects some cold pool water from mixing that occurs during these storms.

Interaction between the surface tide and the sloping

canyon floor produces internal tides in Hudson Canyon. In the outer part of the canyon, the near-floor velocity field is dominated by oscillations at tidal periods which vary in amplitude with the phases of the moon. A bottom mixed layer apparently grows during the up-canyon flow (flood tide) because of the instability of the density gradient in the frictional boundary layer. Nonlinear waves are then able to propagate on the interface of the bottom mixed layer and produce high-frequency velocity spikes near the canyon floor. Our current records suggest that these waves are present in the outer part of Hudson Canyon and that they cause significant amounts of bottom stress.

The details of our theory of mixed layer growth and interface wave propagation need to be tested against field measurements with shorter sampling intervals and higher vertical sampling densities. The essential physical conditions are stratification, a sloping floor, and predominantly tidal currents. These conditions may be observed more easily in coastal inlets. Velocity profiles of the tidal boundary layer should be measured at intervals of a few minutes, with concurrent monitoring of the density field. Ideally, the oceanographic instruments used should not alter the turbulent mixing in the layer being measured. Acoustic doppler current meters may be the best choice.

We found that the internal waves that enter Hudson Canyon from the deep sea and from the shelf are concentrated

near the canyon floor and funnelled into the canyon head, consistent with the mathematical theory developed by Wunsch (1969) and McKee (1973) and the kinematic reasoning of Gordon and Marshall (1976). The trapped internal waves are largely dissipated by bottom friction.

High-frequency internal waves are strongest in the head of the canyon where the floor sediment is being actively sorted by grain size: the largest grains are found where the canyon is shallowest so internal waves should be strongest. Our moorings were deployed at the deep end of the canyon head, and landed near the canyon wall instead of on its axis. A more detailed study of the head of the canyon is necessary to fully describe the processes which accompany internal wave breaking and which sort sediment in this region. Ideally, mooring emplacement should be aided by a submersible and currents should be measured within a few meters of the floor.

A layer of mud has been observed to be accumulating on the canyon floor in the region where tidal oscillations dominate the near-floor currents. This is consistent with deposition during the low-amplitude oscillations that occur at new moon. During the rest of the month, the bottom stress in this region regularly exceeded critical values for the movement of noncohesive grains the size of mud. Full understanding of sediment transport in this region of Hudson Canyon requires further work on the conditions necessary to resuspend cohesive bioturbated mud.

A slow mean circulation of slope water through the outer part of Hudson Canyon brings with it low-frequency temperature variations. While the slope water is in the canyon, internal waves and the density instability in the frictional boundary layer apparently cause mixing. The mixed water produces a salinity anomaly at the boundary between Irminger Atlantic water and North Atlantic central water. This anomaly was also observed in Baltimore, Wilmington, Veatch, Hydrographer, and Oceanographer Canyons. Isolated patches of mixed slope water were along the continental slope outside Baltimore, Wilmington, Hudson and Hydrographer Canyons.

The mixed slope water is found within 400 m of the canyon floor, in layers that apparently intrude down the canyon from the floor; this suggests that breaking internal waves may cause the mixing. In Hudson Canyon, breaking internal waves could produce potential energy at a rate of $3(10^5)$ joules/sec. This is easily sufficient to produce the $5(10^8)$ joules of potential energy contained in the mixed slope water.

Appendix A

Hydrographic Data from Oceanus Cruise 34

A hydrographic survey of the submarine canyons of the Middle Atlantic Bight was conducted as part of cruise 34 of R/V Oceanus, September 22 through October 3, 1979. Carl Wunsch was chief scientist.

Conductivity, pressure, temperature, and dissolved oxygen concentration were measured using a Neil Brown CTD with an added Beckman oxygen sensor. These data were converted to salinity, temperature, and oxygen concentration at one-decibar intervals by R. Millard and N. Galbraith of the Woods Hole Oceanographic Institution. The data were calibrated using laboratory comparisons before and after the cruise, oxygen concentrations from shipboard titration of water samples, and salinities based on the conductivities of water samples determined during and after the cruise. The calibrated CTD oxygen values are within 0.05 ml/l and the salinities within 0.02 parts per thousand of those obtained from the water samples.

The locations of the 135 CTD stations are shown in figure A-1. An array of sixty stations surrounds Hudson Canyon, arranged roughly 10 km apart in ten sections that

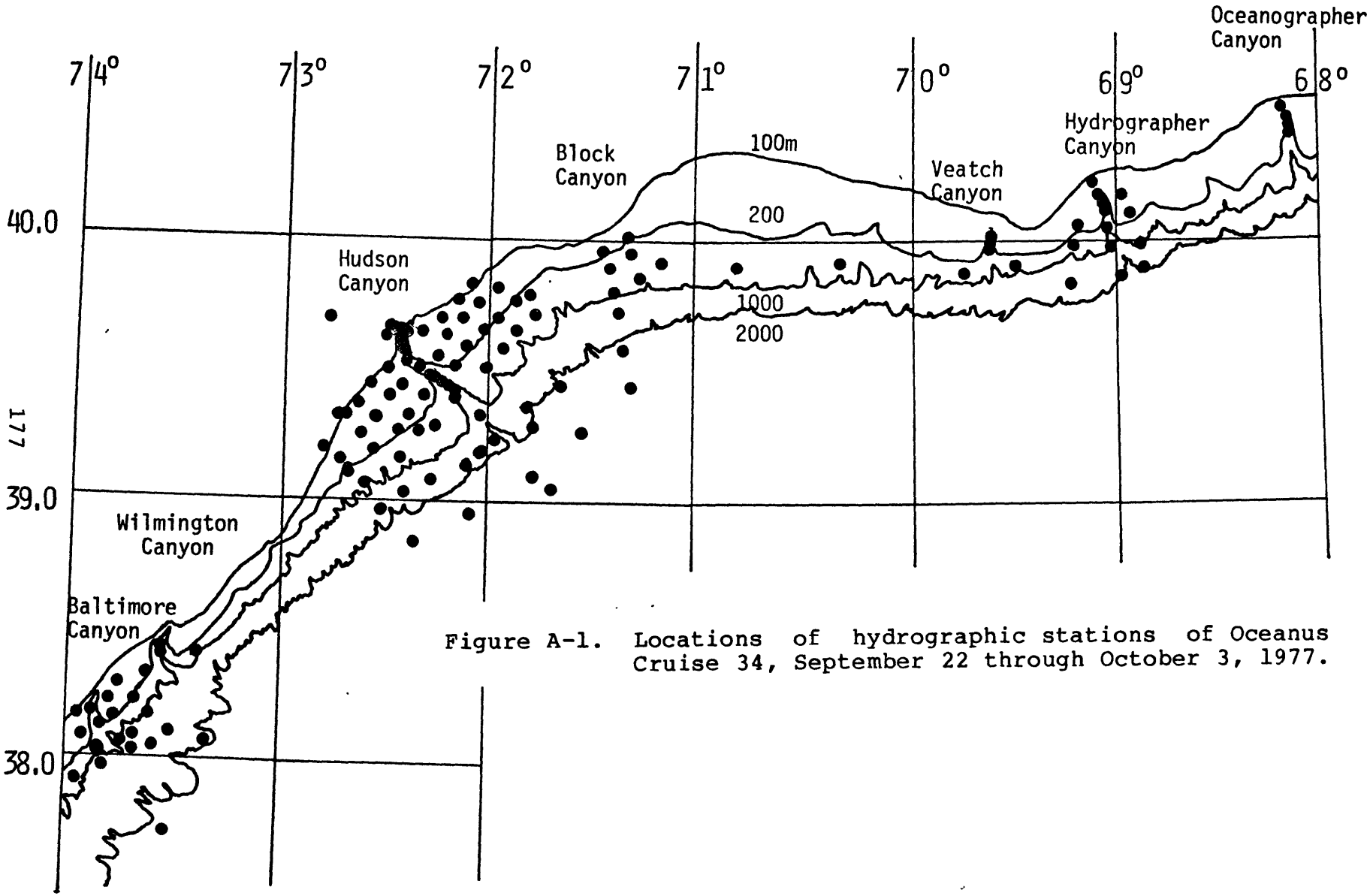

Figure A-1. Locations of hydrographic stations of Oceanus Cruise 34, September 22 through October 3, 1977.

Oceanus Cruise 34 Hydrographic Stations

No.	Depth	Date			Time			Latitude	Longitude
1	1915.0	9	22	77	15	11	38	38.073	73.325
2	2220.0	9	22	77	18	40	31	37.717	73.500
3	790.0	9	23	77	0	22	21	37.908	73.928
4	1465.0	9	23	77	2	42	29	37.967	73.800
5	400.0	9	23	77	5	51	10	38.025	73.833
6	125.0	9	23	77	7	40	57	38.075	73.912
7	115.0	9	23	77	8	37	42	38.163	73.937
8	410.0	9	23	77	9	48	7	38.175	73.867
9	120.0	9	23	77	11	5	0	38.225	73.775
10	270.0	9	23	77	11	48	5	38.150	73.753
11	845.0	9	23	77	12	44	2	38.117	73.825
12	1300.0	9	23	77	14	21	21	38.050	73.725
13	1175.0	9	23	77	16	19	43	38.083	73.667
14	1380.0	9	23	77	18	21	35	38.033	73.660
15	1540.0	9	23	77	20	11	48	38.050	73.567
16	1720.0	9	23	77	21	47	19	38.103	73.500
17	1235.0	9	23	77	23	28	57	38.168	73.583
18	190.0	9	24	77	1	16	21	38.225	73.668
19	115.0	9	24	77	1	58	32	38.280	73.747
20	180.0	9	24	77	2	48	46	38.310	73.612
21	820.0	9	24	77	4	28	6	38.405	73.550
22	680.0	9	24	77	6	20	5	38.422	73.547
23	120.0	9	24	77	8	3	51	38.400	73.370
24	370.0	9	24	77	22	46	41	39.624	72.427
25	120.0	9	24	77	23	56	0	39.650	72.308
26	130.0	9	25	77	0	56	16	39.700	72.220
27	115.0	9	25	77	2	12	22	39.763	72.142
28	105.0	9	25	77	3	38	49	39.820	72.072
29	280.0	9	25	77	6	23	11	39.783	71.800
30	145.0	9	25	77	11	19	59	39.808	71.958
31	135.0	9	25	77	12	30	54	39.752	72.042
32	130.0	9	25	77	13	31	59	39.697	72.125
33	130.0	9	25	77	14	39	41	39.638	72.192
34	130.0	9	25	77	16	14	7	39.550	72.250
35	710.0	9	25	77	17	18	49	39.513	72.322
36	130.0	9	25	77	18	54	36	39.438	72.417
37	130.0	9	25	77	19	40	36	39.392	72.475
38	140.0	9	25	77	20	33	5	39.317	72.542
39	140.0	9	25	77	21	34	37	39.250	72.608
40	115.0	9	25	77	22	17	43	39.317	72.700
41	115.0	9	25	77	23	16	26	39.368	72.625
42	120.0	9	26	77	0	19	52	39.447	72.567
43	120.0	9	26	77	1	22	18	39.505	72.492
44	495.0	9	26	77	2	28	39	39.567	72.417
45	210.0	9	26	77	5	14	.33	39.192	72.550
46	170.0	9	26	77	6	19	0	39.267	72.433
47	160.0	9	26	77	7	2	30	39.333	72.375
48	155.0	9	26	77	7	59	44	39.408	72.312
49	825.0	9	26	77	8	44	6	39.458	72.240
50	215.0	9	26	77	10	3	28	39.517	72.167
51	500.0	9	26	77	21	38	32	39.558	72.427
52	160.0	9	26	77	22	51	33	39.667	72.467
53	160.0	9	27	77	0	33	42	39.585	72.103
54	195.0	9	27	77	1	22	47	39.653	72.015
55	275.0	9	27	77	2	6	34	39.700	71.942
56	240.0	9	27	77	2	56	15	39.763	71.862
57	485.0	9	27	77	3	42	42	39.718	71.777
58	535.0	9	27	77	5	54	25	39.650	71.862
59	575.0	9	27	77	7	20	30	39.583	71.928
60	750.0	9	27	77	8	46	12	39.508	72.000
61	510.0	9	27	77	9	54	29	39.458	72.258
62	1070.0	9	27	77	12	0	7	39.392	72.147
63	380.0	9	27	77	13	42	56	39.288	72.258
64	625.0	9	27	77	14	52	48	39.267	72.325
65	680.0	9	27	77	15	50	24	39.165	72.412
66	925.0	9	27	77	20	12	18	39.117	72.517
67	1380.0	9	27	77	21	37	22	39.033	72.400

No.	Depth	Date			Time			Latitude	Longitude
68	1700.0	9	27	77	23	49	53	39.083	72.258
69	1615.0	9	28	77	2	1	18	39.135	72.100
70	1780.0	9	28	77	3	53	1	39.192	72.008
71	1660.0	9	28	77	5	46	41	39.233	71.950
72	1825.0	9	28	77	7	49	34	39.283	71.767
73	1760.0	9	28	77	10	9	49	39.353	71.792
74	2085.0	9	28	77	12	28	37	39.442	71.642
75	190.0	9	29	77	10	39	12	39.672	72.483
76	95.0	9	29	77	11	45	0	39.625	72.500
77	315.0	9	29	77	12	34	0	39.642	72.442
78	95.0	9	29	77	13	31	35	39.692	72.773
79	270.0	9	29	77	14	10	20	39.650	72.455
80	125.0	9	29	77	15	30	8	39.642	72.392
81	400.0	9	29	77	16	7	31	39.605	72.408
82	505.0	9	29	77	17	7	41	39.575	72.400
83	575.0	9	29	77	18	43	43	39.533	72.400
84	915.0	9	29	77	20	7	17	39.483	72.275
85	950.0	9	29	77	21	29	54	39.463	72.213
86	1360.0	9	29	77	23	21	27	39.413	72.152
87	1925.0	9	30	77	1	15	59	39.330	72.037
88	110.0	9	30	77	5	22	40	39.317	72.717
89	100.0	9	30	77	6	17	29	39.200	72.800
90	130.0	9	30	77	7	0	9	39.158	72.717
91	745.0	9	30	77	7	41	29	39.100	72.667
92	960.0	9	30	77	9	16	37	39.067	72.600
93	1635.0	9	30	77	10	42	13	38.967	72.500
94	2430.0	9	30	77	12	51	0	38.842	72.348
95	2435.0	9	30	77	15	32	36	38.950	72.083
96	2245.0	9	30	77	18	38	32	39.050	71.683
97	2185.0	9	30	77	20	48	43	39.100	71.767
98	2540.0	9	30	77	23	28	59	39.267	71.542
99	2490.0	10	1	77	2	3	18	39.443	71.300
100	2320.0	10	1	77	4	24	14	39.575	71.350
101	1495.0	10	1	77	6	49	18	39.717	71.367
102	960.0	10	1	77	8	34	58	39.792	71.383
103	505.0	10	1	77	10	1	16	39.883	71.408
104	180.0	10	1	77	11	3	30	39.958	71.442
105	200.0	10	1	77	12	3	50	40.025	71.342
106	435.0	10	1	77	13	9	33	39.945	71.302
107	815.0	10	1	77	14	11	31	39.852	71.267
108	540.0	10	1	77	15	12	41	39.918	71.150
109	520.0	10	1	77	17	12	36	39.908	70.775
110	490.0	10	1	77	19	39	51	39.917	70.358
111	475.0	10	1	77	22	35	51	39.875	69.750
112	250.0	10	2	77	1	53	7	40.010	69.607
113	340.0	10	2	77	3	13	16	39.993	69.603
114	520.0	10	2	77	5	8	53	39.967	69.617
115	1350.0	10	2	77	10	23	40	39.900	69.483
116	1160.0	10	2	77	12	18	21	39.900	69.483
117	1650.0	10	2	77	14	23	44	39.833	69.217
118	560.0	10	2	77	16	30	40	39.983	69.200
119	160.0	10	2	77	17	47	47	40.057	69.183
120	160.0	10	2	77	20	4	22	40.225	69.100
121	250.0	10	2	77	21	0	43	40.175	69.075
122	360.0	10	2	77	21	46	59	40.148	69.055
123	420.0	10	2	77	22	52	54	40.130	69.065
124	605.0	10	3	77	0	20	12	40.102	69.050
125	900.0	10	3	77	1	39	7	40.052	69.042
126	1650.0	10	3	77	3	31	36	39.975	69.008
127	2000.0	10	3	77	6	4	59	39.858	68.983
128	1990.0	10	3	77	8	19	35	39.883	68.867
129	1385.0	10	3	77	10	28	4	39.983	68.900
130	175.0	10	3	77	12	41	33	40.108	68.923
131	145.0	10	3	77	13	39	29	40.180	68.960
132	240.0	10	3	77	16	54	1	40.498	68.177
133	325.0	10	3	77	17	55	2	40.428	68.127
134	600.0	10	3	77	18	58	46	40.408	68.125
135	810.0	10	3	77	20	38	45	40.317	68.125

cross the outer continental shelf and slope. Two sections through Hudson Canyon were surveyed several days apart. The other CTD stations cluster around Baltimore, Wilmington, and Hydrographer Canyons and form sections through Block, Veatch and Oceanographer Canyons.

In two regions, one near Wilmington and Baltimore Canyons and the other near Hudson and Block Canyons, the CTD data were interpreted as distributions of water masses defined by temperature-salinity correlations. The composite temperature-salinity diagram for each region was compiled and used to define water masses and their mixtures, using a simplified version of the method developed by Miller (1950). The distribution of water masses is displayed on vertical sections and on charts showing the surface water mass or the locations of stations containing any volume of one of the rarer water masses.

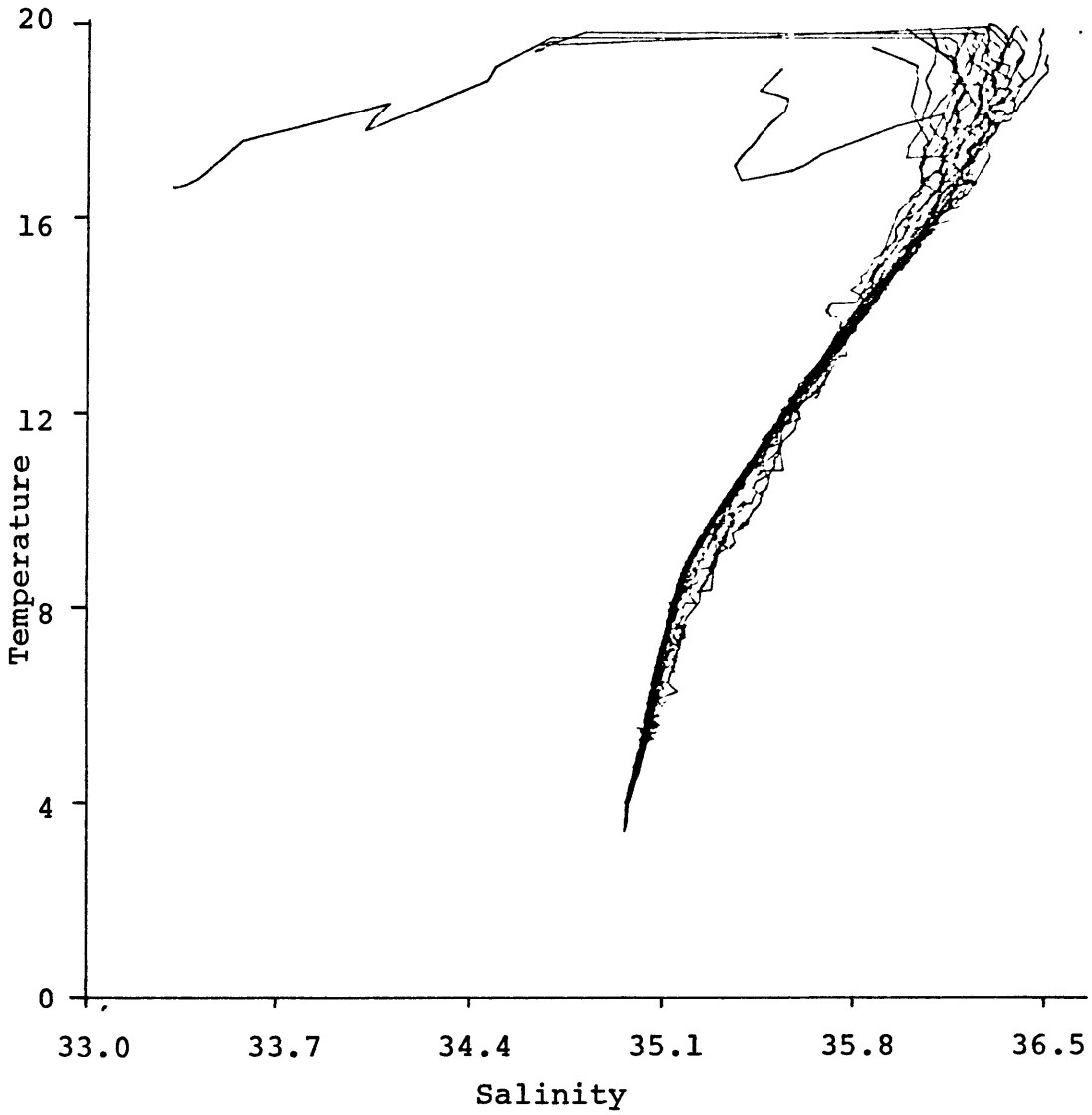

Figure A-2. Composite temperature-salinity diagram for stations 109-135, east of Block Canyon.

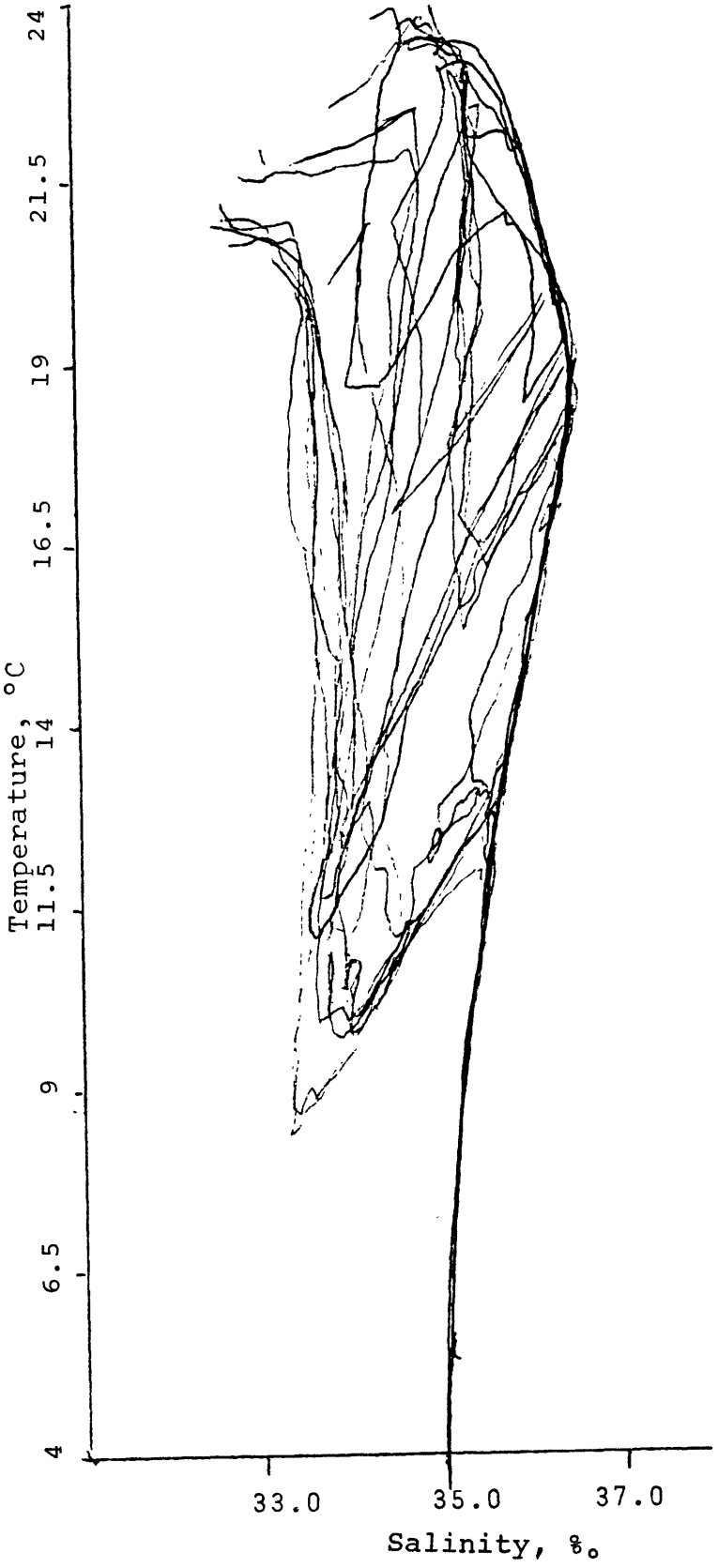

Figure A-3. Composite temperature-salinity diagram for Oceanus 34 data in the region of Baltimore and Wilmington canyons (stations 1-23).

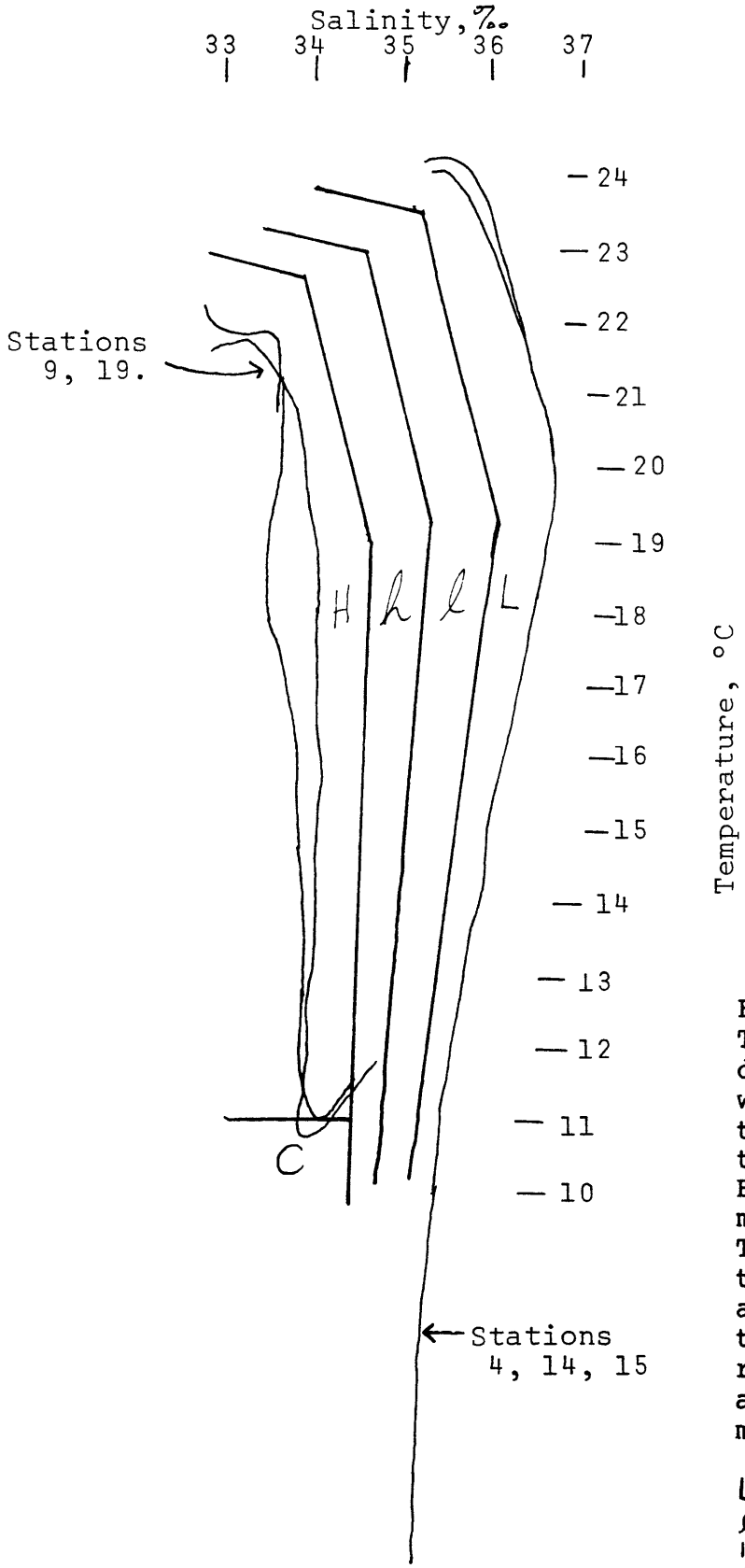

Figure A-4. Temperature-salinity diagram showing the water mass definitions used for stations 1-23, near Baltimore and Wilmington Canyons. T-S curves for extreme shelf water and slope water stations are shown for reference. Abbreviations for water masses are:

L 75-100% slope water
l 50-100% slope water
H 75-100% shelf water
h 50-75% shelf water
C cold pool

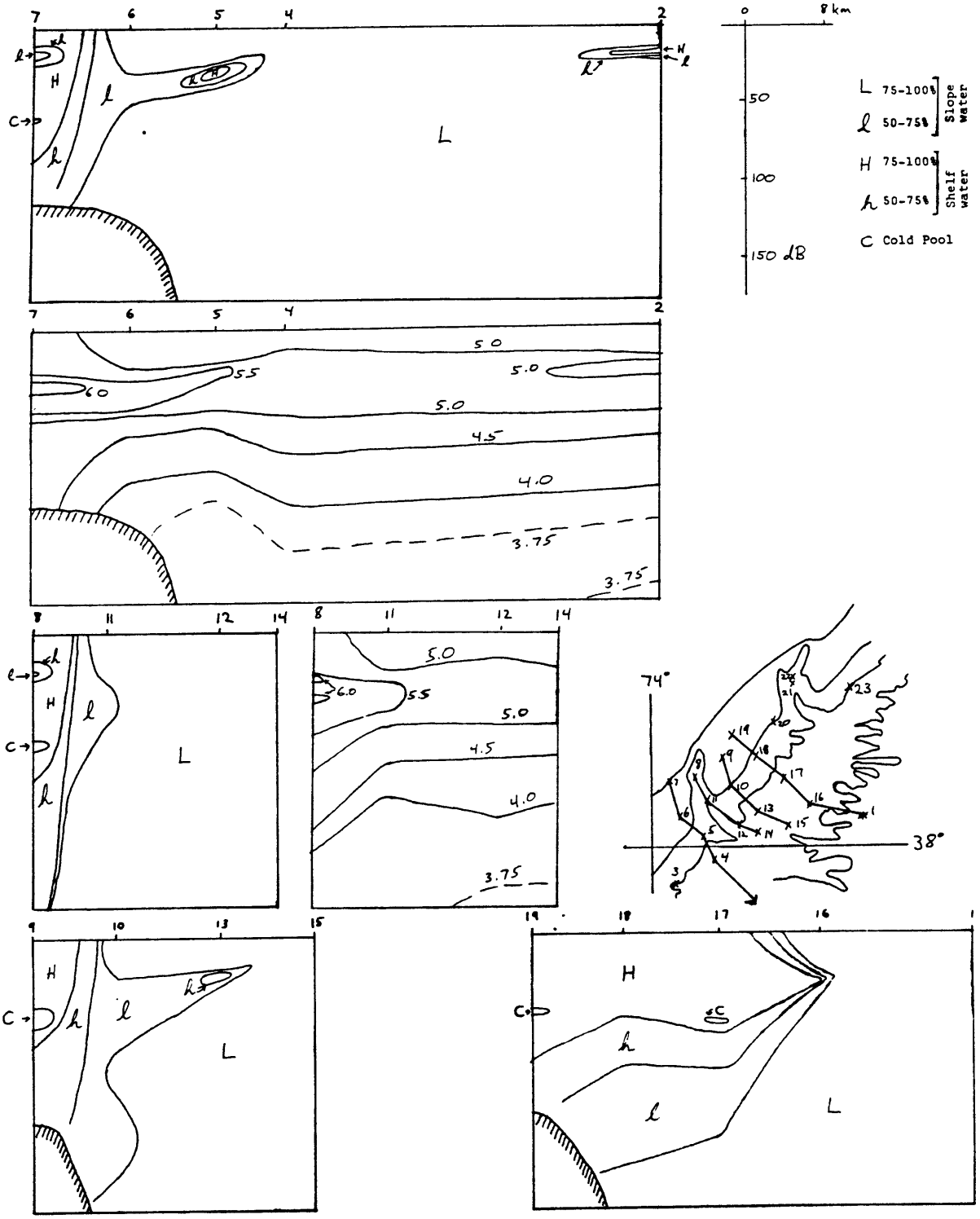

Figure A-5. Sections across the continental slope near Baltimore Canyon showing water masses and oxygen concentration in the top 175 db.

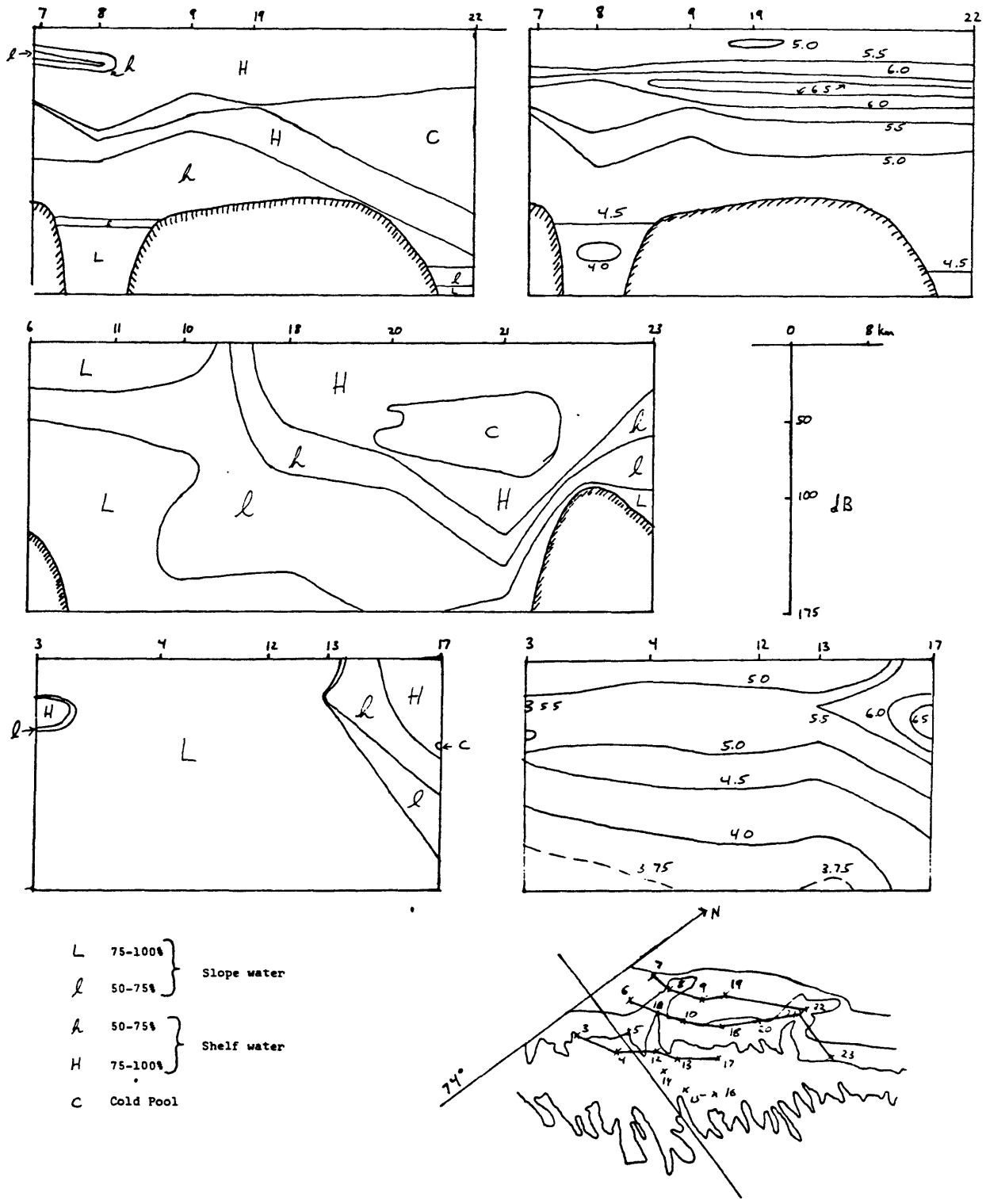

Figure A-6. Sections parallel to the continental slope across Baltimore and Wilmington Canyons showing water masses and oxygen concentration in the top 175 db.

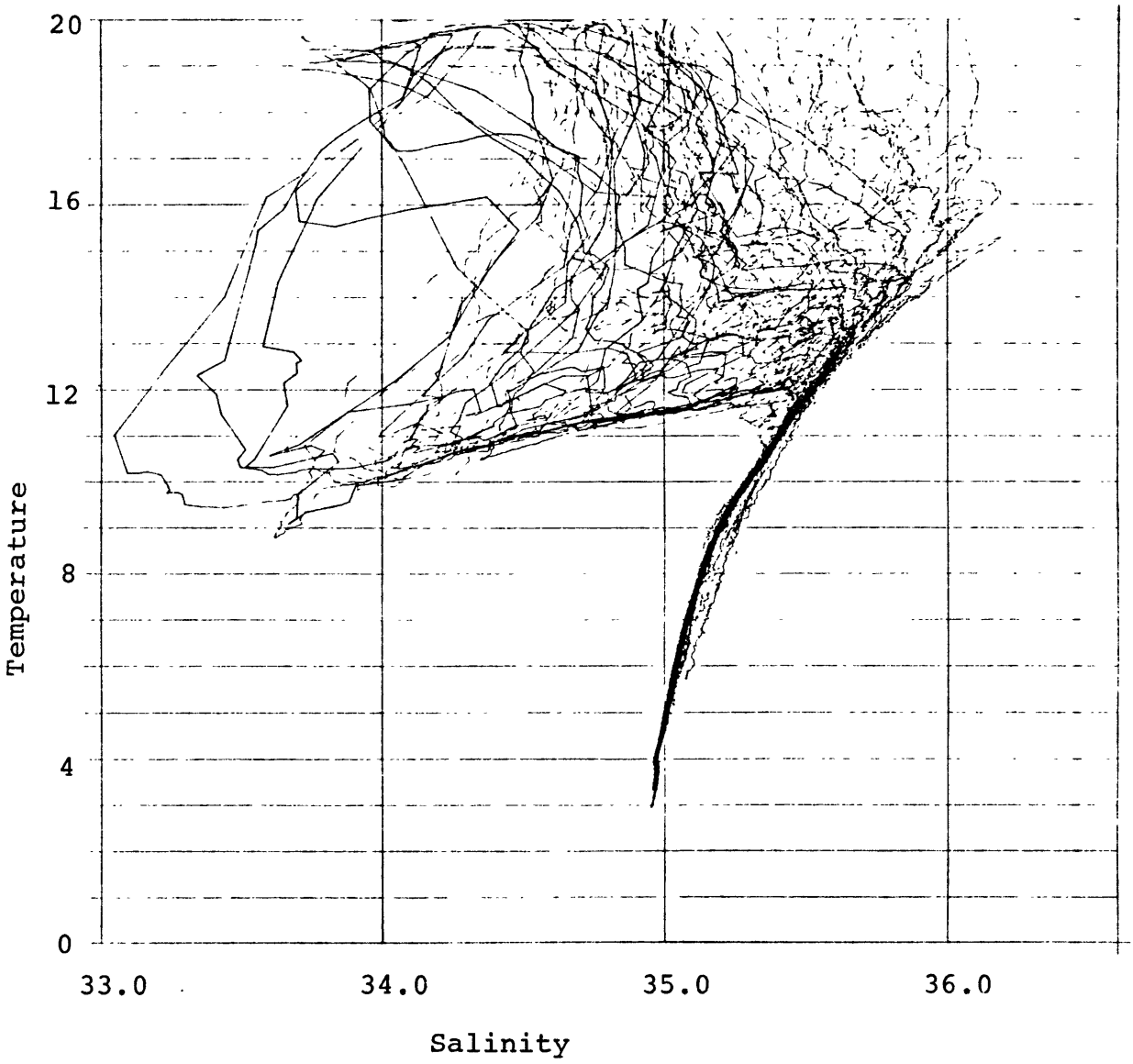

Figure A-7. Composite temperature-salinity diagram for Oceanus 34 data from the region of Hudson and Block Canyons (stations 24-108).

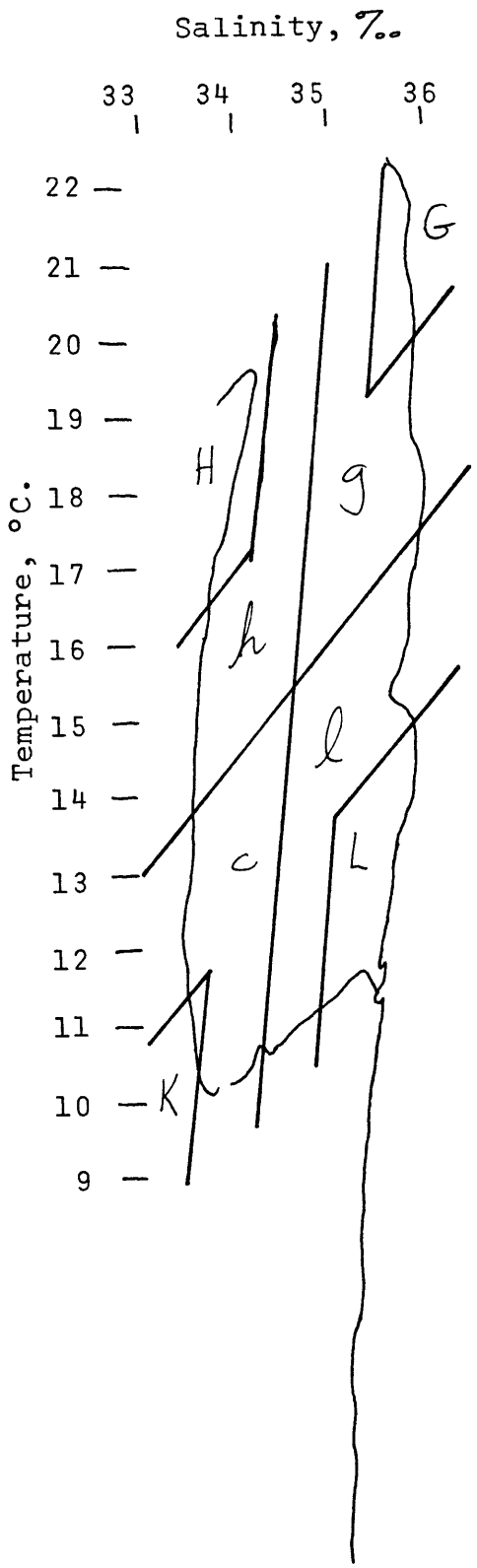

Figure A-8. Temperature-salinity diagram showing the water mass definitions used for stations 24 to 108, near Hudson and Block Canyons. T-S curves for extreme shelf water and slope water stations are shown for reference. Abbreviations for water masses are:

H	75-100%	(surface) shelf water
h	50-75%	
G	75-100%	"Gulf Stream" (surface slope water)
g	50-75%	
K	75-100%	cold pool water
c	50-75%	
L	75-100%	slope water
l	50-75%	

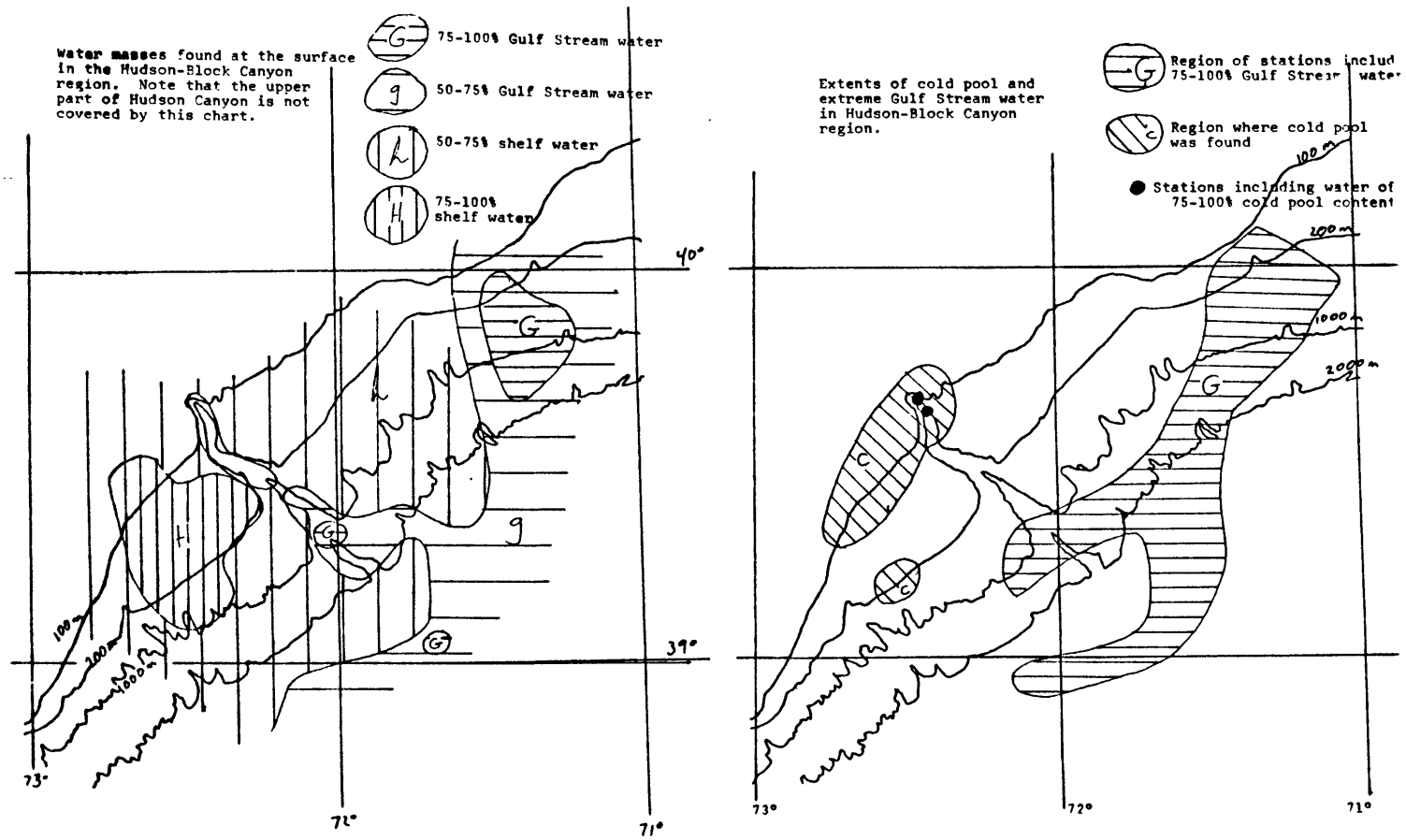

Figure A-9. Charts of the Hudson-Block Canyon region showing (a) surface water masses and (b) the locations of stations where the cold pool water masses or concentrated Gulf Stream water were found.

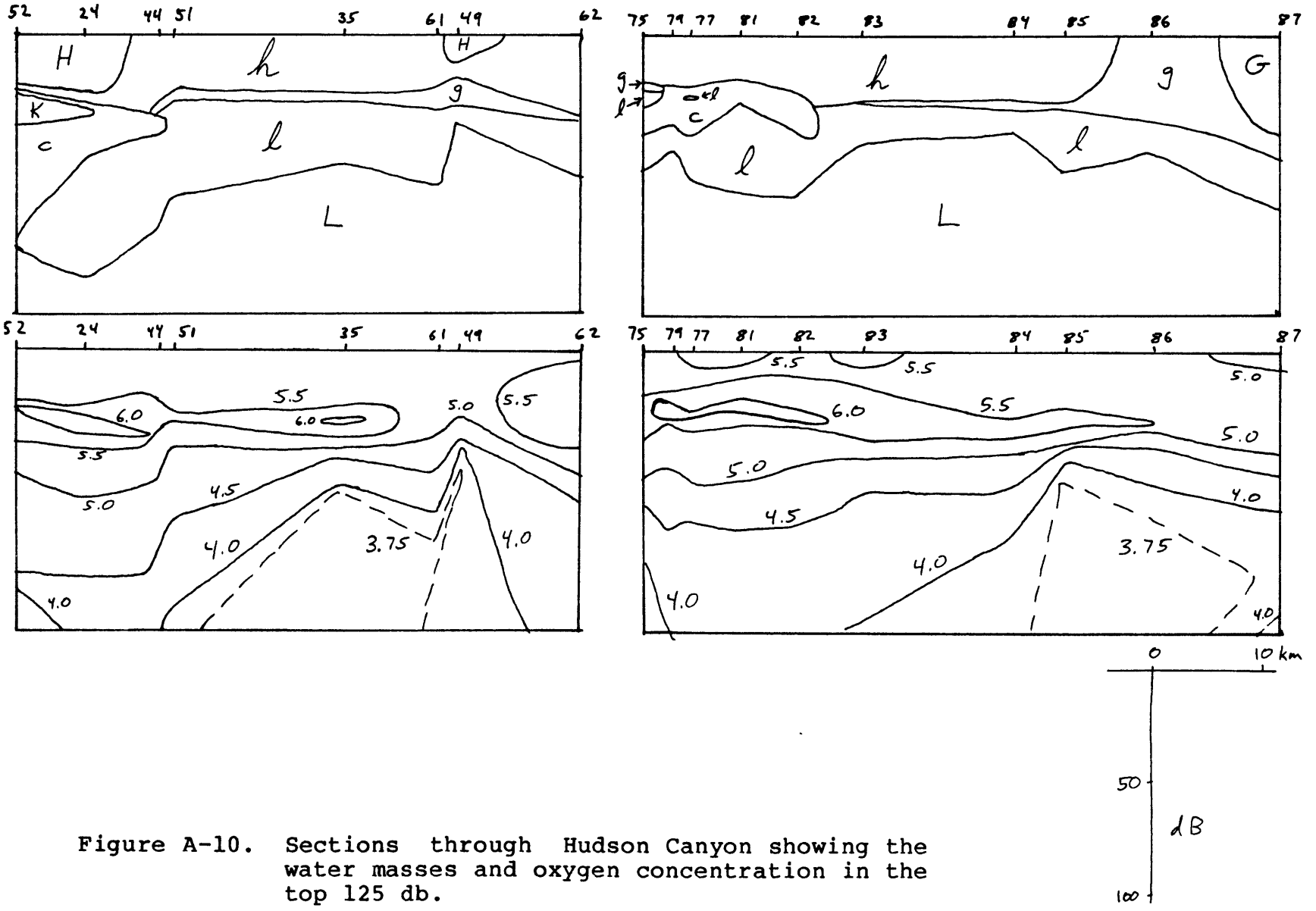

Figure A-10. Sections through Hudson Canyon showing the water masses and oxygen concentration in the top 125 db.

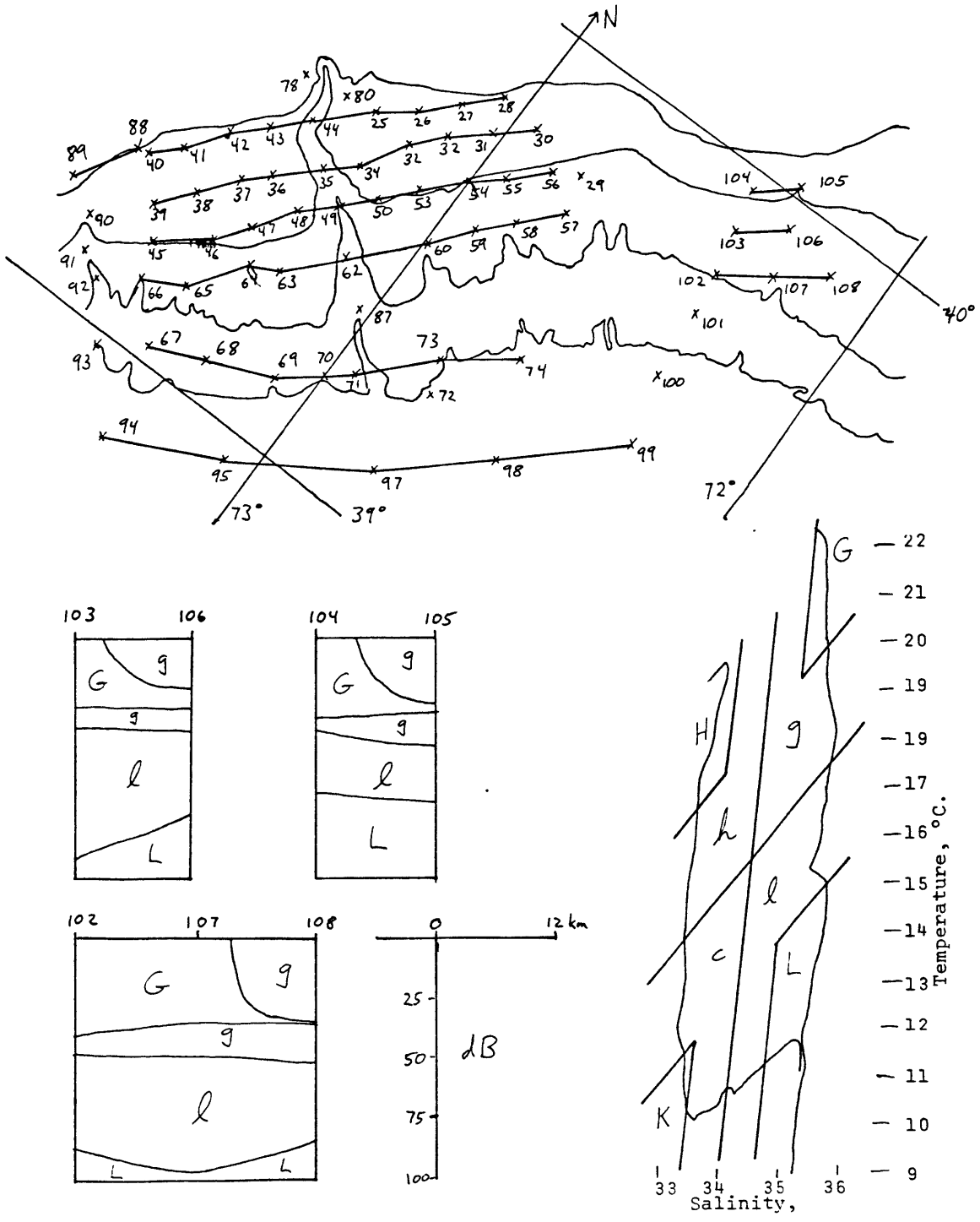

Figure A-11. (a) Key map for along-slope sections across Hudson and Block canyons. (b) Sections across Block Canyon showing water masses of top 100 db. (c) T-S diagram showing definitions of water masses.

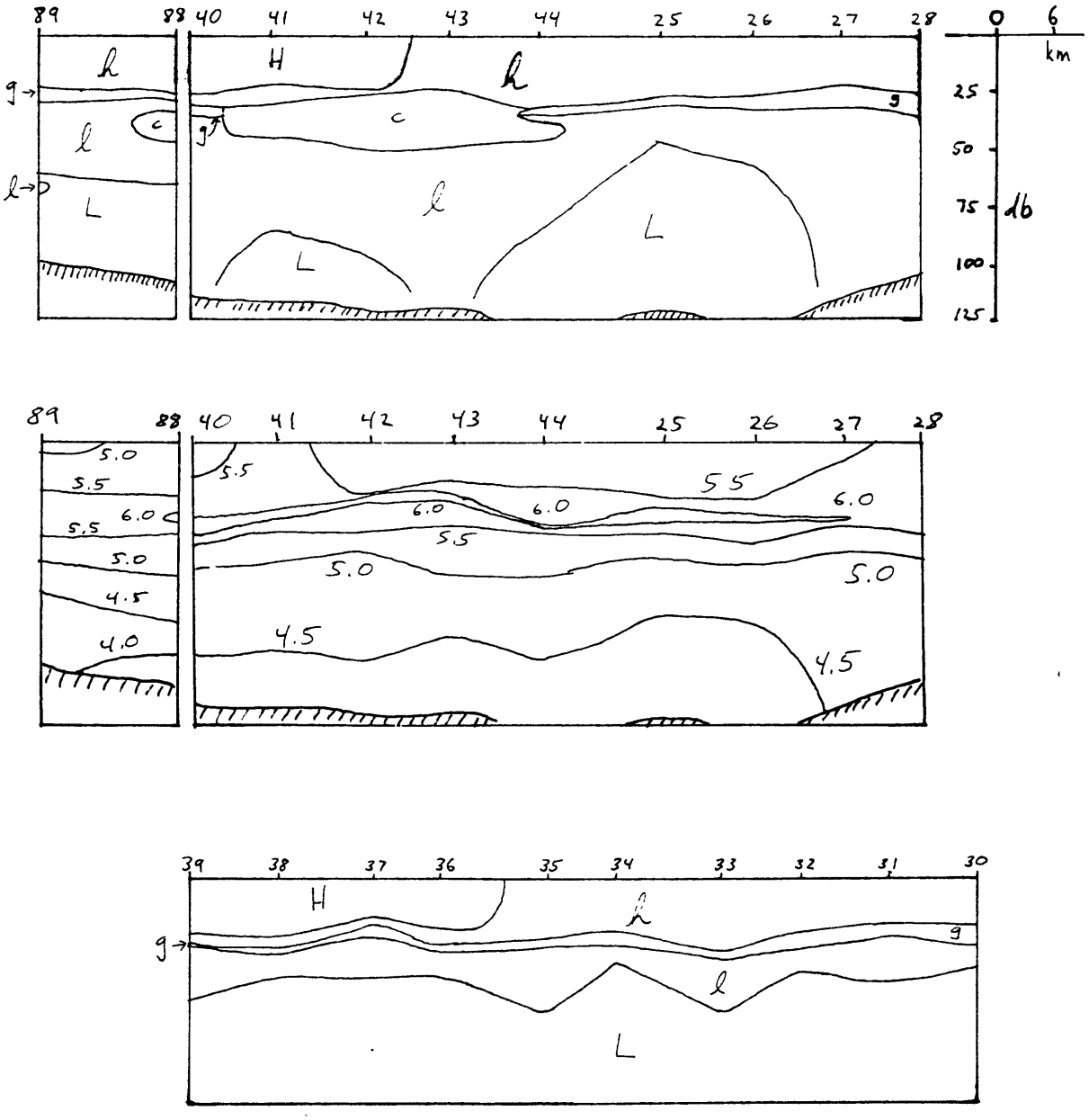

Figure A-12. Sections along the continental shelf across Hudson Canyon showing water masses and oxygen concentration in the top 125 or 100 db.

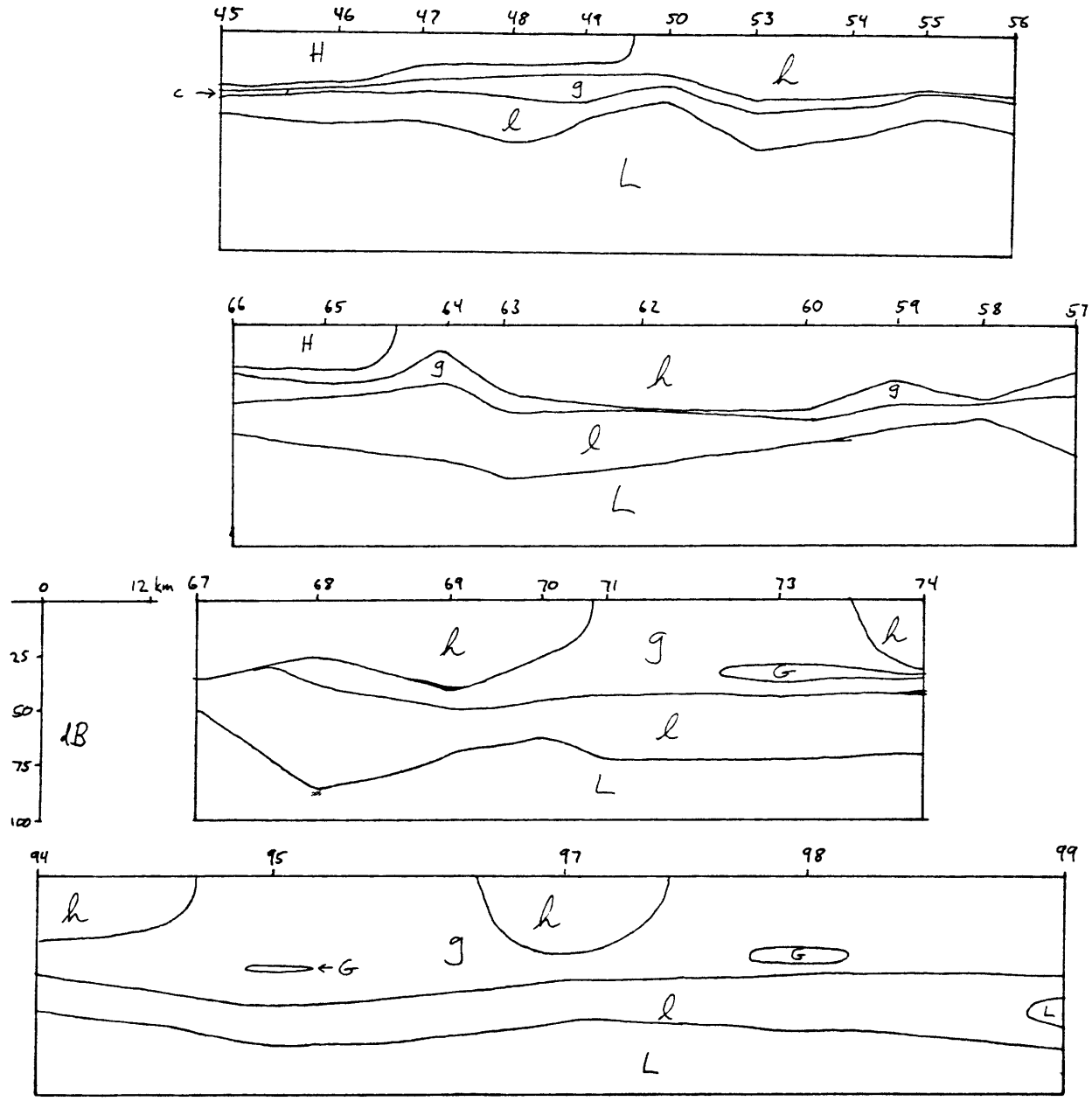

Figure A-13. Sections along the continental slope across Hudson Canyon showing water masses in the top 100 db.

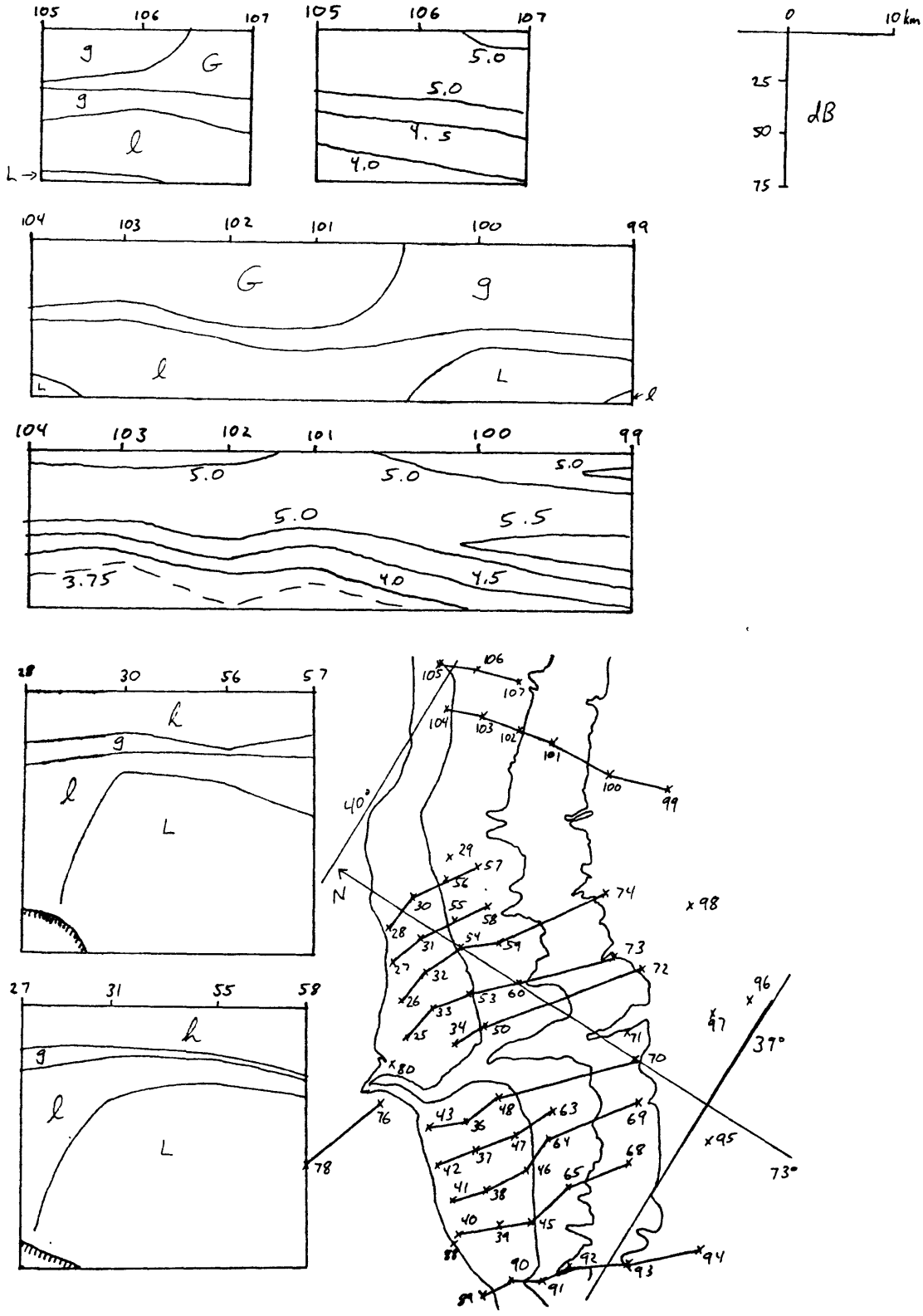

Figure A-14. Sections along Block Canyon and across the continental slope at the northeast end of the Hudson Canyon survey, showing water masses and oxygen concentration in the upper layers.

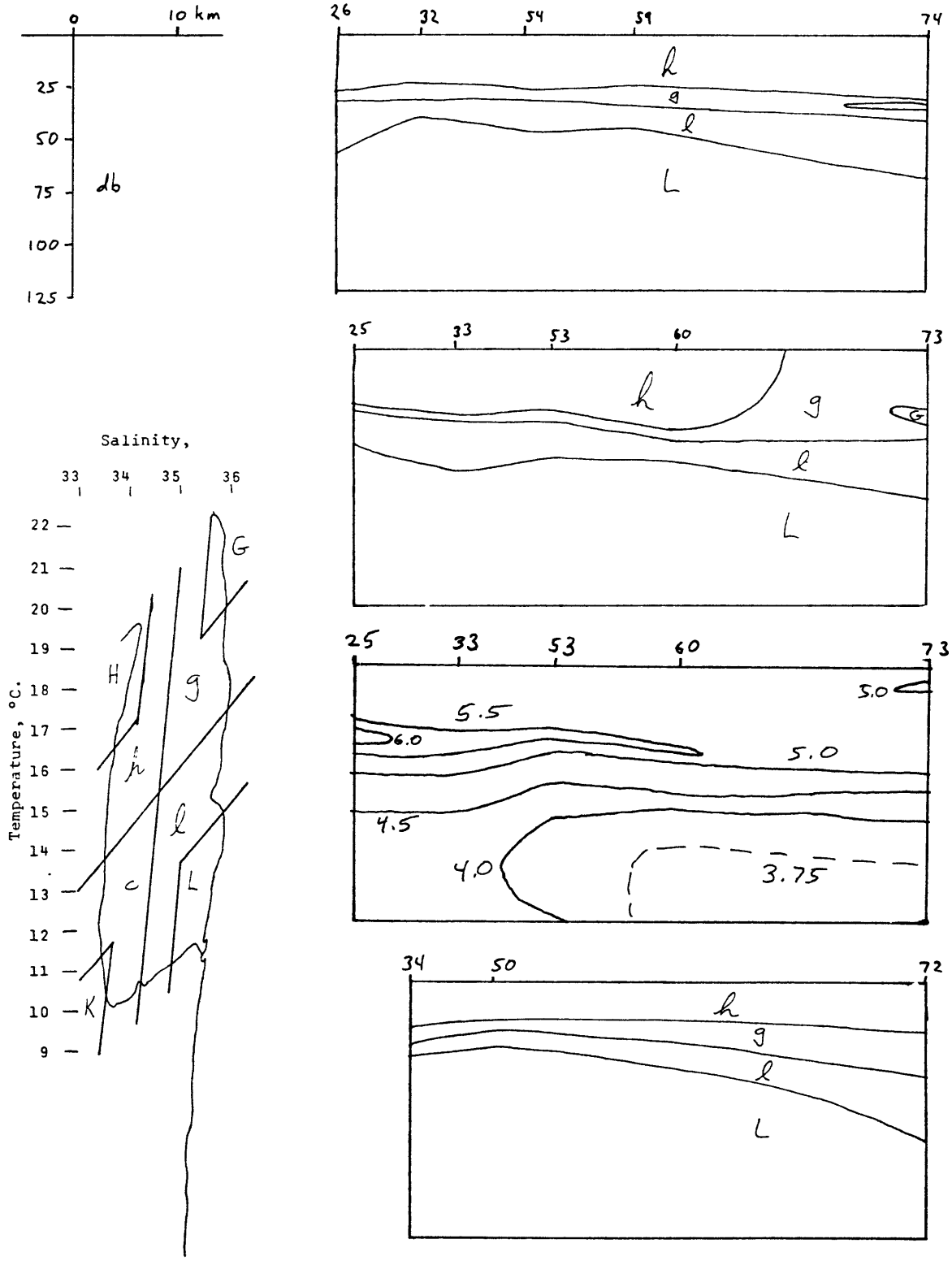

Figure A-15. Sections across the continental slope northeast of Hudson Canyon showing water masses and oxygen concentration in the top 125 db.

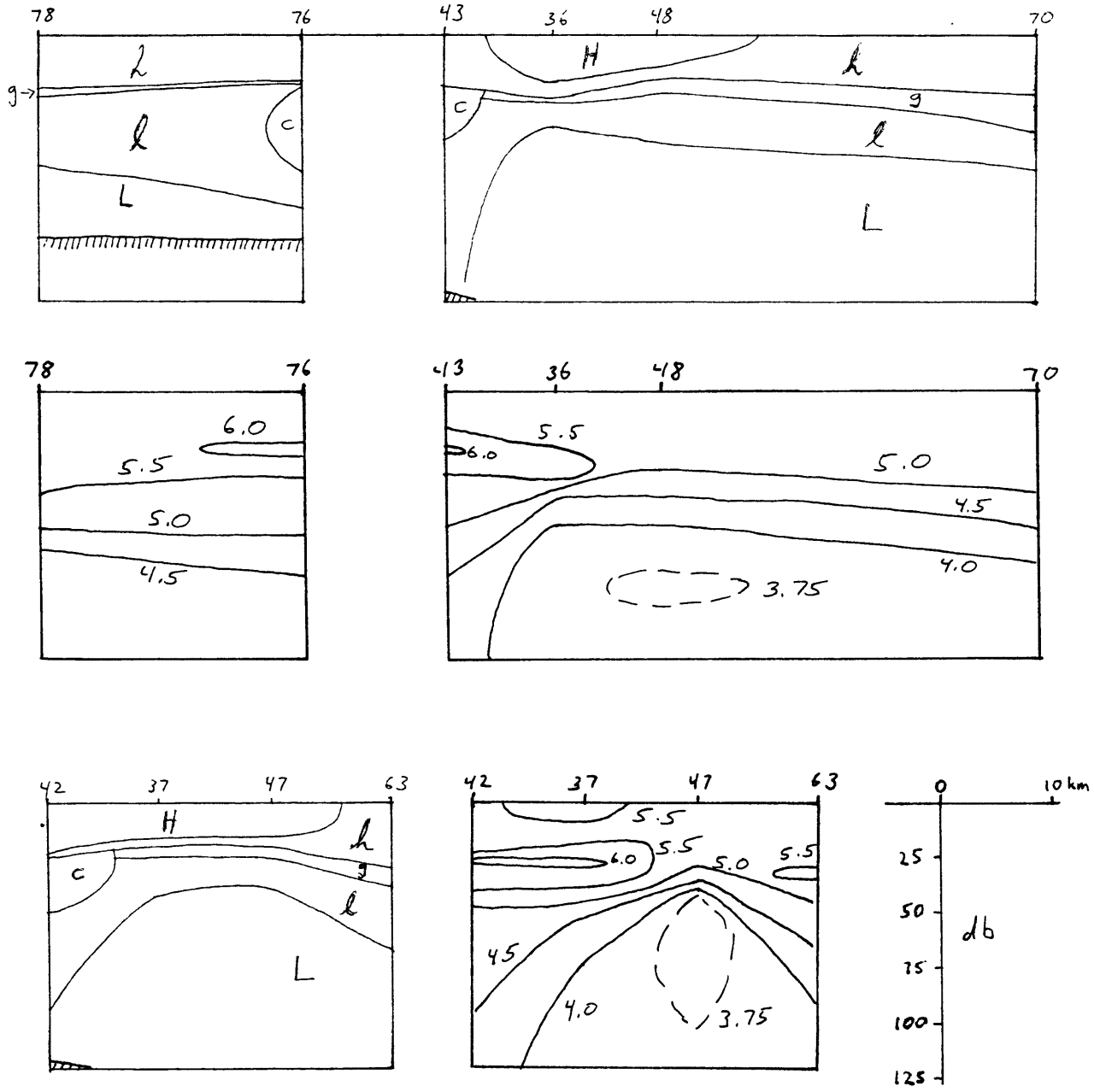

Figure A-16. Sections across the continental slope southwest of Hudson Canyon showing water masses and oxygen concentration in the top 125 db.

Appendix B

Program for Mixed Boundary Layer Under Tidal Flow

This program uses the physics described in Chapter 4. The program is written in Model III Basic for a TRS-80 (Radio Shack) microcomputer and requires 48K of memory. The operator can choose to have velocity and density profiles graphed on the computer's display screen or on a Radio Shack Line Printer VIII or equivalent dot-addressable graphics printer. Graphs are drawn using an assembly language subroutine written by Daniel Hotchkiss.

Variable	(line no. of definition)	Definition
A	(4015)	misc. parameter
	(13020)	misc. parameter
A2	(700)	coefficient in friction sublayer velocity
A3	(12160)	coefficient in mixed layer velocity
A4	(12220)	coefficient in stratified region velocity
B	(13040)	misc. parameter
B2	(710)	coefficient in friction sublayer velocity
B3	(12180)	coefficient in mixed layer velocity
B4	(12240)	coefficient in stratified region velocity
BI	(10100)	Kelvin function bei(Y)
BR	(10080)	Kelvin function ber(Y)
C	(2940)	cos(Z)
	(12140)	cosine of scaled velocity at top of friction sublayer
C2	(720)	coefficient in friction sublayer velocity
C3	(730)	coefficient of friction in force balance on mixed layer
CT		coth(kh)
D		density array
D0	(360)	base density
D1	(400)	initial density change at top of mixed layer
DD!		density gradient array (single precision)
DM		maximum density
DN		minimum density
DS	(8160)	density scale for line printer graphs

Variable	(line no. of definition)	Definition
EP	(12020)	effective viscosity in mixed layer
ER	(13060)	accuracy of critical K-H wave number solution
FR	(2255)	Froude number
FW	(310)	wave friction factor
G	(340)	acceleration of gravity
I		iteration counter in loops, usually subscript of density or velocity array
I0	(520)	subscript of array members at top of mixed layer
I1	(3120)	subscript of array members at bottom of friction sublayer
I2	(3200)	subscript of array members at top of friction sublayer
IP0	(5160)	previous I0
J		iteration counter in graphing loops
K1,K2,K3		trial values of K-H critical wave number
K9		position of screen plot labels
KD	(13080)	wave-number increment in K-H critical wave number solution
KI	(10140)	Kelvin function kei(Y)
KK		critical wave number for K-H instability
KR	(10120)	Kelvin function ker(Y)
KS	(260)	equivalent sand roughness
L	(330)	friction sublayer length scale

Variable	(line no. of definition)	Definition
L3	(12050)	inverse mixed layer length scale
L4	(250)	inverse stratified region length scale
MI	(11440)	misc. parameter
MX	(480)	size of velocity and density arrays
N	(380)	Brunt-Vaisala frequency of initial state
NN	(390)	along-floor density gradient
NU	(200)	effective viscosity in stratified region
PL	(11420)	misc. parameter
Q	(60)	parameter controlling output mode
R	(4160)	gradient Richardson number
RE	(300)	wave Reynolds number
S	(2960)	sin(Z)
	(12120)	sine of scaled velocity at top of friction sublayer
S1		depth-integrated velocity in mixed layer
T0	(3540)	bottom stress
TH	(12040)	misc. parameter
U		velocity array
U1	(8140)	velocity scale for line-printer graphs
UD		velocity gradient
UM		velocity maximum
UN		velocity minimum
US	(320)	maximum wave friction velocity
UU	(2980)	velocity outside boundary layer
V	(180)	amplitude of velocity outside boundary layer

Variable	(line no. of definition)	Definition
W	(240)	frequency of velocity outside boundary layer
X	(3040,8280,12200)	misc. depth parameter
X0	(220,5380)	depth of mixed layer
XP0	(4010)	previous X0
XR	(460)	depth range
XS	(510)	depth increment, range divided by array size
XX	(3380,3480,11400)	misc. depth parameter
Y		argument of Kelvin functions or misc. parameter
Y1,Y2,Y3		trial discriminants in K-H critical wave number solution
Y2	(10040)	misc. parameter
Y4	(10060)	misc. parameter
Z		non-dimensional time
Z0	(280)	height of bottom boundary condition
ZD	(420)	non-dimensional time increment
ZM	(440)	non-dimensional end time

Main Program Listing

```
1 DEFINT I, J, Q
2 DEFDBL D
10 PRINT "INPUT  NUMBER OF DESIRED OUTPUT OPTION : "
20 PRINT
30 PRINT "1. LIST OF PARAMETERS ONLY"
40 PRINT "2. SCREEN PLOTS"
50 PRINT "3. PRINTER PLOTS"
60 INPUT Q
70 IF Q = 3 THEN PRINT "IS GRAPHING PROGRAM IN MEMORY????"
80 LPRINT CHR$(30)
100 '**********
120 '**********  Program to calculate mixing of a
140 '**********  bottom boundary layer under tidal flow
160 '**********              FSH   4-1-82
175 '**********  Set parameters
180 V =  - 15
200 NU = 10
220 X0 = 800
240 W = 1.4E - 4
250 L4 = SQR(W/2/NU)
260 KS = 3
280 Z0 = KS/30
300 RE = V*V/W/.014
310 GOSUB 14000
320 US = ABS(V*SQR(FW/2))
330 L = .4*US/W
340 G = 981
360 D0 = 1.027
380 N = 6.28/3600
390 NN = D0*.02*N*N/G
400 D1 = X0*N*N*D0/G/2
420 INPUT "Non - dim size of time step"; ZD
440 INPUT "Start time  =  0. End time"; ZM
460 INPUT "Depth range in cm."; XR
480 IF Q = 3 THEN MX = 419 ELSE MX = 109
500 DIM U(MX), D(MX), DD!(MX)
510 XS = XR/MX
520 I0 = INT(X0/XS) + 1
660 Y = 2*SQR(Z0/L)
680 GOSUB 10000
700 A2 = KR
710 B2 = KI
720 C2 = KR*KR + KI*KI
730 C3 = .4*US*Z0/XS
1000 '**********  Initialize density array
```

```
1020 Z =  - ZD
1040 FOR I = 0 TO MX
1100 IF I<I0 THEN D(I) = D1 + D0 - NN*50*X0 : DD!(I) = 0 :
GOTO  1140
1120 D(I) = D0 - NN*50*I*XS
1130 IF I>I0 THEN DD!(I) =  - 50*NN
1140 NEXT I
1150 DD!(I0) =  - D1/XS
1160 IF Q = 0 THEN GOTO  1380
1180 LPRINT "Boundary layer under tide on gently sloping
canyon floor"
1190 LPRINT
1200 LPRINT "Floor slope  =  0.02"
1210 LPRINT "Initial stratification : "
1220 LPRINT , "BV frequency above mixed layer        N = ";
N; " rad/sec"
1230 LPRINT , "Depth of mixed layer                 X0 = ";
X0; " cm"
1240 LPRINT , "Density change at mixed layer top    D1 = ";
D1
1250 LPRINT , "Density at floor (g/cm3)           D(0) = ";
D(0)
1260 LPRINT
1270 LPRINT "Velocity imposed outside boundary layer : "
1280 LPRINT , "Amplitude            V = "; V, "cm/sec"
1290 LPRINT , "Frequency            W = "; W, "rad/sec"
1300 LPRINT , "Effective viscosity NU = "; NU, "cm2/sec"
1310 LPRINT
1320 LPRINT "Frictional boundary layer : "
1330 LPRINT , "Wave friction velocity (u*)  US = "; US,
"cm/sec"
1340 LPRINT , "Coefficients of ker and kei  A2 = "; A2
1350 LPRINT , "                             B2 = "; B2
1360 LPRINT , "                             C2 = "; C2
1370 LPRINT , "Depth scale                   L = "; L, "cm"
1380 LPRINT  : GOTO  12000
1400 IF Q <> 3 GOTO  2900
1420 DEFUSR 0 = &HFF00
1460 FOR I =  - 28 TO  - 16STEP2
1480 POKE I, 0
1500 POKE I + 14, 1
1520 NEXT I
1540 FOR I = 0 TO 6
1560 POKE ( - 36 + I), 2[I
1580 NEXT I
1600 GOTO  2900
2000 '**********  Display results
2010 IF Q = 0 GOTO  2900
2020 UN = U(0) : UM = UN
2040 DN = D(0) : DM = DN
2080 FOR I = 1 TO MX
```

```
2100 IF U(I)<UN THEN UN = U(I)
2120 IF U(I)>UM THEN UM = U(I)
2140 IF D(I)<DN THEN DN = D(I)
2160 IF D(I)>DM THEN DM = D(I)
2180 NEXT I
2200 LPRINT "Time  =  "; Z; " rad.,  or "; Z/W/3600; "
hours."
2210 LPRINT
2220 LPRINT "At floor, ", "stress            T0 = "; T0,
"dyne/cm2"
2230 LPRINT , "friction velocity U* = ";
SQR(ABS(T0)/D(0))*SGN(T0), "cm/sec"
2240 LPRINT , "density         D(0) = "; D(0), "g/cm3"
2250 LPRINT  : Y = .02*G*(D(0) - D(I0))/D(I0) - C3*U(1)/X0 +
W*V * COS(Z)
2255 FR = S1/I0/SQR(ABS(G*(D(0) - D(I0)))/D(I0)*X0)
2260 LPRINT "At top of mixed layer,  Fr = "; FR
2270 LPRINT "       linear wave speed  = "; S1/I0/FR, ,
"cm/sec"
2280 LPRINT "       density change  = "; D(0) - D(I0),
"g/cm3"
2282 IF KK < 1E-6 THEN LPRINT "K-H instab. at wavelengths as
large as 6283.185 m." : GOTO  2290
2285 IF KK < 1E6 THEN LPRINT "       max wavelength of K-H
instab.  = "; 6.283185/KK/100; "  m." : GOTO  2290
2287 LPRINT "No K-H instab. at wavelengths over 6.283185 cm."
2290 LPRINT "Average velocity in mixed layer  = "; S1/I0,
"cm/sec"
2300 LPRINT "Force per unit mass on mixed layer  = "; Y,
"cm/sec2"
2305 LPRINT
2310 LPRINT "Far from floor,  velocity is V*sin(wt) = "; UU;
" cm/sec"
2313 LPRINT "Depth range,  0 to "; XR; " cm."
2315 LPRINT
2317 IF Q = 3 THEN GOTO  8000
2320 LPRINT "Velocity Min,  Max : "; UN, , UM; "   cm/sec"
2340 LPRINT "Density Min,  Max : "; DN, DM; "   g/cm3"
2380 LPRINT
2400 ON Q GOTO  2900, 7000, 8000
2900 Z = Z + ZD
2920 IF Z>ZM THEN LPRINT "DONE" : GOTO  9000
2940 C = COS(Z)
2960 S = SIN(Z)
2980 UU = V*S
3000 '**********  Calculate velocity profile
3020 FOR I = 0 TO I0
3040 X = I*XS
3060 IF X>Z0 THEN GOTO  3120
3080 U(I) = 0
3100 NEXT I
```

```
3120 I1 = I
3180 S1 = 0
3200 I2 = I0/6
3220 FOR I = I1 TO I2
3260 Y = 2 * SQR(I*XS/L)
3280 GOSUB 10000
3300 U(I) = UU*(1 - (A2*KR + B2*KI)/C2)
3320 S1 = S1 + U(I)
3340 NEXT I
3360 FOR I = I2 + 1 TO I0 - 1
3380 XX = I*XS*L3
3400 U(I) = UU + (S*(A3 * COS(XX) + B3 * SIN(XX)) + C*(B3 *
COS(XX) - A3 * SIN(XX))) / EXP(XX)
3420 S1 = S1 + U(I)
3440 NEXT I
3460 FOR I = I0 TO MX
3480 XX = I*XS*L4
3500 U(I) = UU + (S*(A4*COS(XX) + B4*SIN(XX)) + C*(B4*COS(XX)
- A4*SIN(XX)))/EXP(XX)
3520 NEXT I
3540 T0 = D(0)*FW/2*UU*ABS(UU)
4000 '**********  Calculate density profile before mixing,
4005 '**********  layer depth
4010 XP0 = X0
4015 A = ZD/W*NN
4020 FOR I = 0 TO MX
4040 GOSUB 11000
4100 D(I) = D(I) - A*U(I)
4120 DD!(I) = DD!(I) - A*UD
4140 IF ABS(UD)<1E - 19 THEN GOTO  4240
4160 R =  - G*DD!(I)/D(I)/UD/UD
4180 IF R >= 1 THEN GOTO  4240
4200 I0 = I + 1
4220 X0 = I0*XS
4240 NEXT I
5000 '**********  Calculate density after mixing
5020 FOR I = 1 TO I0 - 1
5040 D(0) = D(0) + D(I)
5060 NEXT I
5080 D(0) = D(0)/I0
5090 DD!(0) = 0
5100 FOR I = 1 TO I0 - 1
5120 D(I) = D(0)
5130 DD!(I) = 0
5140 NEXT I
5160 IP0 = I0
5180 '**********  Check for stability after each round of
5190 '**********  mixing
5200 FOR I = 0 TO MX
5220 GOSUB 11000
5280 IF I = I0 THEN DD!(I) = (D(I) - D(I - 1))/XS
```

```
5300 IF ABS(UD)<1E - 19 THEN GOTO  5400
5320 R =  - G*DD!(I)/D(I)/UD/UD
5340 IF R> = 1 THEN GOTO  5400
5360 I0 = I + 1
5380 X0 = I0*XS
5400 NEXT I
5420 IF I0 = IP0 THEN GOTO  6000
5500 GOTO  5020
6000 IF X0 <> XP0 THEN GOTO  12000
6020 IF Q <> 3 THEN GOTO  6100
6040 FOR I = 1 TO 7
6060 LPRINT
6080 NEXT I
6100 GOSUB 13000
6520 GOTO  2000
7000 '**********  Plot U,D on screen
7020 CLS
7040 FOR I = 0 TO 109
7060 J = (UM - U(I))*47/(UM - UN)
7080 SET(I, J)
7100 NEXT I
7120 K9 = 64*INT(J/3) + 54
7140 PRINT@ K9, "U";
7160 FOR I = 0 TO 109
7180 J = (DM - D(I))*47/(DM - DN)
7200 SET(I, J)
7220 NEXT I
7240 K9 = 64*INT(J/3) + 56
7260 PRINT@ K9, "D";
7280 GOTO  2900
8000 '**********  Plot U,D on printer
8020 LPRINT TAB(15) "Velocity"; TAB(45) "Density"
8040 LPRINT TAB(5) UN; TAB(30) UM; TAB(40) DN; TAB(60) DM;
CHR$(18)
8060 LPRINT CHR$(27); CHR$(16); CHR$(0); CHR$(30); CHR$(255);
8080 LPRINT CHR$(27); CHR$(16); CHR$(0); CHR$(210);
CHR$(255);
8100 LPRINT CHR$(27); CHR$(16); CHR$(1); CHR$(15); CHR$(255);
8120 LPRINT CHR$(27); CHR$(16); CHR$(1); CHR$(195); CHR$(255)
8140 U1 = 180/(UM - UN)
8160 DS = 180/(DM - DN)
8180 FOR I = MX TO 0 STEP - 7
8200 FOR J = 0 TO 6
8220 POKE( - 29 + 2*J), INT((U(I - J) - UN)*U1) + 30
8240 POKE( - 15 + 2*J), INT((D(I - J) - DN)*DS) + 15
8260 NEXT J
8280 X = USR0 (0)
8300 NEXT I
8320 FOR I = 1 TO 4
8340 LPRINT
8360 NEXT I
```

```
8380 LPRINT CHR$(30)
8700 GOTO  2900
9000 IF Q = 2 THEN GOTO  9000  ELSE  STOP
10000 '**********  Calculate Kelvin functions of Y
10020 IF Y < 0 OR Y > 8 THEN PRINT "Argument of Kelvin
functions out of range :  Y = "; Y : STOP
10040 Y2 = Y*Y/64
10060 Y4 = Y2*Y2
10080 BR = 1 + Y4*( - 64 + Y4*(113.778 + Y4*( - 32.363 +
Y4*(2.642 - Y4*.083))))
10100 BI = Y2*(16 + Y4*( - 113.778 + Y4*(72.818 + Y4*( -
10.568 + Y4*(.522 - Y4*.011)))))
10120 KR =  - LOG(Y/2)*BR + .7854*BI - .577 + Y4*( - 59.058 +
Y4*(171.363 + Y4*( - 60.61 + Y4*(5.655 - Y4*.196))))
10140 KI =  - LOG(Y/2)*BI - .7854*BR + Y2*(6.765 + Y4*( -
142.918 + Y4*(124.236 + Y4*( - 21.301 + Y4*(1.175 -
Y4*.027)))))
10160 RETURN
11000 '**********  Calculate velocity gradient
11020 IF I + 1 < I1 THEN UD = 0 : RETURN
11040 IF I>I2 THEN GOTO  11400
11060 UD = (U(I + 1) - U(I))/XS
11080 RETURN
11400 IF I>I0 THEN XX = I*XS*L4 ELSE XX = I*XS*L3
11420 PL = COS(XX) + SIN(XX)
11440 MI = COS(XX) - SIN(XX)
11460 IF I>I0 THEN UD = L4/EXP(XX)*(S*(MI*B4 - PL*A4) -
C*(MI*A4 + PL*B4)) : RETURN
11480 UD = L3/EXP(XX)*(S*(MI*B3 - PL*A3) - C*(MI*A3 + PL*B3))
11500 RETURN
12000 '**********  Change parameters for new layer depth
12020 EP = X0*US/15
12030 IF EP< = NU THEN PRINT "Mixed layer viscosity no longer
greater than stratified viscosity :  EP = "; EP : STOP
12040 TH = SQR(X0/6/L)
12050 L3 = SQR(W/2/EP)
12060 Y = 2*TH
12080 GOSUB 10000
12100 X = TH/1.4142
12120 S = SIN(X)
12140 C = COS(X)
12160 A3 =  - V*EXP(X)*(A2*KR + B2*KI)/C2/(C + S*S/C)
12180 B3 = A3*S/C
12200 X = X0*(L4 - L3)
12220 A4 = EXP(X)*(A3*COS(X) - B3*SIN(X))
12240 B4 = EXP(X)*(A3*SIN(X) + B3*COS(X))
12250 IF Q = 0 THEN RETURN
12260 LPRINT ">>>>> NEW Mixed layer depth        X0 = "; X0,
"cm"
12270 LPRINT "      Frictional layer depth     X0/6 = ";
X0/6, "cm"
```

```
12280 LPRINT "Effective viscosity in mixed layer EP = "; EP,
"cm2/sec"
12290 LPRINT
12300 LPRINT "Coefficients : ", "A3 = "; A3, "B3 = "; B3,
"cm/sec"
12310 LPRINT , "A4 = "; A4, "B4 = "; B4, "cm/sec"
12315 LPRINT
12318 IF Z<0 THEN GOTO  1400
12320 GOTO  6100
13000 '**********  Calculate min. k for K-H instability
13020 A = D(0)*D(I0)*(UU - S1/I0)*(UU - S1/I0)
13040 B = G*(D(0) - D(I0))
13060 ER = 1.01
13080 KD = .1
13120 K1 = 1
13130 IF K1*X0 > 87 THEN CT = 1 : GOTO  13180
13140 Y = EXP(K1*X0)
13160 CT = (Y + 1/Y) / (Y - 1/Y)
13180 Y1 = K1*B*(D(I0) + D(0)*CT) - A*K1*K1*CT
13200 IF Y1 = 0 THEN KK = K1 : RETURN
13210 IF Y1>0 THEN KK = 1E10 : RETURN
13220 K2 = K1*KD
13225 IF K2<.00001 THEN KK = 1E - 10 : RETURN
13230 IF K2*X0>87 THEN CT = 1 : GOTO  13280
13240 Y = EXP(K2*X0)
13260 CT = (Y + 1/Y)/(Y - 1/Y)
13280 Y2 = K2*B*(D(I0) + D(0)*CT) - A*K2*K2*CT
13300 IF Y2 = 0 THEN KK = K2 : RETURN
13320 IF Y2*Y1<0 THEN GOTO  13500
13400 K1 = K2
13420 Y1 = Y2
13440 GOTO  13220
13500 IF K1/K2<ER AND K2/K1<ER THEN KK = K1 : RETURN
13520 K3 = K1 - Y1*(K2 - K1)/(Y2 - Y1)
13530 IF K3*X0>87 THEN CT = 1 : GOTO  13580
13540 Y = EXP(K3*X0)
13560 CT = (Y + 1/Y)/(Y - 1/Y)
13580 Y3 = K3*B*(D(I0) + D(0)*CT) - A*K3*K3*CT
13600 IF K3 = K1 THEN KK = K1 : RETURN
13620 IF K3 = K2 THEN KK = K2 : RETURN
13640 IF ABS(Y3) < 1E - 5 THEN KK = K3 : RETURN
13660 IF Y1*Y3 < 0 THEN K2 = K3 : Y2 = Y3 : GOTO  13500
13680 K1 = K3 : Y1 = Y3 : GOTO  13500
14000 '**********  Calculate wave friction factor
14010 DEF FN U2(W, FW) = W*3*10[(.25/SQR(FW) +
.43429*LOG(.25/SQR(FW)) + .12)
14020 FD = .001
14030 E1 = .01
14040 E2 = .000001
14050 F1 = .0005
14060 Y1 = ABS(V) - FNU2(W, F1)
```

```
14070 II = 1
14080 IF ABS(Y1)<E1 THEN FW = F1 : RETURN
14090  :
14100 F2 = F1 + FD
14110 Y2 = ABS(V) - FNU2(W, F2)
14120 IF ABS(Y2)<E1 THEN FW = F2 : RETURN
14130 IF Y1*Y2<0 THEN GOTO  14220
14140 IF II<>1 THEN GOTO  14180
14150 IF ABS(Y2)>ABS(Y1) THEN FD =  - FD
14160 II = 2
14170  :
14180 F1 = F2
14190 Y1 = Y2
14200 GOTO  14100
14210  :
14220 IF ABS(F1 - F2)<E2 THEN FW = F1 : RETURN
14230 F3 = F1 - Y1*(F2 - F1)/(Y2 - Y1)
14240 Y3 = ABS(V) - FNU2(W, F3)
14250 IF F3 = F1 THEN FW = F1 : RETURN
14260 IF F3 = F2 THEN FW = F2 : RETURN
14270 IF ABS(Y3)<E1 THEN FW = F3 : RETURN
14280 IF Y1*Y3<0 THEN F2 = F3 : Y2 = Y3 : GOTO  14220
14290 F1 = F3 : Y1 = Y3 : GOTO  14220
```

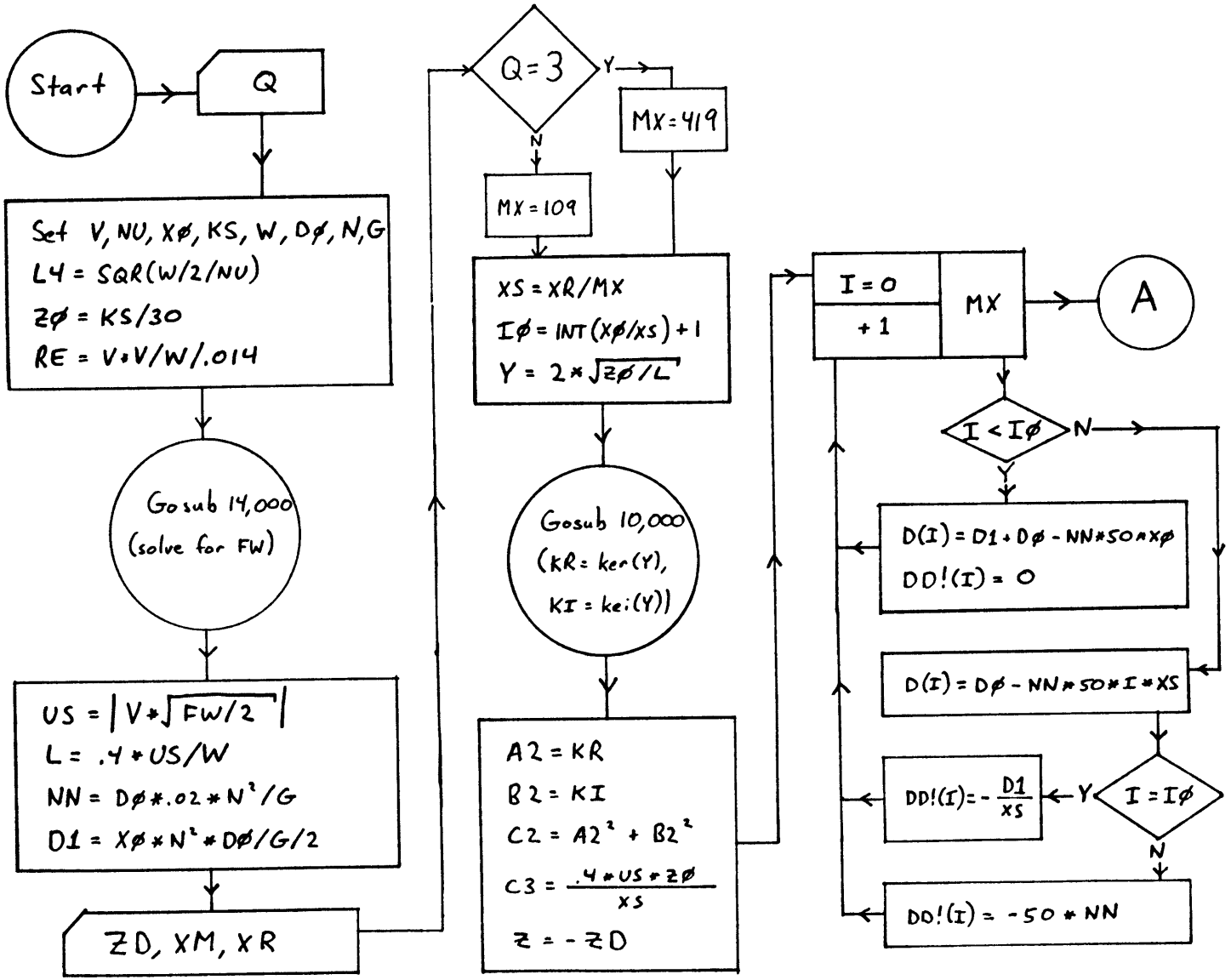
Start
Q
Set V, NU, XØ, KS, W, DØ, N, G
L4 = SQR(W/2/NU)
ZØ = KS/30
RE = V*V/W/.014
Gosub 14,000
(solve for FW)
US = |V*√FW/2|
L = .4*US/W
NN = DØ*.02*N²/G
D1 = XØ*N²*DØ/G/2
ZD, XM, XR
Q=3
Y
N
MX=419
MX=109
XS = XR/MX
IØ = INT(XØ/XS)+1
Y = 2*√ZØ/L
Gosub 10,000
(KR = ker(Y),
KI = kei(Y))
A2 = KR
B2 = KI
C2 = A2² + B2²
C3 = .4*US*ZØ / XS
Z = -ZD
I = 0
+1
MX
A
I < IØ
N
Y
D(I) = D1 + DØ - NN*50*XØ
DD!(I) = 0
D(I) = DØ - NN*50*I*XS
I = IØ
Y
DD!(I) = -D1/XS
N
DD!(I) = -50*NN

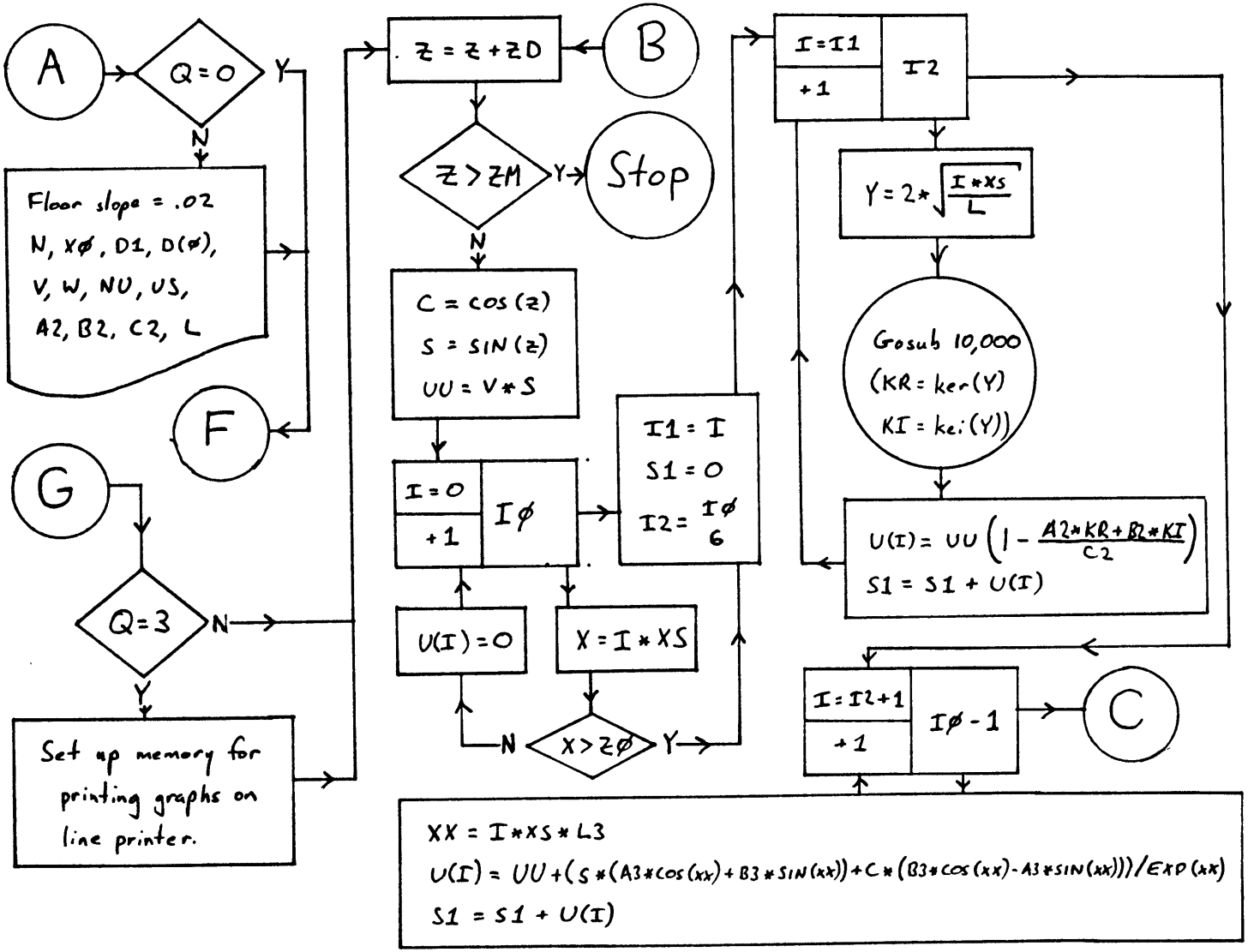
A
Q=0
Y
N
Floor slope = .02
N, XØ, D1, D(Ø),
V, W, NU, US,
A2, B2, C2, L
F
G
Q=3
N
Y
Set up memory for
printing graphs on
line printer.
Z = Z + ZD
B
Z > ZM
Y
Stop
N
C = cos(z)
S = SIN(z)
UU = V * S
I = 0
+1
IØ
I1 = I
S1 = 0
I2 = IØ/6
U(I) = 0
X = I * XS
N
X > ZØ
Y
I = I1
+1
I2
Y = 2 * √(I * XS / L)
Gosub 10,000
(KR = ker(Y)
KI = kei(Y))
U(I) = UU (1 - (A2*KR + B2*KI)/C2)
S1 = S1 + U(I)
I = I2+1
+1
IØ - 1
C
XX = I * XS * L3
U(I) = UU + (S * (A3 * cos(xx) + B3 * SIN(xx)) + C * (B3 * cos(xx) - A3 * SIN(xx))) / EXP(xx)
S1 = S1 + U(I)

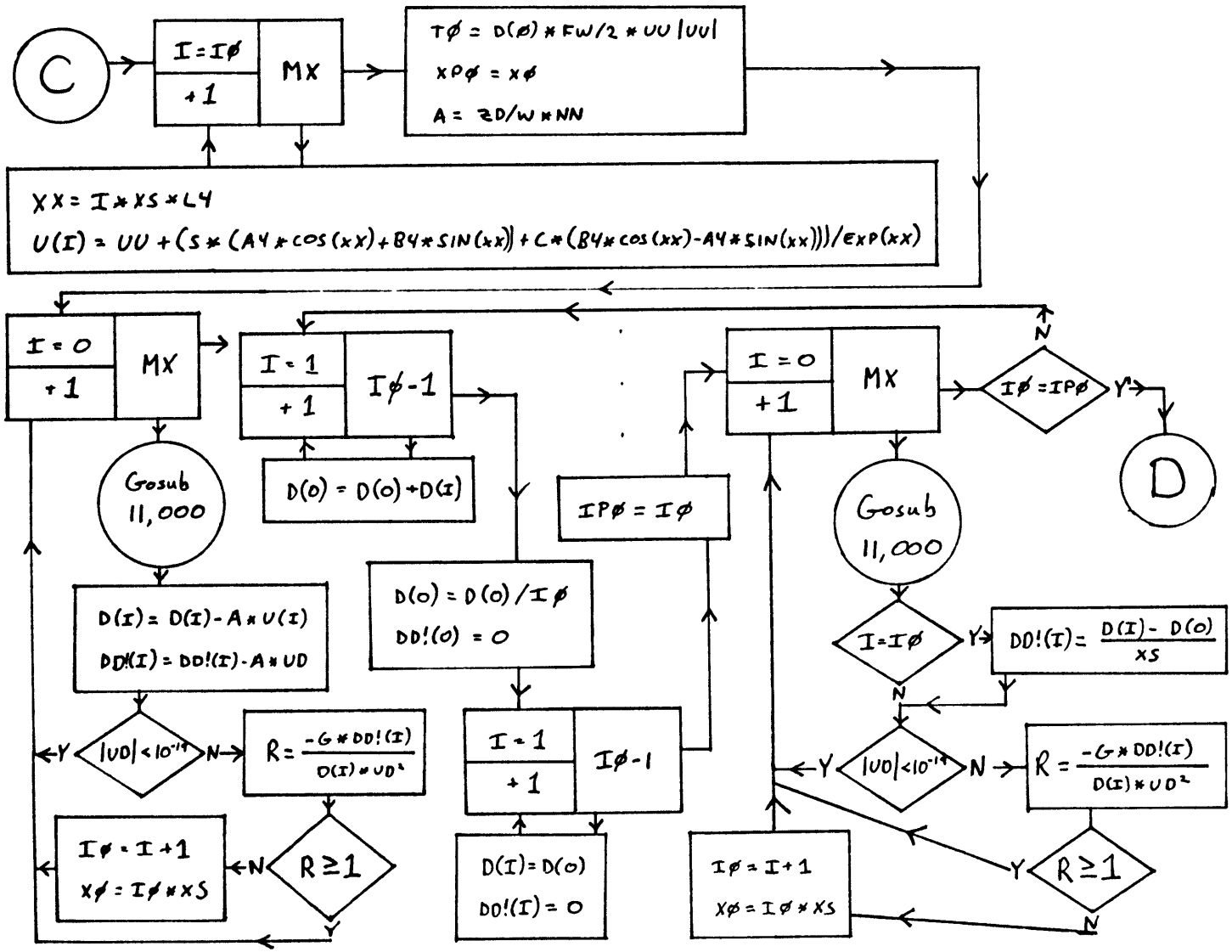
C
I=Iφ
+1
MX
Tφ = D(φ) * FW/2 * UU |UU|
XPφ = Xφ
A = ZD/W * NN
XX = I * XS * L4
U(I) = UU + (S * (A4 * cos(xX) + B4 * SIN(xx)) + C * (B4 * cos(xx) - A4 * SIN(xx)))/EXP(xX)
I = 0
+1
MX
I = 1
+1
Iφ-1
D(0) = D(0) + D(I)
Gosub 11,000
D(I) = D(I) - A * U(I)
DD!(I) = DD!(I) - A * UD
|UD| < 10^-14
Y
N
R = -G * DD!(I) / D(I) * UD^2
R ≥ 1
Iφ = I + 1
Xφ = Iφ * XS
D(0) = D(0)/Iφ
DD!(0) = 0
I = 1
+1
Iφ-1
D(I) = D(0)
DD!(I) = 0
IPφ = Iφ
I = 0
+1
MX
Iφ = IPφ
Y
N
D
Gosub 11,000
I = Iφ
Y
N
DD!(I) = (D(I) - D(0))/XS
|UD| < 10^-14
Y
N
R = -G * DD!(I) / D(I) * UD^2
R ≥ 1
Y
N
Iφ = I + 1
Xφ = Iφ * XS

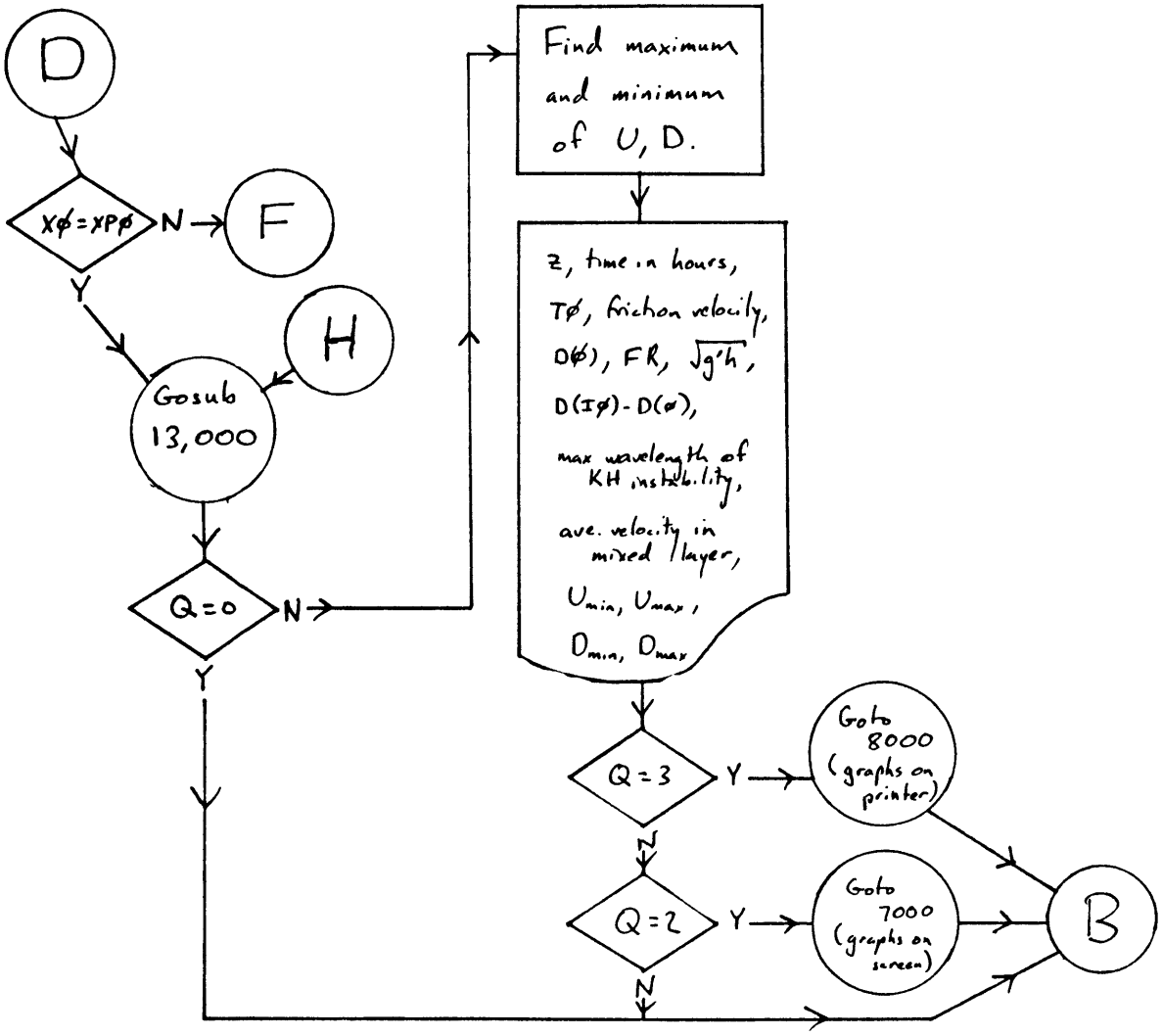
D
Xφ=XPφ
N
F
Y
H
Gosub
13,000
Q=0
N
Y
Find maximum
and minimum
of U, D.
z, time in hours,
Tφ, frichon velocity,
Dφ), FR, √g'h,
D(Iφ)-D(φ),
max wavelength of
KH instability,
ave. velocity in
mixed layer,
Umin, Umax,
Dmin, Dmax
Q=3
Y
Goto
8000
(graphs on
printer)
N
Q=2
Y
Goto
7000
(graphs on
screen)
N
B

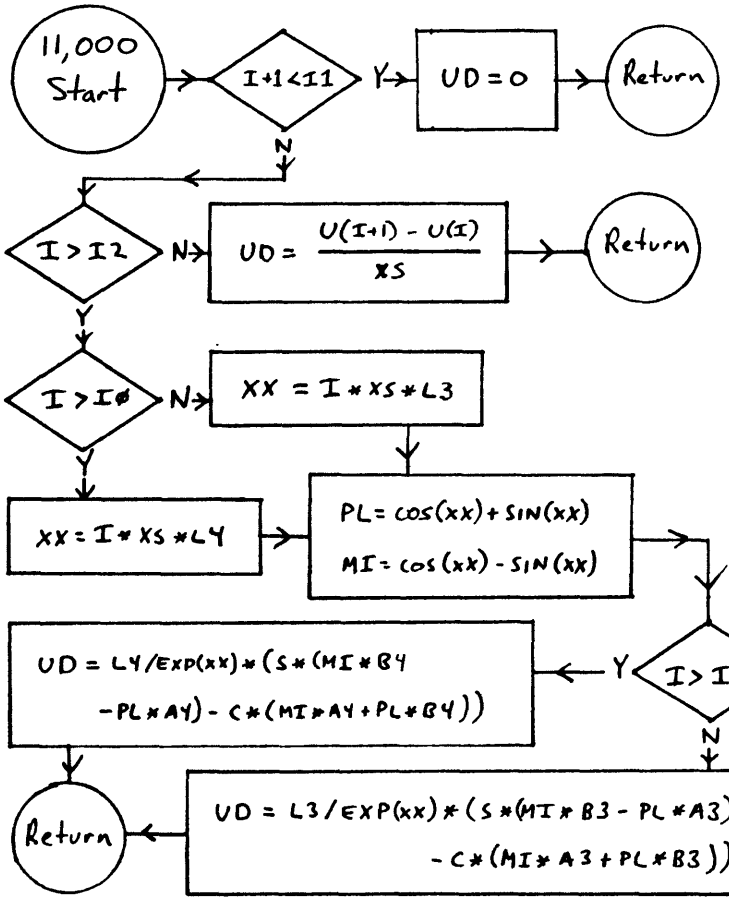

Subroutine calculates velocity gradients.

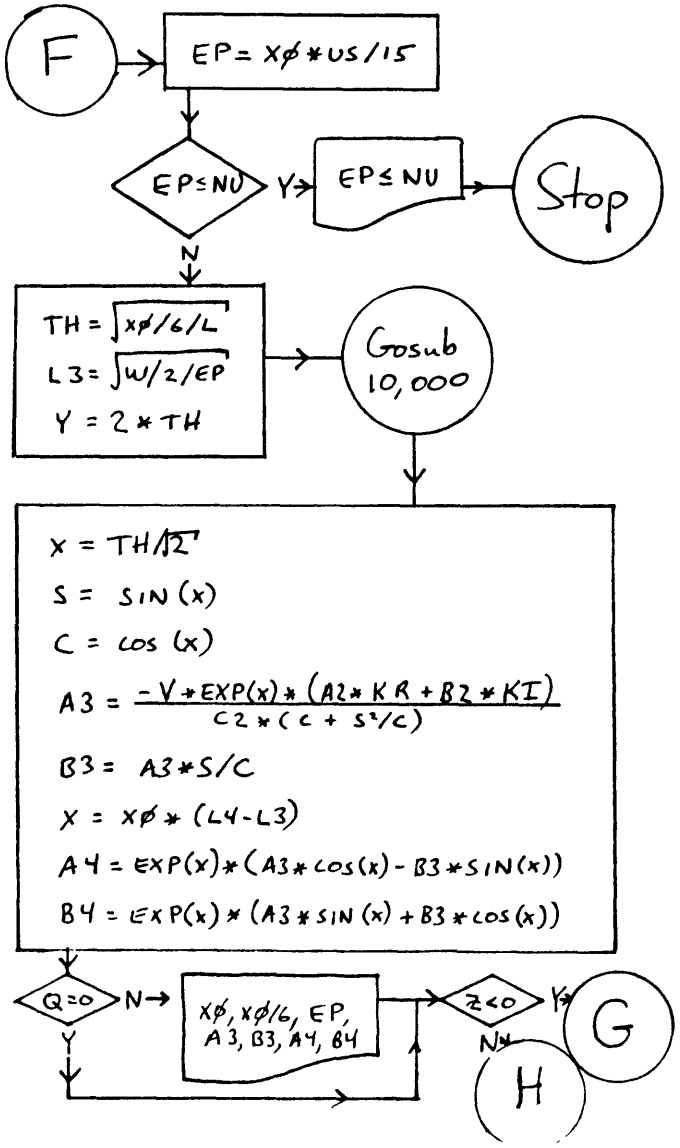

Subroutine calculates minimum k for K-H instability.

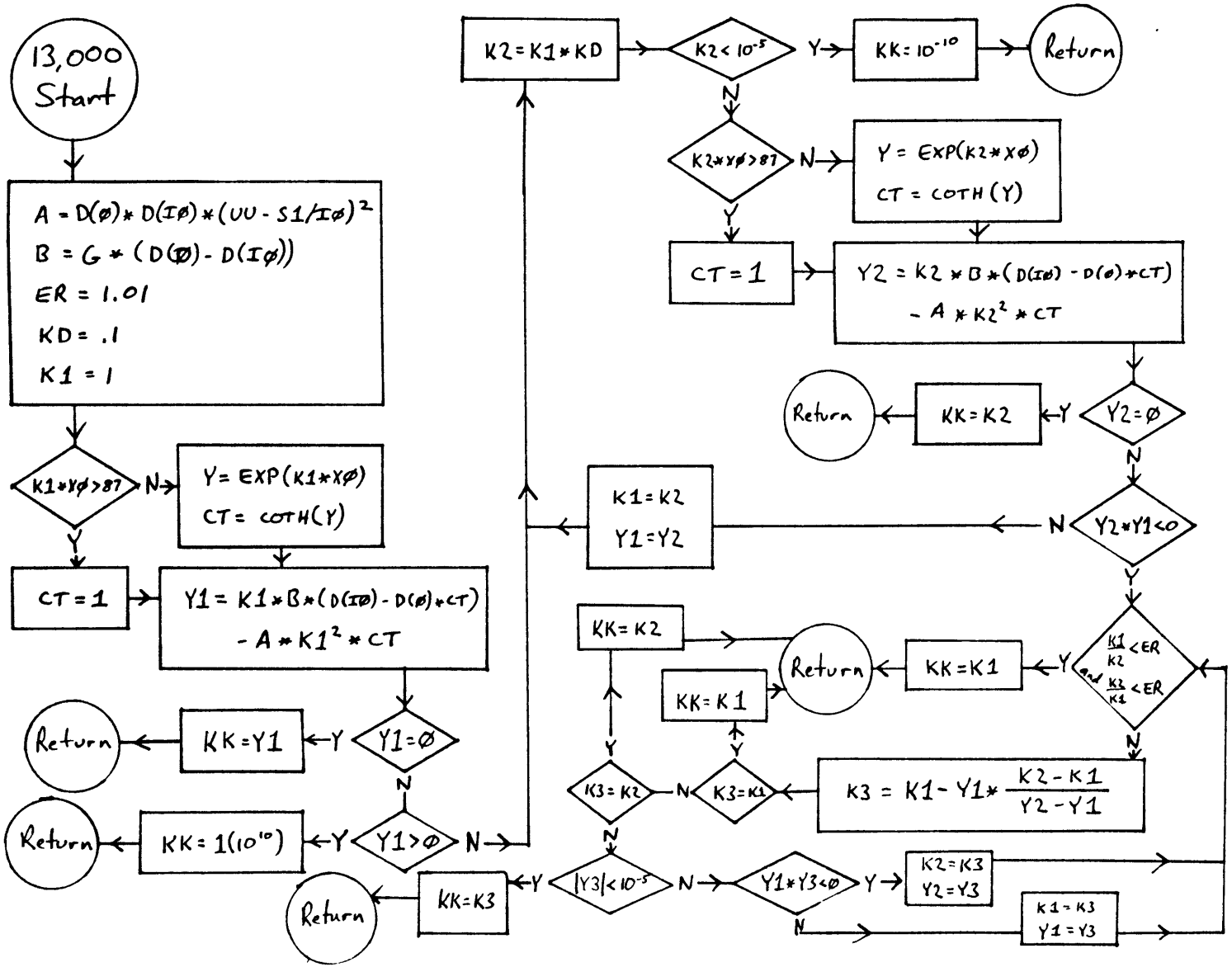

Subroutine calculates wave friction factor

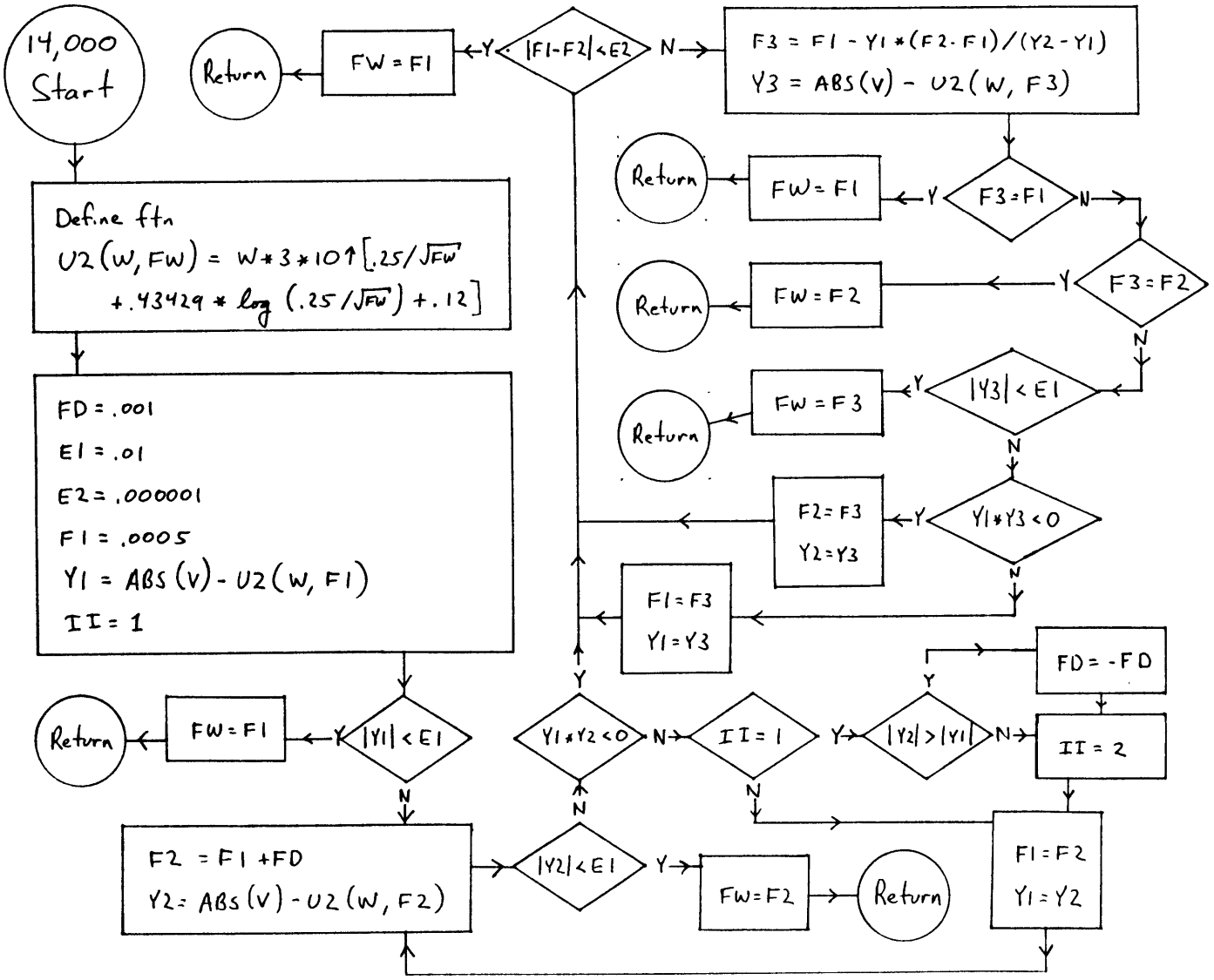

```
                00100 ;PROGRAM TO MAKE GRAPHS OF VELOCITY AND DENSITY
                00110 ;MEMORY = 65200
FF00            00120          ORG     0FF00H
                00130 ;INITIALIZE REGISTERS
FF00 010000     00140          LD      BC,0              ;CLR COUNTER
FF03 FD21DCFF   00150          LD      IY,0FFFFH-35      ;TOP OF BIT FILE
FF07 DD21E3FF   00160          LD      IX,0FFFFH-28      ;TOP OF VELOCITY FILE
                00170 ;SET PRINTER CARRIAGE TO CORRECT POSITION
FF0B 3E1B       00180 POSIT    LD      A,27              ;"ESC"
FF0D CD3B00     00190          CALL    3BH               ;PRINT
FF10 3E10       00200          LD      A,16              ;"POS"
FF12 CD3B00     00210          CALL    3BH               ;PRINT
FF15 DD7E01     00220          LD      A,(IX+1)          ;MSB OF POSITION INSTRUC.

FF18 CD3B00     00230          CALL    3BH               ;PRINT
FF1B DD7E00     00240          LD      A,(IX)            ;LSB OF POSITION INSTRUC.
FF1E CD3B00     00250          CALL    3BH               ;PRINT
FF21 1E00       00260          LD      E,0               ;CLEAR PRINT INSTRUC.
                00270 ;SET CTH BIT OF E
FF23 21DCFF     00280 BIT      LD      HL,0FFFFH-35      ;TOP OF BIT FILE
FF26 ED4A       00290          ADC     HL,BC             ;ADD COUNTER
FF28 7E         00300          LD      A,(HL)            ;BCTH BIT FILE ENTRY
FF29 83         00310          ADD     A,E               ;ADD OLD PRINT INSTR.
FF2A 5F         00320          LD      E,A               ;E NOW HAS CTH BIT SET
                00330 ;INCREMENT COUNTER BY ONE, INDEX BY TWO
FF2B 0C         00340          INC     C                 ;COUNTER
FF2C DD23       00350          INC     IX                ;INDEX
FF2E DD23       00360          INC     IX                ;INDEX
FF30 3E07       00370          LD      A,7               ;IF C=7 ...
FF32 B9         00380          CP      C
FF33 CA48FF     00390          JP      Z,PRINT           ;GOTO PRINT
                00400 ;IF POSITION VALUE HAS NOT CHANGED, SET NEXT BIT
FF36 DD7E00     00410          LD      A,(IX)            ;NEW POSITION VALUE (LSB)
FF39 DDBEFE     00420          CP      (IX-2)            ;IF NOT = LAST VALUE (LSB)
FF3C C248FF     00430          JP      NZ,PRINT          ;    ...JUMP TO PRINT
FF3F DD7E01     00440          LD      A,(IX+1)          ;NEW POSITION VALUE (MSB)
FF42 DDBEFF     00450          CP      (IX-1)            ;IF = LAST VALUE (MSB)...
FF45 CA23FF     00460          JP      Z,BIT             ;    ...CHECK NEXT BIT
                00470 ;PRINT GRAPHICS CHARACTER PER CURRENT VALUE OF E
FF48 CBFB       00480 PRINT    SET     7,E               ;SET REQUIRED 7TH BIT
FF4A 7B         00490          LD      A,E               ;READY...
FF4B CD3B00     00500          CALL    3BH               ;    ...PRINT
                00510 ;CHECK FOR EOF CONDITIONS
FF4E 21FFFF     00520          LD      HL,0FFFFH         ;EOF DENSITY
FF51 DD22D5FF   00530          LD      (0FFD5H),IX       ;PARK IX IN MEMORY
FF55 ED5BD5FF   00540          LD      DE,(0FFD5H)       ;THENCE TO DE
FF59 ED52       00550          SBC     HL,DE             ;IF IX=EOF DENSITY...
FF5B CA6CFF     00560          JP      Z,QUIT            ;    ...QUIT
FF5E 21F1FF     00570          LD      HL,0FFF1H         ;EOF VELOCITY
FF61 ED52       00580          SBC     HL,DE             ;IF NOT EOF VELOCITY ...
FF63 C20BFF     00590          JP      NZ,POSIT          ;    ...SET NEW POSITION
FF66 010000     00600          LD      BC,0              ;CLEAR COUNTER
FF69 C30BFF     00610          JP      POSIT             ;START DENSITY FILE
FF6C 3E0D       00620 QUIT     LD      A,13              ;CARRIAGE RETURN...
FF6E CD3B00     00630          CALL    3BH               ;    ...PRINT
FF71 C9         00650          RET
0000            00660          END
00000 Total Errors

QUIT    FF6C
PRINT   FF48
BIT     FF23
POSIT   FF0B
```

References

Abramowitz, M., and I.A. Stegun, eds., (1965) Handbook of Mathematical Functions with Formulas, Graphs, and Mathematical Tables, Dover, New York, 1046 pp.

Amos, A.F., T.N. Baker, and S.C. Daubin, Jr., (1977) Near-bottom currents and sediment transport in the Hudson Canyon, unpublished manuscript.

Baines, P.G., (1973) The generation of internal tides by flat-bump topography, Deep-Sea Research, 20, 179-205.

Baines, P.G., (1974) The generation of internal tides over steep continental slopes, Philosophical Transactions of the Royal Society of London, Series A, 277, 27-58.

Beardsley, R.C., and W.C. Boicourt, (1981) On estuarine and continental shelf circulation in the Middle Atlantic Bight, in Evolution of Physical Oceanography, B.A. Warren and C. Wunsch, eds., M.I.T. Press, Cambridge, pp. 198-233.

Bendat, J.S., and A.G. Piersol, (1971) Random Data: Analysis and Measurement Procedures, Wiley-Interscience, New York, 407 pp.

Benjamin, T.B., (1967) Internal waves of permanent form in fluids of great depth, Journal of Fluid Mechanics, 29, 559-592.

Biscaye, P.E., and R. Olsen, (1976) Suspended particulate concentrations and compositions in the New York Bight, Middle Atlantic Continental Shelf and the New York Bight, M. Grant Gross, ed., American Society of Limnologists and Oceanographers Special Symposium 2, 124-137.

Butman, B., M. Noble and D.W. Folger, (1979) Long-term observations of bottom current and bottom sediment movement on the Mid-Atlantic Continental Shelf, Journal of Geophysical Research, 84, 1187-1205.

Cacchione, D.A., G.T. Rowe, and A. Malahoff, (1978) Submersible investigation of outer Hudson Submarine Canyon, Sedimentation in Submarine Canyons, Fans and Trenches, D.J. Stanley and G. Kelling, eds., Dowden, Hutchinson and Ross, Stroudsburg, PA, pp. 42-50.

Cacchione, D.A. and C. Wunsch, (1974) Experimental study of internal waves over a slope, Journal of Fluid Mechanics, 66, 223-239.

Dillon, W.P., and H.B. Zimmerman, (1970) Erosion by biological activity in two New England submarine Canyons, Journal of Sedimentary Petrology, 40, 542-547.

Drake, D.E., P.G. Hatcher, and G.F. Keller, (1978) Suspended particulate deposition in upper Hudson Submarine Canyon, Sedimentation in Submarine Canyons, Fans and Trenches, D.J. Stanley and G. Kelling, eds., Dowden, Hutchinson and Ross, Stroudsburg, PA, pp. 33-41.

Eriksen, C.C., (1978) Measurements and models of fine structure, internal gravity waves, and wave breaking in the deep ocean, Journal of Geophysical Research, 83, 2989-3009.

Eriksen, C.C., (1982) Observations of internal wave reflection off sloping bottoms, Journal of Geophysical Research, 87, 525-538.

Farmer, D.M. and J.D. Smith, (1980) Tidal interaction of stratified flow with a sill in Knight Inlet, Deep-Sea Research, 27A, 239-254.

Flagg, C.N. and R.C. Beardsley, (1978) On the stability of the shelf water/slope water front south of New England, Journal of Geophysical Research, 83, 4623-4631.

Forde, E.B. (1981) Evolution of Veatch, Washington, and Norfolk Submarine Canyons: Inferences from strata and morphology, Marine Geology, 39, 197-214.

Freeland, G.L., and D.J.P. Swift, (1978) Surficial Sediments: MESA NY Bight Atlas Monograph 10, New York Sea Grant Institute.

Garrett, C.J.R. and W.H. Munk, (1972) Space-time scales of internal waves, Geophysical Fluid Dynamics, 2, 225-264.

Garrett, C.J.R. and W.H. Munk, (1975) Space-time scales of internal waves; a progress report, Journal of Geophysical Research, 80, 291-297.

Gordon, A.L., A.F. Amos, and R.D. Gerard, (1976) New York Bight water stratification - October 1974, Middle Atlantic Continental Shelf and the New York Bight, M. Grant Gross, ed., Special Sympositum Volume 2, The American Society of Limnology and Oceanography, Lawrence, KS, pp. 45-57.

Gordon, R.L., (1978) Internal wave climate near the coast of northwest Africa during JOINT-1, Deep-Sea Research, 25, 625-643.

Gordon, R.L., and N.F. Marshall, (1976) Submarine Canyons, internal wave traps?, Geophysical Research Letters, 3, 10, 622-624.

Graf, W.H. (1971) Hydraulics of Sediment Transport, McGraw-Hill, New York, 513 pp.

Grant, W.D. and O.S. Madsen, (1974) Combined wave and current interaction with a rough bottom. Journal of Geophysical Research, 84, 1797-1808.

Hotchkiss, F.L.S., (1980) Internal Gravity Waves and Sediment Transport in Hudson Submarine Canyon, S.M. Thesis, MIT, 116 pp.

Houghton, R.W., R. Schlitz, R.C. Beardsley, B. Butman, and J.C. Chamberlin, (1982) The Middle Atlantic Bight cold pool: Evolution of the temperature structure during summer 1979, submitted to the Journal of Physical Oceanography, 18 pp.

Inman, D.L., C.E. Nordstrom, and R.E. Flick, (1976) Currents in submarine canyons: an air-sea-land interaction, Annual Reviews of Fluid Mechanics, 8, 275-310.

Jonsson, I.G., (1966) Wave boundary layers and friction factors, Proceedings of the 10th Conference on Coastal Engineering, American Society of Civil Engineers, pp. 127-148.

Kajiura, K., (1968) A model of the bottom boundary layer in water waves, Bulletin of the Earthquake Research Institute, University of Tokyo, 46, 75-123.

Keller, G.H., D. Lambert, G. Rowe, and N. Staresinic, (1973) Bottom currents in Hudson Canyon, Science, 180, 181-183.

Keller, G.H., and F.P. Shepard, (1978) Currents and sedimentary processes in submarine canyons off the Northeast United States, in Sedimentation in Submarine Canyons, Fans and Trenches, D.J. Stanley and G. Kelling, eds., Dowden, Hutchinson and Ross, Stroudsburg, PA, pp. 15-32.

Kelling, G. and D.J. Stanley, (1976) Sedimentation in canyon, slope, and base-of-slope environments, Marine Sediment Transport and Environmental Management, D.J. Stanley and D.J.P. Swift, eds., Wiley, New York, pp. 379-435.

Komar, P.D., (1977) Computer simulation of turbidity current flow and the study of deep-sea channels and fan sedimentation, The Sea, Volume 6, E.D. Goldberg, I.I. McCave, J.J. O'Brien, J.H. Steele, eds., John Wiley & Sons, New York, pp. 603-621.

Lamb, H., (1945) Hydrodynamics, 6th ed., Dover, New York, 738 pp.

Madsen, O.S. (1976) Wave climate of the continental margin: Elements of its mathematical description. Marine Sediment Transport and Environmental Management, D.J. Stanley and D.J.P. Swift, eds., Wiley, New York, pp. 65-87.

Madsen, O.S., and W.D. Grant, (1976) Sediment transport in the coastal environment, Report No. 209, Ralph M. Parsons Laboratory for Water Resources and Hydrodynamics, Department of Civil Engineering, MIT, 105 pp.

Mayer, D.A., D.V. Hansen, and D.A. Ortman, (1979) Long-term current and temperature observations on the Middle Atlantic Shelf, Journal of Geophysical Research, 84, 1776-1792.

McKee, W.D., (1973) Internal-inertia waves in a fluid of variable depth, Proceedings of the Cambridge Philosophical Society, 73, 205-213.

Miller, A.R., 1950. A study of mixing processes over the edge of the continental shelf, Journal of Marine Research, 9, 145-160.

Miller, M.C., I.N. McCave, and P.D. Komar, 1977. Threshold of sediment motion under unidirectional currents, Sedimentology, 24, 507-527.

Mooers, C.N.K., R.W. Garvine, and W.W. Martin, (1979) Summertime synoptic variability of the Middle Atlantic shelf water/slope water front, Journal of Geophysical Research, 84, 4837-4854.

Ou, H.W. and R.C. Beardsley, (1980) On the propagation of free topographic Rossby Waves near continental margins. Part 2: Numerical Model, Journal of Physical Oceanography, 10, 1323-1339.

Pollard, R.J., P.B. Rhines, and R.O.R.Y. Thompson (1973) The deepening of the wind-mixed layer, Geophysical Fluid Dynamics, 3, 381-404.

Prinsenberg, S.J., W.L. Wilmot, and M. Rattray, (1974) Generation and dissipation of coastal internal tides, Deep-Sea Research, 21, 263-281.

Regal, R. and C. Wunsch, (1973) M tidal currents in the Western North Atlantic, Deep-Sea Research, 20, 493-502.

Ross, D.A., (1968) Current action in a submarine canyon, Nature, 218, 1242-1245.

Rowe, G.T., G. Keller, H. Edgerton, N. Staresnic, and J. MacIlvaine, (1974) Time-lapse photography of the biological reworking of sediments in Hudson Submarine Canyon, Journal of Sedimentary Petrology, 44, 549-552.

Ruzecki, E.P., (1979) On the Water Masses of Norfolk Canyon, Ph.D. thesis, University of Virginia, 293 pp.

Schlichting, H., (1979) Boundary Layer Theory, 7th ed., McGraw-Hill, New York, 817 pp.

Schroeder, E.H., (1966) Average surface temperatures of the Western North Atlantic, Bulletin of Marine Science, 16, 302-323.

Shepard, F.P., (1973) Submarine Geology, Harper and Row, New York, 517 pp.

Shepard, F.P., and G.V. Cohee, (1936) Continental-shelf sediments off the Mid-Atlantic States, Bulletin of the Geological Society of America, 47, 441-458.

Shepard, F.P. and R.F. Dill, (1966) Submarine Canyons and Other Sea Valleys, Rand McNally, Chicago, 381 pp.

Shepard, F.P., N.F. Marshall, P.A. McLoughlin, G.G. Sullivan, (1979) Currents in Submarine Canyons and Other Sea Valleys, American Association of Petroleum Geologists Studies in Geology, no. 8, Tulsa, OK, 173 pp.

Smith, J.D., (1977) Modeling of sediment transport on continental shelves, The Sea, E.D. Goldberg, I.N. McCave, J.J. O'Brien, and J.H. Steele, eds., 6, 539-537.

Stanley, D.J., (1967) Comparing patterns of sedimentation in some modern and ancient submarine canyons. Earth and Planetary Science Letters, 3, 371-380.

Stanley, D.J., (1974) Pebbly mud transport in the head of Wilmington Canyon, Marine Geology, 16, M1-M8.

Stanley, D.J., and G. Kelling, eds., Sedimentation in Submarine Canyons, Fans and Trenches, Dowden, Hutchinson and Ross, Stroudsburg, PA, 395 pp.

Stanley, E.M. and R.C. Batten, (1969) Viscosity of sea water at moderate temperatures and pressures, Journal of Geophysical Research, 74, 3415-3420.

Stern, M.E., (1975) Ocean Circulation Physics, Academic Press, New York, 246 pp.

Thompson, R.O.R.Y., (1980) Efficiency of conversion of kinetic energy to potential energy by a breaking internal gravity wave. Journal of Geophysical Research, 85, 6631-6635.

Turner, J.S., (1973) Buoyancy Effects in Fluids, Cambridge University Press, 367 pp.

Uchupi, E., (1963) Sediments on the continental margin off Eastern United States, U.S. Geological Survey Professional Paper 475-C, C132-C137.

Uchupi, E., (1965) Map showing relation of land and submarine topography, Nova Scotia to Florida, U.S. Geological Survey, Miscellaneous Geological Investigation, Map Series, I-451.

Wang, D-P., (1979) Low frequency sea level variability on the Middle Atlantic Bight, Journal of Marine Research, 37, 683-697.

Welch, C.S., (1981) Mid-level intrusions at the continental shelf edge, Journal of Geophysical Research, 86, 11013-11019.

Wunsch, C., (1969) Progressive internal waves on slopes, Journal of Fluid Mechanics, 35, 131-144.

Wunsch, C., (1975) Internal tides in the ocean, Reviews of Geophysics and Space Physics, 13, 167-182.

Wunsch, C., (1976) Geophysical variability of the internal wave field: a search for sources and sinks, Journal of Physical Oceanography, 6, 471-485.

Wunsch, C., and S. Webb, (1979) The climatology of deep ocean internal waves, Journal of Physical Oceanography, 9, 235-243.

Zenk, W., and M.G. Briscoe, (1974) The Cape Cod experiment on near-surface internal waves, WHOI Technical Report 74-87, 56 pp.

Biographical Statement

Frances S. Hotchkiss was born in 1954 in Albuquerque, New Mexico, and grew up in Alabama and Tennessee. She has a B.A. in geology and physics from Oberlin College and an M.S. in physical oceanography from MIT. Her graduate work in the Joint Program has been supported in part by a National Science Foundation Graduate Fellowship. Fran is married to the Reverend Daniel D. Hotchkiss, who is minister of the Unitarian Universalist Fellowship of Boca Raton, Florida.